Introduction to climate dynamics and climate modelling

Goosse H., P.Y. Barriat, W. Lefebvre, M.F. Loutre, and V. Zunz

If you want to cite this textbook, please use the following reference:

Goosse H., P.Y. Barriat, W. Lefebvre, M.F. Loutre, and V. Zunz (2010). Introduction to climate dynamics and climate modeling. Online textbook available at http://www.climate.be/textbook.

Université catholique de Louvain
Institut d'Astronomie et de Géophysique Georges Lemaître
2 Chemin du Cyclotron
B-1348 Louvain-la-Neuve
Belgium

Contents

Preface

The climate has a significant impact on life on Earth as well as on human activities. Temperature and precipitation strongly constrain the type of vegetation that could grow in a particular region. The design and location of houses depend on summer and winter temperatures but also on the probability of flooding. One single late frost or a heavy hail storm could ruin an entire crop. Since the beginning of humanity, people had thus to cope with climate and, if possible, to adapt to it. As a consequence, the various human civilisations have observed and have tried to understand the climate variations. They first provide mythological or religious explanations, often relying on weather lore to obtain forecast. In parallel, climate has evolved as a science, elaborating more and more sophisticated representations of the observed phenomena. Such a description of climate involves now a very broad range of expertise, corresponding to different domains of the sciences including physics, chemistry, biology and geology.

A comprehensive analysis of all the components of the climate system (atmosphere, ocean, ice sheets, etc) and of all the interactions between them is out of the scope of any course or book. We have thus chosen here to provide only a brief overview of the processes that rule the behaviour of those different components. More detailed descriptions are provided in meteorology, oceanography and glaciology courses, for instance. Our first goal here is rather to provide enough information on the interactions between the different elements of the climate system and on the dominant feedbacks to allow the student to analyse the variability of the climate and its response to a perturbation. By this mean, the reader should be able to understand the dominant causes of past climate changes and to critically evaluate the projections of the climate change over the next centuries or millennia.

Because of the complexity of the climate system, many analyses devoted to a quantitative estimate of climate change or climate variability rely on the use of comprehensive three-dimensional numerical models. However, simple models are also widely used to underline clearly the fundamental properties of the climate. Our second goal is thus to give the student the bases to understand how climate model are built and how they could be used to make quantitative estimate of climate variability and climate change as well as to illustrate how models could be used to understand the most important concepts of climate science.

At the origin, this textbook was designed as a support to a course proposed to students in their first year of Master at the Université catholique de Louvain. However, the majority of the sections could already be followed by undergraduate students. Quizzes including questions that provide an overview of the matter covered in the different chapters are available online. If you are able to answer all of them, this likely shows that you have not missed the most important elements of the discussion. As the textbook is devoted to an audience presenting different backgrounds, some fundamental terms or concepts, highlighted using **bold** characters, are explicated in the glossary. If you do not understand some terms or notion, do not hesitate to contact us so that we could append the glossary.

In addition to the material freely proposed online, the UCL students registered for the course PHY2153 “Introduction à l’étude du système climatique et à sa modélisation” will also receive some practical information on the course, including a precise list of the chapters or sections of the online textbook that will be studied during the academic year. Registered students are also encouraged to answer the quizzes on the virtual campus of UCL rather than on the textbook web site.

Acknowledgements

Many colleagues have read carefully the various sections of this online textbook and suggested modifications that improved significantly the quality of the published material. We would like to thank particularly André Berger, Victor Brovkin, Michel Crucifix, Eric Deleersnijder, Anne de Montety, Thierry Fichefet, Hans Renssen, Benoit Tartinville and Kevin Trenberth. We benefit of very useful advices from Françoise Docq, Marcel Lebrun, Denis Smidts of the Institut de Pédagogie universitaire et des Multimédias of the Université catholique de Louvain (IPM, http://www.ipm.ucl.ac.be). Antoine Barthélemy helped in the introduction of revisions in the text and on the textbook web site. We also want to acknowledge the organisations, publishers and scientists who allow us to reproduce their work without any charge. This work is supported by the Fonds de Développement Pédagogique of the Université catholique de Louvain in the framework of the project: "Réalisation de simulations interactives comme support à l'apprentissage dans le cadre du cours d'introduction à la physique du système climatique et à sa modélisation."

Chapter 1. Description of the climate system and its components

1.1 Introduction

Climate is traditionally defined as the description in terms of the mean and variability of relevant atmospheric variables such as temperature, precipitation and wind. Climate can thus be viewed as a synthesis or aggregate of weather. This implies that the portrayal of the climate in a particular region must contain an analysis of mean conditions, of the seasonal cycle, of the probability of extremes such as severe frost and storms, etc. Following the World Meteorological Organisation (WMO), 30 years is the classical period for performing the **statistics** used to define climate. This is well adapted for studying recent decades since it requires a reasonable amount of data while still providing a good sample of the different types of weather that can occur in a particular area. However, when analysing the most distant past, such as the last glacial maximum around 20 000 years ago, climatologists are often interested in variables characteristic of longer time intervals. As a consequence, the 30-year period proposed by the WMO should be considered more as an indicator than a norm that must be followed in all cases. This definition of the climate as representative of conditions over several decades should, of course, not mask the fact that climate can change rapidly. Nevertheless, a substantial time interval is needed to observe a difference in climate between any two periods. In general, the less the difference between the two periods, the longer is the time needed to be able to identify with confidence any changes in the climate between them.

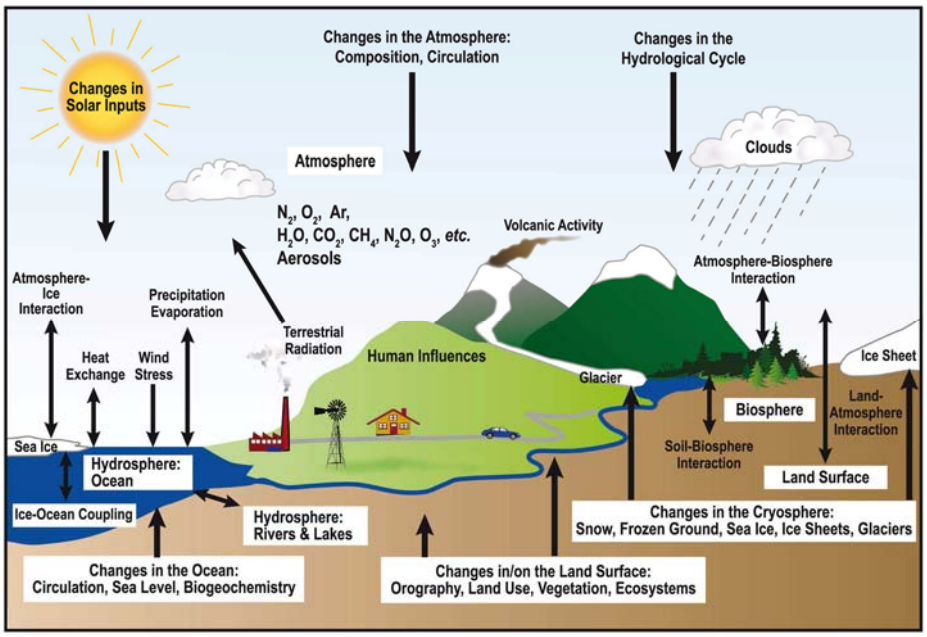

Figure 1.1: Schematic view of the components of the climate system and of their potential changes. FAQ 1.2, figure 1 from IPCC (2007) using a modified legend, published in: Climate Change 2007: The Physical Science Basis. Contribution of Working Group I to the Fourth Assessment Report of the Intergovernmental Panel on Climate Change, Cambridge University Press, copyright IPCC 2007. Reproduced with permission.

We must also take into account the fact that the state of the atmosphere used in the definition of the climate given above is influenced by numerous processes involving not only the atmosphere but also the ocean, the sea ice, the vegetation, etc. Climate is thus now more and more frequently defined in a wider sense as the statistical description of the **climate system**. This includes the analysis of the behaviour of its five major components: the atmosphere (the gaseous envelope surrounding the Earth), the **hydrosphere** (liquid water, i.e. ocean, lakes, underground water, etc), the **cryosphere** (solid water, i.e. **sea ice**, glaciers, ice sheets, etc), the land surface and the **biosphere** (all the living organisms), and of the interactions between them (IPCC 2007, Fig. 1.1). We will use this wider definition when we use the word **climate**. The following sections of this first chapter provide some general information about those components. Note that the climate system itself is often considered as part of the broader **Earth System**, which includes all the parts of the Earth and not only the elements that are directly or indirectly related to the temperature or precipitation.

1.2 The atmosphere

1.2.1 Composition and temperature

Dry air is mainly composed of nitrogen (78.08 % in volume), oxygen (20.95% in volume), argon (0.93% in volume) and to a lesser extent carbon dioxide[1] (380 ppm or 0.038% in volume). The remaining fraction is made up of various trace constituents such as neon (18 ppm), helium (5 ppm), methane[1] (1.75 ppm), and krypton (1 ppm). In addition, a highly variable amount of water vapour is present in the air. This ranges from approximately 0% in the coldest part of the atmosphere to as much as 5% in moist and hot regions. On average, water vapour accounts for 0.25% of the mass of the atmosphere.

On a large-scale, the atmosphere is very close to **hydrostatic equilibrium**, meaning that at a height z, the force due to the pressure p on a 1 m^2 horizontal surface balances the force due to the weight of the air above z. The atmospheric pressure is thus at its maximum at the Earth's surface and the surface pressure p_s is directly related the mass of the whole air column at a particular location. Pressure then decreases with height, closely following an exponential law:

$$p \simeq p_s e^{-z/H} \tag{1.1}$$

where H is a scale height (which is between 7 and 8 km for the lowest 100 km of the atmosphere). Because of this clear and monotonic relationship between height and pressure, pressure is often used as a vertical coordinate for the atmosphere. Indeed, pressure is easier to measure than height and choosing a pressure coordinate simplifies the formulation of some equations.

The temperature in the **troposphere**, roughly the lowest 10 km of the atmosphere, generally decreases with height. The rate of this decrease is called the **lapse rate** Γ:

$$\Gamma = -\frac{\partial T}{\partial z} \tag{1.2}$$

where T is the temperature. The lapse rate depends mainly on the radiative balance of the atmosphere (see section 2.1) and on **convection** as well as on the horizontal heat transport. Its global mean value is about 6.5 K km^{-1}, but Γ varies with the location and season.

[1] The concentrations of carbon dioxide and methane are changing quickly (see section 2.3).

The lapse rate is an important characteristic of the atmosphere. For instance, it determines its vertical stability. For low values of the lapse rate, the atmosphere is very stable, inhibiting vertical movements. Negative lapse rates (i.e. temperature increasing with height), called temperature inversions, correspond to highly stable conditions. When the lapse rate rises, the stability decreases, leading in some cases to vertical instability and convection. The lapse rate is also involved in **feedbacks** playing an important role in the response of the climate system to a perturbation (see section 4.2.1).

At an altitude of about 10 km, a region of weak vertical temperature **gradients**, called the **tropopause**, separates the **troposphere** from the **stratosphere** where the temperature generally increases with height until the stratopause at around 50 km (Fig. 1.2). Above the stratopause, temperature decreases strongly with height in the mesosphere, until the mesopause is reached at an altitude of about 80 km, and then increases again in the thermosphere above this height. The vertical **gradients** above 10 km are strongly influenced by the absorption of solar **radiation** by different atmospheric constituents and by chemical reactions driven by the incoming light. In particular, the warming in the stratosphere at heights of about 30-50 km is mostly due to the absorption of ultraviolet **radiation** by stratospheric **ozone**, which protects life on Earth from this dangerous **radiation**.

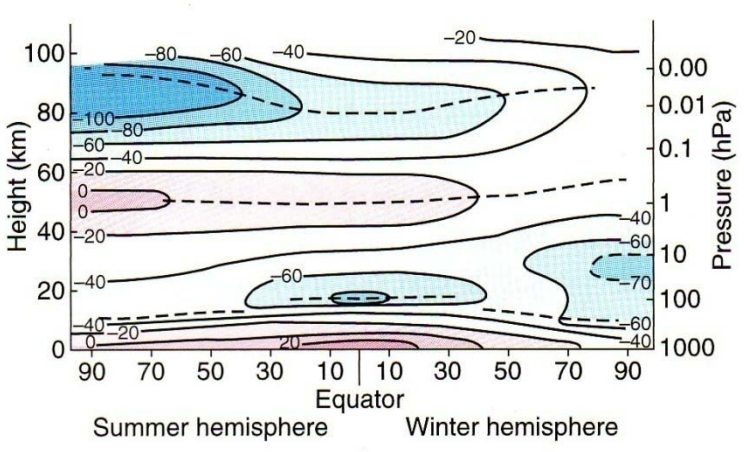

Figure 1.2: Idealised **zonal** mean temperature (in °C) in the atmosphere as a function of the height (or of the pressure). The dashed lines represent schematically the location of the tropopause, stratopause and mesopause. This figure was published in Atmospheric science: an introductory survey, Wallace and Hobbs, International Geophysics Series 92, Copyright Elsevier (Academic Press) 2006.

Atmospheric **specific humidity** also displays a characteristic vertical profile with maximum values in the lower levels and a marked decrease with height. As a consequence, the air above the tropopause is nearly dry. This vertical distribution is mainly due to two processes. First, the major source of atmospheric water vapour is evaporation at the surface. Secondly, the warmer air close to the surface can contain a much larger quantity of water before it becomes saturated than the colder air further away; saturation that leads to the formation of water or ice droplets, clouds and eventually precipitation.

At the Earth's surface, the temperature reaches its maximum in equatorial regions (Fig. 1.3) because of the higher incoming radiations (see section 2.1). In those regions, the temperature is relatively constant throughout the year. Because of the much stronger seasonal cycle at mid and high latitudes, the north-south gradients are much larger in winter than in summer. The distribution of the surface temperature is also influenced by

atmospheric and oceanic heat transport as well as by the thermal inertia of the ocean (see section 2.1.5). Furthermore, the role of topography is important, with a temperature decrease at higher altitudes associated with the positive lapse rate in the troposphere.

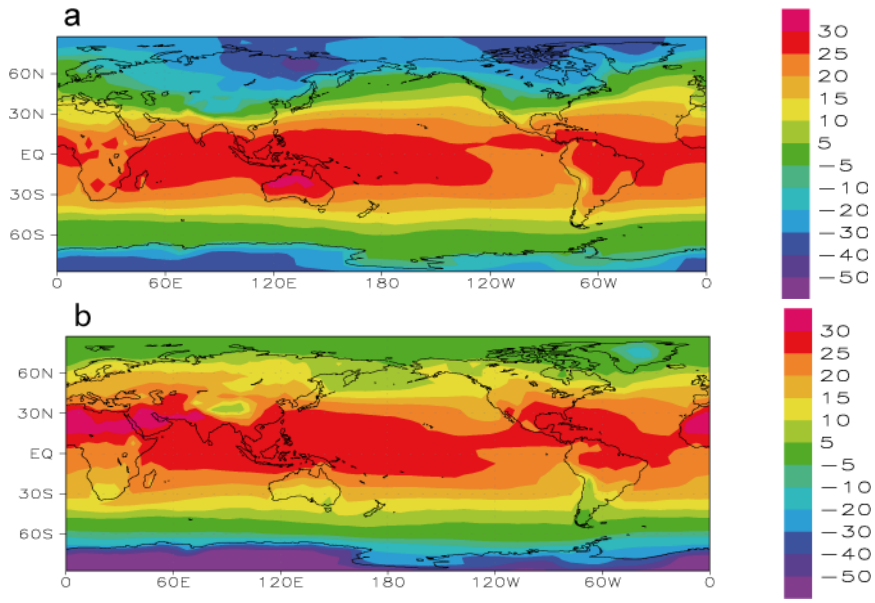

Figure 1.3: Surface air temperature (in °C) averaged over (a) December, January, and February and (b) June, July, and August. Data source : Brohan et al. (2005). http://www.cru.uea.ac.uk/cru/data/temperature/.

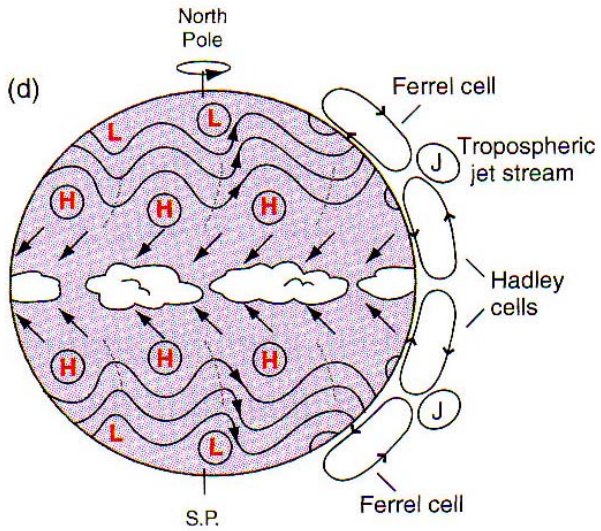

Figure 1.4: Schematic representation of the annual mean general atmospheric circulation. H (L) represents high (low) pressure systems. This figure was published in Atmospheric science: an introductory survey, Wallace and Hobbs, International Geophysics Series 92, Copyright Elsevier (Academic Press) 2006.

1.2.2 General circulation of the atmosphere

The high temperatures at the equator make the air there less dense. It thus tends to rise before being transported poleward at high altitudes in the **troposphere**. This motion is compensated for at the surface by an equatorward displacement of the air. On a motionless Earth, this big **convection** cell would reach the poles, inducing direct exchanges between the warmest and coldest places on Earth. However, because of the Earth's rotation, such an atmospheric structure would be unstable. Consequently, the two cells driven by the **ascendance** at the Equator, called the **Hadley cells**, close with a downward branch at a latitude of about 30° (Fig. 1.4). The northern boundary of these cells is marked by strong westerly winds in the upper troposphere called the tropospheric jets. At the surface, the Earth's rotation is responsible for a deflection toward the right in the northern hemisphere and toward the left in the southern hemisphere (due to the **Coriolis force**) of the flow coming from the mid-latitudes to the Equator. This gives rise to the easterly **trade winds** characteristics of the tropical regions (Fig. 1.5).

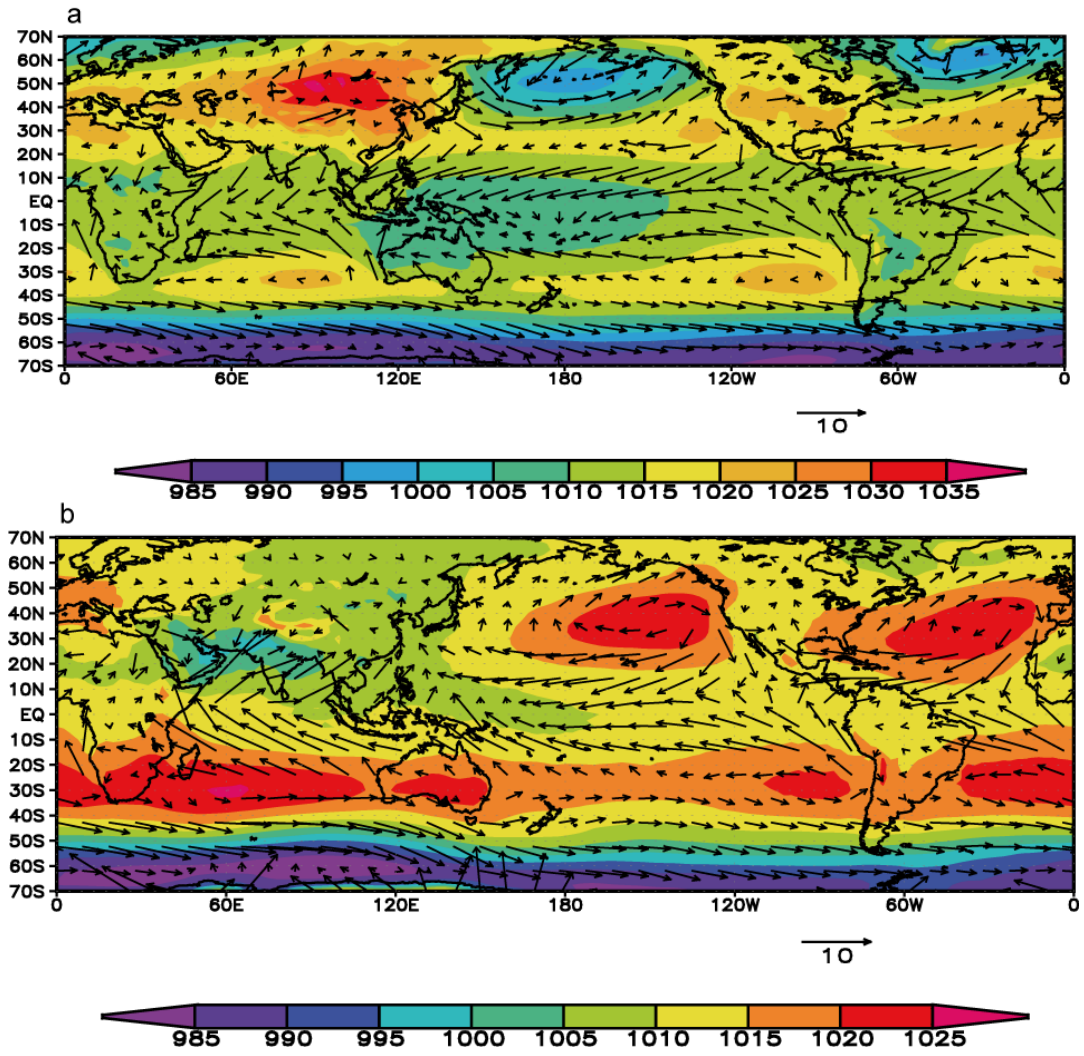

Figure 1.5: 10m winds (arrows, in m/s) and sea level pressure (colours, in hPa) in (a) December, January, and February and (b) June, July, and August. Data source: NCEP/NCAR **reanalyses** (Kalnay et al. 1996).

The extratropical circulation is dominated at the surface by westerly winds whose **zonal** symmetry is perturbed by large wave-like patterns and the continuous succession of disturbances that governs the day-to-day variations in the weather in these regions. The

dominant feature of the **meridional** circulation at those latitudes is the Ferrell cell, which is weaker than the **Hadley cell**. As it is characterized by rising motion in its poleward branch and downward motion in the equator branch, it is termed an indirect cell by contrast with the Hadley cell, which is termed a direct cell.

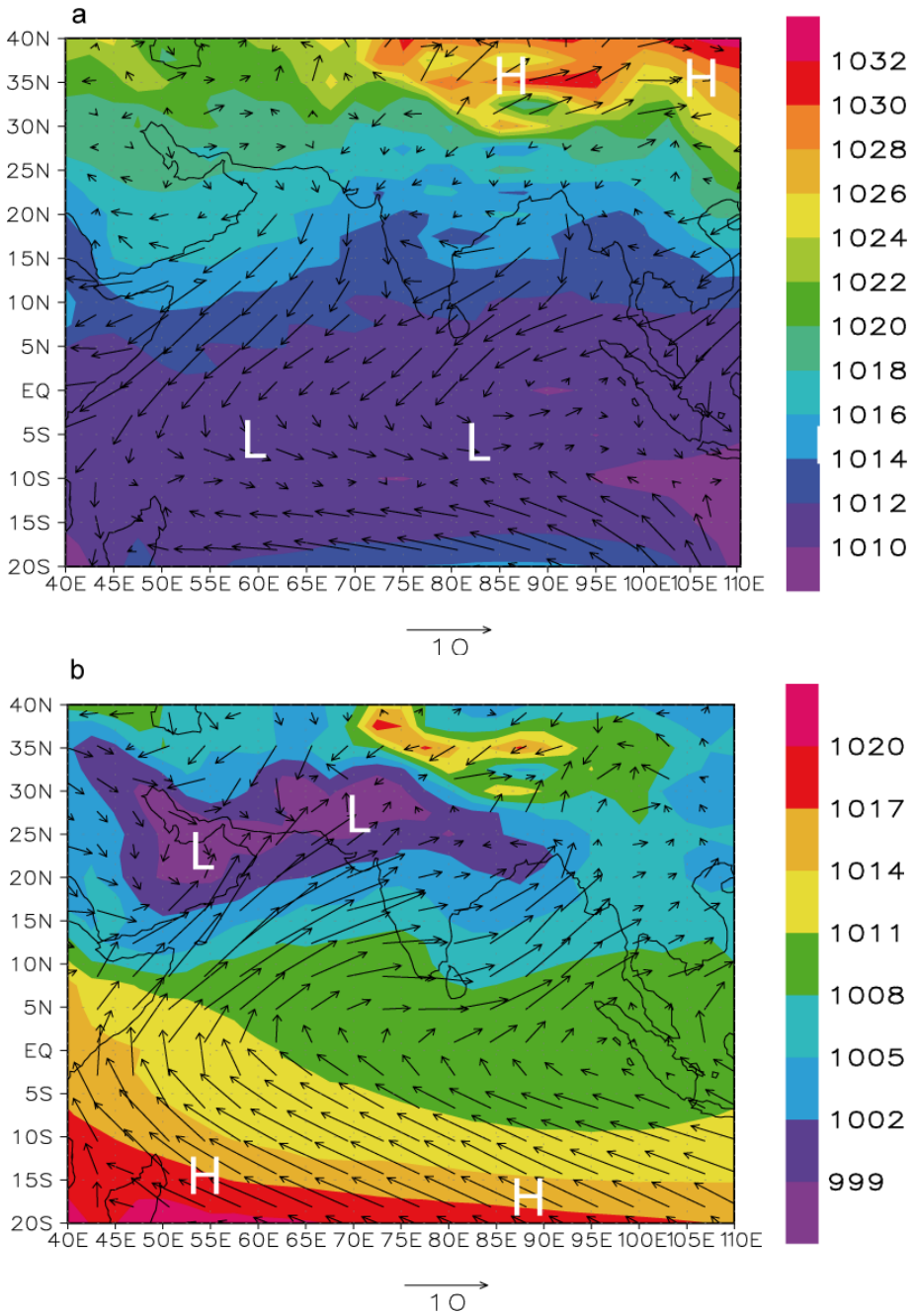

Figure 1.6: 10 m winds (arrows, in m/s) and sea level pressure (colours, in hPa) in (a) January and (b) July illustrating the wind reversal between the winter and the summer monsoon. Data source: NCEP/NCAR **reanalyses** (Kalnay et al. 1996).

Outside a narrow equatorial band and above the **surface boundary layer**, the large-scale atmospheric circulation is close to **geostrophic equilibrium**. The surface pressure and winds are thus closely related. In the Northern Hemisphere, the winds rotate clockwise around a high pressure and conterclockwise around a low pressure, while the

reverse is true in the Southern Hemisphere. Consequently, the mid-latitude westerlies are associated with high pressure in the subtropics and low pressure at around 50-60°. Rather than a continuous structure, this subtropical high pressure belt is characterised by distinct high pressure centres, often referred to by the name of a region close to their maximum (e.g., Azores high and St Helena high). In the Northern Hemisphere, the low pressures at around 50-60°N manifest themselves on **climatological** maps as cyclonic centres called the Icelandic low and the Aleutian low. In the Southern Ocean, because of the absence of large land masses in the corresponding band of latitude, the pressure is more zonally homogenous, with a minimum in surface pressure around 60°S.

In the real atmosphere, the convergence of surface winds and the resulting **ascendance** does not occur exactly at the equator but in a band called the **Intertropical Convergence Zone** (ITCZ). Because of the present geometry of the continents, it is located around 5°N, with some seasonal shifts. The presence of land surfaces also has a critical role in **monsoon** circulation. In summer, the continents warm faster than the oceans because of their lower thermal inertia (see section 2.1.5). This induces a warming of the air close to the surface and a decrease in surface pressure there. This pressure difference between land and sea induces a transport of moist air from the sea to the land. In winter, the situation reverses, with high pressure over the cold continent and a flow generally from land to sea. Such a monsoonal circulation, with seasonal reversals of the wind direction, is present in many tropical areas of Africa, Asia and Australia. Nevertheless, the most famous monsoon is probably the South Asian one that strongly affects the Indian sub-continent (Fig. 1.6).

1.2.3 Precipitation

The large-scale atmospheric circulation has a strong influence on precipitation, which is, with temperature, the most important variable in defining the climate of a region. Along the ITCZ, the cooling of warm and moist surface air during its rising motion leads to condensation and heavy precipitation in this area. For instance, the western tropical Pacific receives more than 3 m of rainfall per year. By contrast, the downward motion in the subtropics is associated with the presence of very dry air and very low precipitation rates. As a consequence, the majority of the large deserts on Earth are located in the sub-tropical belt.

The **monsoon** strongly affects the precipitation over subtropical continents. During the winter **monsoon**, the inflow of dry continental air is associated with low precipitation. On the other hand, the summer brings moist air from the ocean inducing rainfall that can reach several metres in a few months. The topography also plays a large role as it can generate significant vertical motion. Where **ascendance** of moist air is topographically induced, massive precipitation can occur, as on the slopes of the Himalaya during the summer monsoon. If **subsidence** of dry air is generated at a location because of the mountains nearby, the precipitation will be lower, even contributing to the presence of a desert. Mountains are also barriers to moist air coming from oceanic regions. In this framework, the distance from the oceanic source must also be taken into account when studying the precipitation regime in a region. This explains why, for example, rainfall is less in central Asia than in western Europe at the same latitude.

Notable features are also present over the ocean, for instance the South Pacific Convergence Zone (SPCZ) associated with the high precipitation rates in a NW-SE band from Indonesia towards 30°S, 130W. In the mid-latitudes, precipitation in winter is mainly due to **cyclones**, which tend to follow a common path at about 45°N in the Pacific and the Atlantic. This **storm track** manifests itself as maximum rainfall in this region. These effects are visible in the precipitation maps reproduced in Fig. 1.7.

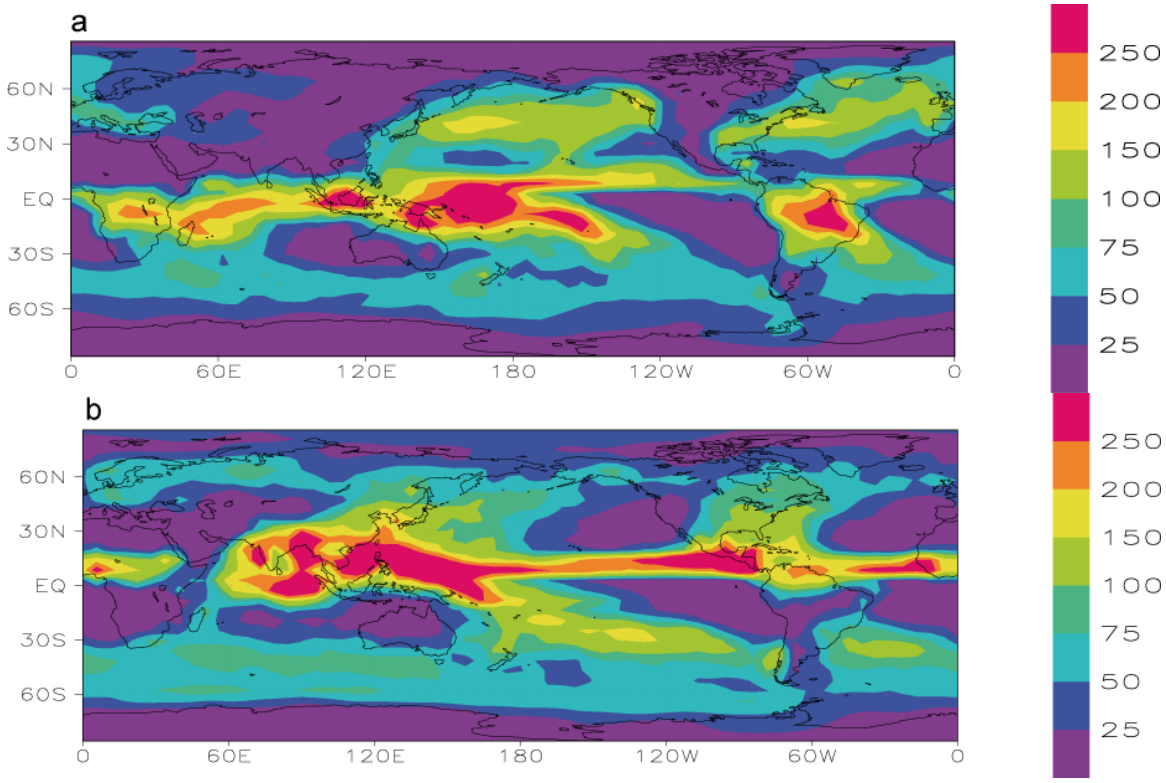

Figure 1.7: Precipitation in cm in (a) December, January and February; and (b) June, July and August. Data source: Xie, P., and P. A. Arkin, 1997 and updates

1.3 The ocean

1.3.1 Composition and properties

The ocean is a very important element of the climate system which covers about 71% of the Earth's surface and has an average depth of roughly 3700 m. Sea water is composed of 96.5% water and 3.5% dissolved salts, particles, gases and organic matter. The most important of these components are chloride and sodium, which represent about 85% of the dissolved material. Although the total quantity of dissolved salts varies from place to place, their relative contribution is very stable in sea water. Rather than specifying each of the components, it is thus very convenient to define a bulk salinity as the total amount of dissolved material (in grams) in a kilogram of sea water. This dimensionless salinity is then given in ‰ (parts per thousand). However, in practice, measuring the total amount of dissolved material is difficult. The salinity scale is thus based nowadays on the conductivity of sea water and given in psu (practical salinity unit). For simplicity, this new scale has been chosen so that the salinity in psu is very close to that in ‰.

The density of sea water increases with salinity as well as with pressure (thus with depth as the ocean is also in **hydrostatic equilibrium** on a large-scale), while it decreases with increasing temperature. In a very simplified picture, it is often considered that temperature dominates the density changes at high temperatures, while the role of salinity is larger at low temperatures. Salinity also influences the freezing point of sea water which, at the surface, decreases from 0°C for pure water to -1.8°C at a salinity of 35 psu.

1.3.2 Oceanic circulation

The surface ocean circulation is mainly driven by the winds. At mid-latitudes, the atmospheric westerlies induce eastward currents in the ocean while the **trade** winds are responsible for westward currents in the tropics (Fig. 1.8). Because of the presence of continental barriers, those currents form loops called the subtropical **gyres**. The surface currents in those gyres are intensified along the western boundaries of the oceans (the east coasts of continents) inducing well-known strong currents such as the **Gulf Stream** off the east coast of the USA and the Kuroshio off Japan. At higher latitudes in the Northern Hemisphere, the easterlies allow the formation of weaker subpolar gyres. In the Southern Ocean, because of the absence of continental barriers, a current that connects all the ocean basins can be maintained: the Antarctic Circumpolar Current (ACC). This is one of the strongest currents on Earth, which transports about 130 Sv (1 Sverdrup = 10^6 m^3 s^{-1}). All these currents run basically parallel to the surface winds. By contrast, the equatorial counter-currents, which are present at or just below the surface in all the ocean basins, run in the direction opposite to the trade winds.

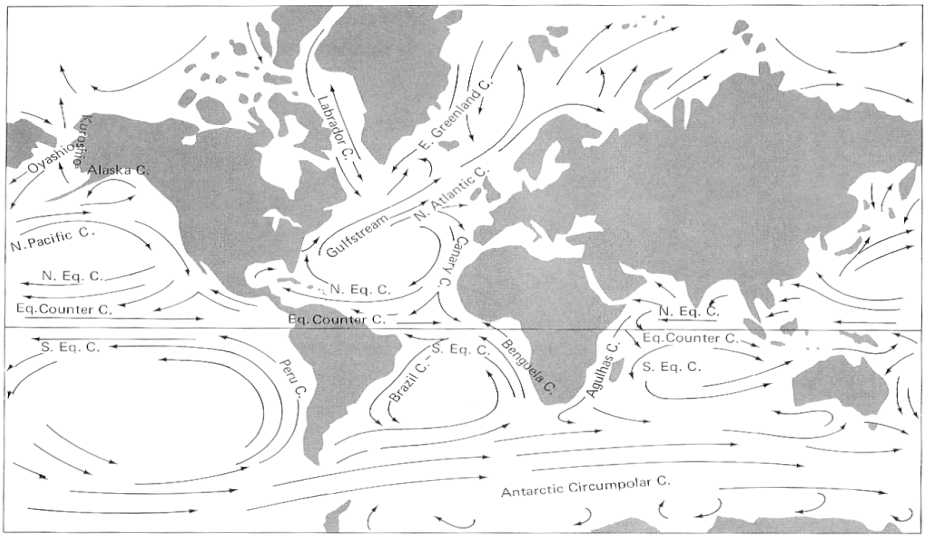

Figure 1.8: Schematic representation of the major surface currents. Eq. is an abbreviation for equatorial, C. for current, N. for North, S. for South and E. East. Reprinted by permission of Waveland Press, Inc. From Knauss, Introduction to Physical Oceanography. (Long Grove, IL: Waveland Press, Inc, 1997 (reissued 2005)). All rights reserved.

Because of the Earth's rotation, the ocean transport induced by the wind is perpendicular to the wind stress (to the right in the Northern Hemisphere, to the left in the Southern Hemisphere). This transport, known as the **Ekman transport**, plays an important role in explaining the path of the wind-driven surface currents (Fig. 1.8). Furthermore, along a coastline or if the transport has horizontal variations, this can lead to surface convergence/divergence that has to be compensated by vertical movements in the ocean. An important example is the equatorial upwelling (Fig 1.9). In the Northern Hemisphere, the **Ekman transport** is directed to the right of the easterly wind stress and is thus northward. By contrast, it is southward in the Southern Hemisphere. This results in a divergence at the surface at the equator that has to be compensated by an **upwelling** there. In coastal **upwelling**, the wind stress has to be parallel to coast, with the coast on the left when looking in the wind direction in the northern hemisphere (for instance, northerly winds along a coast oriented north-south). This causes an offshore transport and an upwelling to compensate for this transport.

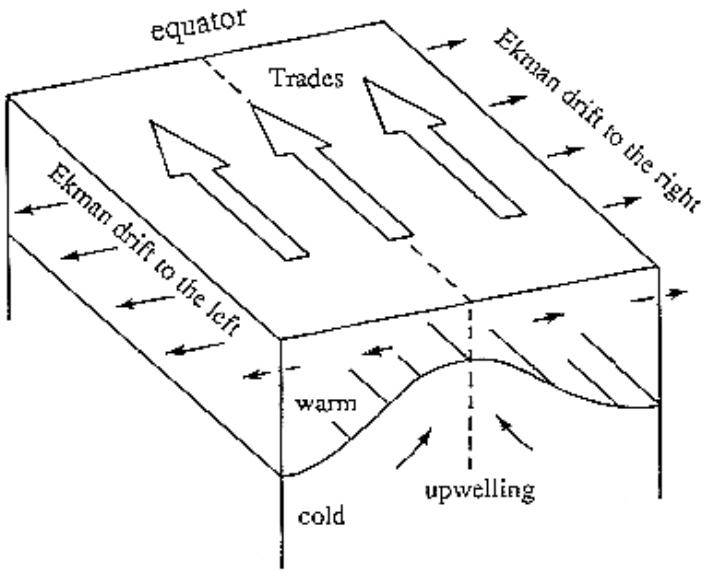

Figure 1.9: Schematic representation of the equatorial upwelling. Figure from Cushman-Roisin et al. (1994). Copyright B. Cushman-Roisin (1994), reproduced with permission.

At high latitudes, because of its low temperature and relatively high salinity, surface water can be dense enough to sink to great depths. This process, often referred to as deep oceanic **convection**, is only possible in a few places in the world, mainly in the North Atlantic and in the Southern Ocean. In the North Atlantic, the Labrador and Greenland-Norwegian Seas are the main sources of the North Atlantic Deep Water (NADW) which flows southward along the western boundary of the Atlantic towards the Southern Ocean. There, it is transported to the other oceanic basins after some mixing with ambient water masses. This deep water then slowly **upwells** towards the surface in the different oceanic basins. This is very schematically represented on Fig.1.10 by upward fluxes in the North Indian and North Pacific Oceans. However, while sinking occurs in very small regions, the **upwelling** is broadly distributed throughout the ocean. The return flow to the sinking regions is achieved through surface and intermediate depth circulation. In the Southern Ocean, Antarctic Bottom Water (AABW) is mainly produced in the Weddell and Ross Seas. This **water mass** is colder and denser than the NADW and thus flows below it. Note that, because of the mixing of water masses of different origins in the Southern Ocean, the water that enters the Pacific and Indian basins is generally called Circumpolar Deep Water (CDW).

This large-scale circulation (Fig. 1.10), which is associated with currents at all depths, is often called the oceanic **thermohaline circulation** as it is driven by temperature and salinity (and thus density) contrasts. However, winds also play a significant role in this circulation. First, they influence the surface circulation and thus the upper branch of the thermohaline circulation which feeds the regions where sinking occurs with dense enough surface waters. Secondly, because of the divergence of the **Ekman transport**, the winds influence the **upwelling** of deep water masses towards the surface in some regions. This plays a particularly important role in the Southern Ocean. Winds could also act as a local/regional preconditioning factor that favours deep convection.

The thermohaline circulation is quite slow. The time needed for water masses formed in the North Atlantic to reach the Southern Ocean is of the order of a century. If the whole cycle is taken into account, the **timescale** is estimated as several centuries to a

few millennia, depending of the exact location and mechanism studied. On the other hand, this circulation transports huge amounts of water, salts and energy. In particular, the rate of NADW formation is estimated to be around 15 Sv. Uncertainties are larger for the Southern Ocean, but the production rate of AABW is likely quite close to that of NADW. As a consequence, the thermohaline circulation has a important role in oceanographic as well as in climatology (see section 2.2).

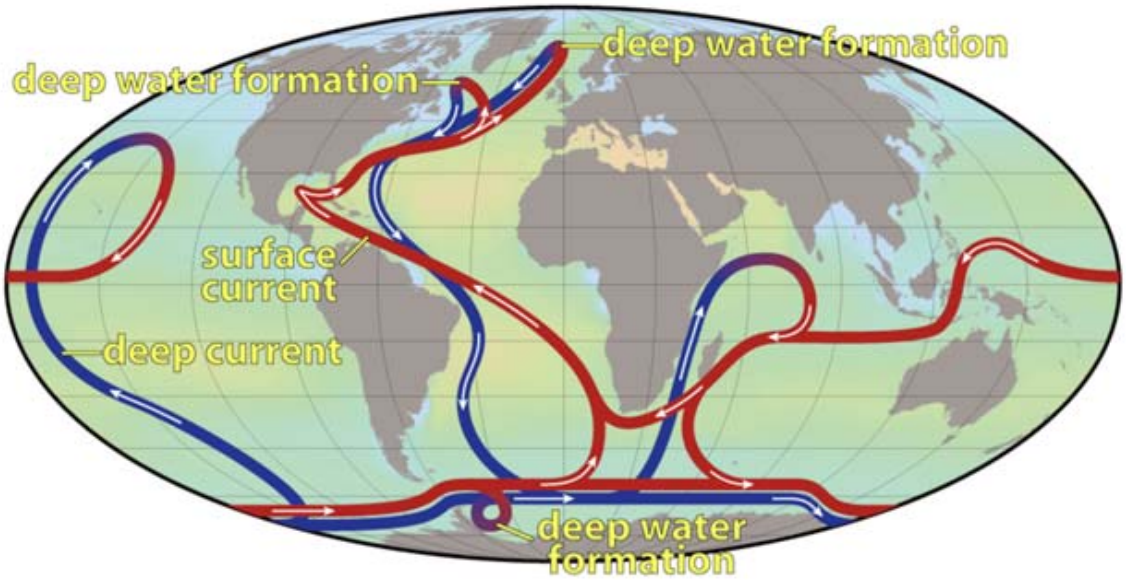

Figure 1.10: Schematic representation of the oceanic thermohaline circulation. *Source*: http://en.wikipedia.org/wiki/Thermohaline_circulation. Author Robert Simmon, NASA with Minor modifications by Robert A. Rohde. http://en.wikipedia.org/wiki/User:Dragons_flight. Not protected by copyright.

1.3.3 Temperature and salinity

1.3.3.1 Surface layer

Because of the strong interactions between the ocean and the atmosphere, the sea surface temperature (SST) (Fig.1.11) is very close to the temperature of the air above it (Fig. 1.3). One exception is the polar regions where **sea ice** (see section 1.4) insulates the ocean from the cold polar atmosphere.

The sea surface salinity is strongly influenced by the freshwater fluxes at the surface. The salinity reaches a maximum in subtropical areas because of the large evaporation and low rainfall there. The high precipitation rates induce lower salinity at the equator, while the weak evaporation is responsible for the lower salinity observed at mid and high latitudes. River input also has a large regional impact, as seen in Fig. 1.11, with low values close to the mouths of the Amazon and Mississippi rivers.

As with the surface temperature over land, the first tenths of metres of the ocean at mid- and high latitudes show a clear seasonal cycle (Fig. 1.12). However, this cycle is shifted by 1 to 3 months compared to that of land surface temperature and its amplitude is weaker because of the large thermal inertia of the ocean (see section 2.1). In winter, the stirring by the winds and the cooling at the surface, which tend to destabilise the water column and generate shallow **convection**, induce strong mixing in the ocean. This homogenises a surface layer, called the **oceanic mixed layer**. Its depth is generally about

50 to 100 metres in winter but can reach several hundred metres in some regions. When temperature rises in spring and summer, the density at the surface decreases. This tends to stabilise the water column. As the winds also tend to be weaker in spring and summer, generating less mixing, the mixed layer becomes shallower. The warming is thus concentrated in a shallow layer, whose depth is generally lower than 40m. Below this summer mixed layer, the temperature is insulated from the surface and thus still conserves the properties that it has acquired by contact with the atmosphere in winter. This seasonal process induces the formation of a region with strong vertical **gradients** at the base of the summer mixed layer referred to as the seasonal **thermocline** (Fig 1.12).

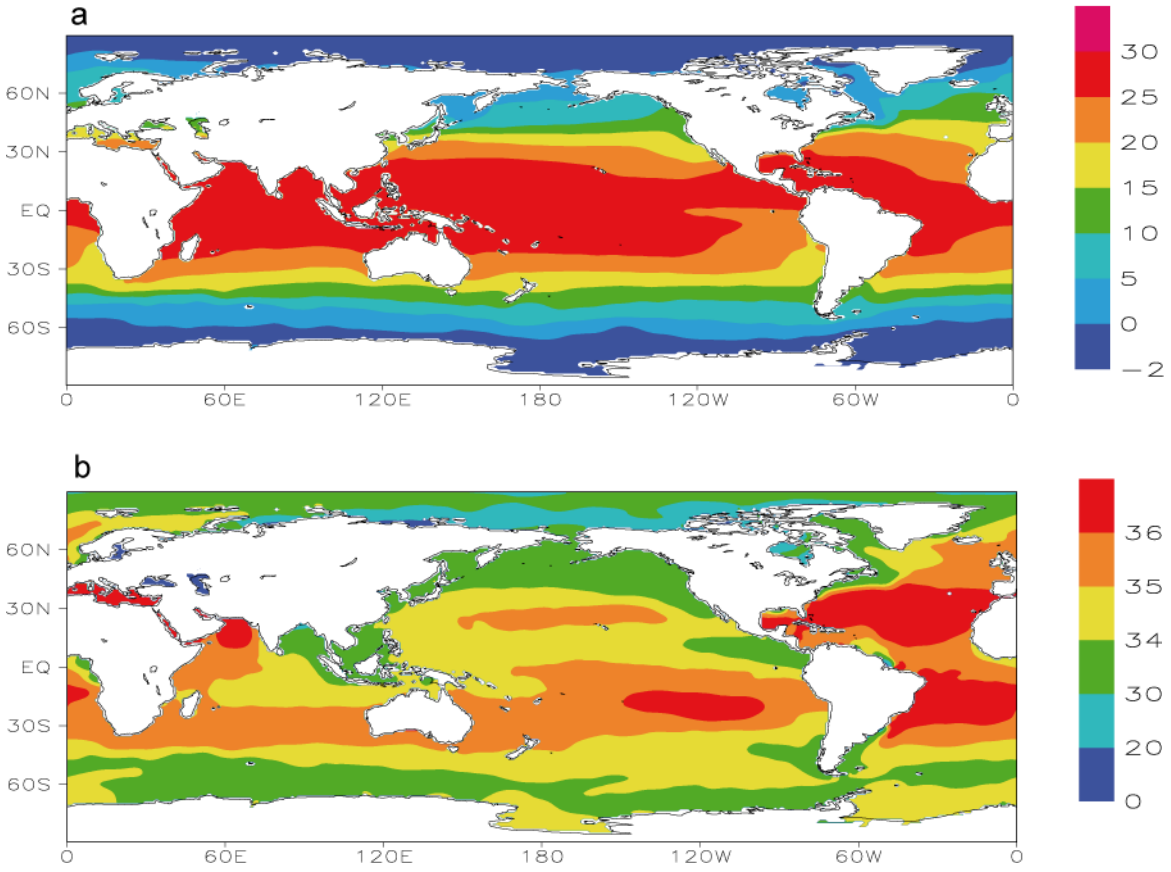

Figure 1.11: (a) Annual mean sea surface temperature (°C) and (b) surface salinity (psu). Data source: Levitus (1998).

The mixed layer dynamics, and in particular the seasonal changes in its depth, have a considerable influence on the surface ocean properties and on the exchanges of heat, water and gases between the ocean and the atmosphere (see section 2.1). Its development also has a large impact on the growth of phytoplankton, which is the basis of the whole oceanic food web. In order for photosynthesis to occur, phytoplankton need light, which is only available close to the surface. If the mixed layer is deep, as in winter, the phytoplankton is mixed over a large depth range by surface turbulence and thus spends a large part of its time in the dark, deep levels. If the relatively low flux of solar radiation at the surface during winter is also taken into account, it is easy to see why photosynthesis cannot take place in winter. By contrast, the availability of light is high in summer because of the shallow mixed layer and the large amount of incoming solar radiation. However, the shallow mixed layer limits the exchanges between the surface and the deep water which is rich in the nutrients required by the phytoplankton (see section 2.3). The concentration of those nutrients is thus generally too low to sustain a large production in

summer. As a consequence, the phytoplankton growth generally reaches its maximum during spring **blooms**. The mixed layer is relatively shallow during this period, but the nutrient concentration is high enough, thanks to the exchanges with deeper layers that occurred during the previous winter.

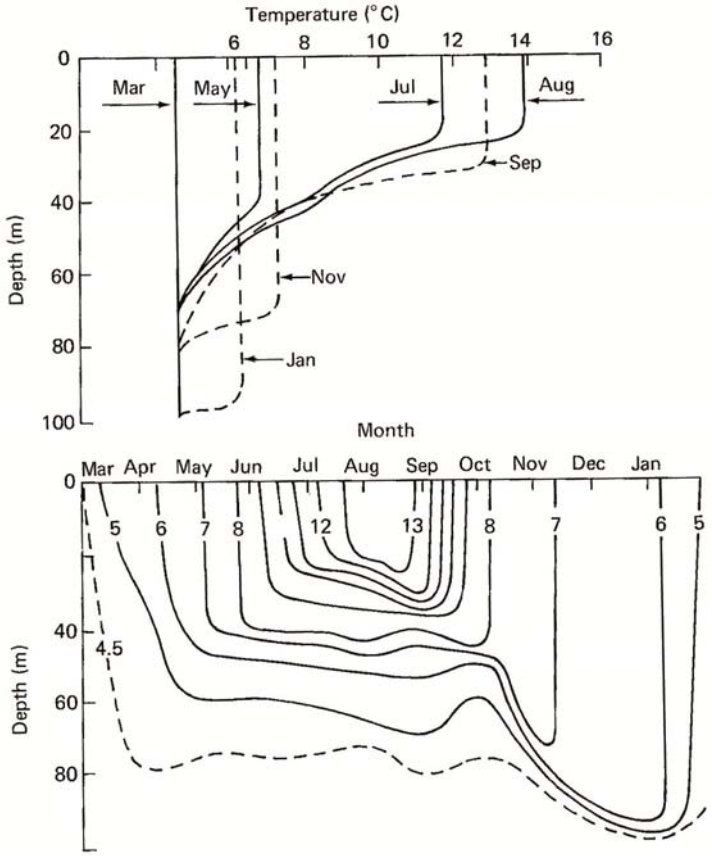

Figure 1.12: Typical growth and decay of the seasonal thermocline at a mid-latitude site in the Northern Hemisphere (50° N, 145° W). Reprinted by permission of Waveland Press, Inc. From Knauss, Introduction to Physical Oceanography. (Long Grove, IL: Waveland Press, Inc, 1997 (reissued 2005)). All rights reserved.

1.3.3.2 Intermediate and deep layers

Below the mixed layer, a strong vertical temperature **gradient** is observed (except in some regions at high latitudes), which defines the permanent **thermocline** (Figs. 1.13 and 1.14). This shows that the majority of the ocean is strongly stratified, meaning that light water sits above dense water as required by the vertical stability of the water column. In the deep ocean, the vertical gradients are much weaker. It is somehow surprising that, near the equator, the temperature difference between the surface and a depth of 1000 m could be more than 20°C while the temperature difference between 1000 m and the ocean bottom is only of the order of 3°C.

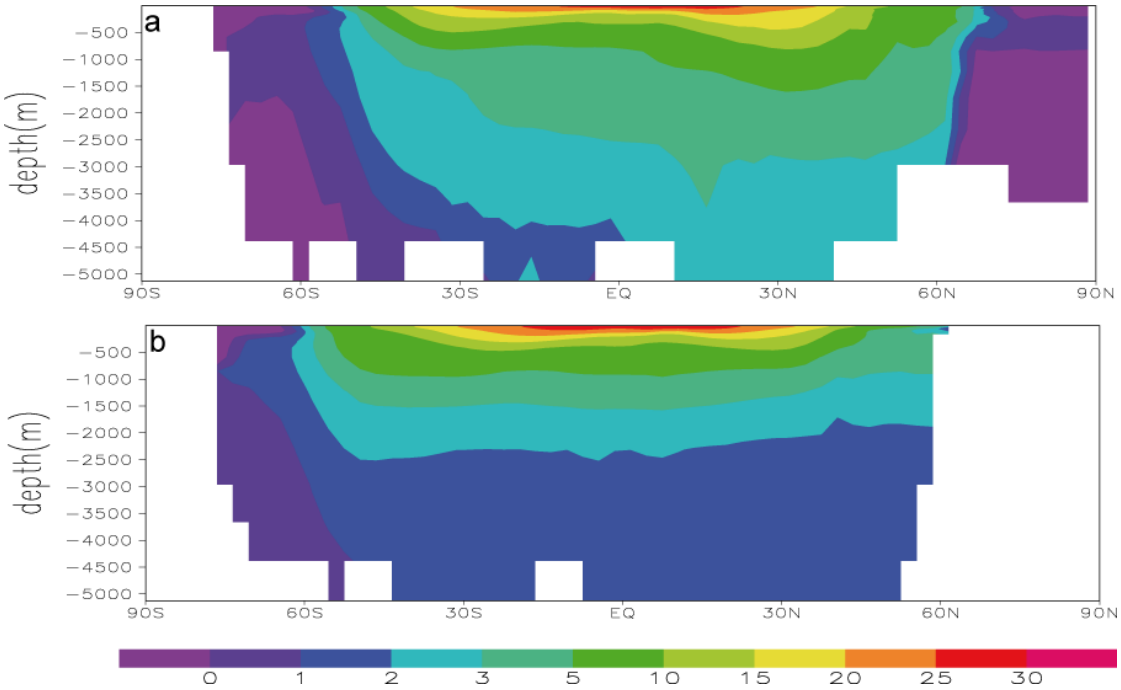

Fig. 1.13: Temperature (°C) averaged over all latitudes (i.e. zonal mean) in (a) the Atlantic and in (b) the Pacific. Data source: from Levitus (1998).

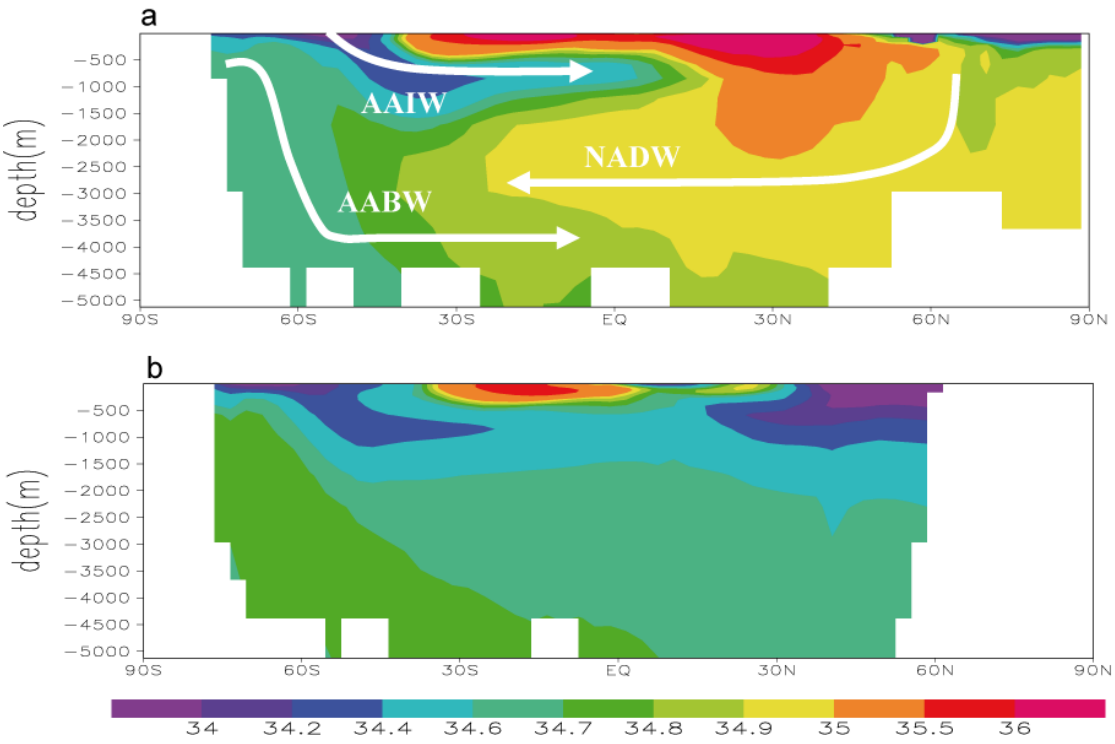

Figure 1.14: Salinity (psu) averaged over all latitudes (i.e. **zonal** mean) in (a) the Atlantic and in (b) the Pacific. The schematic paths of three important water masses are shown for the Atlantic. Data source: from Levitus (1998).

The temperature and salinity of sea water are modified by interactions with the atmosphere only in the oceanic mixed layer. The mixed layer is also the area where the greatest mixing occurs, diffusion being weaker in the ocean interior. **Water mass formation** and transformation thus mainly occur close to the surface. When these waters flow beneath the mixed layer, they tend to keep the properties they have acquired close to the surface. This is particularly clear in the deep ocean. As a consequence, the path of important water masses, like NADW and AABW, can easily be followed from their region of formation on temperature and salinity vertical sections (Fig.1.13 and 1.14). The influence of Antarctic Intermediate Water (AAIW), originating from the Southern Ocean, is also clearly identified as a low salinity tongue reaching the equator at intermediate depth. More generally, in the **thermocline**, water can originate from a nearby location (generally poleward), where surface density in winter is high enough to allow water to sink to intermediate depths.

1.4 The cryosphere

1.4.1 Components of the cryosphere

The cryosphere is the portion of the Earth's surface where water is in solid form. It thus includes sea ice, lake ice and river-ice, snow cover, glaciers, ice caps and ice sheets, and frozen ground. The snow cover has the largest extent, with a maximum area of more than $45\ 10^6$ km^2 (Table 1.1). Because of the present distribution of continents, land surfaces at high latitudes are much larger in the Northern Hemisphere than in the Southern Hemisphere. As a consequence, the large majority of the snow cover is located in the Northern Hemisphere (Figs. 1.15 and 1.16). The same is true for the freshwater ice that forms on rivers and lakes in winter. Both the snow cover and freshwater ice have a very strong seasonal cycle, as they nearly disappear in summer in both hemispheres (Table 1.1).

Component	Maximum area (10^6 km^2)	Minimum area (10^6 km^2)	Maximum Ice volume (10^6 km^3)	Minimum Ice volume (10^6 km^3)
Northern Hemisphere Snow cover	46.5 (late January)	3.9 (late August)	0.002	
Southern Hemisphere Snow cover	0.83 (late July)	0.07 (early May)		
Sea ice in the Northern Hemisphere	14.0 (late March)	6.0 (early September)	0.05	0.02
Sea ice in the Southern Hemisphere	15.0 (late September)	2.0 (late February)	0.02	0.002

Table 1.1: Areal extent and volume of snow cover and sea ice. Data compiled in Climate and Cryosphere (CliC) project science and co-ordination plan (2001).

Sea ice, which is a moving medium formed when sea water freezes, generally does not cover the whole oceanic surface in a region. Relatively narrow elongated areas of open water inside the pack are called **leads**, while larger areas of open water are called **polynyas**. The sea-ice concentration is defined as the fraction of the surface of interest (pixel from a satellite image, area surrounding a boat, etc) that is effectively covered by sea ice. A concentration of ice of 1 (or 100%) thus corresponds to a continuous ice pack, while a value of 0 corresponds to open ocean.

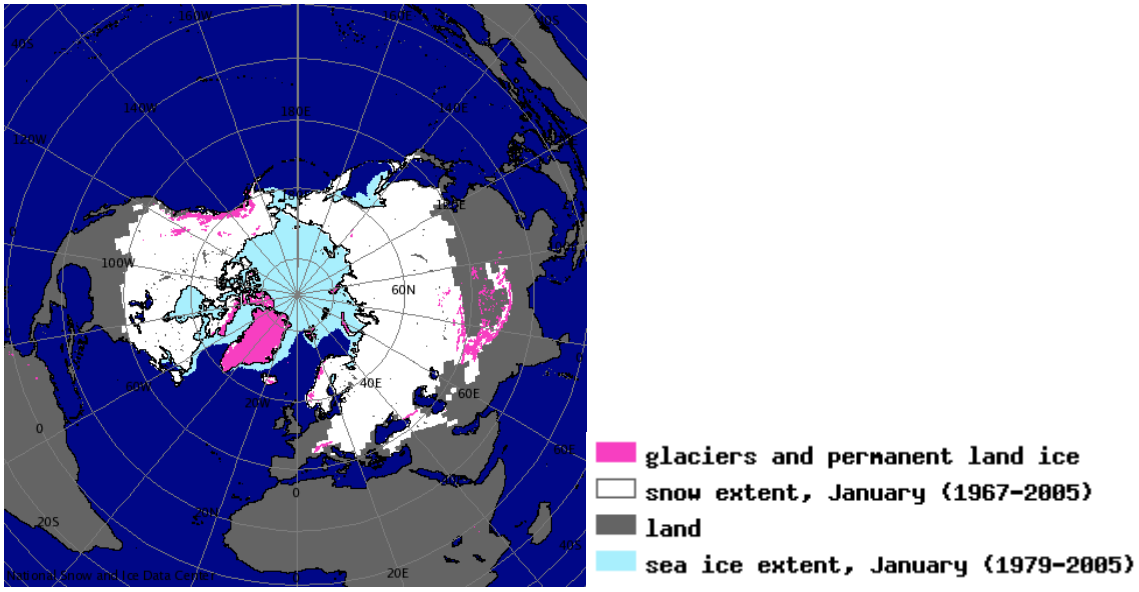

Figure 1.15: The distribution of sea ice, snow and land ice in January in the Northern Hemisphere. Source: Atlas of the Cryosphere, National Snow and Ice Data Center (NSIDC), http://nsidc.org/data/atlas/ .

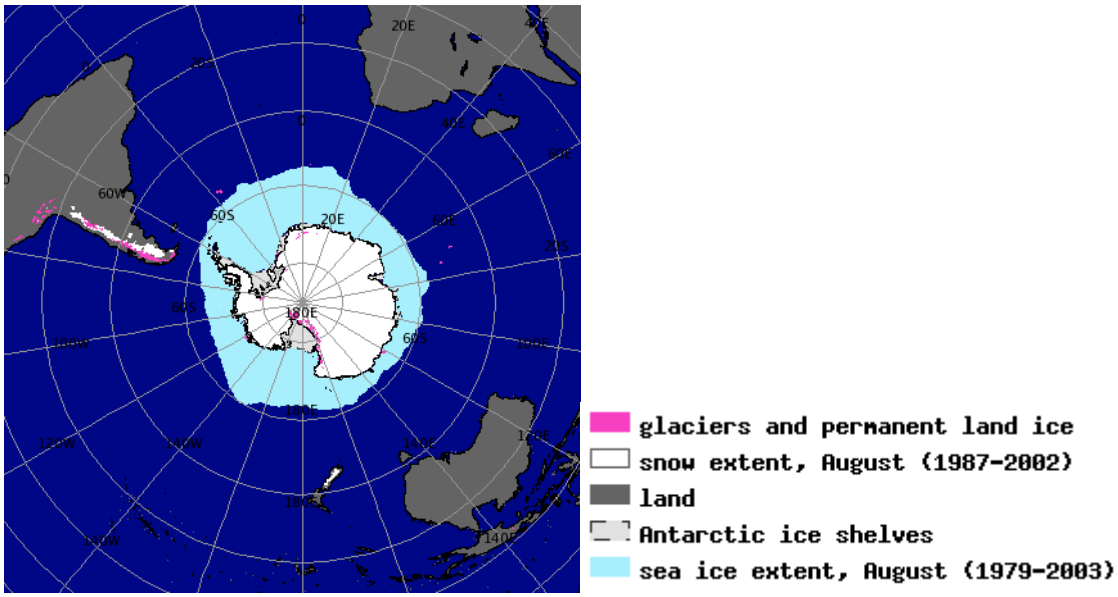

Figure 1.16: Location of sea ice, snow and land ice in August in the Southern Hemisphere. Source; Atlas of the Cryosphere, National Snow and Ice Data Center (NSIDC), http://nsidc.org/data/atlas/ .

Sea ice covers a similar area in both hemispheres (Table 1.1). Its seasonal cycle is larger in the Southern Ocean (Fig. 1.17) where the majority of the ice cover is first-year sea ice (i.e. sea ice that has not survived one summer). Because of the large thermal

inertia of the ocean (see section 2.1.5), the minimum and maximum sea ice extent are shifted by about two months compared to the snow cover on land, with maximum/minimum values around March and September in both hemispheres (Fig. 1.17). The sea ice is thinner in the Southern Hemisphere, with a mean thickness of less than 1 m, while the mean ice thickness in the central Arctic is around 3m.

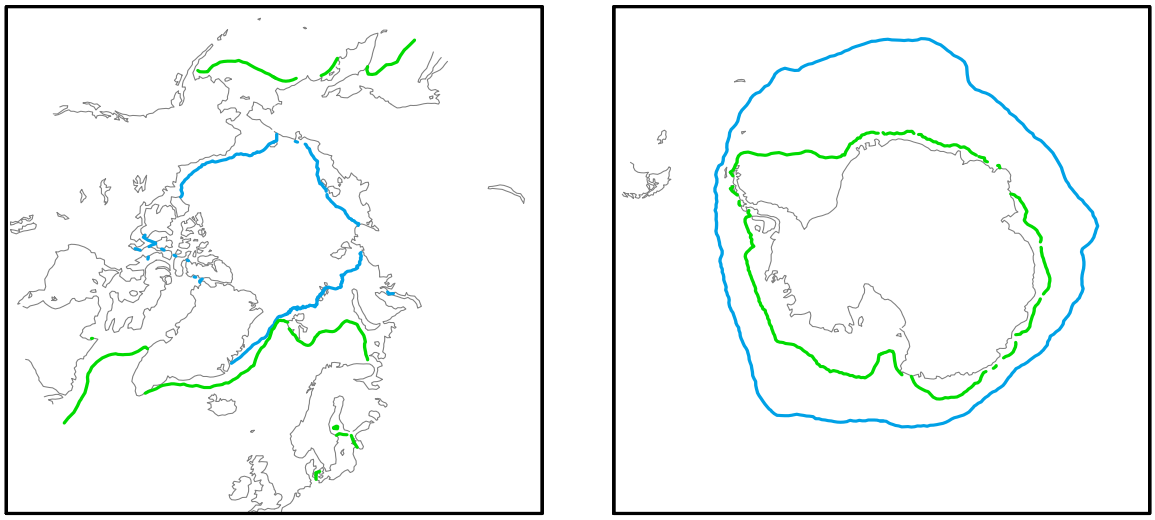

Figure 1.17: Location of the ice edge in March (green) and September (blue) in both hemispheres. The ice edge is commonly defined as the line where the ice concentration is 15%. Data from Rayner et al. (2003).

Component	Area (10^6 km^2)	Ice volume (10^6 km^3)	Sea level equivalent (m)
Continuous permafrost	10.69	0.0097-0.0250	0.024-0.063
Discontinuous permafrost	12.10	0.0017-0.0115	0.004-0.028
East Antarctica	10.1	22.7	56.8
West Antarctica and Antarctic Peninsula	2.3	3.0	7.5
Greenland	1.8	2.6	6.6
Small ice caps and mountain glaciers	0.68	0.18	0.5
Ice shelves	1.5	0.66	-

Table 1.2: Areal extent and volume of permafrost and land ice. Data compiled in the Climate and Cryosphere (Clic) project science and co-ordination plan (2001). *N.B.* The sea-level equivalent is computed as the thickness of a water layer corresponding to the ice mass distributed over the whole World Ocean. This is not directly equal to the resulting sea-level rise as parts of the Antarctic and Greenland ice sheets are presently below sea level.

Like snow, the seasonally frozen ground covers a large fraction of the continents in the Northern Hemisphere. Where the annual mean temperature is below -1°C, the ground can be perennially frozen below an active layer which melts in summer. This is the **permafrost**, which is estimated to cover more than 20% of the land area in the Northern Hemisphere (Table 1.2). The thickness of the frozen layer can exceed 600 m at high latitudes. Further south this layer thins, and the permafrost becomes discontinuous close to its margins (Fig. 1.18).

A large majority of the ice present on Earth today is located in two big ice-sheets: the Greenland and Antarctic ice sheets. The Antarctic ice sheet is itself commonly divided into two parts, East Antarctica and West Antarctica, roughly corresponding to the eastern and western hemispheres relative to the Greenwich meridian. The thickness of ice on these ice sheets can reach several kilometres (Fig 1.19 and 1.20). Ice sheets are formed by the accumulation of snow layers over tens of thousand years. As snow falls at the surface, the pressure on the older snow layers increases, transforming them into ice. Ice sheets (like glaciers) are not stagnant and generally flow slowly towards their margins. However, in some regions (called ice streams), the flow is much faster than in other parts of the ice sheet, sometimes reaching several kilometres per year.

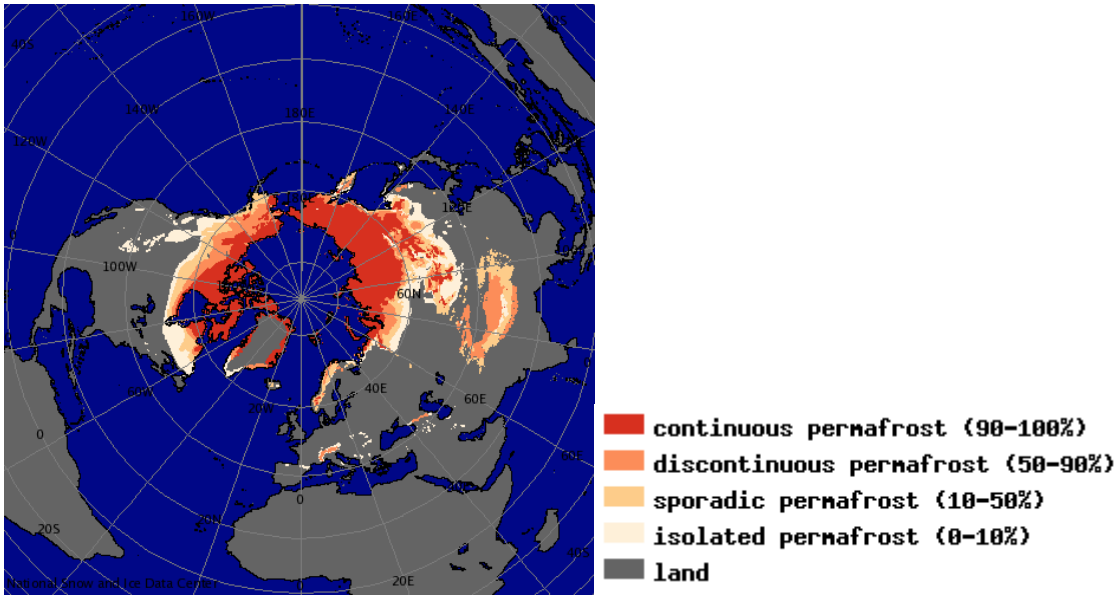

Figure 1.18: Location of permafrost in the Northern Hemisphere. Source: Atlas of the Cryosphere, National Snow and Ice Data Center (NSIDC), http://nsidc.org/data/atlas/ .

Because of the weight of the ice, the bedrock is depressed and, in some areas, is well below the sea level. For instance, most of the East Antarctic ice sheet is a high ice plateau that rests on bedrock, but large areas of the West Antarctic ice sheet are grounded below sea level. The total volume of the West Antarctic ice sheet that is below sea level has been estimated at around 1.9 10^6 km^3.

Antarctica is surrounded by **ice shelves**. These are floating platforms made of ice originating from the continent which has flowed down the coastline into the ocean. The two largest ice shelves are the Ross and Filchner shelves, which together cover more than 800 000 km^2. Ice shelves and glaciers which reach the shore are able to release **icebergs** that can drift over long distances, pushed by the ocean currents and winds. **Icebergs** are

thus found in the open ocean, but they should not be confused with sea ice. They are usually much thicker (sometimes more than 100 m) and consist of freshwater, while sea ice is salty and is formed directly from sea water

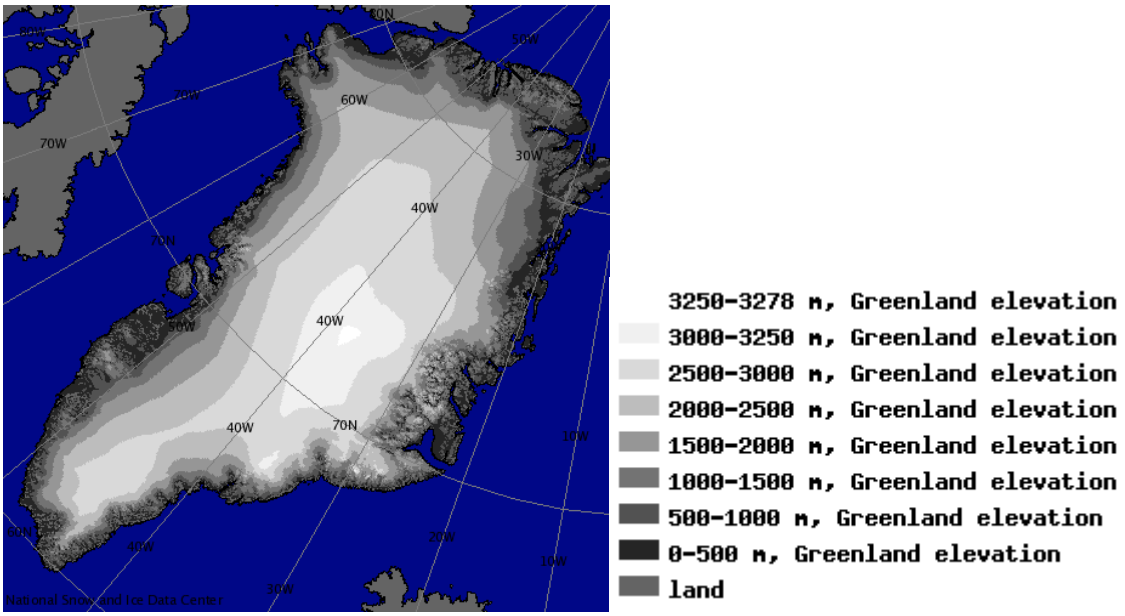

Figure 1.19: Greenland surface elevation. To obtain the ice thickness, the bedrock elevation has to be subtracted from this figure. Source: Atlas of the Cryosphere, National Snow and Ice Data Center (NSIDC), http://nsidc.org/data/atlas/ .

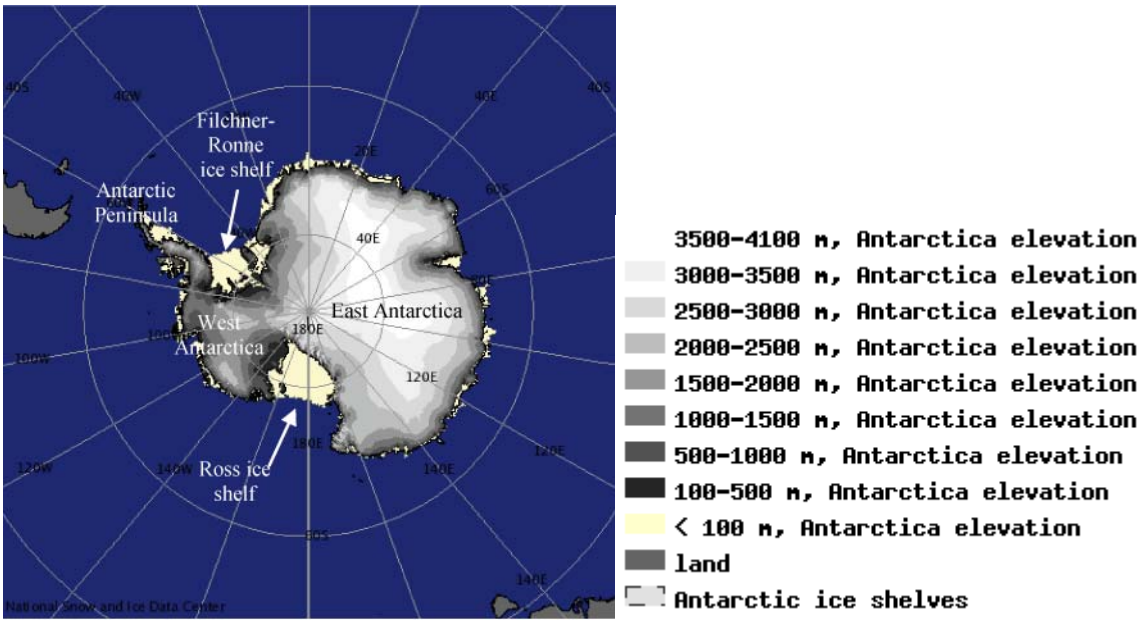

Figure 1.20: Antarctica surface elevation. To obtain the ice thickness, the bedrock elevation has to be subtracted from this figure. Source: Atlas of the Cryosphere, National Snow and Ice Data Center (NSIDC), http://nsidc.org/data/atlas/.

1.4.2 Properties of the cryosphere

Snow and ice have a very large **albedo**, i.e. they reflect the majority of the incoming solar radiation. They thus play a major role in the global heat balance of the Earth (see section 2.1). By storing and releasing **latent heat**, they affect the seasonal cycle of the surface temperature (see section 2.1). They are also good insulators that reduce the heat loss from the underlying surface (land or ocean) towards the cold atmosphere in winter. More generally, the presence of sea ice restricts the exchanges of heat and gases between the ocean and the atmosphere. When sea ice forms, only a fraction of the salt present in the ocean is trapped in the ice, the remainder being ejected towards the ocean (this is called brine rejection). The resulting sea ice salinity is between 10 psu in relatively young ice and less than 2 psu in very old ice (compared to around 35 psu for the ocean, see section 1.3). Because of this brine rejection, sea ice formation increases the salinity at the ocean surface while, melting sea ice is associated with surface freshening. Sea ice drift is also associated with a horizontal freshwater transport. If there is a net convergence of the sea-ice transport and intense ice melting in a region, this will decrease the salinity of surface water there. On the other hand, in regions such as coastal **polynyas**, the strong winds in winter continually push the newly formed ice off shore, leading to a strong divergence of the sea-ice transport. This implies very high ice formation rates in these **polynyas** (up to 10 m per year at some locations) and thus large amounts of brine rejection which can lead to very high ocean salinities in those regions.

Ice sheets store large amounts of water on land. Any change in their volume thus has a considerable effect on the sea level. It is estimated that, if all the ice sheets melted completely, taking into account the fact that some ice sheets are grounded below sea level, the sea level would rise by more than 60 m. On the other hand, if we neglect the effect of dilution on sea water density and volume, the melting of sea ice and **ice shelves** does not influence sea levels. Indeed, because of Archimedes' law, floating ice displaces its own weight of sea water and the melt water thus simply replaces the volume of ice previously below sea level. Ice sheets are also big mountains that, because of their height, help to maintain cold conditions on the surface. The presence of cold air on the ice sheet also has a regional influence, cooling the surrounding areas.

1.5 The land surface and the terrestrial biosphere

As discussed above, many characteristics of the climate are influenced by the distribution and topography of land surface. For instance, mountain chains such as the Andes or the Rocky mountains (Fig. 1.21) are formidable barriers to the westerly winds that influence the climate on a continental scale. Mountains also have an important role at the hemispheric scale, by affecting planetary waves and the global atmospheric circulation (section 1.2). The distance to the coast influences the temperature and aridity of a region. The presence of land boundaries to the ocean (and more generally the ocean bathymetry) affects the location of the strong western boundary currents and of the straits that allow water exchanges between the different basins (section 1.3). The shape and even the existence of an ice sheet is strongly conditioned by the underlying bedrock (section 1.4).

In addition to the influence of the land geometry, the type of vegetation present on land also has a critical influence on climate at all spatial and temporal scales. One of the most important roles of terrestrial vegetation is related to its **albedo** (Fig.1.22), (see section 2.1). Vegetation usually has a lower albedo than soil (Table 1.3), in particular much smaller than that of deserts. This is why subtropical deserts such as the Sahara appear as regions of particularly high albedo on global maps (Fig. 1.22). A maximum is also observed at high latitudes because of the presence of snow and ice. At these

latitudes, the vegetation modulates the influence of the snow. In the absence of vegetation or in the presence of low-growing vegetation such as grass, the snow can cover the whole area, leading to highly reflective white areas with a high **albedo**. If snow falls on a forest, relatively dark trunks, branches and possibly needles or leaves will partially emerge from the snow, resulting in a much lower **albedo** than with an homogenous snow blanket.

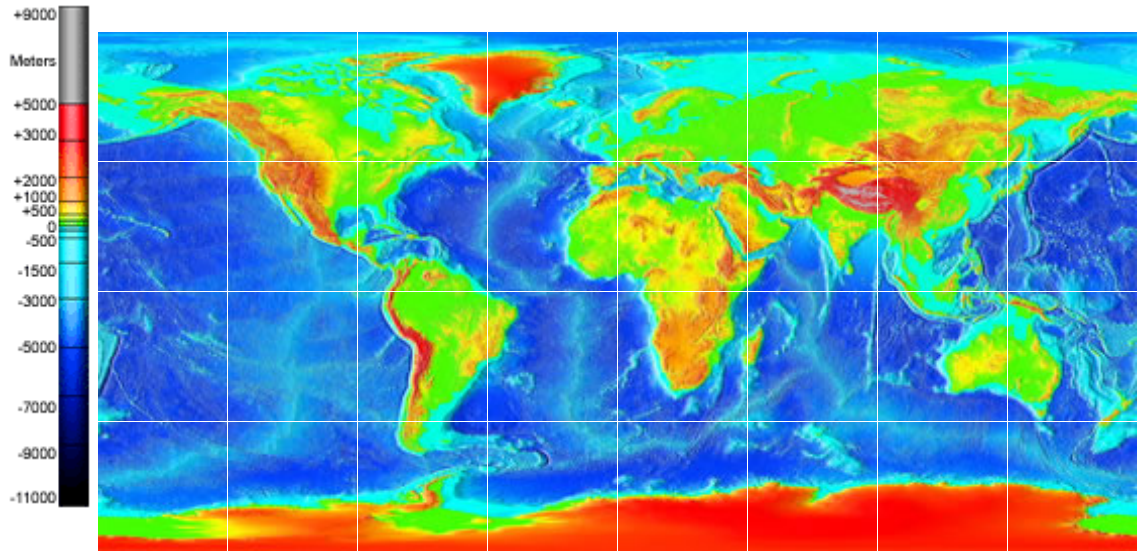

Figure 1.21: High resolution map of the surface topography. *Source* : Etopo2v2, http://www.ngdc.noaa.gov/mgg/image/2minsurface. Following the policy of U.S. governments agencies, this figure is not subject to copyright protection.

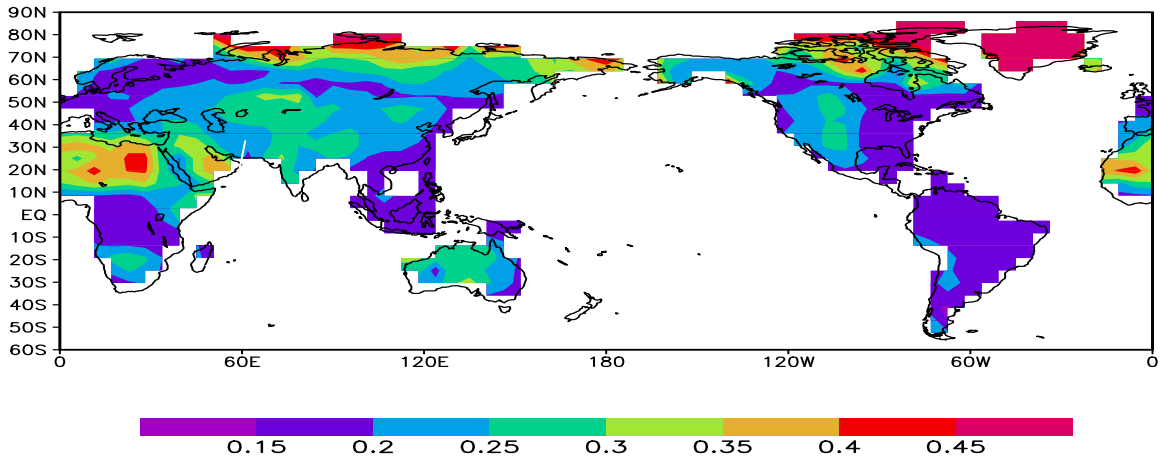

Figure 1.22: Surface **albedo**. Average of visible and near infra-red albedo. Data from Global Soil Wetness Project (GSWP2). Data source http://www.monsoondata.org:9090/dods

Surface type	**Albedo**
Ocean	0.05-0.15
Fresh snow	0.75-0.90
Old snow	0.40-0.70
Sea ice	0.3-0.6
Soil	0.05-0.40
Desert	0.20-0.45
Cropland	0.18-0.25
Grassland	0.16-0.26
Deciduous forest	0.15-0.20
Coniferous forest	0.05-0.15
Snow covered coniferous forest	0.13-0.3

Table 1.3: Typical range of the **albedo** of various surfaces.

The terrestrial **biosphere** also has a clear impact on the hydrological cycle (see section 2.2). Water storage is generally greater in soil covered by vegetation than on bare land where direct runoff often follows precipitation. Stored water can later be taken up by plant roots and transferred back to the atmosphere by **evapotranspiration**. A third effect of the vegetation cover is related to the surface roughness that influences the stress at the atmosphere-land interface and the turbulent exchanges at the surface (see section 2.1). Finally, the role of the terrestrial biosphere in the global carbon cycle will be discussed in section 2.3.

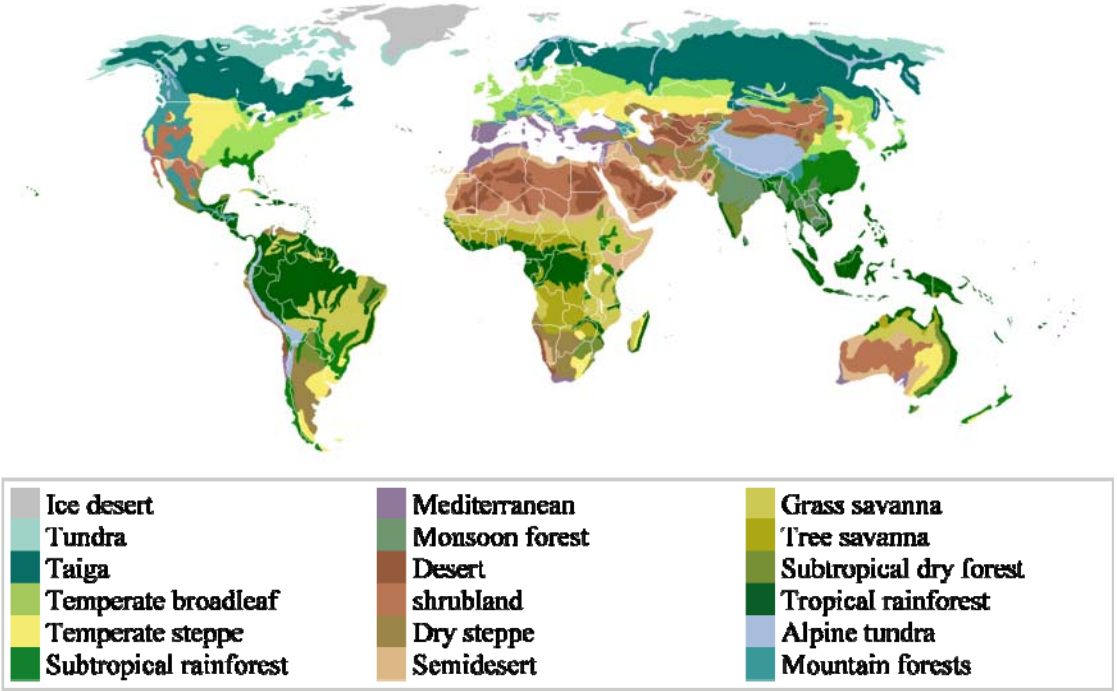

Figure 1.23: Terrestrial biomes. *Source*: http://en.wikipedia.org/wiki/Biome#Map_of_Biomes.

Because of this climatic role of vegetation, it is useful to describe the general distribution of the different **biomes**, which are regions with distinctive large-scale vegetation types (Fig. 1.23). Their exact definition, as well as the number of important biomes that are considered, differ from one study to the other. Nevertheless, it is generally considered that the natural biomes can be classified, according to their typical percentage of grass and trees, into five groups: desert, grassland, shrubland, woodland and forest. Cropland and built-up areas can be added to take into account the role of land use associated with human activities.

Deserts are characterised by a very small amount of vegetation. Grassland, as indicated by its name, is mainly covered by grass and lichens. It can be found at various latitudes and includes **tundra**, steppe and savannah. In shrubland, low woody plants are present in addition to grass. The fraction of trees is higher in woodland, but there are still significant areas covered by grass and often relatively large distances between trees. Finally, in forests, a dense cover of trees is observed (as in tropical rainforest and boreal conifer forest, also called **taiga**).

We have discussed above how vegetation influences **climate**, but of course climate also influences vegetation. This leads to powerful **feedback** loops that will be described in more detail in section 4.3.3. The dominant features of the climate are achieved through the distribution of incoming solar radiation, temperature and precipitation. If precipitation and/or temperature are too low, desert **biomes** dominate (as in the Sahara or Antarctica). At higher temperatures, forests can be maintained if a sufficient supply of water by rainfall is available. Between those two extremes, different combinations of grass and trees are found (see also Fig. 3.9).

Cited references and further reading

Brohan P., J.J. Kennedy, I. Harris, S.F.B. Tett SFB, and P.D. Jones (2006). Uncertainty estimates in regional and global observed temperature changes: A new data set from 1850. J. Geophys. Res. 111 (D12): D12106.

Climate and Cryosphere (Clic) project science and co-ordination plan (2001). Edited by I. Allison, R.G. Barry and B.E. Goodison. WCRP-114 WMO/TD No. 1053.

Cushman-Roisin, B. (1994). Introduction to geophysical fluid dynamics. Prentice Hall, London, 319pp.

Hartmann D.L. (1994). Global physical climatology. International Geophysics series, volume 56. Academic Press, 412 pp.

IPCC (2007): *Climate Change 2007: The Physical Science Basis. Contribution of Working Group I to the Fourth Assessment Report of the Intergovernmental Panel on Climate Change* [Solomon, S., D. Qin, M. Manning, Z. Chen, M. Marquis, K.B. Averyt, M.Tignor and H.L. Miller (eds.)]. Cambridge University Press, Cambridge, United Kingdom and New York, NY, USA.

Kalnay, E. and XXI others (1996). The NCEP/NCAR 40-year reanalysis project. Bull. Amer. Meteor. Soc. 77, 437-471

Knauss J.A. (1997). Introduction to physical oceanography. Prentice Hall.

Levitus S. (1998). NODC World Ocean Atlas 1998 data, report, 1998 :NOAA-CIRES Clim. Diag. Cent. Boulder, Colorado

Rayner N.A., D.E. Parker, E.B. Horton, C.K. Folland, L.V. Alexander, D.P. Rowell, E.C. Kent and A. Kaplan (2003). Global analyses of sea surface temperature, sea ice, and nigh marine aire temperature since the late nineteenth century. J. Geophys. Res. 108 (D14): 4407, doi:10.1029/2002JD002670

Wallace J.M. and P.V. Hobbs (2006). Atmospheric science: an introductory survey (2nd edition). International Geophysics Series 92, Academic press, 484pp.

Xie, P., and P. A. Arkin (1997). Global Precipitation: A 17-Year Monthly Analysis Based on Gauge Observations, Satellite Estimates, and Numerical Model Outputs. Bull. Amer. Meteor. Soc. 78: 2539--2558.

Exercises

Exercises are available on the textbook website (http://www.climate.be/textbook) and on iCampus for registered students.

Chapter 2. The Energy balance, hydrological and carbon cycles

2.1 The Earth's energy budget

2.1.1 The heat balance at the top of the atmosphere: a global view

Nearly all the energy entering the **climate system** comes from the Sun in the form of **electromagnetic radiation**. Additional sources are present, such as geothermal heating for instance, but their contribution is so small that their influence can safely be neglected. At the top of the Earth's atmosphere, a surface at the mean Earth-Sun distance perpendicular to the rays receives about 1368 W/m^2 (see also Figure 5.27). This is often called the **Total Solar Irradiance (TSI)** or **solar constant** S_0. A bit less than half of this energy comes in the form of radiation in the visible part of the **electromagnetic spectrum**, the remaining part being mainly in the near infrared, with a smaller contribution from the ultraviolet part of the spectrum (Fig. 2.1).

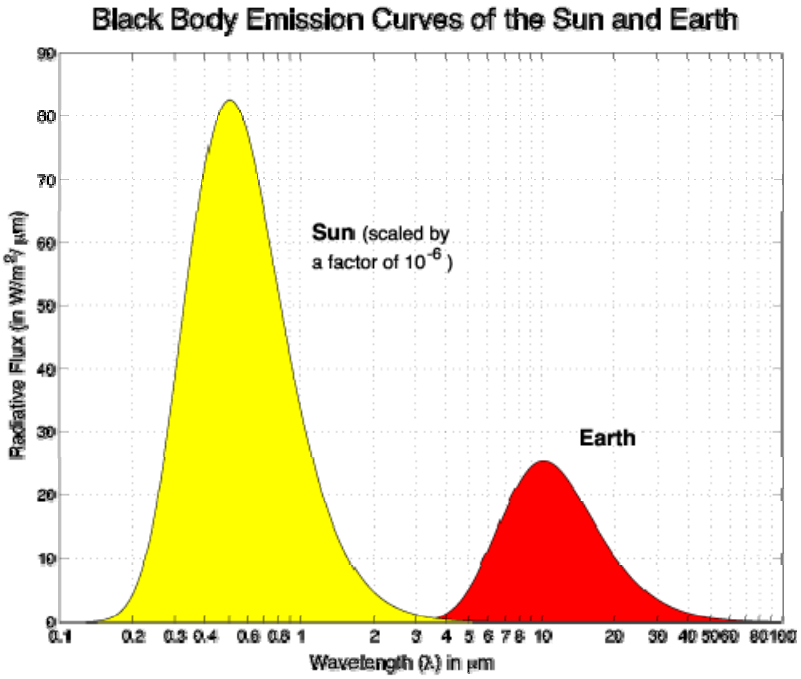

Figure 2.1: **Spectrum** of the energy received from the Sun and emitted by the Earth at the top of the atmosphere. Figure from Y. Kushnir available at http://www.ldeo.columbia.edu/~kushnir/MPA-ENVP/Climate/lectures/energy/. Reproduced with permission.

On average, the total amount of incoming solar energy outside the Earth's atmosphere (Fig 2.2) is the **solar constant** times the cross-sectional surface (i.e., the surface that intercepts the solar rays, which corresponds to a surface πR^2 where R is the Earth's radius of 6371 km^2). For simplicity and because it is a reasonable approximation, we will neglect the thickness of the atmosphere compared to the Earth's radius in our computations of distances or surfaces. Some of this incoming flux is reflected straight back to space by the atmosphere, the clouds and the Earth's surface. The fraction of the radiation that is reflected is called the **albedo** of the Earth or planetary albedo (α_p). In present-day conditions, it has a value of about 0.3.

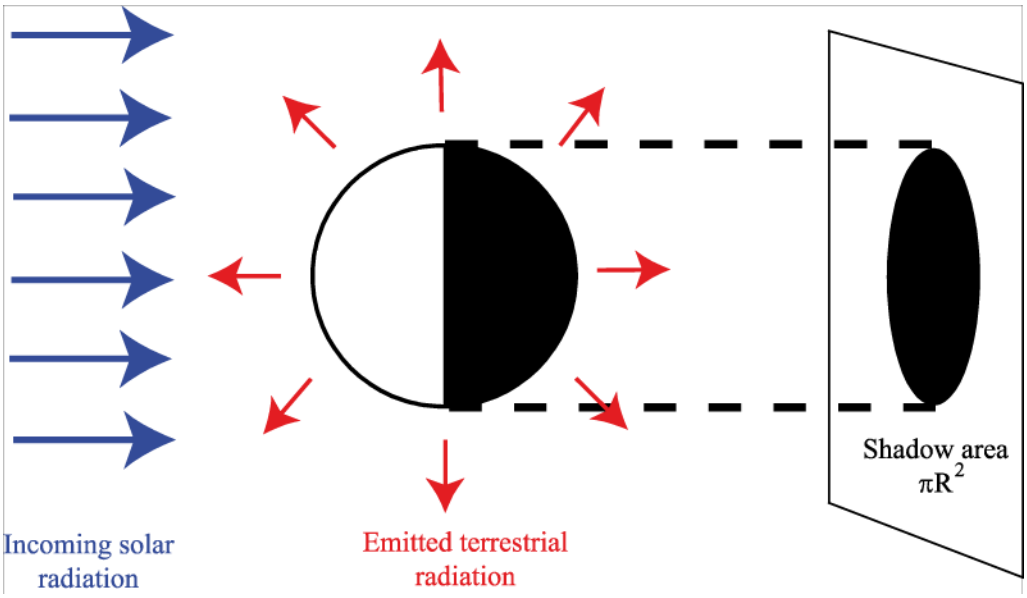

Figure 2.2: Heat absorbed and emitted by the Earth.

In order to achieve a heat balance, the heat flux coming from the Sun must be compensated for by an equivalent heat loss. If this were not true, the Earth's temperature would rapidly rise or fall. At the Earth's temperature, following **Wien's Law**, this is achieved by radiating energy in the infrared part of the electromagnetic spectrum. As the radiations emitted by the Earth have a much longer wavelength than those received from the Sun, they are often termed **longwave radiation** while those from the Sun are called **shortwave radiation**. Treating the Earth as a **black body**, the total amount of energy that is emitted by a 1 m^2 surface ($A\uparrow$) can be computed by **Stefan-Boltzmann's** law:

$$A\uparrow = \sigma T_e^4 \tag{2.1}$$

where σ is the Stefan Boltzmann constant (σ=5.67 10^{-8} W m^{-2} K^{-4}). This equation defines T_e , effective emission temperature of the Earth. The Earth emits energy in the directions, so the total amount of energy emitted by the Earth is $A\uparrow$ times the surface of the Earth, 4 π R^2. To achieve equilibrium, we must thus have (Fig. 2.3):

Absorbed solar radiation = emitted terrestrial radiation

$$\pi R^2 \left(1-\alpha_p\right) S_0 = 4\pi R^2 \sigma T_e^4 \tag{2.2}$$

This leads to

$$\frac{1}{4}\left(1-\alpha_p\right) S_0 = \sigma T_e^4 \tag{2.3}$$

and finally to

$$T_e = \left(\frac{1}{4\sigma}\left(1-\alpha_p\right) S_0\right)^{1/4} \tag{2.4}$$

This corresponds to T_e=255 K (=-18°C). Note that we can interpret Eq. (2.3) as the mean balance between the emitted terrestrial radiation and the absorbed solar flux for 1 m^2 of the Earth's surface. As shown above, the factor 1/4 arises from the spherical geometry of the Earth, because only part of the Earth's surface receives solar radiation directly.

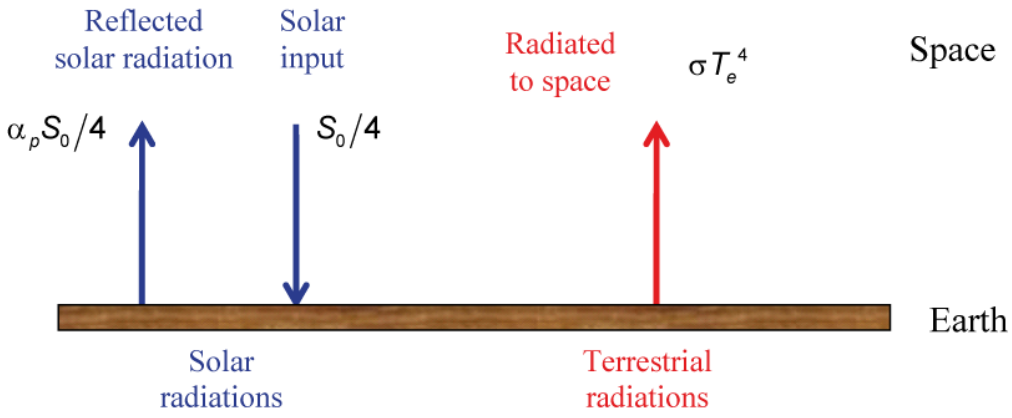

Figure 2.3: Simple heat balance of the Earth (assuming it behaves like a perfect blackbody).

The temperature T_e is not a real temperature that could be measured somewhere on Earth. It is only the black body temperature required to balance the solar energy input. It can also be interpreted as the temperature that would occur on the Earth's surface if it were a perfect black body, there were no atmosphere, and the temperature was the same at every point.

2.1.2 The greenhouse effect

The atmosphere is nearly transparent to visible light, absorbing about 20% of the incoming solar radiation. As a consequence, the majority of the absorption takes place at Earth's surface (see section 2.1.6). On the other hand, the atmosphere is almost opaque across most of the infrared part of the **electromagnetic spectrum**. This is related to the radiative properties of some minor constituents of the atmosphere, especially water vapour, carbon dioxide, methane and ozone. Those gases constitute only a small fraction of the atmospheric composition, while the two dominant components (molecular nitrogen and oxygen, see section 1.2) play nearly no part in this opacity. Nevertheless, a significant fraction of the energy emitted by the Earth's surface is absorbed by the atmosphere and re-emitted, significantly increasing the temperature of the system.

In a garden greenhouse, panes of glass are transparent to visible light but opaque to infra-red radiation, 'trapping' part of the energy emitted by the surface and resulting in a warming of the air. By analogy, the alteration of the energy budget by some minor atmospheric constituents described above is called the greenhouse effect and those minor constituents the greenhouse gases. However, the climate system is much more complex than a greenhouse and in a garden greenhouse a significant fraction of the warming is related to the reduction of the turbulent heat exchanges with atmosphere, not in the modification of the radiative fluxes. The analogy should be used with caution.

The greenhouse effect can be illustrated by a very simple model in which the atmosphere is represented by a single homogenous layer of temperature T_a, totally transparent to the solar radiation and totally opaque to the infrared radiations emitted by the Earth's surface (Fig. 2.4). Because of this opacity of the atmosphere to surface radiation, all the energy radiated to space is from the atmosphere. Using Equation 2.3, the balance at the top of the atmosphere is thus:

$$\sigma T_a^4 = \frac{1}{4}\left(1-\alpha_p\right)S_0 = \sigma T_e^4 \qquad (2.5)$$

In this simple model, T_a is thus equal to T_e, the effective emission temperature of the Earth. At the Earth's surface, the balance between the energy emitted by the surface, and the incoming solar fluxes, and the infra-red flux coming from the atmosphere gives:

$$\sigma T_s^4 = \frac{1}{4}(1-\alpha_p)S_0 + \sigma T_a^4 \tag{2.6}$$

Combining (2.5) and (2.6) leads to

$$\sigma T_s^4 = \sigma T_e^4 + \sigma T_e^4 \tag{2.7}$$

and

$$T_s = 2^{1/4} T_e = 1.19 T_e \tag{2.8}$$

Because of the greenhouse effect, the surface temperature is thus much higher than T_e, reaching 303K (30°C) in this example. This temperature is actually higher that the observed mean surface temperature of 288K (15°C) because of some crude approximations in this simple model.

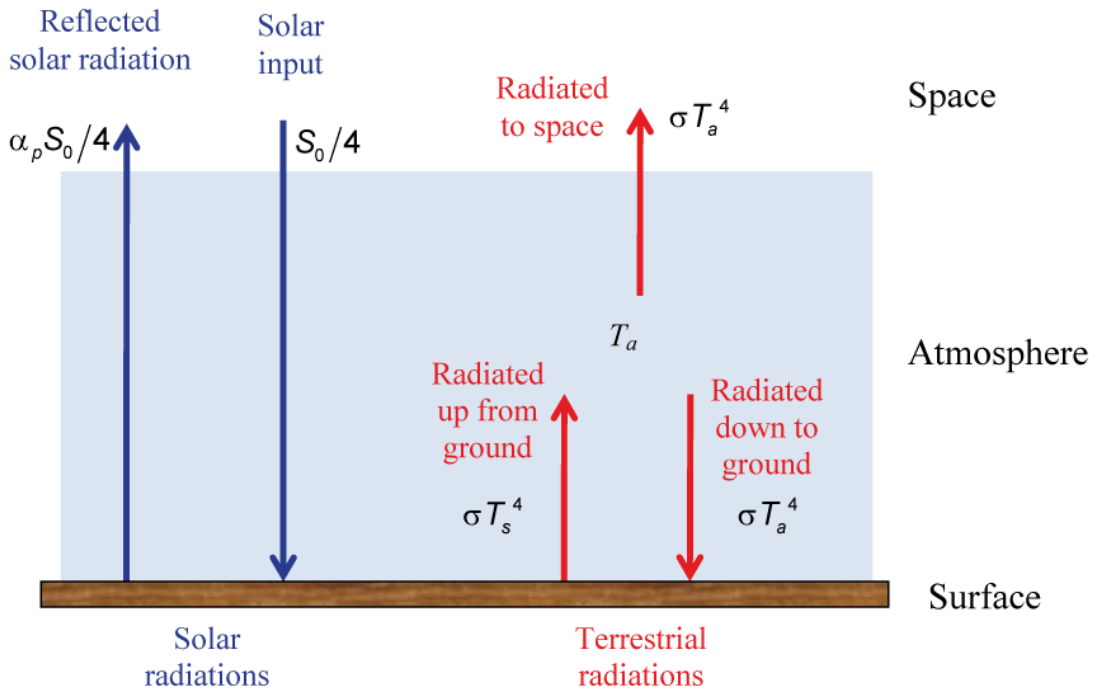

Figure 2.4: Heat balance of the Earth with an atmosphere represented by a single layer which is totally transparent to solar radiation and opaque to infrared radiations (modified from Marshall and Plumb, 2007).

We can improve our model by taking into account the fact that the atmosphere is not a perfect blackbody (Fig. 2.5). Using the emissivity of an object (ε) (which is defined as the ratio of energy radiated by this object to energy radiated by a black body at the same temperature), we can write the balance at the surface as:

$$\sigma T_s^4 = \frac{1}{4}(1-\alpha_p)S_0 + \varepsilon\sigma T_a^4 \tag{2.9}$$

The emissivity is also equal to the fraction of the radiation that is absorbed by the object. The fraction being transmitted through the object is thus equal to (1-ε) and the balance at the top of the atmosphere is:

$$\frac{1}{4}(1-\alpha_p)S_0 = \varepsilon\sigma T_a^4 + (1-\varepsilon)\sigma T_s^4 = \sigma T_e^4 \tag{2.10}$$

Eqs. (2.9) and (2.10) lead to:

$$\sigma T_s^4 = \frac{2}{2-\varepsilon}\frac{1}{4}(1-\alpha_p)S_0 = \frac{2}{2-\varepsilon}\sigma T_e^4 \tag{2.11}$$

$$T_s = \left(\frac{2}{2-\varepsilon}\right)^{1/4} T_e \tag{2.12}$$

For ε=0, corresponding to an atmosphere totally transparent to infra-red radiations T_s=T_e, which is well in agreement with the result of section 2.1. For a perfect **black body**, we get a result identical to Eq. (2.7), as expected. A typical value of 0.97 for the atmosphere provides a value of T_s=1.18 T_e, i.e. 301 K (28°C). We can also compute T_a as:

$$T_a = \left(\frac{1}{2-\varepsilon}\right)^{\frac{1}{4}} T_e = \left(\frac{1}{2}\right)^{\frac{1}{4}} T_s \tag{2.13}$$

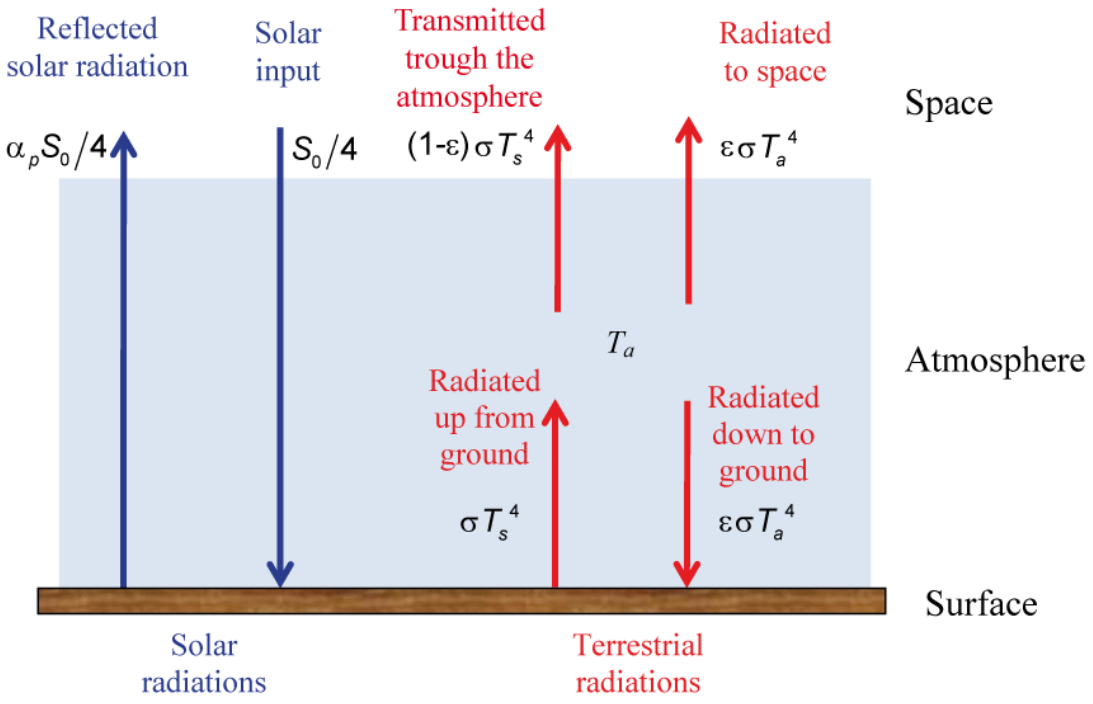

Figure 2.5: Heat balance of the Earth with an atmosphere represented by a single layer totally transparent to solar radiation and with an infrared emissivity ε.

2.1.3 Present-day insolation at the top of the atmosphere

The instantaneous **insolation**, defined as the energy received per unit time and unit surface on a horizontal plane at the top of the atmosphere (or on a horizontal plane at the Earth's surface, if we neglect the influence of the atmosphere) depends on the geographical position on Earth as well as on the position of the Earth relative to the Sun. The influence of those factors is described in the following sections.

2.1.3.1 Earth's orbit around the Sun.

According to Kepler's first law, the Earth's trajectory around the Sun is an ellipse with the Sun at one focus.

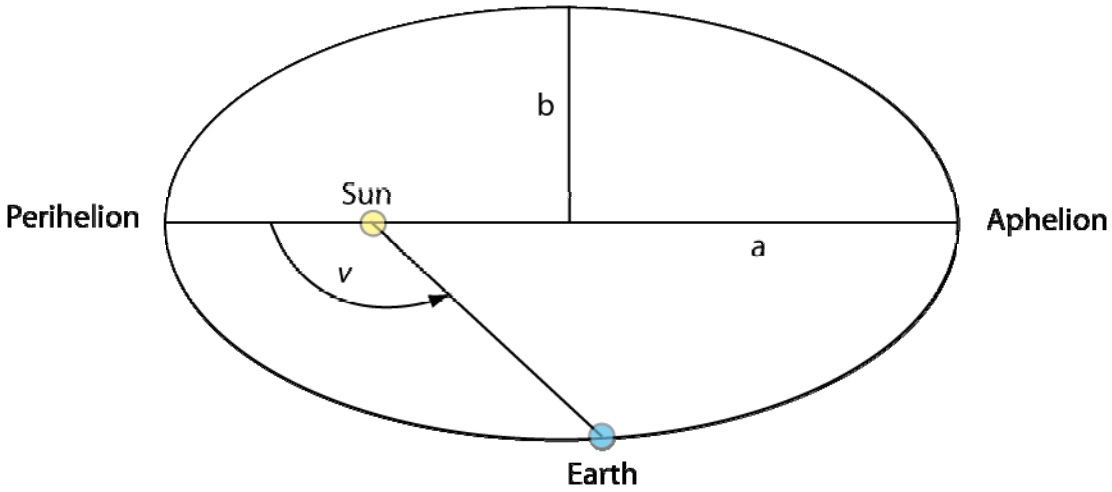

Figure 2.6: Schematic representation of the Earth's orbit around the Sun. The eccentricity has been exaggerated for clarity.

The point of the Earth's orbit that is the closest to the Sun is called the **perihelion** while the **aphelion** is the point that is farthest from the Sun (Fig. 2.6). a is half of the major axis and b half of the minor axis. The shape of the ellipse is then characterised by its **eccentricity** (*ecc*), defined by:

$$ecc = \frac{\sqrt{(a^2 - b^2)}}{a} \tag{2.14}$$

The parameters of the Earth's orbit vary with time (see section 5.4.1) but at present *ecc*=0.0167, meaning that the Earth's orbit is very close to a circle (which of course corresponds to an eccentricity of zero).

The distance from the Sun to the Earth (r) can be computed as a function of v, the true anomaly, according to the formula for an ellipse:

$$r = \frac{a\left(1 - ecc^2\right)}{1 + ecc\cos v} \tag{2.15}$$

The amount of incoming solar electromagnetic radiation per unit area at the top of the atmosphere is a function of r. We can define r_m as the mean distance between the Earth and the Sun by:

$$r_m = \sqrt{ab} = a\sqrt{(1-ecc^2)} \tag{2.16}$$

This means that a circle with radius r_m would have the same area as the ellipse corresponding to the Earth's orbit. The total energy emitted by the Sun is equal to the total energy received on the surface of a sphere of radius r, centred on the Sun, and to that received on a sphere of radius r_m. S_r the amount of solar radiation per unit area measured on the outer surface of the Earth's atmosphere in a plane perpendicular to the rays at a distance r from the Sun can then be computed as a function of the Solar Constant S_o:

Total energy emitted by the Sun measured at a distance r_m=
Total energy emitted by the Sun measured at a distance r

$$4\pi r_m^2 S_0 = 4\pi r^2 S_r \tag{2.17}$$

$$S_r = \frac{r_m^2}{r^2} S_0 \tag{2.18}$$

2.1.3.2 Computation of the zenith angle.

As the rotation axis of the Earth is not perpendicular to its orbital plane, the **ecliptic plane**, which is the geometric plane containing the mean orbit of the Earth around the Sun, is inclined relative to the **celestial equatorial plane**, which is the projection of the Earth's equator into space. This angle is called the **obliquity** of the ecliptic ε_{obl}. At present, it is about 23°26' (Fig. 2.7).

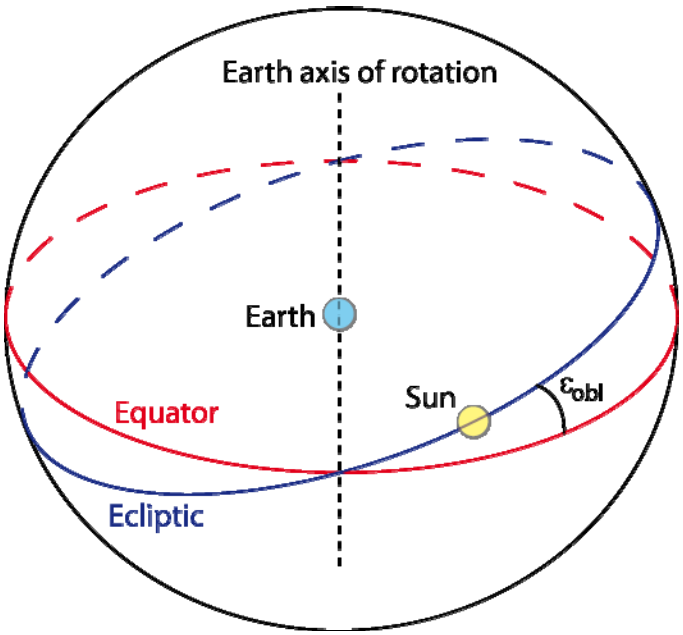

Figure 2.7: Representation of the ecliptic and the obliquity ε_{obl} in a geocentric system.

The intersections of those two planes are used to define the seasons. In particular, the **vernal equinox**, which is often used as a reference in the coordinate system to define the **true longitude** λ_t (or ecliptic longitude, Fig. 2.8.), corresponds to the intersection of the ecliptic plane with the celestial equator when the Sun moves from the austral to the boreal hemisphere in its apparent movement around the Earth. This occurs around March 20-21 and is often called the spring equinox. However, this term could be misleading as this date corresponds to the beginning of autumn in the Southern Hemisphere.

By definition the **vernal equinox** corresponds to a true longitude equal to zero, the solstices to the true longitudes equal to 90° and 270° and the 'autumn' equinox to a true longitude equal to 180°. If we define *PERH* as the longitude of the perihelion measured from the autumn equinox (*PERH*= 102.04 in present-day conditions, corresponding to a true longitude of 180°+PERH=282.04), we can write

$$\lambda_t = 180 + PERH + v \tag{2.19}$$

This definition can be used to compute the length of the different seasons, using Kepler's second law which states that, as the Earth moves in its orbit, a line from the Sun to the planet sweeps out equal areas in equal times.

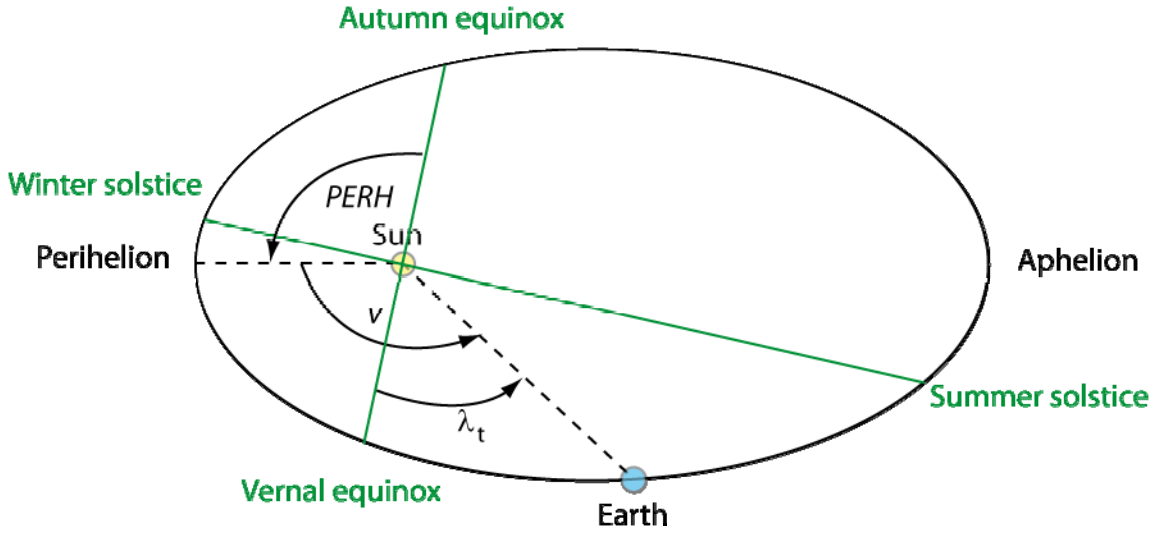

Figure 2.8: Representation of the true longitudes and the seasons in the ecliptic plane.

S_h, the amount of solar energy received per unit time on a unit horizontal surface at the top of the atmosphere is proportional to the cosine of θ_s, the solar **zenith distance** which is defined as the angle between the solar rays and the normal to the Earth's surface at any particular point.

$$S_h = S_r \cos\theta_s \tag{2.20}$$

S_h rises as $\cos\theta_s$ becomes closer to 1, i.e. as the horizontal surface becomes more normal to the Sun's rays. When the surface is inclined at an oblique angle to the solar rays, the amount of energy received by the surface per square metre is lower, because the total amount of energy received by the perpendicular surface ($S_r A_1$ on Fig. 2.9) is distributed across a larger surface ($S_r A_1 = S_h A_2 = S_h A_1 / \cos\theta_s$).

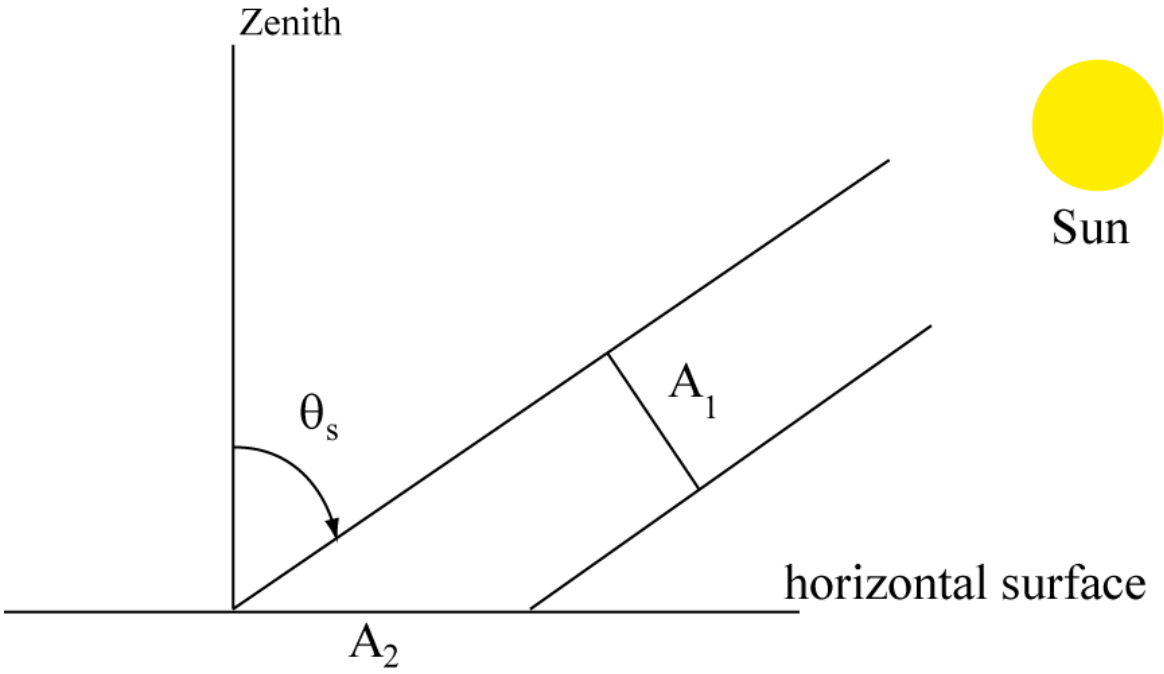

Figure 2.9: Influence of the zenith angle on the amount of radiation received on a horizontal surface. A_1 is the surface perpendicular to the solar beam while A_2 is the horizontal surface illuminated by the rays crossing A_1.

$\cos\theta_s$ can be computed using standard astronomical formula:

$$\cos\theta_s = \sin\phi\sin\delta + \cos\phi\cos\delta\cos HA \tag{2.21}$$

where ϕ is the latitude of the point on Earth, δ is the solar declination, HA is the hour angle. The declination δ is defined as the angle between a line from the centre of the Earth towards the Sun and the celestial equator (Fig. 2.10). It varies from $+\varepsilon_{obl}$ at the summer solstice in the Northern Hemisphere to $-\varepsilon_{obl}$ at the winter solstice and zero at the equinoxes. During the day, its value is constant to a very good approximation. Knowing the true longitude and the obliquity, the declination δ can be estimated using the formula:

$$\sin\delta = \sin\lambda_t \sin\varepsilon_{obl} \tag{2.22}$$

Furthermore, if we denote the number of the day, starting on the first of January, by NDAY, the value of δ can also be estimated by using the raw approximation (zero order to eccentricity):

$$\delta = 23.45° \sin\left(360°\left(NDAY - 80\right)/365\right) \tag{2.23}$$

The hour angle HA indicates the time since the Sun was at local meridian, measured from the observer's meridian westward. HA is thus zero at the local solar noon. It is generally measured in radians or in hours (2π rad=24 hours). It could more formally be defined as the angle between the half plane determined by the Earth's axis and the zenith (local meridian half-plane), and the half plane determined by the Earth's axis and the Sun.

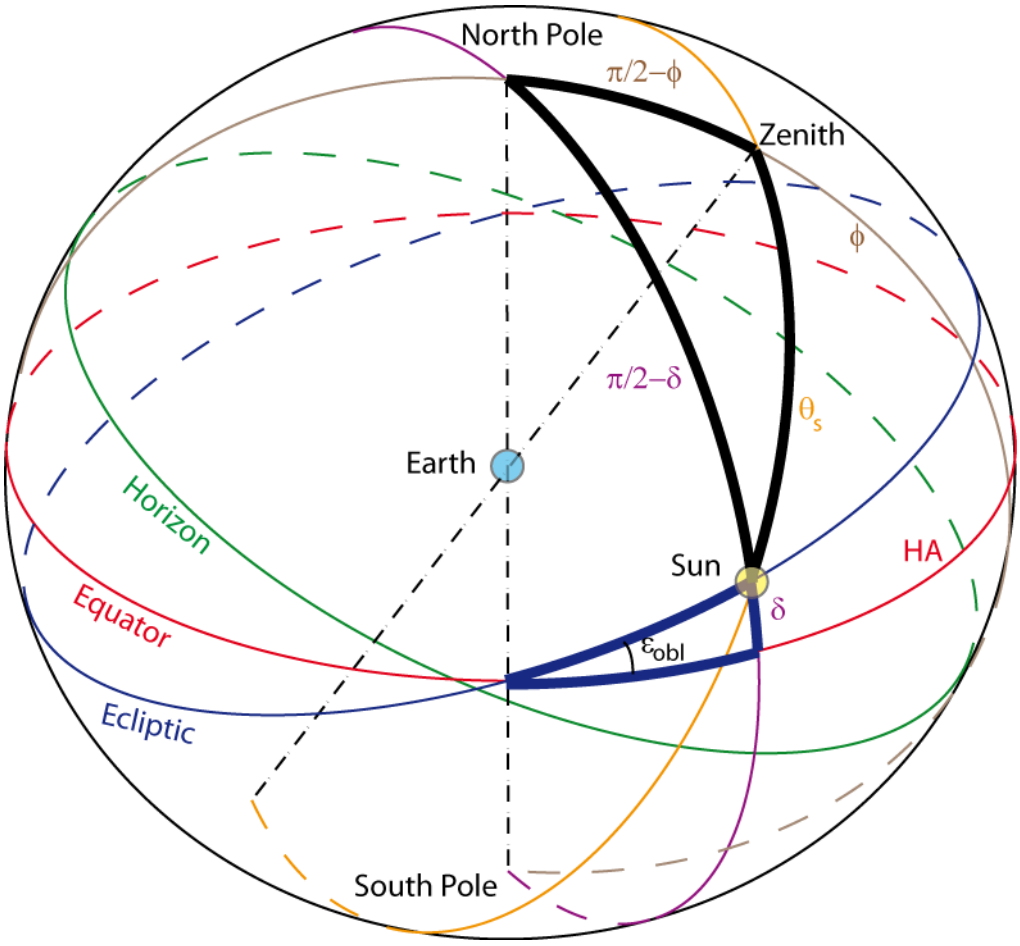

Figure 2.10: Representation of the declination and of the hour angle in a geocentric system. On this figure, the equator and the ecliptic are fixed. The apparent motion of the Sun corresponds to a complete revolution along the ecliptic in one year. The hour angle (and the location of the local meridian (brown circle) through the North Pole and the zenith) change as the Earth makes a complete rotation around its axis in 1 day. Applying the standard spherical trigonometric rules to the black bold triangle allows Eq. 2.21 to be demonstrated. This figure can also be used to demonstrate Eq. 2.22, using the blue bold triangle.

2.1.3.3 Daily insolation at the top of the atmosphere.

If the Sun rises above the horizon on a particular day, we can compute the times of sunrise (HA_{sr}) and sunset (HA_{ss}) using Equation 2.21, since both events correspond to a solar zenith angle of 90°:

$$HA_{SR,SS} = \pm \arccos\left(-\tan\phi \tan\delta\right) \tag{2.24}$$

The length of the day (LOD) is then given by

$$LOD = \frac{24}{\pi} \arccos\left(-\tan\phi \tan\delta\right) \tag{2.25}$$

The coefficient $24/\pi$ is used to convert the result from radians for *HA* to hours for *LOD*.

At the equator, since ϕ is equal to zero, *LOD* is always equal to 12 hours. At the equinoxes, δ is equal to zero so *LOD* is equal to 12 hours everywhere. We can also estimate from Eq. 2.25 that in the polar regions of the Northern Hemisphere, where $\phi + \delta \geq 90°, \tan\phi \tan\delta \geq 1$ in summer, the Sun is visible during the whole day (midnight sun) where $\phi - \delta \geq 90°, \tan\phi \tan\delta \leq -1$ in winter, the Sun is always below the horizon (polar night). Similar formulae can be obtained for the Southern Hemisphere.

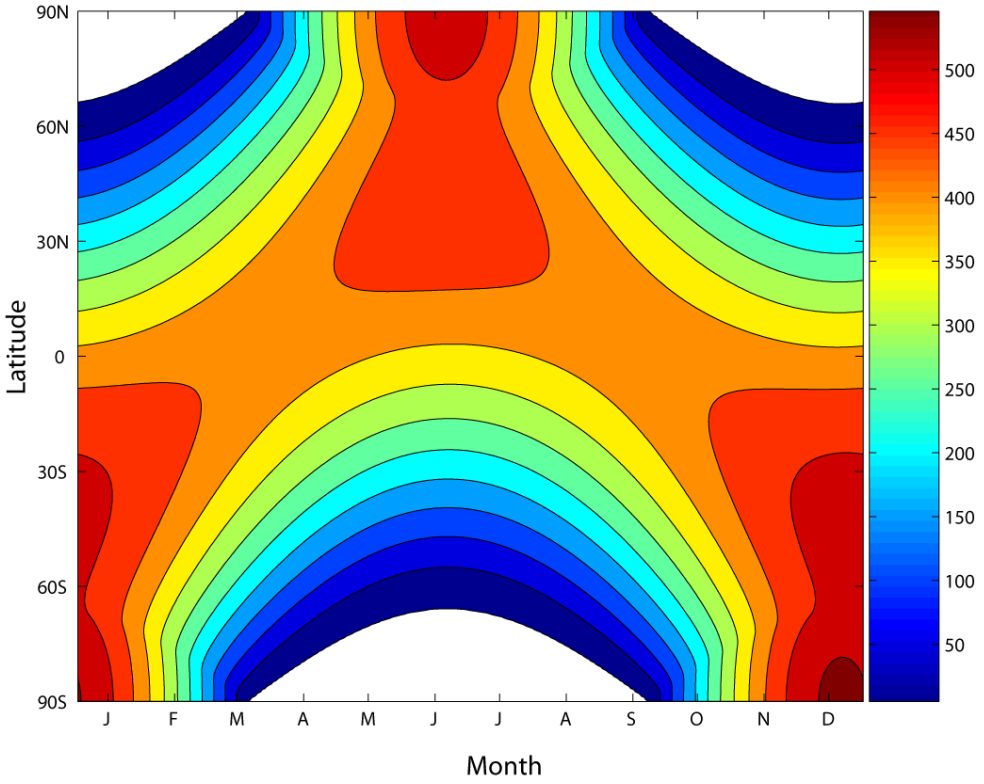

Figure 2.11: Mean daily insolation (in W/m^2) on a horizontal surface at the top of the atmosphere as a function of the day of the year and the latitude. White areas correspond to the polar night.

Using Eqs 2.18, 2.20, 2.21, and 2.24, we can integrate S_h over time to compute $S_{h,day}$ the daily insolation on a horizontal surface (in J m^{-2}). The mean insolation over one day (in W/m^2) is also often used. It is simply $S_{h,day}$ divided by 24 hours

$$\begin{aligned} S_{h,day} &= S_0 \frac{r_m^2}{r^2} \int_{Sunrise}^{Sunset} \left(\sin\phi \sin\delta + \cos\phi \cos\delta \cos HA\right) dt \\ &= S_0 \frac{r_m^2}{r^2} \frac{86400}{2\pi} \int_{HA_{SR}}^{HA_{SS}} \left(\sin\phi \sin\delta + \cos\phi \cos\delta \cos HA\right) dHA \\ &= S_0 \frac{r_m^2}{r^2} \frac{86400}{\pi} \left(HA_{SS} \sin\phi \sin\delta + \cos\phi \cos\delta \sin HA_{SS}\right) \end{aligned} \tag{2.26}$$

As expected, the daily insolation is higher in the summer hemisphere because of the lower zenith distance (i.e. a Sun higher above the horizon) and longer duration of the day. Averaged over one day, the maximum solar insolation occurs at the poles at the summer

solstice (see Fig. 2.11), while averaged over one year the solar energy received at the top of the atmosphere at the equator is about twice that received at the poles.

2.1.4 The heat balance at the top of the atmosphere: geographical distribution

The geographical distribution of the net incoming solar radiation at the top of the atmosphere (i.e., the incoming minus the reflected solar radiation) that is absorbed by the Earth is a function of the insolation distribution as well as of the regional variations of the planetary **albedo** (Fig. 2.12). The latter is influenced by several factors, including the **albedo** of the surface (see section 1.5) and the presence of clouds which reflect a significant fraction of the incoming solar radiation back to space. The influence of clouds is particularly evident in the Tropical Regions, where it explains, for instance, why the absorbed solar radiation is larger in the relatively cloud free eastern Equatorial Pacific than in the cloudier western Pacific. At high latitudes, the surface albedo is high because of the high zenith distance (Sun low above the horizon) and the high reflectance of snow and ice (see section 1.4). This high surface albedo at high latitudes amplifies the latitudinal variations in solar radiation associated with the Earth's geometry (Fig. 2.11), resulting in a difference of nearly a factor of five in annual mean absorbed solar radiation at the poles, compared to the equator.

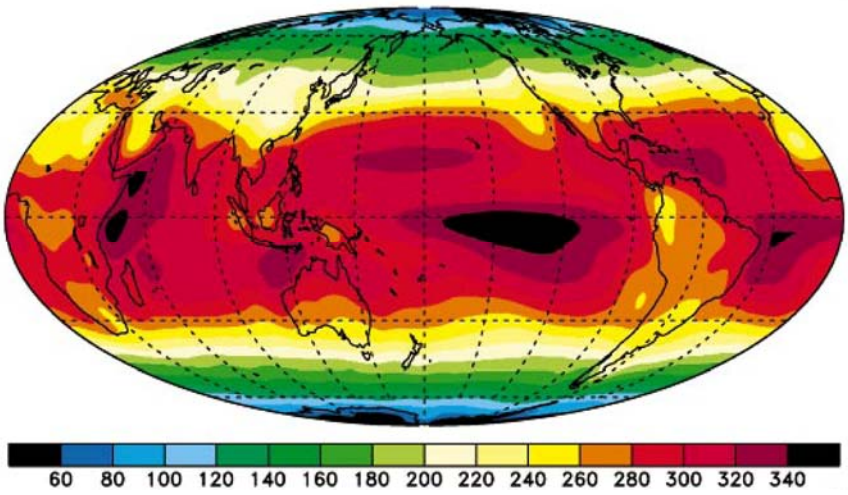

Figure 2.12: Annual mean net incoming solar radiation at the top of the atmosphere that is absorbed by the Earth (in W/m^2). Figure from Trenberth and Stepaniak (2003). Copyright 2003 American Meteorological Society (AMS).

The **Stefan-Boltzmann law** says that the **longwave radiation** emitted is a function of the temperature of the emitting surface. A difference of about 50°C between the equator and the poles roughly corresponds to a variation in the emitted thermal radiation of about 50 W/m^2, which is in reasonable agreement with the estimated values (Fig. 2.13). The presence of clouds and water vapour also has a large influence. Indeed, water vapour is a strong greenhouse gas. It absorbs part of the infra-red radiation emitted by the surface before re-emitting radiation, generally at a lower temperature as clouds are located higher in the atmosphere (see section 2.1.2). This results in less outgoing longwave radiation. As a consequence, the maximum outgoing longwave radiation is found above warm dry areas such as the subtropical deserts. More generally, wet equatorial areas generally emit less radiation than dry tropical areas (Fig. 2.13).

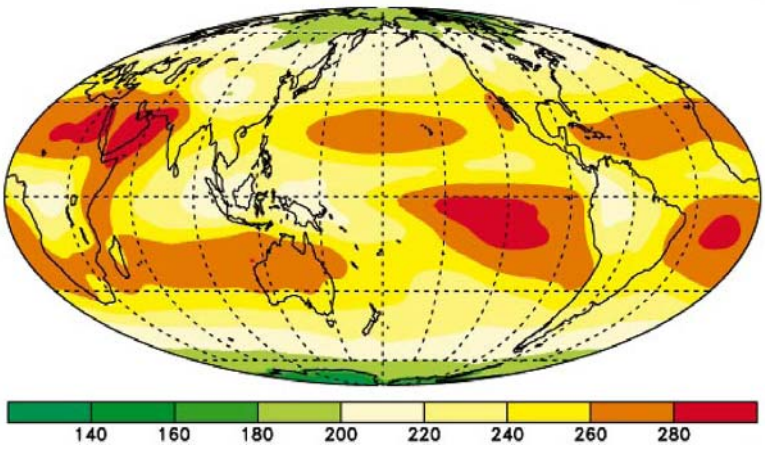

Figure 2.13: Net annual mean outgoing longwave radiation at the top of the atmosphere (in W/m^2). Figure from Trenberth and Stepaniak (2003). Copyright 2003 American Meteorological Society (AMS).

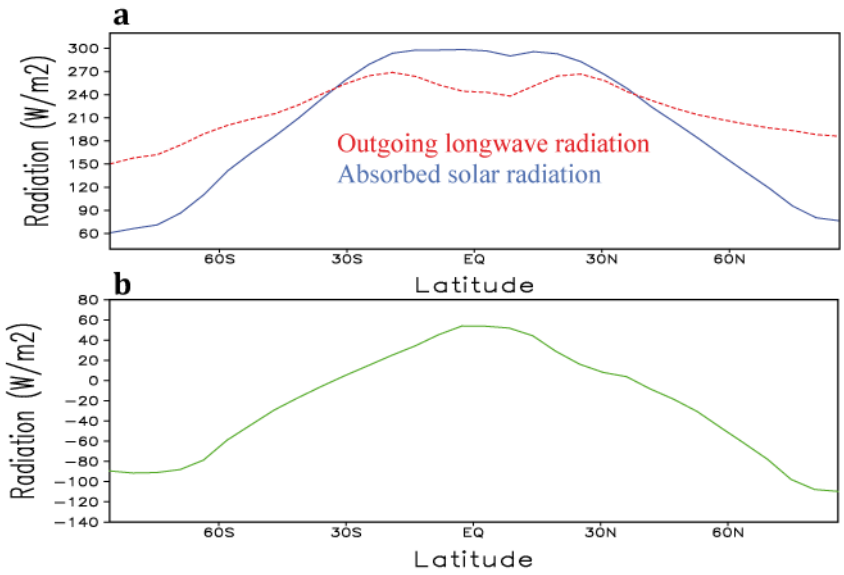

Figure 2.14: (a) **Zonal mean** of the absorbed solar radiation (blue) and the outgoing longwave radiation (dashed red) at the top of the atmosphere in annual mean (in W/m^2). (b) **Zonal mean** of the difference between the absorbed solar radiation and the outgoing longwave radiation at the top of the atmosphere in annual mean (in W/m^2). Data from NCEP-NCAR **reanalysis** (Kalnay et al. 1996).

When averaged over longitude, the outgoing **longwave radiation** clearly shows less latitudinal variation than the net incoming solar radiation absorbed by the Earth. As a consequence, the absorbed solar radiation outbalances the outgoing radiation in regions located between roughly 40°S and 40°N, while a net deficit in the net radiative flux at the top of the atmosphere (RF_{TOA}) is observed poleward of 40°N and 40°S (Fig. 2. 14). RF_{TOA} also displays some longitudinal variations, the most spectacular being probably the net negative flux over the Sahara because of the dry conditions there and of the high albedo of its sand.

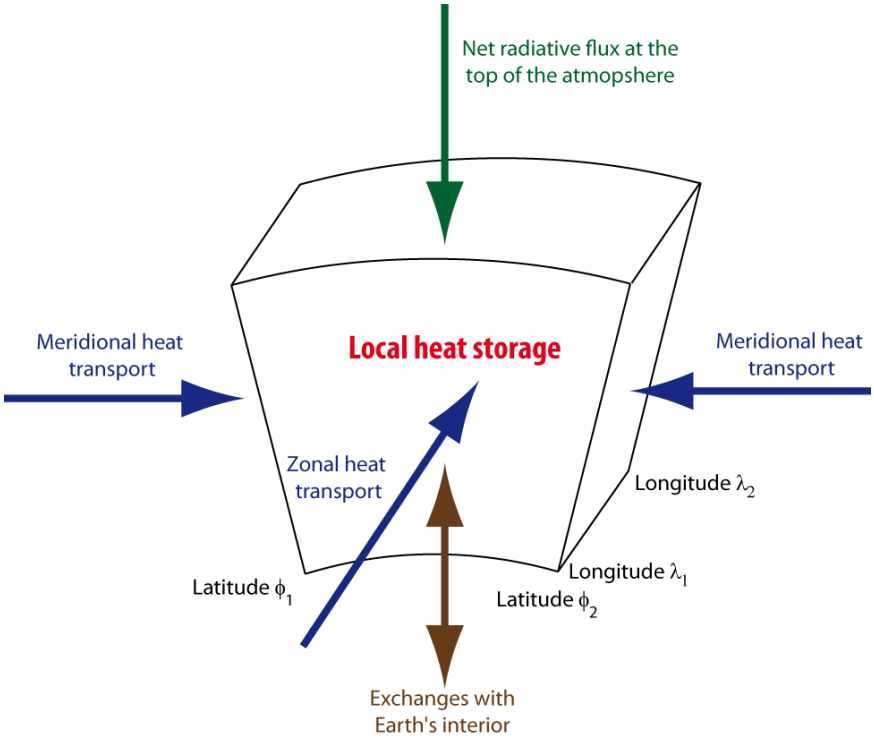

Figure 2.15: Schematic representation of the heat balance for the atmosphere, ocean, land surface and the ground in a volume lying between latitudes ϕ_1, ϕ_2 and longitudes λ_1, λ_2.

2.1.5 Heat storage and transport

In an area delimited by latitudes ϕ_1, ϕ_2 and longitudes λ_1, λ_2 (Fig. 2.15), the net radiative heat flux at the top of the atmosphere RF_{TOA} must be balanced by the sum of the horizontal heat transport, the heat exchanges with the deep ground, and the contribution to the heat budget associated with changes in the heat storage in the atmosphere, the ocean and the ground. As the ground has a very low thermal conductivity, only the top few metres interact with the surface on seasonal to decadal **timescales**. In the majority of climatic applications, it is thus sufficient to take the top few metres of the ground (typically 10 metres) into account, and assume that exchanges with the deep ground or the Earth's interior can be represented by a geothermal heat flux. The value of this flux is weak in the majority of the regions (~0.075 W/m^2) and it is thus often neglected in heat balance computations.

2.1.5.1 Heat storage.

On daily and seasonal timescales, the heat storage by the climate system plays a large role in mitigating the influence of the changes in the radiative flux at the top of the atmosphere. Those variations in heat storage for the ocean, atmosphere and ground can be estimated by:

$$\text{rate of change in heat storage} = \int_V \rho c_m \frac{\partial T}{\partial t} dV \qquad (2.27)$$

where ρ, c_m and T are the density, specific heat capacity and temperature of the media (i.e. atmosphere, sea or ground) included in the volume V. This term can be approximated by:

$$\text{rate of change in heat storage} \simeq m_m c_m \frac{\partial T_m}{\partial t} = C_m \frac{\partial T_m}{\partial t} \tag{2.28}$$

where m_m, c_m and T_m are the characteristic mass, specific heat capacity and temperature of the media that is storing heat and C_m is the effective heat capacity of the media (measured in J m^{-2} K^{-1}). The value of m_m is strongly dependent on the volume that displays significant changes in heat content on the **timescale** of interest.

On the seasonal **timescale**, the heat content of the whole atmosphere changes. If we use a value for c_p of 1000 J K^{-1} Kg^{-1} and a mass of 10^4 kg m^{-2} (assuming **hydrostatic equilibrium**, this corresponds roughly to a pressure of 10^5 Pa), we get an estimate of C_m for the atmosphere of:

$$C_{m,atmosphere} = 1000 \cdot 10^4 = 10^7 \text{ J K}^{-1}\text{m}^{-2} \tag{2.29}$$

Only the top 50 to 100 metres of the sea display a significant seasonal cycle in temperature. Using a specific heat capacity of water of 4000 J K^{-1} kg^{-1}, and a mass of 7.5 10^4 kg m^{-2},(i.e. 75 m times 1000 kg m^{-3}), we have.

$$C_{m,ocean} = 4000 \cdot 7.5\ 10^4 = 3.\ 10^8 \text{ J K}^{-1}\text{m}^{-2} \tag{2.30}$$

The ground has a specific heat capacity similar to that of the ocean but only a few metres are affected by the seasonal cycle. As a consequence, the effective heat capacity of the ground is much lower than that of the ocean on this time scale.

This rough comparison clearly shows that the effective thermal capacity of the sea is an order of magnitude larger than that of the atmosphere and the ground on a seasonal timescale. As a consequence, the sea stores much more energy during summer than the other media, energy that is released during winter. This moderates the amplitude of the seasonal cycle over the sea, by comparison with the land. A strong difference in the amplitude of the seasonal cycle is also seen in land areas that are directly influenced by the sea (at mid-latitudes, because of the westerly winds, this means land masses to the east of the oceans, such as Europe) compared to land masses far away from sea (Fig. 2.16). A similar analysis on a daily timescale shows that, heat storage by land, sea and atmosphere are all important.

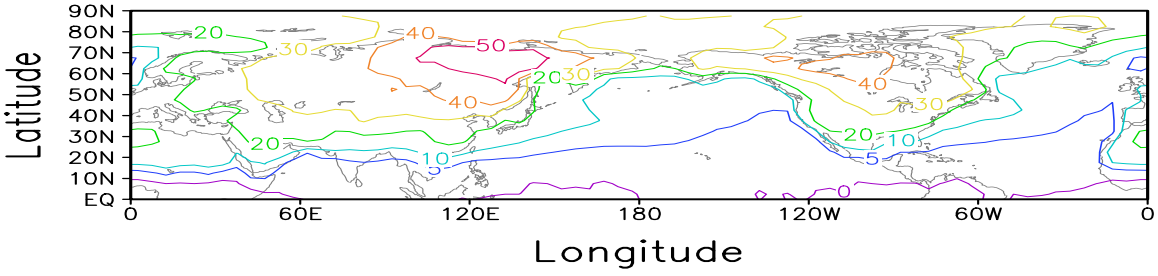

Figure 2.16: Amplitude of the seasonal cycle in surface temperature (in °C) in the northern hemisphere measured as the difference between July and January monthly mean temperatures. Data from the HadCRUT2 dataset (Rayner et al., 2003).

For decadal to centennial variations, such as the warming observed since the mid 19th century, thermal heat storage in the first hundred metres depth of the ocean (and at greater depths in regions of **deep water formation**) also moderates the transient temperature changes (see Chapter 6). On much longer time scales, such as the glacial-interglacial cycles, we have to take into account the full depth of the ocean (~4000 m). For deglaciation, which is faster than the glacial inception (see Chapter 5), we can estimate the order of magnitude of the mean ocean temperature at a 2°C change in 5000 years. This corresponds to a mean heat flux at the ocean surface of 0.03 W m^{-2} (= 4000 m . 1000 kg m^{-3} . 4000 J K^{-1} kg^{-1} . 3°C / [5000 . 365 . 24 . 3600 s]). This demonstrates that the change in oceanic heat storage plays a negligible role but the inertia of the ice sheets has to be taken into account on these timescales.

2.1.5.2 Heat transport.

Locally, heat storage by the **climate system** cannot compensate for the net radiative flux imbalance at the top of the atmosphere and, annually, the balance is nearly entirely achieved by heat transport from regions with a positive net radiative flux to regions with a negative net radiative flux. When the balance is averaged over latitudinal circles (**zonal** mean), this corresponds to a **meridional** heat transport from equatorial to polar regions (Fig. 2.17). This poleward heat transport at a latitude ϕ can be estimated by integrating the net radiative balance at the top of the atmosphere from the South Pole to latitude ϕ:

$$RT(\phi) = \int_{-\pi/2}^{\phi} \int_{0}^{2\pi} RF_{TOA}(\lambda, \phi') R^2 \cos\phi' d\lambda d\phi' \qquad (2.31)$$

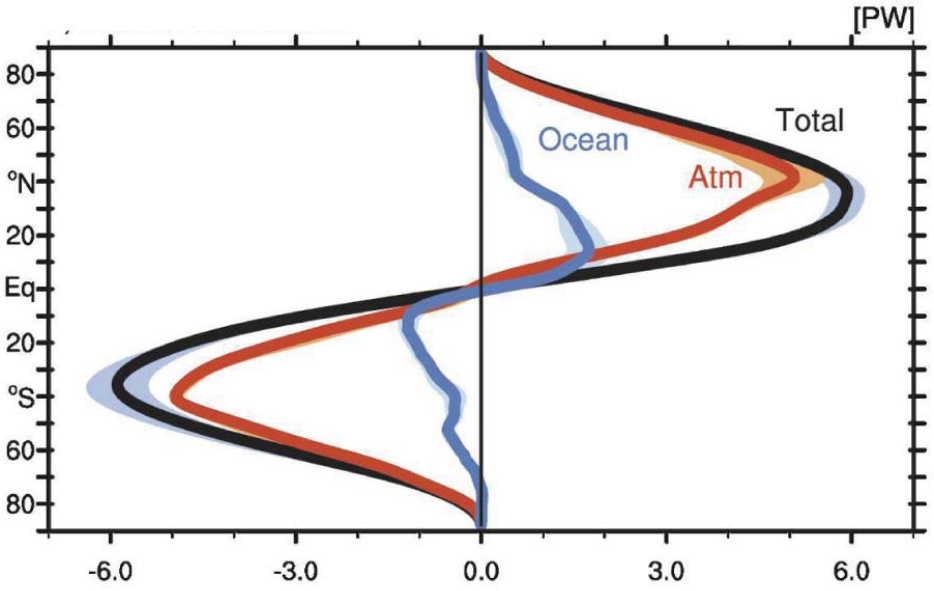

Figure 2.17: The required total (RT) heat transport in PW (10^{15} W), needed to balance the net radiation imbalance at the top of the atmosphere (in black) and the repartition of this transport in oceanic (blue) and atmospheric (red) contributions, accompanied with the associated uncertainty range (shaded). A positive value of the transport on the x axis corresponds to a northward transport. Figure from Fasullo and Trenberth (2008). Copyright 2008 American Meteorological Society (AMS).

The heat transport obtained is nearly zero at the equator, rising to more than 5 PW at latitudes of about 35°, before declining again towards zero at the poles (Fig. 2.17). It can be divided into an oceanic and an atmospheric contribution, the horizontal transport on continental surface being negligible. This shows that, except in tropical areas, the atmospheric transport is much larger than the oceanic transport.

The energy can be transported as **sensible heat** (c_pT, which is related to **internal energy**), potential energy (gz), **latent heat** (Lq) and kinetic energy ($0.5\ u^2$) and is expressed per unit of mass as:

$$E = c_pT + gz + L_vq + 0.5u^2 \tag{2.32}$$

where z is the altitude (or depth), L_v the latent heat of vaporisation of water, q the **specific humidity** and u the velocity of the media. The first term is often called **sensible heat**. The transport of kinetic energy is much weaker than the other transports and is generally neglected. In the atmosphere, the three remaining terms must be taken into account, but in the ocean the transport of sensible heat is clearly dominant. Moreover, in some special cases, an additional term representing the transport of latent heat by sea ice and icebergs must be considered for local or regional analyses at high latitudes.

In the tropics, the majority of the atmospheric poleward heat transport is achieved by the **Hadley circulation**. By contrast, the mean circulation plays a much weaker role at mid to high latitudes where nearly all the transport is effected by **eddies**. In the ocean, both the wind-driven and deep-oceanic circulation are responsible for a significant part of the oceanic poleward heat transport, the latter having a dominant influence in the tropics. The role of the oceanic **eddies** is less well known, but they can be significant in at least some regions (such as the Southern Ocean).

In addition to its dominant role in the reduction of the temperature contrast between the equator and the poles on Earth (compared to a planet without an ocean and an atmosphere), horizontal heat transport is also responsible for some temperature differences on a regional scale. This can be illustrated by analysing the departure of the local temperature from to the **zonal** mean temperature. At first sight, Fig 2.18 emphasises the mountainous area such as the Tibetan Plateau, the Rocky Mountains and Greenland, where the temperature is much lower than at other locations at the same latitude. However, the influence of the atmospheric circulation is also clearly apparent with, for instance, in cold areas such as north-east Canada. This is because the dominant winds have a strong northerly component in this region, while the North Atlantic is warmer, partly because of the south-westerly winds in this region (see section 1.2). Over the ocean, the influence of the northward western boundary currents (see section 1.3) results in generally warmer surface oceanic temperature at about 30-40°N in the western part of the basin than in the eastern part (where the oceanic currents are generally bringing colder water from the North).

The **thermohaline circulation** is an additional source of longitudinal asymmetry as, in the Northern Hemisphere, **deep water formation** only occurs in the North Atlantic and not in the North Pacific (see section 1.3). The associated circulation transports cold water southward at great depths with the mass balance ensured by a corresponding northward transport of warmer water in the surface layer. This results in a net oceanic transport in the North Atlantic of about 0.8 PW at 30°N (i.e. more than twice the estimated transport in the wider Pacific at the same latitude). The **thermohaline circulation** is also responsible for the northward oceanic heat transport at all latitudes in the Atlantic, even in the Southern Hemisphere.

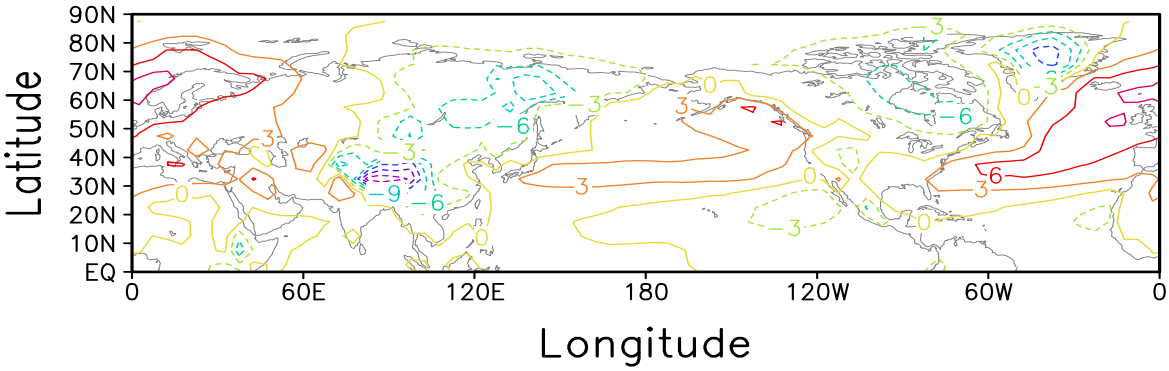

Figure 2.18: Difference between the annual mean surface temperature and the **zonal mean** temperature(computed as the annual mean temperature measured at one particular point minus the mean temperature obtained at the same latitude but averaged over all possible longitudes). Data from the HadCRUT2 dataset (Rayner et al., 2003).

This oceanic heat transport contributes to the fact that higher temperatures are observed in the North Atlantic than in other oceanic basins. Its influence is particularly large in the Barents Sea, north of Norway. Thanks to the oceanic heat transport, this area located north of 70°N (i.e., at the same latitude as the northern part of Alaska) remains free of sea ice all year long. Climate model calculations have shown that, if deep water formation was suppressed in the North Atlantic, the temperature in the North Atlantic and in Western Europe would be reduced by about 3° C at 45° N, while the annual mean temperature would decrease by more than 15° C in northern Norway and the Barents Sea.

2.1.6 Heat balance at the surface

As discussed in section 2.1.1, the incoming solar radiation on a horizontal surface at the top of the atmosphere is about 342 W m^{-2}, with roughly 30% of this being reflected back into space. An analysis of the Earth's global heat balance (Fig. 2.19) shows that more that 70% of the reflection takes place in the atmosphere, mainly because of the presence of clouds and **aerosols**. The remaining 30% is reflected by the surface. By contrast, the majority of the absorption of solar radiation occurs at the surface, which absorbs 2.5 times more solar energy than the whole atmosphere. This shows clearly that the majority of atmospheric warming occurs from below, and not by direct absorption of solar radiation. This important property of the system explains the major characteristics of the Earth's atmosphere, including the vertical temperature profile and the large scale circulation of the atmosphere (see section 1.2).

The outgoing **longwave radiation** required to balance the Earth's budget at the top of the atmosphere is mainly emitted by the atmosphere and clouds. Among the 396 W m^{-2} emitted by the surface, only 40 W m^{-2} can exit the **climate system** directly. The large majority of surface longwave radiation is absorbed by the atmospheric greenhouse gases and re-emitted towards the surface where the downward longwave radiation flux (333 W m^{-2}) becomes the largest term in the surface heat balance.

In addition to the radiative fluxes, the surface and the atmosphere exchange heat through direct contact between the surface and the air (**sensible heat** flux or thermals) as well as through evaporation and transpiration. Indeed, when evaporation (or sublimation) takes place at the surface, the **latent heat** required for the phase transition is taken out of the surface and results in a surface cooling. Later, mainly during the formation of clouds,

the water vapour condensates and the latent heat is released into the atmosphere. This leads to a net mass and heat transfer from the surface into the atmosphere, which is one of the main drivers of the general atmospheric circulation.

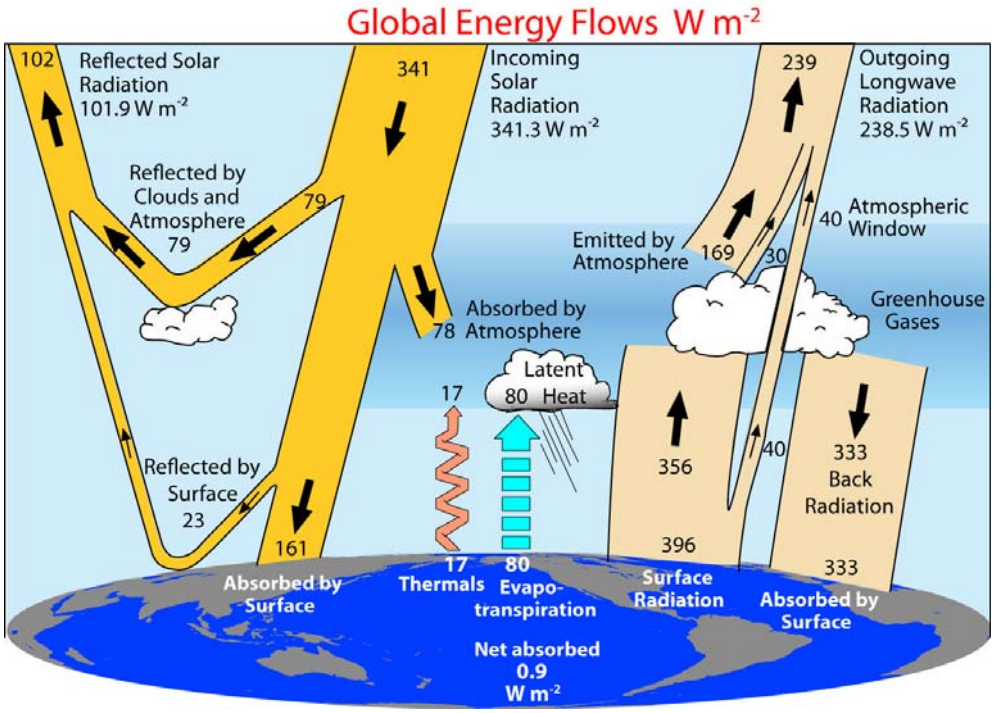

Figure 2.19: Estimate of the Earth's annual and global mean energy balance for the March 2000 to May 2004 period in W m^{-2}. Figure from Trenberth et al. (2009). Copyright 2009 American Meteorological Society (AMS).

The fluxes of sensible and latent heat are generally estimated as a function of the wind speed at a reference level, and the difference in temperature (for the sensible heat flux F_{SH}) or specific humidity (for the latent heat flux F_{LH}) between the surface and the air at this reference level, using classical bulk aerodynamic formulae:

$$F_{SH} = \rho c_p c_h U_a \left(T_s - T_a\right) \tag{2.33}$$

$$F_{LE} = \rho L_v c_L U_a \left(q_s - q_a\right) \tag{2.34}$$

where U_a, T_a, q_a are the wind velocity, air temperature and specific humidity at the reference level (generally 2 m or 10 m), T_s and q_s are the surface temperature and **specific humidity** at the surface, and c_h and c_L are the aerodynamic (bulk) coefficient. In general, they are function of the stability of the **atmospheric boundary layer**, the roughness of the surface, the wind speed and the reference height. In the majority of cases, c_h and c_L are not too different from each other and their value ranges from 1 10^{-3} to 5 10^{-5}. The highest values occur with unstable boundary layers and very rough surfaces which tend to generate strong turbulent motions and thus higher exchanges between the surface and the air than quieter situations.

The **specific humidity**, q_s, above a wet surface is generally very close to saturation. It can thus be expressed using the **Clausius-Clapeyron equation**, which shows that the amount of water vapour in the air at saturation is strongly dependent on temperature. For

instance, the amount of water vapour that can be present in the atmosphere at a temperature of 20°C is more than three times higher than at 0°C. As a consequence, the evaporation and the latent heat flux are much larger at low latitudes than at high ones. The latent heat flux is thus larger than the sensible heat flux at low latitudes, while the two fluxes are generally of the same order of magnitude over the ocean at high latitudes. The ratio between the sensible heat and latent heat fluxes is usually expressed as the Bowen Ratio B_o:

$$B_o = \frac{F_{SH}}{F_{LE}} \tag{2.35}$$

Over land surfaces, the latent heat flux is a function of the water availability and B_o can be much higher than unity over dry areas.

The heat balance shown in Figure 2.19 for the whole Earth can also be computed for any particular surface on Earth. This is generally the method used to obtain T_s. Let us consider a unit volume at the Earth's surface with an area of 1 m^2 and a thickness h_{su} (Fig. 2.20). h_{su} is supposed to be sufficiently small to safely make the approximation that the temperature is constant over h_{su} and equal to T_s. The heat balance of this volume can then be expressed as:

$$\rho c_p h_{su} \frac{\partial T_s}{\partial t} = (1-\alpha) F_{sol} + F_{IR\downarrow} + F_{IR\uparrow} + F_{SE} + F_{LE} + F_{cond} \tag{2.36}$$

The left-hand side of the Eq. 2.36 represents the heat storage in the layer h_{su} (see section 2.1.5). F_{sol} is the incoming solar flux at the surface which is a function of the incoming solar radiation at the top of the atmosphere and of the transmissivity of the atmosphere (related to the presence of clouds, aerosols, the humidity of the air, etc). A fraction α of F_{sol} is reflected by the surface and not absorbed. $F_{IR\downarrow}$ is the downward **longwave** radiation flux at surface. This flux is caused by the emission of infra-red radiation at various levels in the atmosphere. It is thus a complex function of the temperature and humidity profiles in the atmosphere, the cloud cover and the height of the clouds, the presence of various greenhouse gases (in addition to water vapour), etc. The longwave upward radiation flux $F_{IR\uparrow}$ can be computed using the **Stefan-Boltzman law** while the expressions for F_{SE} and F_{LE} are given by Eq. 2.33 and 2.34. F_{cond}, the flux from below the surface, is a conduction flux for solid surfaces (such as the ground and the ice) that can be represented following the **Fourier law**. For the ocean, this flux is related to the dynamics of **the oceanic mixed layer**. Additionally, if the media at the surface is (partly) transparent, a fraction of the radiation is not absorbed in the layer of thickness h_{su} and must be subtracted from the term (1-α F_{sol}) in Eq. 2.36. For the other fluxes, the exchanges take place in a very shallow layer and can reasonably be considered as purely surface processes.

Figure 2.20 displays a relatively simple situation where the surface (i.e. the interface between the atmosphere and the material below) is clearly defined. In complex terrain with very rough topography, for instance over forests or urban areas, defining the lower limit of the atmosphere is less straightforward. Computing the surface fluxes in these regions is a very complex issue which is the currently the subject of intense research.

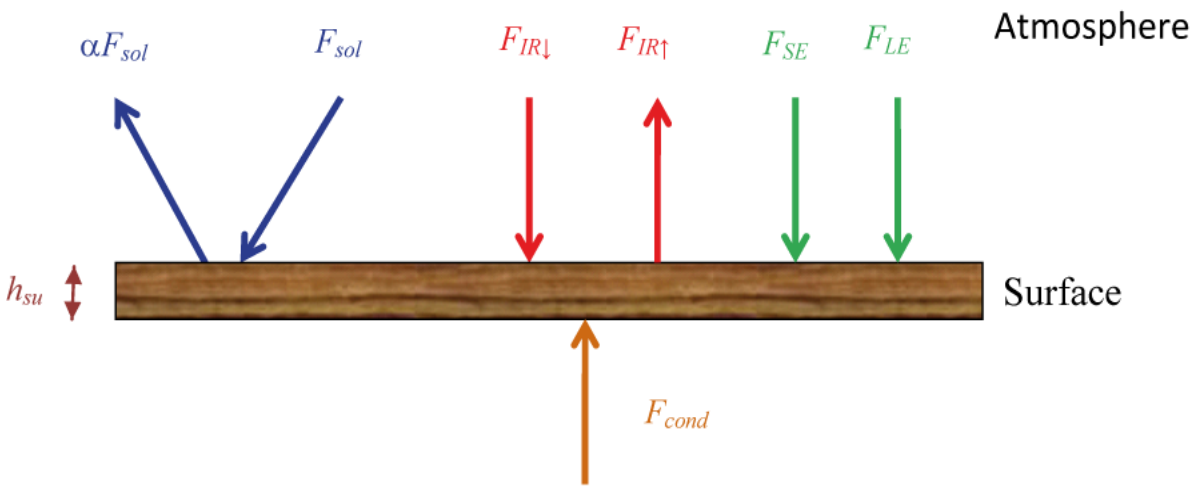

Figure 2.20: The heat balance of a surface.

When snow or ice is present at the surface, the temperature T_s cannot be higher than the freezing point of water. As a consequence, Eq. 2.36 remains valid as long as T_s is below the freezing point. When surface melting occurs (i.e., when T_s equals the freezing point of water) an additional term, corresponding to the latent heat of fusion required to keep the temperature unchanged, must be added to the right-hand side of Eq.2.36.

2.2 The hydrological cycle

As discussed in section 2.1, the water –or hydrological- cycle plays an important role in the energy cycle on Earth. It has a considerable impact on the radiative balance: water vapour is the most important greenhouse gas in the atmosphere (see section 2.1.2); the presence of snow and ice strongly modifies the **albedo** of the surface (see Table 1.3. and sections 2.1.4 and 4.2.3); and clouds influence both the **longwave** and **shortwave** fluxes (see sections 2.1.4, 2.1.6 and 4.2.2). Moreover, water is an essential vehicle for energy: the **latent heat** released during the condensation of water is a dominant heating source for the atmosphere (see section 2.1.6); the transport of water vapour in the atmosphere and of water at different temperatures in the ocean are essential terms in the horizontal heat transport (see section 2.1.5.2).

The hydrological cycle is also essential in shaping the Earth's environment, the availability of water being a critical factor for life as well as for many chemical reactions and transformations affecting the physical environment. Describing the various components of the hydrological cycle and analysing the mechanisms responsible for the exchanges of water between the different reservoirs are thus important elements of climatology.

By far, the largest reservoir of water on Earth is located in the crust, with estimates of the order of 10^{22} kg of water (equivalent to 10^{19} m³ at surface pressure, i.e. about 10 times the amount of water in the oceans, the second largest reservoir). However, exchanges between deep Earth and other reservoirs are so slow that they only have a very weak impact on the hydrological cycle at the surface and are thus generally not taken into account in estimates of the global hydrological cycle (Fig. 2.21).

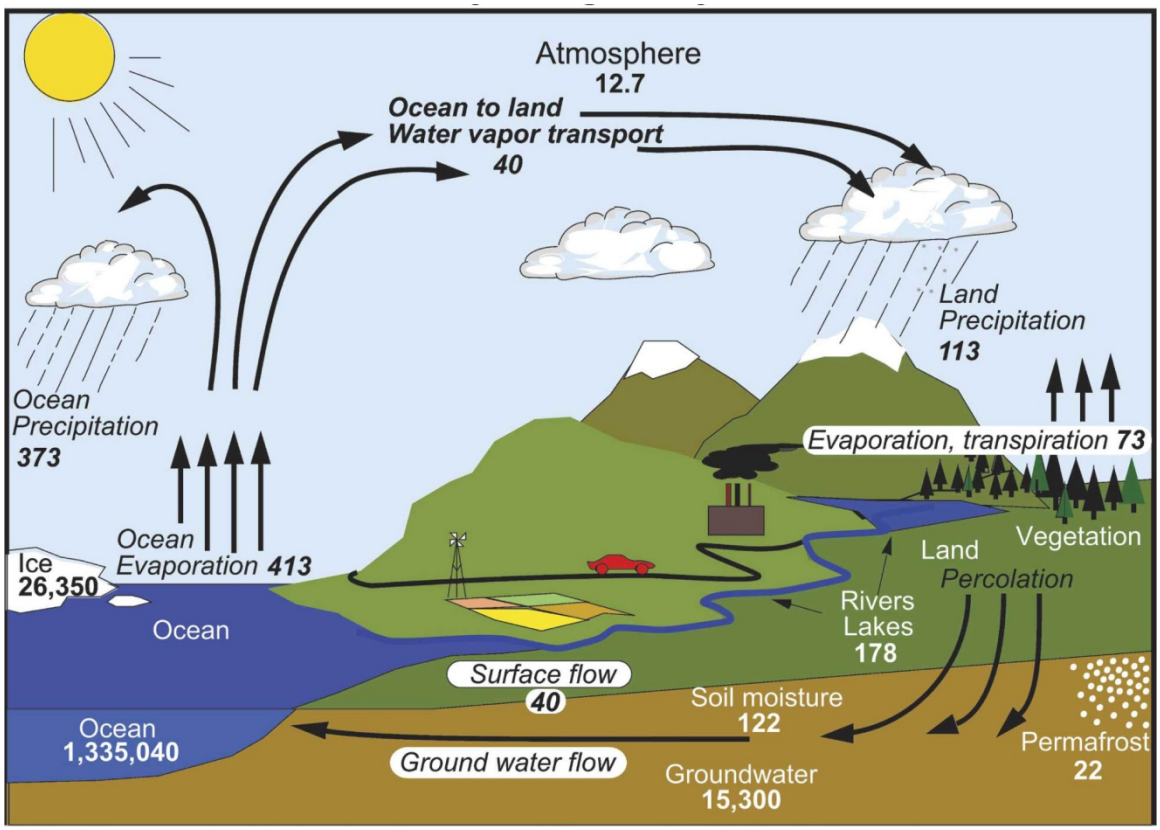

Figure 2.21: The long-term mean global hydrological cycle. Estimates of the main water reservoirs in plain font (e.g. Soil moisture) are given in 10^3 km^3 and estimates of the flows between the reservoirs in italic (e.g. *Surface flow*) are given in 10^3 km^3/year. Figure from Trenberth et al. (2007) who provide information about the sources used to estimate the magnitude of the elements of the cycle and about the uncertainties of the various terms. Copyright 2007 American Meteorological Society (AMS). Reproduced with permission.

A large amount of water is also stored in form of ice, mainly on the Greenland and Antarctic ice sheets (see section 1.4). By contrast, the stock of water in the atmosphere is very low. If the 12.7 10^3 km^3 of atmospheric water estimated in Fig. 2.21 all precipitated, it would correspond to about 2.5 cm of rainfall (=12.7 10^3 km^3/($4\pi R^2$)) over the whole Earth. As the actual precipitation on the Earth's surface is of the order of 1 m per year (see section 1.2), the water in the atmosphere must be being replaced very quickly. This is achieved by evaporation over the ocean and other water bodies as well as by evaporation and transpiration over land. Most of the water that evaporates over the ocean falls back over the ocean (and similarly the water that evaporates over land, falls back over land), but there is also water transfer by the atmosphere from the oceanic area to the land area. This net transfer corresponds to roughly 35% of the total precipitation over land, and is compensated by a surface flow of water (mainly in rivers) from the land to the sea.

According to the **Clausius-Clapeyron equation** (see section 2.1.6), intense evaporation occurs in the warm equatorial areas and in the tropics. In equatorial areas, because of the convergence at the surface and upward motions (see section 1.2), the moist air at low levels rises, reaching colder level. This induces condensation, the formation of clouds and high precipitation rates (see Fig. 1.7). Despite the high temperature and high evaporation rate, equatorial regions thus have more precipitation than evaporation at the

surface (negative *E-P,* Fig. 2.22). In the subtropics, evaporation minus precipitation (*E-P*) is clearly positive, because of the general **subsidence** at these latitudes. At mid to high latitudes, *E-P* is again negative on **zonal** average because of the net moisture transport from tropical areas.

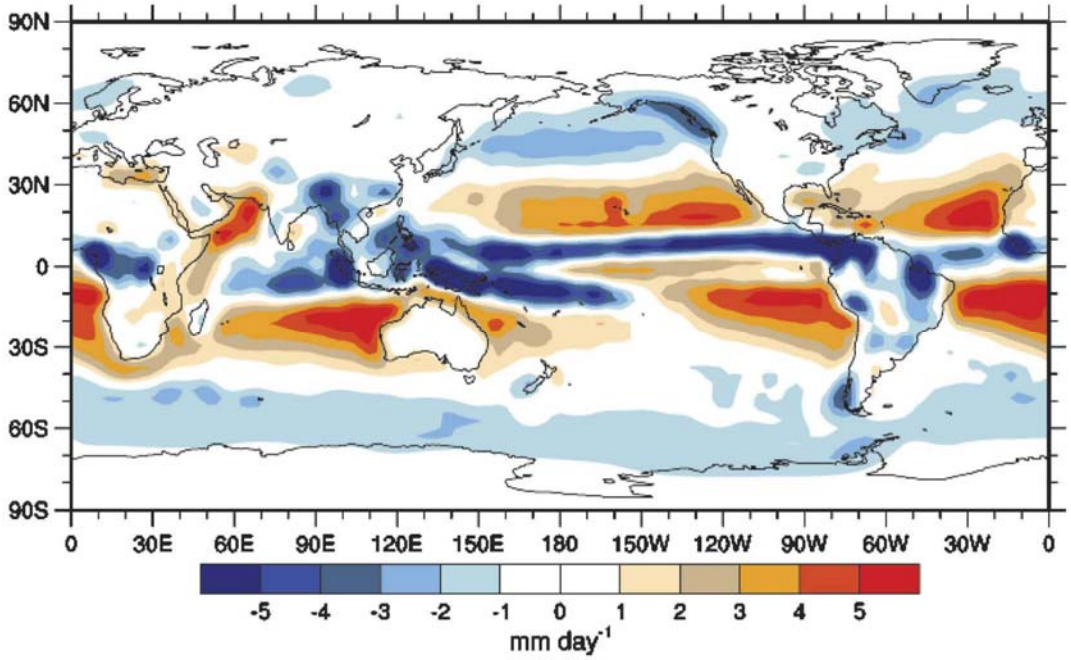

Figure 2.22: Long term annual mean evaporation minus precipitation (*E-P*) budget based on ERA-40 **reanalyses**. Units are mm per day. The major features of the *E-P* budget are represented on this figure, but because of large uncertainties, the values displayed should not be considered as quantitatively correct. There are also some clear discrepancies over land, in particular where net positive evaporation is shown (negative values should generally occur over land as river runoff is positive). Figure from Trenberth et al. (2007). Copyright 2007 American Meteorological Society (AMS), Reproduced with permission.

The imbalance of the water budget over land is generally small and is compensated by river runoff R_{riv} (in the long term mean, R_{riv} nearly equals P-E) which returns water to the sea. Because of the land topography, this river runoff is an important element of the water balance for some ocean basins. For instance, the Arctic Ocean receives about 10% of the total river runoff (mainly from the Russian rivers) although it only constitutes about 3% of the World Ocean. This partly explains why surface water in the Arctic is relatively fresh (see Fig. 1.11).

Over the oceans, the imbalance of the water budget at the surface is larger than over land because it can be compensated for by a net oceanic water transport that is much more efficient (and much larger) than that associated with river runoff. This net oceanic transport counter-balances the large atmospheric moisture transport out of the subtropics towards the equatorial regions and mid and high latitudes. In a way, the net meridional water transport and the associated energy transport in the atmosphere are only possible because the ocean transport is able to compensate for the imbalance at the surface due to the *E-P* fluxes.

Net oceanic water transport can also counterbalance the **zonal** transport by the atmosphere. In particular, because of high *E-P* rates, the Atlantic Ocean is a net evaporative basin and is thus more saline at the surface than the Pacific where the E-P

balance integrated over the whole basin is negative (see Fig. 1.11). As a consequence, the global oceanic circulation must induce a net water transport from the Pacific to the Atlantic to achieve a water balance in both basins.

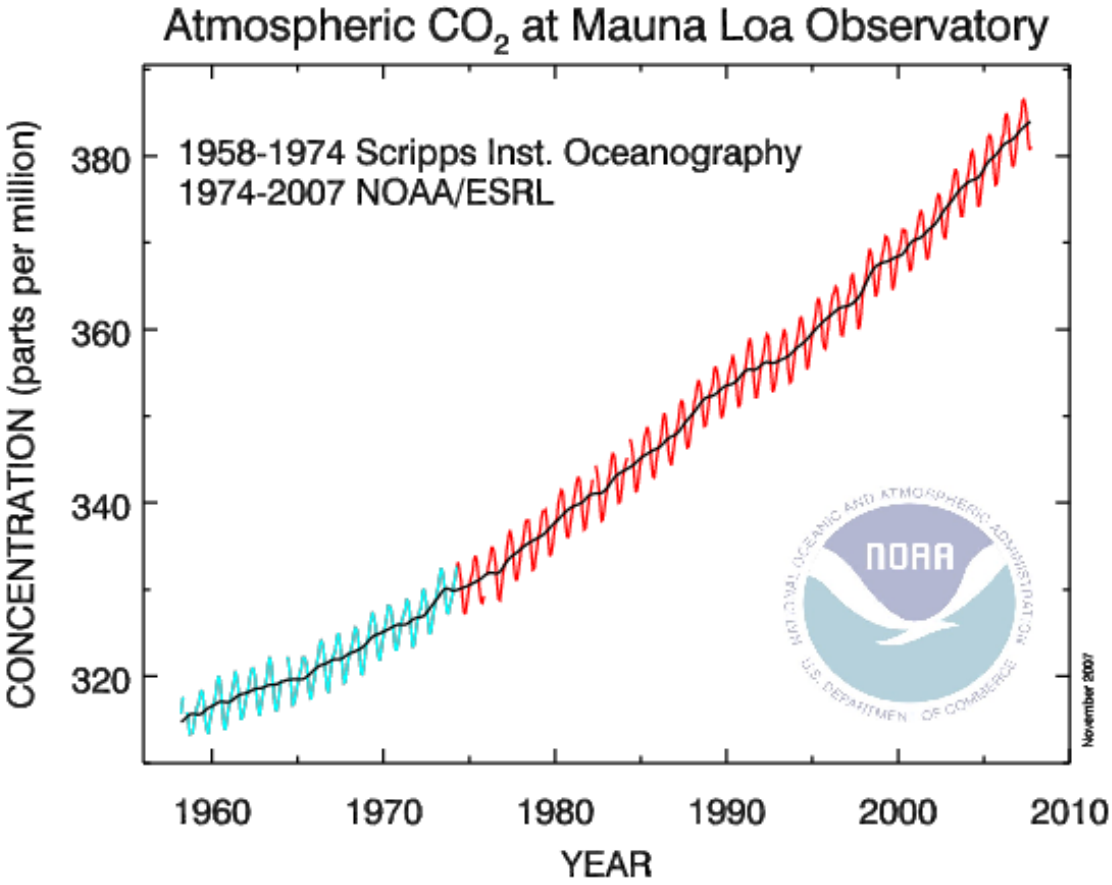

Figure 2.23: Monthly mean atmospheric carbon dioxide at Mauna Loa Observatory, Hawaii (in ppm). The observation were started by C. David Keeling of the Scripps Institution of Oceanography in March of 1958 (blue). The National Oceanic and Atmospheric Administration started its own CO_2 measurements in May of 1974 (red). The black curve represents the seasonally corrected data smoothed with a 6-month window. Source: Dr. Pieter Tans, NOAA/ESRL (www.esrl.noaa.gov/gmd/ccgg/trends/co2_data_flux_rev1.html). Following the policy of U.S. government agencies, this figure is not subject to copyright protection.

2.3 The carbon cycle

2.3.1 Overview

The transfers between the different components of the climate system imply exchanges of heat (section 2.1), exchanges of single molecules such as water (H_2O) with phase changes (section 2.2), and exchanges involving chemical transformations. This latter type of exchange may involve elements such as oxygen, nitrogen, phosphate and sulphur, but one of the most important cycles from a climatic point of view is the carbon cycle because it involves changes in the atmospheric concentration of two important greenhouse gases (section 2.1.2): carbon dioxide (CO_2) and methane (CH_4).

One of the major changes brought about by human activity is the large increase in the atmospheric concentration of those two gases (see Chapter 6). The concentration of carbon dioxide has increased from around 280 ppm in 1800 to 384 ppm in 2007. Because CO_2 is relatively stable, it is well mixed and its concentration in the atmosphere is nearly homogenous away from zones where strong exchanges with the biosphere occur. Those exchanges with the biosphere are also responsible for the weak seasonal cycle observed in the long Mauna Loa record (Fig. 2.23).

CH_4 is more reactive than CO_2 and can be oxidised to form CO_2 and H_2O.

$$CH_4 + 2O_2 \rightarrow CO_2 + 2H_2O \tag{2.37}$$

Its concentration is lower than that of CO_2, but it has increased from 725 ppb to 1780 ppb in 150 years. Methane is naturally produced by the anaerobic breakdown of organic matter in lakes and swamps. Methane is also released into the atmosphere by human activities such as mining, biomass burning and gas production, as well as the production of rice and by ruminants which produce methane as they digest grass.

The atmosphere is a relatively small reservoir of carbon compared to the sedimentary rocks, the ocean and the terrestrial biosphere (which includes non living organic material such as soil carbon) (Fig. 2.24). In particular, more than 50 10^6 GtC (gigatons of carbon or equivalently PgC, petagrams of carbon) are stored in the Earth's crust. This is more than 1000 times the stock in the ocean, more 20 000 times the stock in soil and more than 50 000 times the stock in the atmosphere. However, the changes in the carbon concentration in sedimentary rocks are very small, and the associated fluxes are much lower than those between the ocean, the atmosphere and the soil.

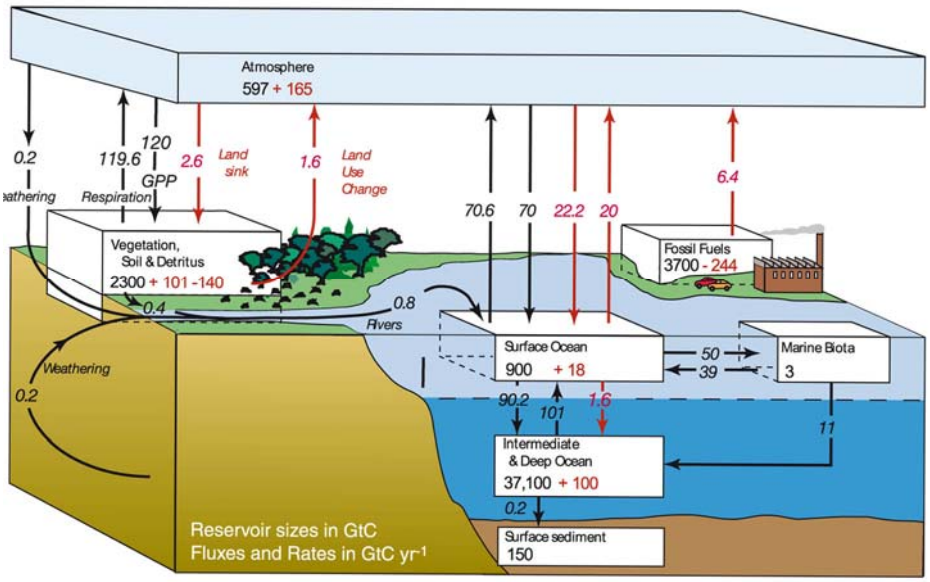

Figure 2.24: The global carbon cycle for the 1990s, showing the main annual fluxes in GtC yr^{-1}: pre-industrial 'natural' fluxes are shown in black and 'anthropogenic' fluxes in red. The carbon stored in deep sediments and in the Earth's crust is estimated at around 50 10^6 GtC. Figure 7.3 from Denman et al. (2007) using a modified legend, published in:Climate Change 2006: The Physical Science Basis. Contribution of Working Group I to the Fourth Assessment Report of the Intergovernmental Panel on Climate Change, Cambridge University Press, copyright IPCC 2007. Reproduced with permission.

Before the industrial era (i.e. before 1750), the exchanges between the various reservoirs were close to equilibrium. However because of anthropogenic carbon release mainly related to fossil-fuel burning and changes in land use (deforestation and agriculture processes), the flux of carbon into the atmosphere has increased dramatically during the last 150 years. Roughly 45% of the anthropogenic carbon released up to now has remained in the atmosphere, which explains the observed rise in atmospheric CO_2. The remaining fraction has been absorbed by the ocean (around 30%) or the terrestrial biosphere (around 25%).

2.3.2 Oceanic carbon cycle

A flux of CO_2 between the ocean and the atmosphere occurs when the CO_2 content of the ocean surface is not in equilibrium with the atmospheric concentration. The flux Φ^{CO_2} from the ocean to the atmosphere is proportional to this imbalance and can be computed as a function of the difference in partial pressure p^{CO_2} between the two media:

$$\Phi^{CO_2} = k^{CO_2}\left(p_W^{CO_2} - p_A^{CO_2}\right) \tag{2.38}$$

where the subscripts A and W refer to air and water, respectively. k^{CO_2} is a transfer coefficient which is strongly dependent on the wind velocity. At equilibrium, $p_W^{CO_2}$ is obviously equal to $p_A^{CO_2}$.

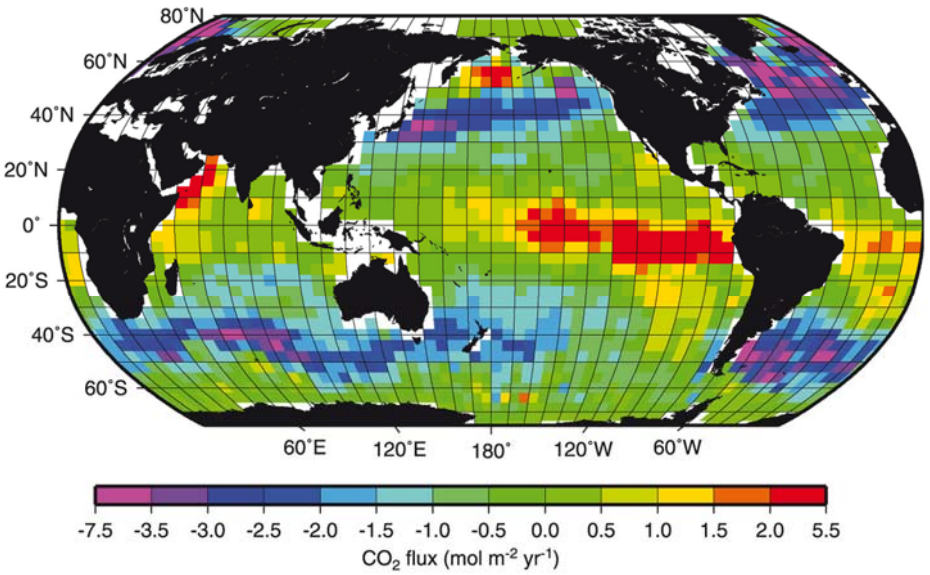

Figure 2.25: Estimates of sea-to-air flux of CO_2. Figure 7.8 from Denman et al. (2007), based on the work of T. Takahashi, available at http://www.ldeo.columbia.edu/res/pi/CO2/carbondioxide/pages/air_sea_flux_rev1.html), using a modified legend, published in: Climate Change 2007: The Physical Science Basis. Contribution of Working Group I to the Fourth Assessment Report of the Intergovernmental Panel on Climate Change, Cambridge University Press, copyright IPCC 2007. Reproduced with permission.

As the surface CO_2 concentration in the atmosphere is nearly homogenous, the repartition of the flux mainly depends on the oceanic p^{CO_2}. Supersaturated zones, where the partial pressure of CO_2 in sea water is higher than in the air, have a positive flux from the ocean to the atmosphere. In present-day conditions, this occurs in tropical regions, particularly in the eastern equatorial Pacific (Fig. 2.25). On the other hand, undersaturated areas, such as the mid to high latitudes around 40°-60° in both hemispheres (except the Northern Pacific), display CO_2 fluxes from the atmosphere to the ocean, i.e. an uptake of CO_2 from the atmosphere.

2.3.2.1 Inorganic carbon cycle

When gaseous CO_2 is transferred from the atmosphere to the ocean, it immediately reacts with water to form carbonic acid (H_2CO_3) which dissociates, leading to the formation of bicarbonate (HCO_3^-) and carbonate ions (CO_3^{2-}):

$$CO_{2(gas)} + H_2O \rightleftharpoons H_2CO_3 \tag{2.39}$$

$$H_2CO_3 \rightleftharpoons H^+ + HCO_3^- \tag{2.40}$$

$$HCO_3^- \rightleftharpoons H^+ + CO_3^{2-} \tag{2.41}$$

The sum of these three forms of carbon is often referred to as Dissolved Inorganic Carbon (***DIC***):

$$DIC = \left[H_2CO_3\right] + \left[HCO_3^-\right] + \left[CO_3^{2-}\right] \tag{2.42}$$

The reactions (2.39 to 2.41) are so fast that, to a good approximation, the three components are always in equilibrium. The equilibrium relationship between the different molecules involved in reaction (2.39) can then be used to define the **solubility** K_H of CO_2, which relates the concentration of carbonic acid to the partial pressure of carbon dioxide (pCO_2).

$$K_H = \frac{\left[H_2CO_3\right]}{pCO_2} \tag{2.43}$$

By definition, for the same atmospheric pCO_2, the amount of carbonic acid in the ocean at equilibrium will be larger for a high solubility than for a low solubility. The transfer of CO_2 between the ocean and the atmosphere (Eq. 2.38) can then easily be expressed as a function of $[H_2CO_3]$ using (Eq. 2.43).

In the sea, the equilibrium between the different forms of carbon occurs when nearly 90% of the dissolved inorganic carbon is in the form of bicarbonate, around 10% is carbonate, and only 0.5% is carbonic acid. This predominance of carbonate and bicarbonate ions explains why the ocean is able to store much more carbon than the atmosphere, while it is not true for other gases (such as oxygen) which have similar solubility to CO_2. Furthermore, reactions (2.39 to 2.41) show that atmospheric CO_2 must balance the whole pool of *DIC*, not just H_2CO_3. As *DIC* is dominated by HCO_3^- and

CO_3^{2-}, the atmosphere-ocean exchanges will be strongly influenced by the concentration in these ions. For instance, it has been estimated that only 1 molecule in 20 of the CO_2 entering the ocean stays as H_2CO_3, the large majority reacting with CO_3^{2-} to form HCO_3^-, the dominant species in *DIC*:

$$H_2CO_3 + CO_3^{2-} \rightleftharpoons 2HCO_3^- \tag{2.44}$$

The ocean-atmosphere fluxes are thus strongly influenced by the availability of CO_3^{2-}. Additionally, because of the small fraction of incoming CO_2 staying as H_2CO_3 and thus influencing the p^{CO_2} in the ocean, the time taken to reach equilibrium between the ocean and the atmosphere is about 6 months - around 20 times longer than if this reaction were not active.

As shown in reactions (2.40 and 2.41), the dissociation of H_2CO_3 causes the water to become more acidic. This effect is commonly measured through the alkalinity *Alk*, defined as the excess of bases over acid in water:

$$Alk = \left[HCO_3^-\right] + 2\left[CO_3^{2-}\right] + \left[OH^-\right] - \left[H^+\right] + \left[B(OH)_4^-\right] + \text{minor bases} \tag{2.45}$$

where $\left[B(OH)_4^-\right]$ is the borate ion. The total alkalinity is dominated by the influence of bicarbonate and carbonate ions, meaning that a tight link exists between *Alk* and the concentration of the three forms of carbon. Conversely, changes in total alkalinity or in the acidity of the ocean can have a strong influence on the equilibrium of the reactions (2.40 and 2.41). For instance, if *Alk* decreases (or equivalently if the system become more acid), the equilibrium of reactions (2.40) and (2.41) will be pushed toward the formation of more H_2CO_3 and HCO_3^-, increasing the concentration of H_2CO_3 and thus the p^{CO_2} with a potential influence on air-sea fluxes. The estimates of this effect suggest an increase in 10% of the p^{CO_2} for a 1% decrease in *Alk*.

On the basis of this discussion, we can return to Fig. 2.25 and try to explain the distribution of the air-sea fluxes of CO_2. The solubility of CO_2, or equivalently the equilibrium constant of reaction (2.39) is strongly dependent on temperature. A water parcel that is cooled, as it flows northward for instance, will take up atmospheric CO_2, while a water parcel that is warmed will release CO_2 to the atmosphere. This generally leads to positive ocean-atmosphere fluxes in tropical regions and negative ones at high latitudes, as shown in Fig. 2.25.

2.3.2.2 Biological pumps

In addition to the purely thermal effect, biological processes also play a significant role in the distribution of surface fluxes of CO_2 by affecting *DIC* and *Alk*. A first important reaction is the photosynthesis in which phytoplankton uses solar radiation to form organic matter from CO_2 and water:

$$6CO_2 + 6H_2O \rightleftharpoons C_6H_{12}O_6 + 6O_2 \tag{2.46}$$

Conversely, organic matter can be dissociated to form inorganic carbon (the reverse process of photosynthesis) by respiration and remineralisation of dead phytoplankton and detritus.

Reaction 2.46 is a highly simplified representation of the complex biological processes associated with photosynthesis. In particular, it hides the fact that, in order to produce organic matter, phytoplankton need nutrients (mainly nitrates and phosphates) as well as minor elements such as iron. As those nutrients generally have low concentrations in surface water where light is available for photosynthesis, their concentration is often the limiting factor for biological production.

Because particles whose density is more than that of water settle out, and some particles are transported by ocean currents, a fraction of the organic matter is exported downward out of the surface layer. The net downward flux of carbon associated with this transport of organic matter is called the **soft tissue pump**. A significant part of the remineralisation thus occurs in the deep layers where it produces an increase in *DIC* and the release of nutrients. The deep waters are thus rich in nutrients. Where they **upwell** toward the surface, the surface concentration of nutrients increases, generally leading to high biological production, such as that observed off the coasts of Peru and Mauritania.

A second important biological process is related to the production of calcium carbonate (in form of **calcite** or **aragonite**) by different species, in particular to form their shells:

$$Ca^{2+} + CO_3^{2-} \rightleftharpoons CaCO_3 \tag{2.47}$$

This production influences both the *DIC* and the *Alk* and can thus have a large influence on the carbon cycle. For instance, $CaCO_3$ production implies a reduction in *Alk* (see Eq. 2.45), which in turns lead to an increase in oceanic p^{CO_2} and reduces the uptake of atmospheric CO_2 by the ocean. An alternative way to view this mechanism is to say that $CaCO_3$ production reduces the concentration of CO_3^{2-} in the ocean and thus the availability of this ion to combine with H_2CO_3 to produce HCO_3^- (reaction 2.44), so increasing [H_2CO_3] and p^{CO_2}.

The dissolution of calcite and aragonite mainly occurs at great depth (see section 4.3.1), following the precipitation of particles and dead organisms. This leads to the *Alk* and *DIC* being transported downwards, a system called the **carbonate pump**. A third pump, called the **solubility pump**, is associated with the sinking of cold surface water, characterised by a relatively high solubility of CO_2 and thus high *DIC,* to great depths at high latitudes. All these downward transports have to be compensated for at equilibrium by an upward flux of inorganic carbon by the oceanic circulation.

Because of the three pumps briefly described above, DIC is about 15% higher at depths than at the surface. The soft tissue pump plays the largest role in the observed vertical gradient. This distribution has a profound influence on the atmospheric CO_2 concentration. Indeed, if *DIC* were perfectly homogenous in the water column (i.e. had higher surface values and lower depth values than currently observed), the concentration of atmospheric CO_2 would be much higher. More realistically, when deep water upwells to the surface, CO_2 will tend to escape from the ocean because of the high *DIC*. However, as the deep waters are rich in nutrients, the biological uptake associated with photosynthesis can compensate for the influence of a higher *DIC*. The net effect depends on the regions, generally resulting in positive ocean-atmosphere CO_2 fluxes at high

latitudes and negative ones at low latitudes, partly offsetting the direct temperature effect (Fig. 2.25).

2.3.3 Terrestrial carbon cycle

The uptake of carbon through photosynthesis by land plants is larger than the corresponding uptake by phytoplankton, in particular in spring because of the greening of forest at mid and high latitudes and of the growth of herbaceous plants (Fig. 2.26). About half of this primary production is directly transferred back to the atmosphere by the respiration of the land plants themselves, the remaining part being incorporated into leaves, woods and roots (this fraction is defined as the **net primary production, NPP**).

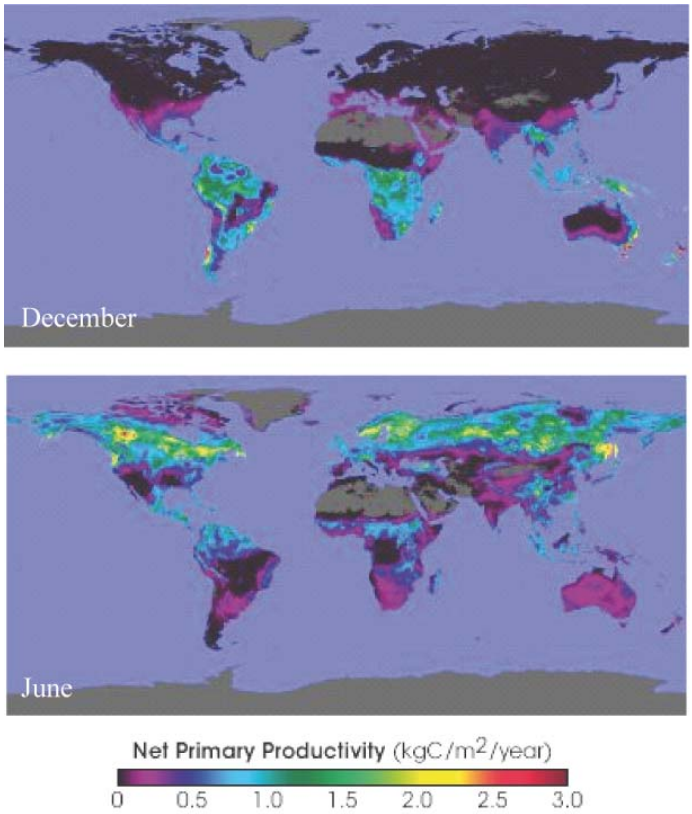

Figrue 2.26: Net productivity over land in December 2004 and June 2005. *Source*: NASA Earth Observatory, http://earthobservatory.nasa.gov/. Following the policy of U.S. government agencies, this figure is not subject to copyright protection.

The large majority of the carbon fixed by NPP returns to the atmosphere through decomposition in soil, the respiration of herbivores and carnivores, and fire. However, the time needed for this transfer back to the atmosphere is related to a large number of relatively complex processes. For instance, the carbon is stored for much longer in trees than in leaves or grasses. When plants die or leaves fall on the ground and enter the pool of organic matter in the soil, the decomposition rate depends strongly on the chemical composition of the organic material, the temperature and humidity of the soil, etc. Some of the organic matter in the soil is quickly remineralised, but much of it remains in the soil pool for decades or longer.

2.3.4 Geological reservoirs

The majority of the organic carbon that is exported downward from the surface layer is remineralised in the water column. In particular, the ocean is undersaturated with respect to calcite (aragonite) below 4500m (3000m) in the Atlantic and below 800 m (600m) in the Pacific. As a consequence, the long-term burial of $CaCO_3$ in the sediments to produce **limestone** mainly occurs in shallow seas (for instance in coral reefs). Averaged over the whole ocean, this long term burial corresponds to 13% of the export of $CaCO_3$ out of the surface layer. On short **timescales**, this is a small fraction of the whole carbon cycle, but it becomes a crucial component on timescales longer than a century. An even smaller percentage of the organic carbon is stored in the form of natural gas, oil and coal.

Because the sea floor spreads due to plate tectonics, sediments are transported horizontally and are eventually incorporated within the mantle through **subduction** along plate boundaries. At higher temperatures and pressure, limestone is transformed during **subduction** into calcium-silicate rocks (this is called **metamorphism**) by the reaction:

$$CaCO_3 + SiO_2 \rightarrow CaSiO_3 + CO_2 \tag{2.48}$$

The CO_2 that is released in this reaction can return to the atmosphere, in particular through volcanic eruptions.

The plate motion also allows the calcium-silicate rocks to be uplifted to the continental surface, where they are affected by physical and chemical **weathering**. In particular, the carbonic acid contained in rain water (in the same process as reaction 2.39) can interact with the calcium-silicate rocks:

$$CaSiO_3 + H_2CO_3 \rightarrow CaCO_3 + SiO_2 + H_2O \tag{2.49}$$

The products of this reaction are transported by rivers to the sea where they can compensate for the net export of $CaCO_3$ by sedimentation. Weathering thus tends to reduce atmospheric CO_2 by taking up carbonic acid to make $CaCO_3$ and increasing ocean alkalinity while metamorphism and sedimentation tend to increase atmospheric CO_2. Overall sedimentation, subduction and metamorphism, and weathering form a closed loop that takes place over millions of years, and is sometimes referred to as the long term inorganic carbon cycle (Fig. 2.27).

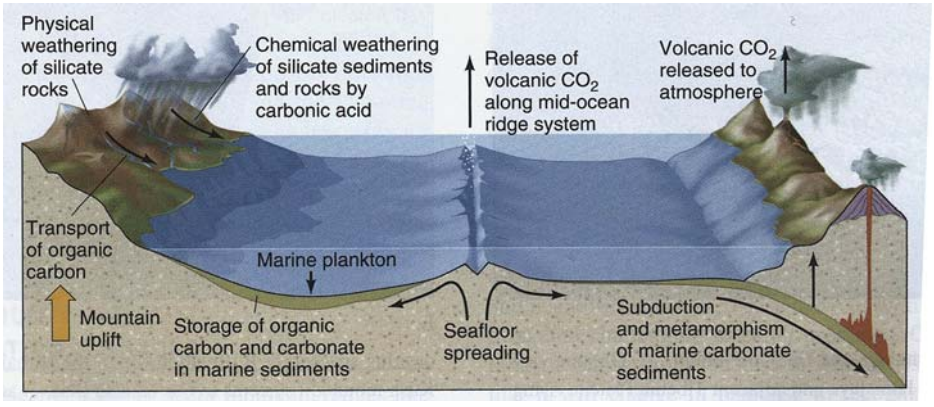

Figure 2.27: Long term inorganic carbon cycle through sedimentation, subduction and metamorphism, and weathering. Figure from Skinner et al. (2004). Copyright 2004 John Wiley & Sons, Inc. Reproduced with permission.

Cited references and further reading

Adams J. (2007). Vegetation-climate interaction. How vegetation makes the global environment. Springer in association with Praxis Publishing, Chichester, UK, 232pp.

Curry J.A. and P.J. Webster (1999). Thermodynamics of atmosphere and oceans. International Geophysics series, volume 65. Academic Press, 468 pp.

Denman, K.L., G. Brasseur, A. Chidthaisong, P. Ciais, P.M. Cox, R.E. Dickinson, D. Hauglustaine, C. Heinze, E. Holland, D. Jacob, U. Lohmann, S Ramachandran, P.L. da Silva Dias, S.C. Wofsy and X. Zhang (2007). Couplings Between Changes in the Climate System and Biogeochemistry. In: *Climate Change 2007: The Physical Science Basis. Contribution of Working Group I to the Fourth Assessment Report of the Intergovernmental Panel on Climate Change.* Solomon, S., D. Qin, M. Manning, Z. Chen, M. Marquis, K.B. Averyt, M.Tignor and H.L. Miller (Eds.). Cambridge University Press, Cambridge, United Kingdom and New York, NY, USA.

Fasullo, J. T., and K. E. Trenberth, 2008: The annual cycle of the energy budget. Part II: Meridional structures and poleward transports. J. Climate 21: 2313-2325.

Hartmann D.L. (1994). Global physical climatology. International Geophysics series, volume 56. Academic Press, 412 pp.

IPCC (2007). *Climate Change 2007: The Physical Basis. Contribution of Working Group I to the Fourth Assessment Report of the Intergovernmental Panel on Climate Change*. Solomon, S., Qin, D., Manning, M., Chen, Z., Marquis, M., Averyt, K.B., Tignor, M., and Miller H.L. (Eds.). Cambridge University Press, Cambridge, United Kingdom and New York, NY, USA, 996 pp.

Kalnay, E. and 21 others (1996). The NCEP/NCAR 40-year reanalysis project. Bulletin of the American Meteorological Society 77: 437-471.

Kiehl J. and K. Trenberth (1997). Earth's annual global mean energy budget. Bulletin of the American Meteorological Society 78: 197-2006.

Marshall J. and R.A. Plumb (2007). Atmosphere, ocean and climate dynamics: an introductory text. International Geophysics, volume 93. Academic Press, 344 pp.

Millero F.J. (2005). Chemical oceanography (third edition). Taylor and Francis, 496pp.

Rayner N.A., D.E. Parker, E.B. Horton, C.K. Folland, L.V. Alexander, D.P. Rowell, E.C. Kent and A. Kaplan (2003). Global analyses of sea surface temperature, sea ice, and nigh marine aire temperature since the late nineteenth century. Journal of Geophysical Research 108 (D14): 4407, doi:10.1029/2002JD002670.

Sarmiento G.L and N. Gruber (2006). Ocean biogeochemical dynamics. Princeton University Press, 503pp.

Skinner B.J., S.C. Porter and J. Park (2004). Dynamic Earth, an introduction to physical geology, fifth edition. Wiley, 584pp.

Taylor F.W. (2005). Elementary Climate Physics. Oxford University Press. 212pp

Trenberth K.E. and J.M. Caron, (2001). Estimates of meridional atmosphere and ocean heat transport. Journal of Climate 14: 3433-3443.

Trenberth, K. E. and D. P. Stepaniak (2003). Seamless poleward atmospheric energy transports and implications for the Hadley circulation. J. Climate 16: 3705-3721.

Trenberth K.E., L. Smith, T.T. Qian , A.G. Dai and J. Fasullo (2007). Estimates of the global water budget and its annual cycle using observational and model data. Journal of Hydrometeorology 8 (4): 758-769.

Trenberth, K. E., J. T. Fasullo and J. Kiehl (2009). Earth's global energy budget. Bull. Amer. Meteor. Soc., 90: 311-323.

Wallace J.M. and P.V. Hobbs (2006). Atmospheric science: an introductory survey (2nd edition). International Geophysics Series 92, Associated press, 484pp.

Exercises

1. Using a model similar to the one described in section 2.1.2, derive the relation between T_e and T_s for an arbitrary number n of atmospheric layers in radiative equilibrium, each having an emissivity of 1.
2. Using the information provided in section 2.1.3, compute the length of the various seasons.
3. Demonstrate Eq. 2.19.
4. Compute the temperature that would occur at the pole and the equator if the incoming radiation were the same as presently observed on Earth but there was no heat transport.
5. On the basis of the transport of water by the thermohaline circulation and of the temperature of the different water masses, estimate the amount of heat transported by the thermohaline circulation.

Additional exercises available on the textbook website (http://www.climate.be/textbook) and on iCampus for registered students.

Chapter 3. Modelling the climate system

3.1 Introduction

3.1.1 What is a climate model ?

In general terms, a climate model could be defined as a mathematical representation of the climate system based on physical, biological and chemical principles (Fig. 3.1). The equations derived from these laws are so complex that they must be solved numerically. As a consequence, climate models provide a solution which is discrete in space and time, meaning that the results obtained represent averages over regions, whose size depends on model **resolution**, and for specific times. For instance, some models provide only globally or **zonally** averaged values while others have a **numerical grid** whose spatial **resolution** could be less than 100 km. The time step could be between minutes and several years, depending on the process studied.

Even for models with the highest resolution, the **numerical grid** is still much too coarse to represent small scale processes such as turbulence in the **atmospheric and oceanic boundary layers**, the interactions of the circulation with small scale topography features, thunderstorms, cloud micro-physics processes, etc. Furthermore, many processes are still not sufficiently well-known to include their detailed behaviour in models. As a consequence, **parameterisations** have to be designed, based on empirical evidence and/or on theoretical arguments, to account for the large-scale influence of these processes not included explicitly. Because these **parameterisations** reproduce only the first order effects and are usually not valid for all possible conditions, they are often a large source of considerable uncertainty in models.

In addition to the physical, biological and chemical knowledge included in the model equations, climate models require some input from observations or other model studies. For a climate model describing nearly all the components of the system, only a relatively small amount of data is required: the solar irradiance, the Earth's radius and period of rotation, the land topography and bathymetry of the ocean, some properties of rocks and soils, etc. On the other hand, for a model that only represents explicitly the physics of the atmosphere, the ocean and the sea ice, information in the form of boundary conditions should be provided for all sub-systems of the climate system not explicitly included in the model: the distribution of vegetation, the topography of the ice sheets, etc.

Those model inputs are often separated into boundary conditions (which are generally fixed during the course of the simulation) and external forcings (such as the changes in solar irradiance) which drives the changes in climate. However, those definitions can sometimes be misleading. The forcing of one model could be a key state variable of another. For instance, changes in CO_2 concentration could be prescribed in some models, but it is directly computed in models including a representation of the carbon cycle. Furthermore, a fixed boundary in some models, such as the topography of the ice sheet, can evolve interactively in a model designed to study climate variations on a longer time scale.

In this framework, some data are required as input during the simulation. However, the importance of data is probably even greater during the development phase of the model, as they provide essential information on the properties of the system that is being modelled (see Fig. 3.1). In addition, large numbers of observations are needed to test the validity of the models in order to gain confidence in the conclusions derived from their results (see section 3.5.2).

Many climate models have been developed to perform climate projections, i.e. to simulate and understand climate changes in response to the emission of greenhouse gases and aerosols. In addition, models can be formidable tools to improve our knowledge of the most important characteristics of the climate system and of the causes of climate variations. Obviously, climatologists cannot perform experiments on the real climate system to identify the role of a particular process clearly or to test a hypothesis. However, this can be done in the virtual world of climate models. For highly non-linear systems, the design of such tests, often called sensitivity experiments, has to be very carefully planned. However, in simple experiments, neglecting a process or an element of the modelled system (for instance the influence of the increase in CO_2 concentration on the radiative properties of the atmosphere) can often provide a first estimate of the role of this process or this element in the system.

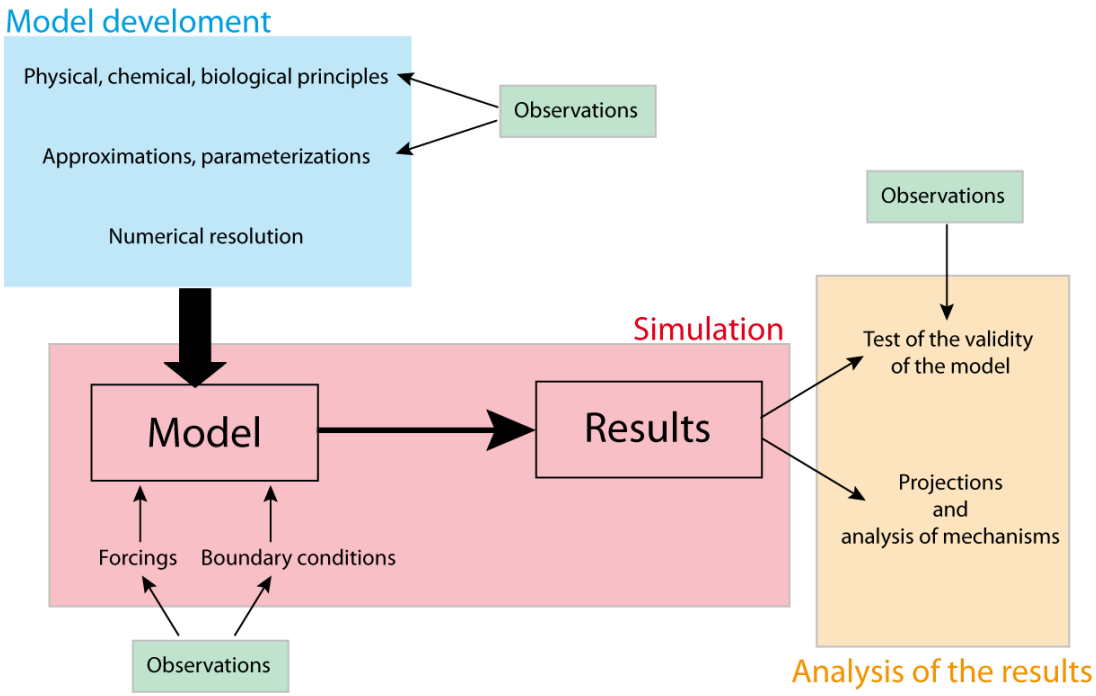

Figure 3.1: Schematic representation of the development and use of a climate model.

3.1.2 Types of models

Simplifications are unavoidable when designing a climate model as the processes that should be taken into account range from the scale of centimetres (for instance for atmospheric turbulence) to that of the Earth itself. The involved time scales also vary widely from the order of seconds for some waves, to billions of years when analysing the evolution of the climate since the formation of Earth. It is thus an important skill for a modeller to be able to select the processes that must be explicitly included compared to those that can be neglected or represented in a simplified way. This choice is of course based on the scientific goal of the study. However, it also depends on technical issues since the most sophisticated models require a lot of computational power: even on the largest computer presently available, the models cannot be routinely used for periods longer than a few centuries to millennia. On longer time scales, or when quite a large number of experiments are needed, it is thus necessary to user simpler and faster models. Furthermore, it is often very illuminating to deliberately design a model that includes

only the most important properties, so as to understand in depth the nature of a feedback or the complex interaction between the various components of the system. This is also the reason why simple models are often used to analyse the results of more complex models in which the fundamental characteristics of the system could be hidden by the number of processes represented and the details provided.

Modellers have first to decide the variables or processes to be taken into account and those that will be taken as constants. This provides a method of classifying the models as a function of the components that are represented interactively. In the majority of climate studies, at least the physical behaviour of the atmosphere, ocean and sea ice must be represented. In addition, the terrestrial and marine carbon cycles, the dynamic vegetation and the ice sheet components are more and more regularly included, leading to what are called Earth-system models.

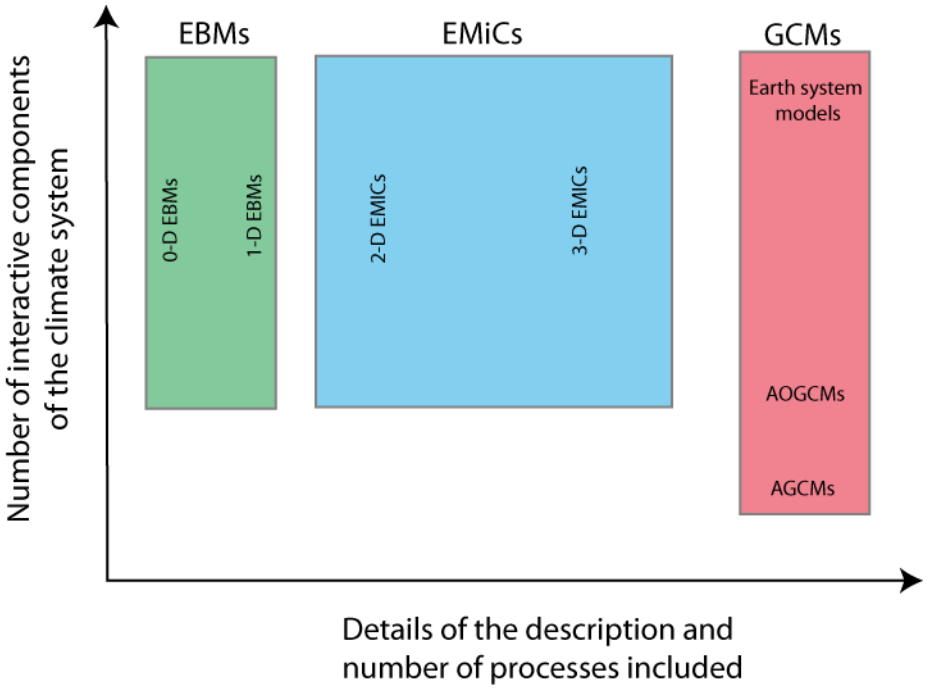

Figure 3.2: Types of climate model.

A second way of differentiating between models is related to the complexity of the processes that are included (Fig. 3.2). At one end of the spectrum, General Circulation Models (GCMs) try to account for all the important properties of the system at the highest affordable resolution. The term GCM was introduced because one of the first goals of these models is to simulate the three dimensional structure of winds and currents realistically. They have classically been divided into Atmospheric General Circulation Models (AGCMs) and Ocean General Circulation Models (OGCMs). For climate studies using interactive atmospheric and oceanic components, the acronyms AOGCM (Atmosphere Ocean General Circulation Model) and the broader CGCM (Coupled General Circulation Model) are generally used.

At the other end of the spectrum, simple climate models (such as the Energy Balance Models, or EBMs, see section 3.2.1) propose a highly simplified version of the dynamic of the climate system. The variables are averaged over large regions, sometimes over the whole Earth, and many processes are not represented or accounted for by the **parameterisations**. EBMs thus include a relatively small number of degree of freedom.

EMICs (Earth Models of Intermediate Complexity) are located between those two extremes. They are based on a more complex representation of the system than EBMs but include simplifications and parameterisations for some processes that are explicitly accounted for in GCMs. The EMICs form the broadest category of models. Some of them are relatively close to simple models, while others are slightly degraded GCMs.

When employed correctly, all the model types can produce useful information on the behaviour of the climate system. There is no perfect model, suitable for all purposes. This is why a wide range of climate models exists, forming what is called the spectrum or the hierarchy of models that will be described in section 3.2. Depending on the objective or the question, one type of models could be selected. The best type of model to use depends on the objective or the question. On the other hand, combining the results from various types of models is often the best way to gain a deep understanding of the dominant processes in action.

3.2 A hierarchy of models

3.2.1 Energy balance models

As indicated by their name, energy balance models estimate the changes in the climate system from an analysis of the energy budget of the Earth. In their simplest form, they do not include any explicit spatial dimension, providing only globally averaged values for the computed variables. They are thus referred to as zero-dimensional EBMs. The basis for these EBMs was introduced by both Budyko (1969) and Sellers in (1969). Their fundamental equation is very similar to those analysed in sections 2.1.1 and 2.1.5:

Changes in heat storage = absorbed solar radiation - emitted terrestrial radiation

$$C_E \frac{\partial T_s}{\partial t} = \left(\left(1-\alpha_p\right)\frac{S_0}{4} - A\uparrow \right) \tag{3.1}$$

where, as in Chapter 2, C_E is the effective heat capacity of the media (measured in J m^{-2} K^{-1}), T_s the surface temperature, t the time, α_p the planetary albedo, S_0 the **Total Solar Irradiace** (TSI) and $A\uparrow$ the total amount of energy that is emitted by a 1 m^2 surface of the Earth. $A\uparrow$ could be represented on the basis of the **Stefan-Boltzmann law**, using a factor τ_a to represent the infrared transmissivity of the atmosphere (including the greenhouse gas effect), as.

$$A\uparrow = \varepsilon\sigma T_s^4 \tau_a \tag{3.2}$$

where ε is the emissivity of the surface. Using an albedo of 0.3, an emissivity of 0.97, and a value of τ_a of 0.64 leads to an equilibrium temperature T_s=287K, which is close to the observed one. In some EBMs, Eq. 3.2 is linearised to give an even simpler formulation of the model. On the other hand, τ_a and α_p are often parameterised as a function of the temperature, in particular to take into account the fact that cooling increases the surface area covered by ice and snow, and thus increases the planetary albedo.

In order to take the geographical distribution of temperature at the Earth's surface into account, zero-dimensional EBMs can be extended to include one (generally the latitude) or two horizontal dimensions (Fig. 3.3). An additional term $\Delta transp$ is then included in Eq. 3.1 representing the net effect of heat input and output associated with horizontal transport:

$$C_E \frac{\partial T_{s,i}}{\partial t} = \left((1-\alpha_p)\frac{S_0}{4} - A\uparrow \right) + \Delta transp \qquad (3.3)$$

An index i has been added to the surface temperature to indicate that the variable corresponds to the region i. The simplest form for the transport is to treat it as a linear function of temperature, but more sophisticated parameterisations are also used, including, for instance, a diffusion term.

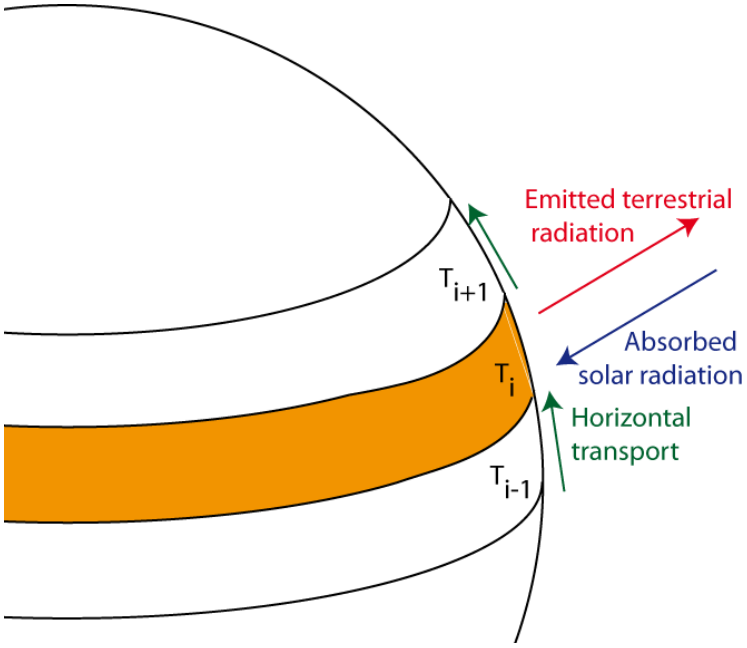

Figure 3.3: Representation of a one-dimensional EBM for which the temperature T_i is averaged over a band of longitude.

Box models have clear similarities to EBMs as they represent large areas or an entire component of the system by an average which describes the mean over one "box". The exchanges between the compartments are then **parameterised** as a function of the characteristics of the different boxes. The exact definition of the boxes depends on the purpose of the model. For instance, some box models have a compartment for the atmosphere, the land surface, the ocean surface layers and the deep ocean, possibly making a distinction between the two hemispheres. Others include additional components allowing a description of the carbon cycle and thus have boxes corresponding to the various reservoirs described in section 2.3.

3.2.2 Intermediate complexity models

Like EBMs, EMICs involve some simplifications, but they always include a representation of the Earth's geography, i.e. they provide more than averages over the whole Earth or large boxes. Secondly, they include many more degrees of freedom than EBMs. As a consequence, the parameters of EMICs cannot easily be adjusted to reproduce the observed characteristics of the climate system, as can be done with some simpler models.

The level of approximation involved in the development of the model varies widely between different EMICs. Some models use a very simple representation of the

geography, with a **zonally** averaged representation of the atmosphere and ocean. A distinction is always made between the Atlantic, Pacific and Indian basins (Fig. 3.4) because of the strong differences between them in the circulation (see section 1.3.2). As the atmospheric and oceanic circulations are fundamentally three-dimensional, some **parameterisations** of the **meridional** transport are required. Those developed for EMICs are generally more complex and physically based than the ones employed in one-dimensional EBMs.

On the other hand, some EMICs include components that are very similar to those developed for GCMs, although a coarser numerical grid is used so that the computations proceed fast enough to allow a large number of relatively long simulations to be run. Some other components are simplified, usually including the atmosphere because this is the component that is most depending on computer time in coupled climate models.

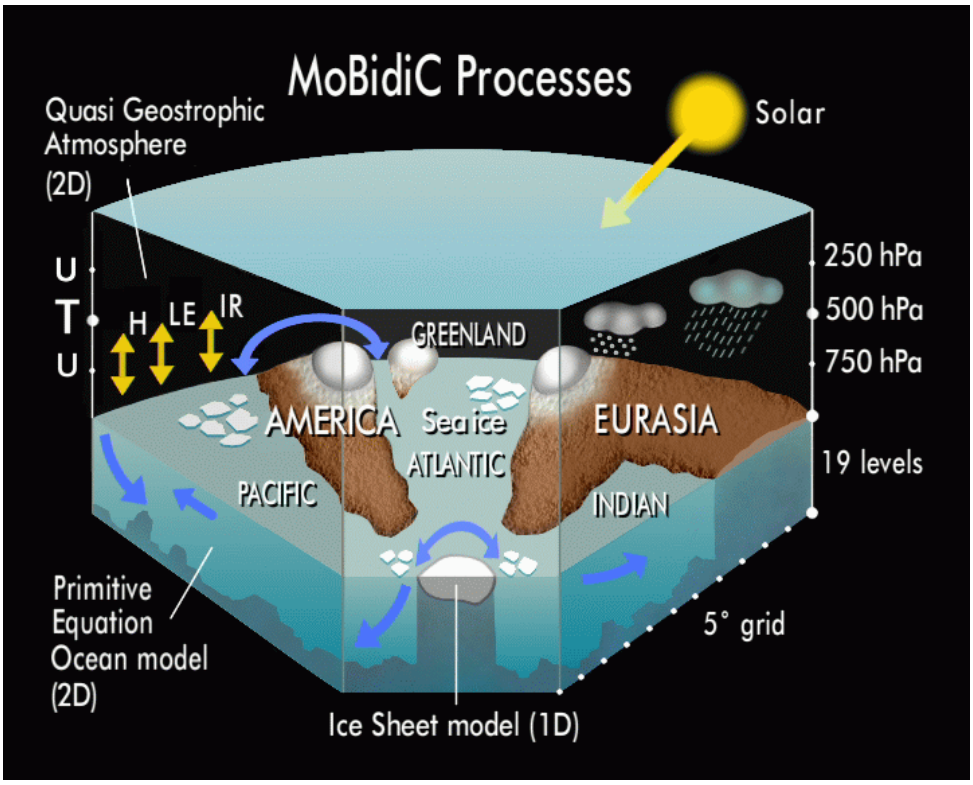

Figure 3.4: Schematic illustration of the structure of the climate model of intermediate complexity MOBIDIC that includes a **zonally** averaged atmosphere, a 3-basin **zonal** oceanic model (corresponding to the Atlantic, the Pacific and the Indian Oceans) and simplified ice sheets. More details about this model are available at http://www.astr.ucl.ac.be/index.php?page=MoBidiC%40Description.

3.2.3 General circulation models

General circulation models provide the most precise and complex description of the climate system. Currently, their **grid** resolution is typically of the order of 100 to 200 km. As a consequence, compared to EMICs (which have a grid resolution between 300 km and thousands of kilometres), they provide much more detailed information on a regional scale. A few years ago, GCMs only included a representation of the atmosphere, the land surface, sometimes the ocean circulation, and a very simplified version of the sea ice. Nowadays, GCMs take more and more components into account, and many new models

now also include sophisticated models of the sea ice, the carbon cycle, ice sheet dynamics and even atmospheric chemistry (Fig. 3.5).

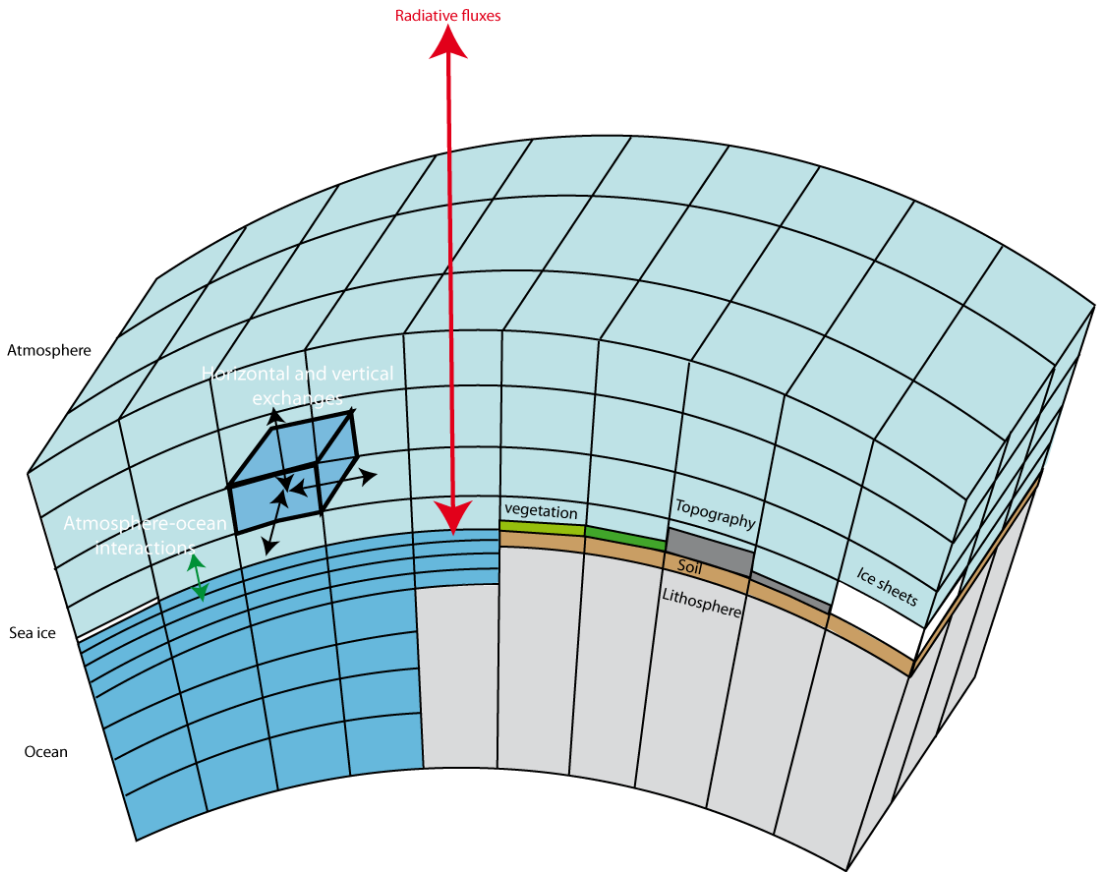

Figure 3.5: A simplified representation of part of the domain of a general circulation model, illustrating some important components and processes. For clarity, the curvature of the Earth has been amplified, the horizontal and vertical coordinates are not to scale and the number of grid points has been reduced compared to state-of-the-art models.

Because of the large number of processes included and their relatively high resolution, GCM simulations require a large amount of computer time. For instance, an experiment covering one century typically takes several weeks to run on the fastest computers. As computing power increases, longer simulations with a higher resolution become affordable, providing more regional details than the previous generation of models.

3.3 Components of a climate model

3.3.1 Atmosphere

The basic equations that govern the atmosphere can be formulated as a set of seven equations with seven unknowns: the three components of the velocity $\vec{v}$ (components *u, v, w*), the pressure *p*, the temperature *T*, the specific humidity *q* and the density. The seven equations, written for the atmosphere, are:

(1-3) Newton's second law (momentum balance, i.e. $\vec{F} = m\vec{a}$, force equals mass times acceleration),

$$\frac{d\vec{v}}{dt} = -\frac{1}{\rho}\vec{\nabla}p - \vec{g} + \vec{F}_{fric} - 2\vec{\Omega}\times\vec{v} \tag{3.4}$$

In this equation, d /dt is the total derivative, including a transport term,

$$\frac{d}{dt} = \frac{\partial}{\partial t} + \vec{v}.\vec{\nabla} \tag{3.5}$$

$\vec{g}$ is the apparent gravity vector (i.e. taking the centrifugal force into account), $\vec{F}_{fric}$ is the force due to friction, and $\vec{\Omega}$ is the angular velocity vector of the Earth (the last term is the **Coriolis force**)

(4) The continuity equation or the conservation of mass

$$\frac{\partial\rho}{\partial t} = -\vec{\nabla}.\left(\rho\vec{v}\right) \tag{3.6}$$

(5) The conservation of the mass of water vapour

$$\frac{\partial\rho q}{\partial t} = -\vec{\nabla}.(\rho\vec{v}q) + \rho(E - C) \tag{3.7}$$

where E and C are evaporation and condensation respectively

(6) The first law of thermodynamics (the conservation of energy)

$$Q = C_p\frac{dT}{dt} - \frac{1}{\rho}\frac{dp}{dt} \tag{3.8}$$

where Q is heating rate per unit mass and C_p the specific heat

(7) The equation of state

$$p = \rho R_g T \tag{3.9}$$

Before these equations are used in models some standard approximations have to be performed. For instance, assuming **hydrostatic equilibrium**, which is a good approximation at the scale of GCMs, provides a considerable simplification of the equation of motion along the vertical. Secondly, the quasi-Boussinesq approximation states that the time variation of the density could be neglected compared to the other terms of the continuity equation, filtering the sound waves. However, supplementary equations for the liquid water content of atmospheric parcels or other variables related to clouds are often added to this set of equations.

Unfortunately, these seven equations do not form a closed system. First, the frictional force and the heating rate must be specified. Computing the heating rate, in particular, requires a detailed analysis of the radiative transfer in the atmosphere,

accounting for both the **longwave** and the **shortwave** radiation in the atmospheric columns (see Fig. 3.5), as well as of the heat transfers associated with evaporation, condensation and sublimation. The influence of clouds in these processes is usually a source of considerable uncertainty. This part of the model is commonly referred to as the model "physics" while the calculation of the transport is called the "dynamics". Secondly, as discussed in section 3.1.1, the models can only adequately resolve some of the processes that are included in the equations. The important processes that occur at scales that could not be resolved by the model grid must thus be **parameterised**, introducing new terms into the equations 3.5, 3.7 and 3.8. The boundary conditions of the equations describing the interactions between the atmosphere and the other components of the climate system also need to be specified (see section 3.3.7).

3.3.2 Ocean

The major equations that govern the ocean dynamics are based on the same principles as the equations for the atmosphere. The only significant difference is that the equation for the specific humidity is not required for the ocean, while a new equation for the salinity needs to be introduced. The equation of state is also fundamentally different. Unlike the atmosphere, there is no simple law for the ocean and the standard equation of state is expressed as a function of the pressure, the temperature and the salinity as a long polynomial series.

It is much easier to compute the heating rate in the ocean than in the atmosphere. In addition to the heat exchanges at the surface, the only significant heat source in the ocean is the absorption of solar radiation. This is taken into account in the model through an exponential decay of the solar irradiance. The situation for salinity is even more straightforward, as there is no source or sink of salinity inside the ocean. The equations governing these two variables are thus relatively simple:

$$\frac{dT}{dt} = F_{sol} + F_{diff} \tag{3.10}$$

$$\frac{dS}{dt} = F_{diff} \tag{3.11}$$

where F_{sol} is the absorption of solar radiation in the ocean. Eq. 3.10 does not apply to the *in situ* temperature, but the **potential temperature** in order to account for the effect of the compressibility of seawater. The difference between those two temperatures is relatively low in the upper ocean, but it can reach several tenths of a degree in the deeper layers, an important difference in areas where the gradients are relatively small (see section 1.3.3.2).

In Eqs. 3.10 and 3.11, in contrast to section 3.3.1, we have explicitly added a term to the right hand side representing the influence of the processes at scales that cannot be included in the model. As small-scale processes tend to mix properties, they are generally modelled as a diffusion term F_{diff}. In its simplest form, a **Laplacian** formulation is retained. This is also often the formulation selected for the friction term (in Eq. 3.4). Because of the very different scales of ocean model grids on the vertical (a few hundred meters) and on the horizontal (tens to hundreds of kilometres), the small-scale processes in these two directions have different properties. As a consequence, the coefficients associated with the **Laplacian** (diffusion coefficient, and viscosity for tracer and momentum equations, respectively) differ by several orders of magnitude in the vertical and the horizontal. Actually, it appears that, rather than separating horizontal and vertical

directions, it is better to use a referential that is aligned with the density surfaces. To this end, **isopycnal** (along surfaces of equal density) and **diapycnal** (normal to surfaces of constant density) diffusion coefficients are calculated. These coefficients can be simply chosen, or they can be computed using sophisticated modules (including turbulence models) that take into account the stirring of the winds, the influence of density gradients, the breaking of surface and internal waves, etc.

However, all small-scale processes cannot be represented by a diffusion term. For instance, dense water formed at high latitudes can flow down the slope in narrow boundary currents called overflows. They have a strong influence on the water mass properties but could not be represented on the model grid scale. In this case, a parameterization of their effects as a transport process rather than a diffusion term appears more appropriate.

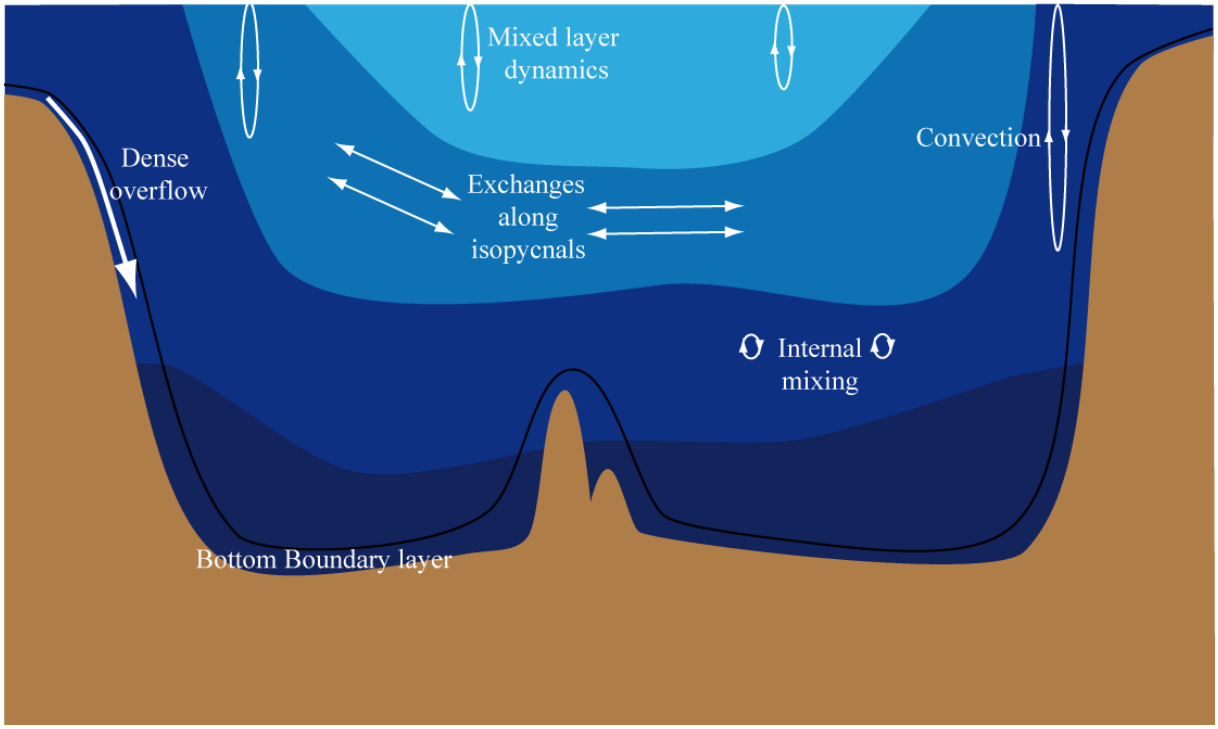

Figure 3.6: Schematic representation of some small-scale processes that have to be parameterized in ocean models. Modified from http://www.gfdl.noaa.gov/ocean-models-at-gfdl.

3.3.3 Sea ice

The physical processes governing the development of sea ice can be conceptually divided into two parts (Fig. 3.7). The first one covers the thermodynamic growth or decay of the ice, which depend on the exchanges with the atmosphere and the ocean. For those processes, the horizontal heat conduction through ice, can be safely neglected because he horizontal scale is much larger than the vertical one. The thermodynamic code of a sea-ice model is thus basically one-dimensional over the vertical, and the conduction equation can be written:

$$\rho_c c_{pc} \frac{\partial T_c}{\partial t} = k_c \frac{\partial^2 T_c}{\partial z^2} \qquad (3.12)$$

where ρ_c, c_{pc}, and k_c are the density, specific heat and thermal conductivity, and T_c is the temperature. The subscript c stands for either ice (i) or snow (s).

The heat balance at the surface (which can be modelled similar to equation 2.36) allows the computation of the surface temperature and of the snow or ice melting. At the bottom of the sea ice, the heat balance provides an estimate of ice melting or formation, the temperature there being considered as equal to the freezing point temperature. Furthermore, the heat budget of the **leads** is used to determine whether new ice will form in the open ocean areas and if lateral melting will occur. Finally, as the ice growth and decay are a function of the ice thickness (the smaller the ice thickness, the faster the growth and decay of the ice), it is necessary to take the distribution of the ice thickness into account in sea-ice models.

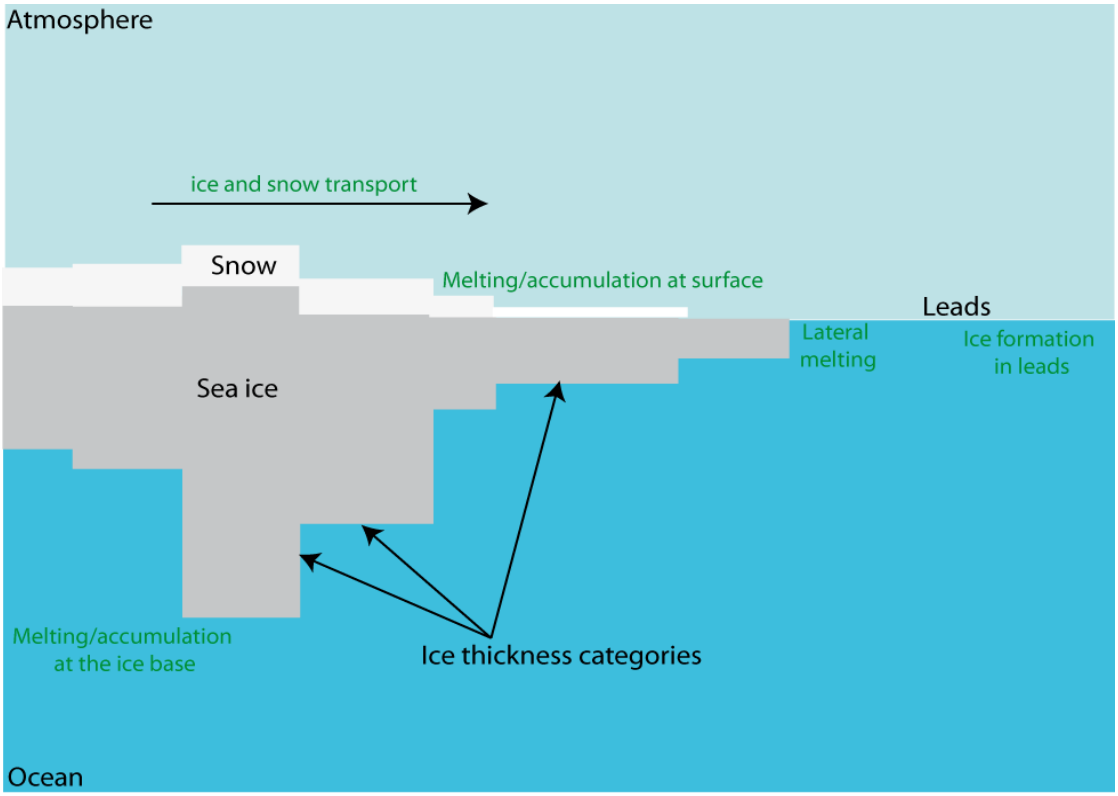

Figure 3.7: The main processes that have to be taken into account in a sea ice model.

When studying the large-scale dynamics of sea ice, the ice is modelled as a two-dimensional continuum. This hypothesis works if, in a model grid box, a large number of ice floes of different sizes and thicknesses are present as well as the **leads**. Newton's second law then gives:

$$m\frac{d\vec{u}_i}{dt} = \vec{\tau}_{ai} + \vec{\tau}_{wi} - m\, f\, \vec{e}_z \times \vec{u}_i - mg\vec{\nabla}\eta + \vec{F}_{\text{int}} \tag{3.13}$$

where m is the mass of snow and ice per unit area, $\vec{u}_i$ is the ice velocity. $\vec{\tau}_{ai}$ and $\vec{\tau}_{wi}$ are the forces per unit area from the air and water. $\vec{F}_{\text{int}}$ is the force per unit area due to internal interactions and f, $\vec{e}_z$, g, and η are respectively the Coriolis parameter, a unit vector

pointing upward, the gravitational acceleration, and the sea-surface elevation. The first two terms on the right hand side represent the interactions with the ocean and the atmosphere. The third term is the **Coriolis force** and the forth term the force due to the oceanic tilt. The internal forces $\vec{F}_{\text{int}}$ are a function of ice thickness and concentration, providing a strong link between dynamics and thermodynamics, while the velocity obtained from equation 3.13 is used in the computation of the transport of the model state variables such as the ice thickness, the concentration of each ice thickness category and the internal sea ice temperature and salinity.

3.3.4 Land surface

As with sea ice, horizontal heat conduction and transport in soil can be safely neglected. Therefore, thermodynamic processes are only computed along the vertical (in a similar way to Eq. 3.12). In the first generation of land surface models, only one soil layer was considered. As in Eq. 2.36, soil temperature can then be computed from the energy balance at the surface:

$$\rho c_p h_{su} \frac{\partial T_s}{\partial t} = (1-\alpha) F_{sol} + F_{IR\downarrow} + F_{IR\uparrow} + F_{SE} + L_f E + F_{cond} \tag{3.14}$$

When a snow layer is present, the computation of the development of the snow depth, density and concentration is part of the surface energy balance. This is very important for the **albedo**, whose **parameterisation** as a function of the soil characteristics (snow depth, vegetation type, etc) is a crucial element of surface models.

The latent heat flux F_{LE} in Eq. 2.36 has been replaced in Eq. 3.14 by the latent heat of fusion times the evaporation rate ($L_f E$), as is classically done in surface models. This evaporation rate depends on the characteristics of the soil and the vegetation cover as well as on the water availability. It can be expressed with the help of the **moisture availability function** β ($0<\beta<1$), defined as the ratio between the evaporation rate of the surface (E) and the potential evaporation (E_p), i.e. the evaporation that would occur on a homogenous wet surface such as a lake:

$$\beta = E/E_p \tag{3.15}$$

A land surface model also simulates the water content of the soil. In the simple early models, this is represented by a bucket model. The bucket is allowed to fill up to a critical level, corresponding to the equivalent of 15 to 30 cm of water everywhere on a grid cell. If, after taking into account precipitation and surface evaporation, the amount of water in the soil exceeds this threshold, the excess water is transferred to a prescribed oceanic grid point through river runoff.

The easiest way is to simply select the parameters (such as the **albedo**, the surface roughness or the **moisture availability function**) in Eq. 3.14 and 3.15 on the basis of observations of surface characteristics. However, the accurate representation of the energy and water exchanged between the atmosphere and the land surface requires a more sophisticated description of the effects of vegetation and soil. Horizontally, instead of a homogenous description as proposed in Eq. 3.14, the heterogeneous nature of the land surface, covered by different types of vegetation, bare soils, cities, etc, must be explicitly accounted for. Vertically, the interactions between the **canopy**, the soil and the roots also have a clear impact that cannot be adequately computed by an equation as simple as 3.14.

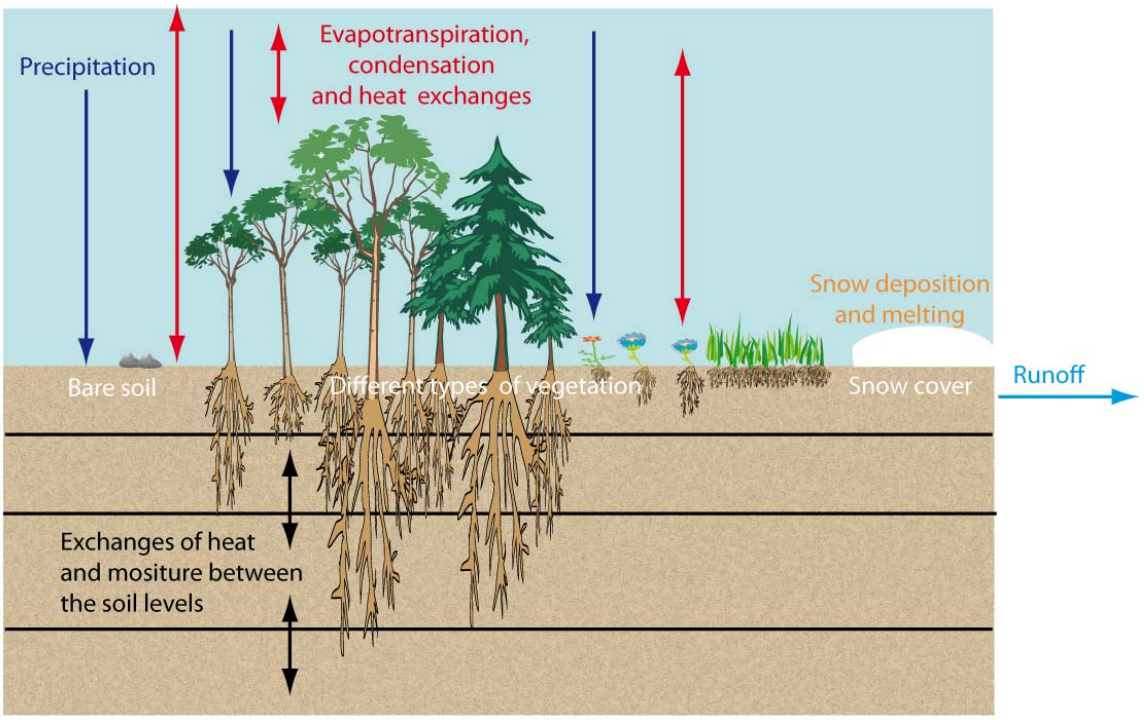

Figure 3.8: The main processes that have to be taken into account in a land surface model. For clarity, the carbon storage in plants and in soils, as well as the exchanges between these reservoirs and with the atmosphere are not shown.

Sophisticated representations of these processes are now included in the state-of-the-art GCMs. In particular, they include a multi-layer soil model, a comprehensive description of the vegetation cover and of the physical and chemical interactions between the plants, the soil and the atmosphere. They also have a sophisticated river-routing scheme which accounts for the duration of the water transport as well as evaporation during the journey to the ocean or the interior sea. These improvements are also essential in an adequate representation of the carbon cycle on land (see section 2.3.3). At present, the majority of climate models do not include a representation of **permafrost**, but this is likely to change because of the large modifications in the extent of permafrost that are expected during the 21st century.

Some models take the community composition and vegetation structure as a boundary condition or forcing (if land use changes are specified for instance). They then use this information to determine the physical characteristics of the surface and the soil, as well as the carbon storage over land. However dynamic global vegetation models (DGVMs) explicitly compute the transient dynamics of the vegetation cover in response to climate changes and disturbances such as fires. DGVMs can also provide the distribution of **biomes** that are in equilibrium with climate conditions (Figure 3.9). It is of course impossible to represent the fraction covered by each of the hundreds of thousands of different plant species in DGVMs. The plants are thus grouped into **plant functional types** (PFTs) that share common characteristics. Very simple models only use two PFTs (trees and grass, the area not covered by trees or grass corresponding to the fraction of desert in a **grid** element), while more sophisticated models use more than ten different PFTs.

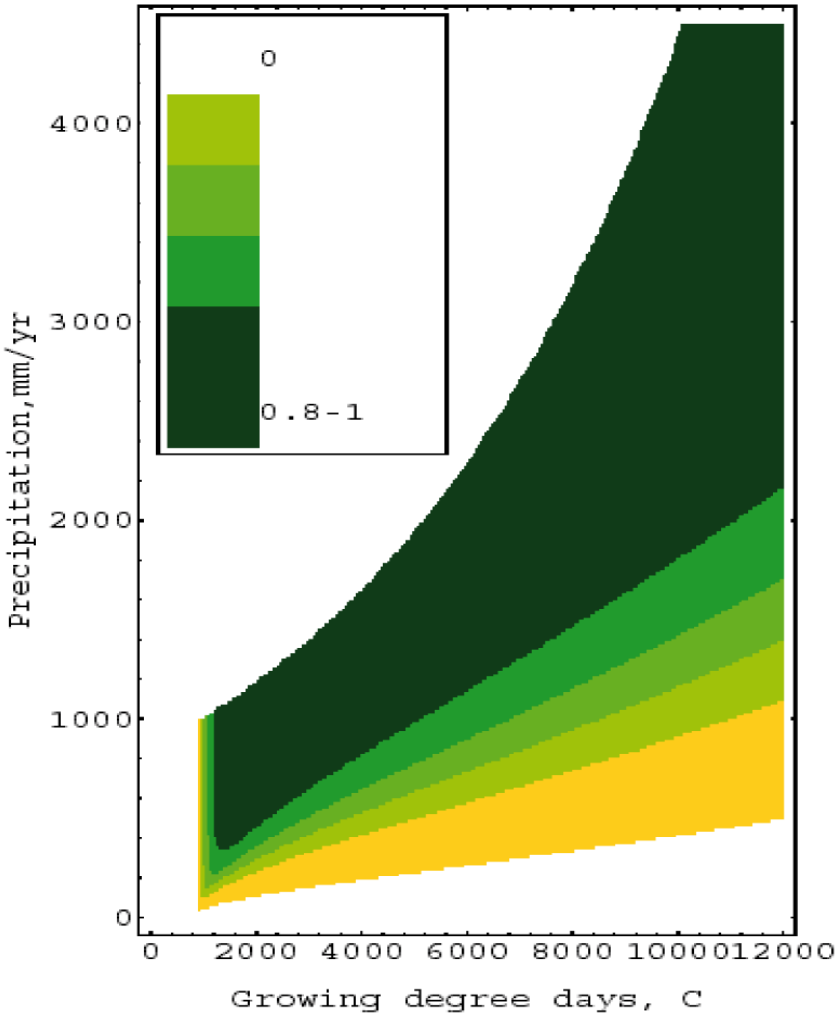

Figure 3.9: The equilibrium fraction of trees in a model that includes two plant functional types and whose community composition is only influenced by precipitation and the growing degree days (GDD) (Brovkin et al. 1997). Growing degree days are defined as the sum of the daily mean near-surface temperatures for the days of a year with a temperature higher than 0°C. Figure Courtesy of V. Brovkin.

3.3.5 Marine biogeochemistry

Models of biogeochemical cycles in the oceans are based on a set of equations whose formulation is very close to that of equations 3.10 and 3.11 for the ocean temperature and salinity:

$$\frac{dTrac_{bgc}}{dt} = F_{diff} + Sources - Sinks \qquad (3.16)$$

where $Trac_{bgc}$ is a biogeochemical variable. Those variables are often called tracers because they are transported and diffused by the oceanic flow (the left hand side of the equation and the term F_{diff}).

$Trac_{bgc}$ can represent *DIC*, *Alk*, the concentration of various chemical species (including nutriments necessary for phytoplankton growth) or the biomass of different groups of phytoplankton, detritus, zooplankton and (more rarely) higher trophic levels. Simplified carbon cycle models include a few state variables while the most sophisticated biogeochemical models have more than 30 of them. The *Sources* and *Sinks* terms account for the increase or decrease of the tracer concentration in response to biogeochemical processes, including thus a representation of the processes described in section 2.3. For instance, for a particular phytoplankton group, the *Sources* term could be related to the growth in the biomass by photosynthesis, while the *Sinks* are the consumption of phytoplankton by zooplankton as well as the mortality of the cells. In addition to the processes taking place in the water column, some models include a comprehensive ocean sediment component in order to be able to study the long-term changes in the carbon cycle.

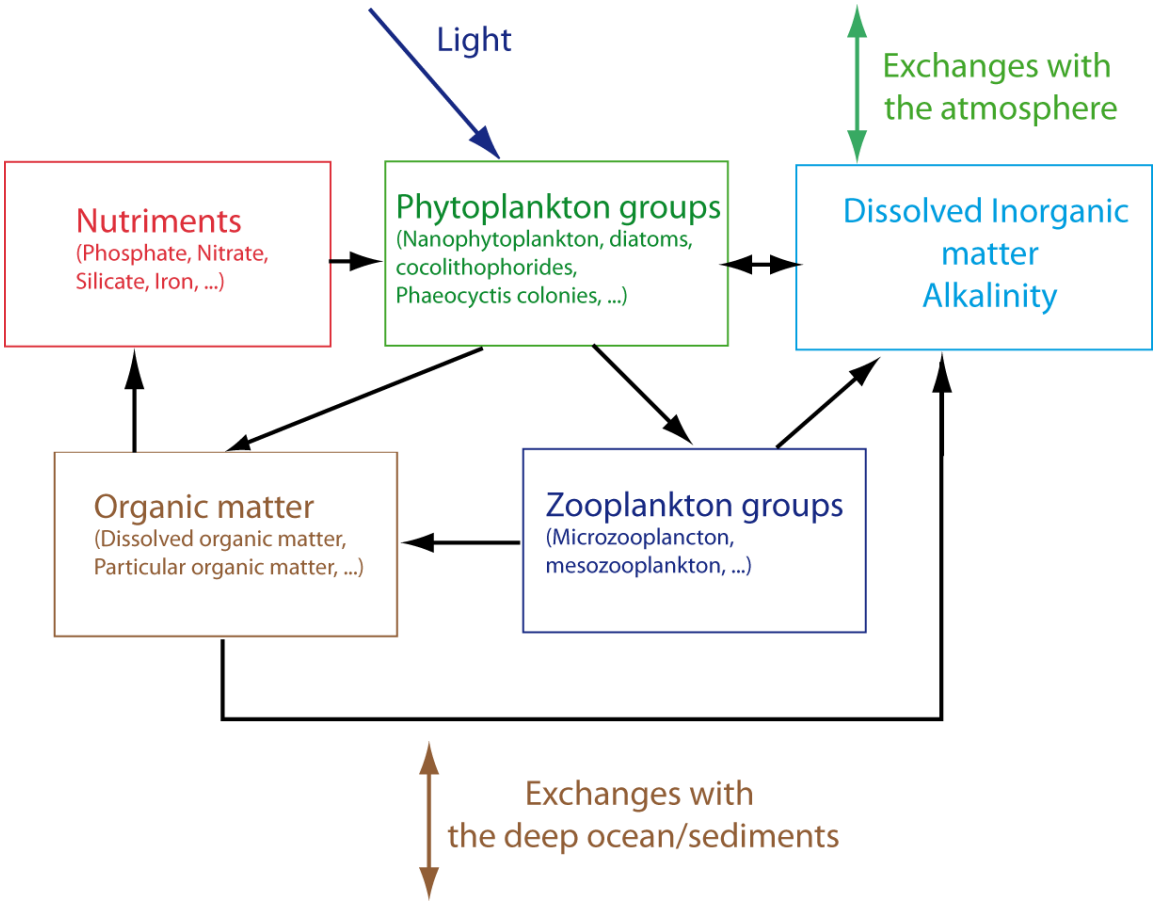

Figure 3.10: A simplified scheme representing some of the variables of a biogeochemical model. The interactions between the groups are complex as the different types of phytoplankton need different nutrients, are grazed by different types of zooplankton etc.

3.3.6 Ice sheets

As already discussed for the atmosphere and the sea ice, ice-sheet models can be decomposed into two major components: a dynamic core that computes the flow of the ice and a thermodynamic part that estimates the changes in ice temperatures, snow accumulation, melting, etc. The ice velocity can be computed using the complete three-

dimensional equation. This is affordable for regional models, focusing on particular regions, but approximations are often necessary for climate models which compute the development of whole ice sheets on long timescales.

The conservation of ice volume can be written as:

$$\frac{\partial H}{\partial t} = -\vec{\nabla}.(\vec{v}_m H) + M_b \tag{3.17}$$

where $\vec{v}_m$ is the depth-averaged horizontal velocity field and M_b is the mass balance accounting for snow accumulation as well as basal and surface meltings. Surface melting can be deduced from the energy budget at the surface (similar to Eq. 2.36, see also section 3.3.3). Simpler formulations of surface melting are based on the positive degree-day methods, which relates the melting to the temperature during the days with temperatures above 0°C. An important element in the mass balance at the surface of the ice sheets is the position of the equilibrium line between the regions where, on a yearly average, snow tends to accumulate and the ablation region (where there is net melting of the snow and ice when the surface mass balance is integrated over the whole year). On the Greenland ice sheet, in present-day conditions, ablation occurs in many areas, whereas on the colder Antarctic ice sheet, it is restricted to a few regions only.

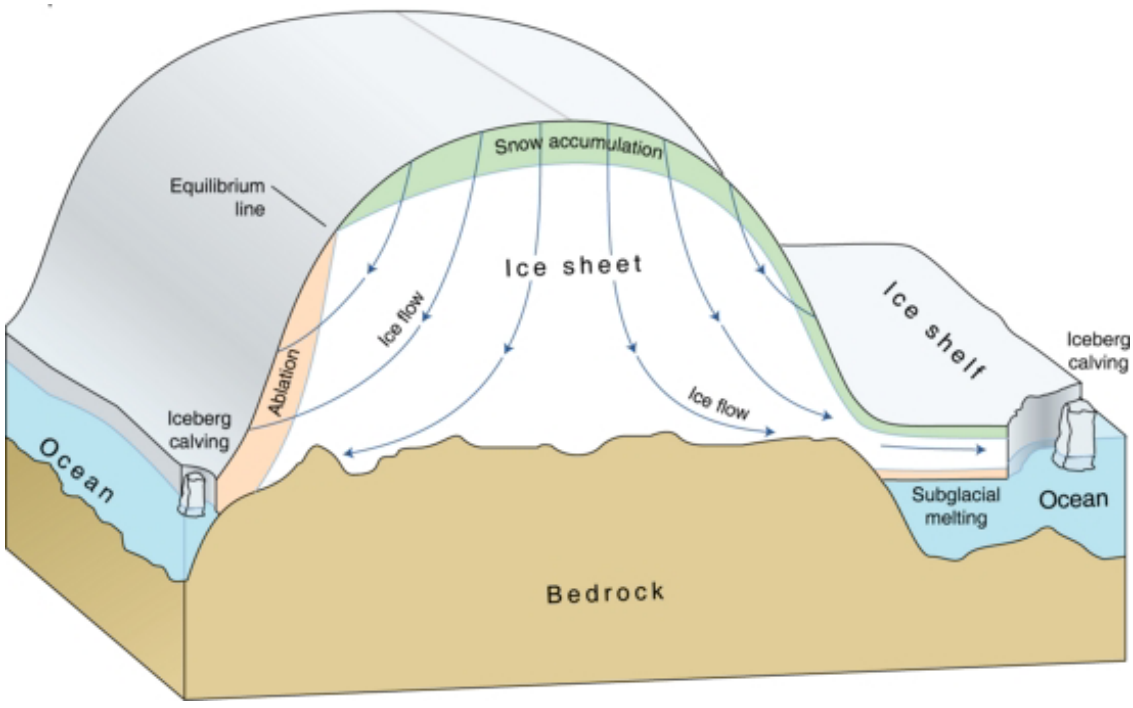

Figure 3.11: The main processes that have to be taken into account in an ice sheet model. Figure reproduced from http://www.solcomhouse.com/icecap.htm.

The melting at the ice base is deduced from the balance between the heat conduction in the ice and in the ground, taking into account the geothermal heat flux. Conditions at the ice base, and in particular the presence of water or ice close to the melting point at the corresponding pressure, have a large impact on the ice velocity as they reduce the stresses greatly, compared to the situation where the ice is well below the freezing point.

Ice sheets models also need to take into account the interactions between grounded ice and **ice shelves**. Because of local melting and iceberg calving, ice shelves can make a large contribution to the mass balance of the ice sheets, as is currently the case for Antarctica. Furthermore, they generate stresses that tend to slow down the ice flow on land. Indeed, observations have shown that the recent breakdown of some ice shelves has produced, in some regions, an acceleration of the land ice.

An additional element in ice-sheet models is the representation of interactions with the underlying bedrock. In particular, as the load of the **ice sheet** tends to depress the bedrock, a bedrock adjustment model is needed to compute the position of the ground as a function of the ice mass. This then yields the elevation of the ice sheet as a function of the ice thickness.

3.3.7 Coupling between the components - Earth system models

The interactions between the various components of the system play a crucial role in the dynamics of climate. Wind stress, heat and freshwater fluxes at the ocean surface are the main drivers of the ocean circulation (see section 1.3.2). The evaporation at the ocean surface is the largest source of water vapour for the atmosphere, which influences the radiative properties of the air (section 2.1.2) and the atmospheric heat transport (section 2.1.5). Snow falling on ice sheets is an essential element of their mass balance. Many other examples could be cited.

Some of those interactions are quite straightforward to compute from the models state variables, while more sophisticated **parameterisations** are required for others. For instance, the parameterisation of the wind stress and of the heat flux at the atmospheric base (e.g., Eqs. 2.33 and 2.34) can be derived from theories of the **atmospheric boundary layer**. However, this computation still requires empirical parameters that depend on the characteristics of the surface, introducing some uncertainties into the determination of the flux.

The technical coupling of the various components to obtain a climate- or Earth-system model brings additional difficulties. The numerical codes have generally been developed independently by different groups, using different coding standards, different **numerical grids**, etc. It is thus necessary to design an interface and to use a coupler, i.e. code specially adapted to represent the exchanges between the various components.

The above presentation includes the main elements of the majority of current Earth-system models. However, the description is far from exhaustive. New components (such as models of the methane cycle, of the nitrogen cycle, more sophisticated representation of atmospheric chemistry, etc) are continuously included in order to obtain a more comprehensive representation of the complex interactions in the system.

3.4 Numerical resolution of the equations

3.4.1 Consistence, convergence and stability

The equations that rule the climate system are **partial differential equations** (PDEs) such as those presented in section 3.3, except when extremely simplified models are used (section 3.2.1). It is first necessary to ensure that those equations are mathematically well-posed, i.e. that the problem has a unique solution that depends on the initial and boundary conditions. This requires that those initial and boundary conditions are properly specified. For instance, to solve the equation for temperature in the ocean knowing the velocity field (Eq. 3.10), we must specify the initial temperature

over the whole domain at a time t_0 as well as one boundary condition over all the points of the spatial boundaries of the domain, which can be the value of the heat flux or of the temperature there. Below, we will consider that all the problems investigated are well-posed.

In order to solve the equations of the mathematical models developed for each component of the climate system (section 3.3), those models have to be transformed into numerical models that can be handled by a computer. The first method, which is probably the easiest to understand, is to approximate the derivatives in the **partial differential equations** by finite differences. This is called the **finite difference method**. The solution is no longer a continuous function (as for the PDEs) but a discrete one, only defined for specific times separated by the time step Δt, and specific locations separated by the spatial step Δx (plus Δy and Δz for a problem with three spatial dimensions).

Imagine for instance, a very simple ordinary differential equation:

$$\frac{du}{dt} = A\cos(t) \tag{3.18}$$

where t is the time, u a state variable (for instance the velocity) which depends here only on the time, and A a constant. The derivative according to time could be approximated by a finite difference, leading to the finite difference equation:

$$\frac{U^{n+1} - U^n}{\Delta t} = A\cos(n\Delta t) \tag{3.19}$$

U^n is the discrete solution of the finite difference equation at time step n. If Δt is constant, t=n Δt, assuming that the initial time is 0.

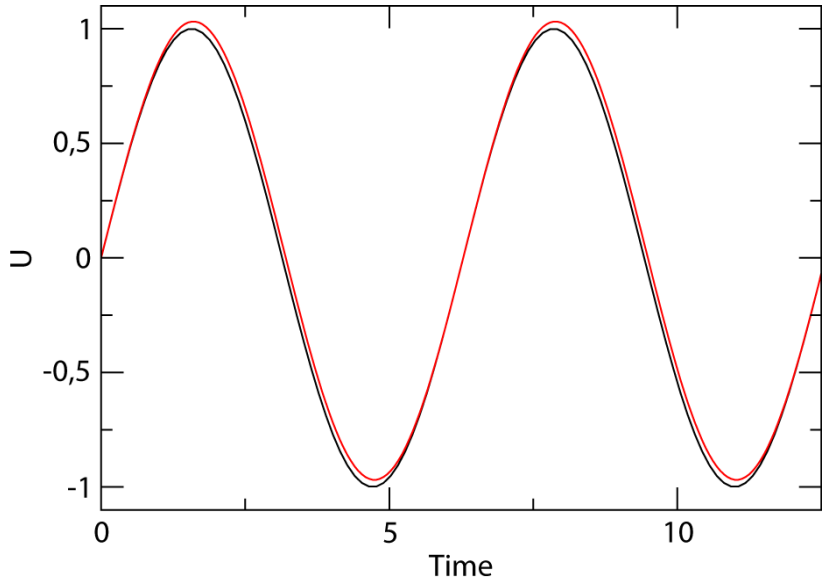

Figure 3.12: The analytical solution of equation 3.18 using A=1 and u(t=0)=0 (black) and the numerical solution using Eq. 3.20 with a time step Δt =π/50 (red). The discrete solution U^n at times $n\Delta t$ have been joined by straight lines. Note that a much more precise solution could be obtained by using $U^{n+1} = U^n + \Delta t\left(A\cos((n+1/2)\Delta t)\right)$ instead of Eq.3.20, i.e. by evaluating the cosine at time t=$(t+1/2)\Delta t$ instead of time $t=n\Delta t$.

Knowing U^n, this equation can be easily solved for U^{n+1}(Fig. 3.12):

$$U^{n+1} = U^n + \Delta t\left(A\cos(n\Delta t)\right) \tag{3.20}$$

Such problems are called initial value problems because, when the initial value is specified, values for any time can be obtained by advancing or "marching" in time.

For a numerical method to be adequate, two fundamental properties must hold. First, the finite difference equation must be consistent with the partial differential equation. This means that as $\Delta t \to 0, \Delta x \to 0$, the finite differential equation coincides with the PDE. This is absolutely essential to ensure that the equation that has been solved numerically is a reasonable approximation to the mathematical model. It can be checked by replacing all the terms by the Taylor series expansion. For the left-hand side of Equation 3.19, this gives:

$$U^{n+1} = U^n + \frac{du}{dt}\Delta t + \frac{1}{2}\frac{d^2u}{dt^2}\Delta t^2 + \text{higher order terms} \tag{3.21}$$

and thus

$$\frac{U^{n+1} - U^n}{\Delta t} = \frac{du}{dt} + \frac{1}{2}\frac{d^2u}{dt^2}\Delta t + \text{higher order terms} \tag{3.22}$$

which effectively tends to du/dt as Δt tends to 0. This shows that the scheme is consistent.

Secondly, the solution of the finite difference must converge to the solution of the PDE as $\Delta t \to 0, \Delta x \to 0$. In our example, this means that

$$U(n\Delta t) \to u(t) \text{ when } \Delta t \to 0 \tag{3.23}$$

This convergence is related to the computational stability which states that a numerical scheme is computationally stable if the solution of the finite difference equation at a fixed time remains bounded as $\Delta t \to 0$. In more colourful language, it can be said that, in this case, the numerical model does not explode. Indeed, the Lax-Richtmyer theorem, which can be formally demonstrated for a well-posed initial-value problem, states that, for a consistent numerical method, stability and convergence are equivalent.

As a consequence, the practical methods used to test the convergence of a numerical scheme are based on an analysis of the stability of the scheme. In some cases, it is possible to explicitly demonstrate that the solution is bounded, a propriety generally conditioned by a criteria that governs Δt and Δx. A more general criterion to determine the largest time and spatial step allowed is the von Neumann method in which the stability of the finite difference equation is analysed by expressing the solution as an expansion of an appropriate set of basis functions, generally **Fourier series**.

Analyses such as the one performed in Equation 3.22 also allow a **truncation error** (i.e. the difference between the PDE and the finite difference equation) to be defined. This error is characterised by an order, corresponding to the power of the first term of the difference. For the scheme described above, the error is thus of the first order in time. In

addition to uncertainties relating to the physical model itself, and the definition of initial and boundary conditions, the representation of numbers by computers using a finite number of digits is also a source of error in the numerical solution.

3.4.2 Time and space discretisations using finite differences

Many options are available for discretising an equation and the choice depends on the properties required in the numerical scheme. In addition to consistency and the stability for reasonably long time steps, the scheme must be precise enough, but not too demanding of computer time. We have presented a first example of time discretisation in section 3.4.1, which is called the upward scheme (or forward Euler method):

$$\frac{U^{n+1} - U^n}{\Delta t} = F(U^n) \tag{3.24}$$

for a right-hand side represented in a general way as a function $F(U^n)$.

An alternative scheme is a centred difference (leapfrog scheme):

$$\frac{U^{n+1} - U^{n-1}}{2\Delta t} = F(U^n) \tag{3.25}$$

which has a second order truncation error and is thus in principle more precise than the first order upward scheme. However, this scheme allows the presence and growth of unphysical modes, and is thus generally stabilised by associating it with a time filter.

In implicit schemes, the right-hand side is not only expressed at time step n but also at time step n+1. F then becomes, in general, a function of both U^n and U^{n+1}. If F is only a function of U^{n+1}, the scheme is called fully implicit or backward. Implicit schemes require an equation or a system of equations to be solved to obtain U^{n+1}, equations that could be non-linear. Implicit schemes could thus be relatively expensive in computer time. On the other hand, implicit schemes allow longer time steps, which in some circumstances is a clear advantage.

The same variety of numerical schemes is available for space discretisation. Consider the diffusion equation:

$$\frac{\partial u}{\partial t} = k \frac{\partial^2 u}{\partial x^2} \tag{3.26}$$

where k is a constant. This can be discretised as:

$$\frac{U_j^{n+1} - U_j^n}{\Delta t} = k \frac{U_{j+1}^n - 2U_j^n + U_{j-1}^n}{\Delta x^2} \tag{3.27}$$

The index j refers to point number j of the spatial grid, which is at a distance $(j\text{-}1)\Delta x$ from the first grid point if the grid spacing Δx is constant. It can easily be shown that this scheme is consistent and that the truncation error is first order in time and second order in space. It is stable if:

$$k\frac{\Delta t}{\Delta x^2} \leq \frac{1}{2} \tag{3.28}$$

illustrating the link usually present between Δt and Δx. Using this scheme, the solution at point j is updated at each time step n+1 from the values computed at time step n for points j-1, j and j+1 (Fig. 3.13).

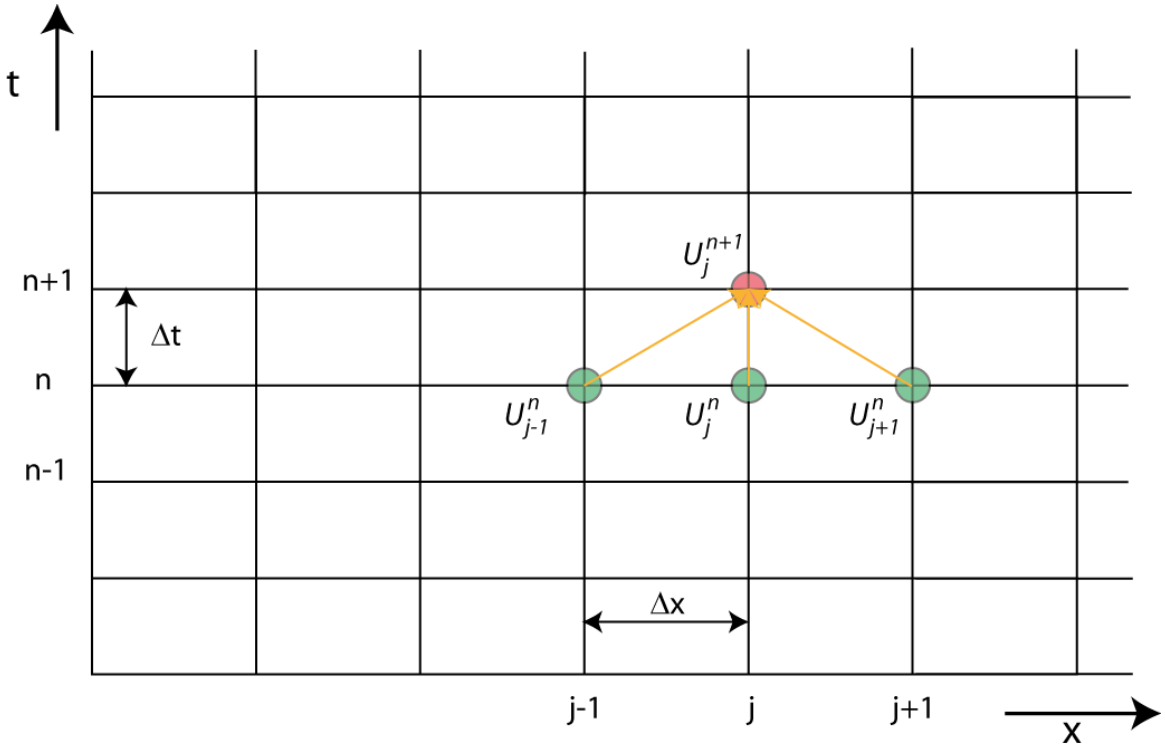

Figure 3.13: Schematic representation of the grid structure in space and time with one spatial dimension for the numerical scheme proposed in Eq. 3.27, showing that U_j^{n+1} dependents on U_{j-1}^n, U_j^n, U_{j+1}^n..

In the two examples above (Eqs. 3.18 and 3.26), only one equation for one variable was solved. However, when all the components of the climate system are considered, equations for several variables must be solved simultaneously. For numerical reasons, those variables are not necessary located at the same place on the grid, leading to what are called staggered grids. Arakawa and Lamb (1977) proposed a classification of these grids. Two popular ones are the B and the C grid. If we consider an elementary square of the grid for an ocean model, for instance, for the B grid, the temperature T (as well as the salinity, the pressure, and the density) are computed at the centres of the grid while the velocity components u and v are obtained at the corners of the grid elements (Figure 3.14). For the C grid, the velocities are computed on the side of the elements. Staggered grids are also widely used for vertical elements, with the velocity usually computed at the boundary between the layers, while the temperature is defined at the centre of the layers.

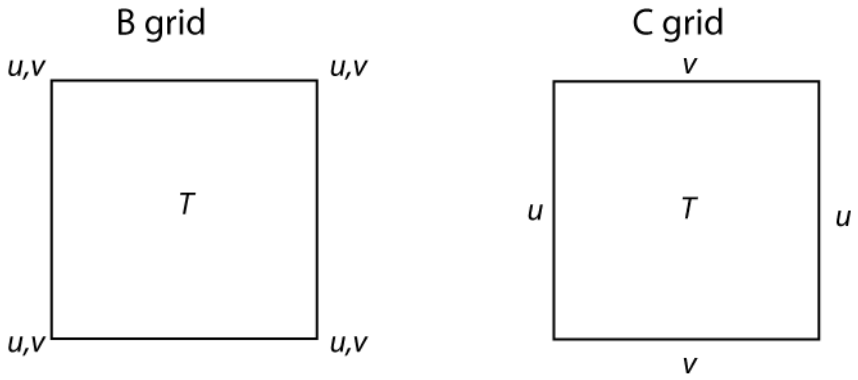

Figure 3.14: The location of some variables on the staggered grids B and C according to Arakawa and Lamb's (1977) classification.

3.4.3 Spectral representation and finite element methods

In addition to finite differences, several other methods can be use to discretise equations. One method is to integrate the basic equation of the system over a finite volume before the discretisation. This finite-volume method, has the advantage that it explicitly and easily ensures the conservation of some important properties. If particular hypotheses are made about the changes in the variables inside the volumes, numerical schemes similar to those described using finite-difference methods can be obtained.

In the Galerkin approach, the numerical solution is discretised in space as a sum of k basis functions $\varphi_k(x)$ using coefficients A_k that depend on the time, leading to a spectral representation of the solution:

$$U(x,t) = \sum_{k=1}^{K} A_k(t)\varphi_k(x) \tag{3.29}$$

The goal of the resolution of the problem is then to determine the coefficients A_k. The larger the number of basis functions retained (i.e. the larger k is), the more precise is the spatial representation of the solution. The big advantage of this method is that the space derivation of $U(x,t)$ can be analytically computed from $\mathrm{d}\varphi_k(x)/\mathrm{d}x$ without any additional approximation. The choice of the basis function must be adequate. For a one-dimensional problem, **Fourier series** are a natural choice. For a problem with spherical geometry, in particular for global atmospheric models, spherical harmonics are used. They are the product of **Fourier series** in longitude and associated **Legendre polynomials** in latitude.

The spectral and grid-point (also referred to as physical space, see for instance Fig. 3.13) representations are complementary. The first provides an accurate computation of horizontal derivatives while the second forms a convenient framework to evaluate non-linear terms as well as the physics of the model (for example, the computation of the radiative transfer). When the two approaches are combined, some transfers of the variables from the physical to the spectral space are required in the transform method. There must be an exact correspondence between the number of basis function and the horizontal resolution of the grid to avoid numerical problems during this transformation.

The finite element approach is based on a similar approximation to Eq. 3.29 but instead of functions $\varphi_k(x)$ that cover the whole domain as in the spectral method, local basis functions are used. For example, $\varphi_k(x)$ can be a piecewise linear function equal to 1 at a grid point and 0 at all the other points.

3.5 Testing the validity of models

3.5.1 Verification, validation, testing

Despite very careful design, there is no guarantee that a computer model will be adequate for its intended use: some processes treated as negligible can turn out to be more important than initially thought; a **parameterisation** may not be valid in the particular conditions of interest or may be incompatible with other hypotheses employed; the selection of parameters can be far from optimal; and so on. As a consequence, climate models have to be tested to assess their quality and evaluate their performance. In this framework, it is always necessary to keep in mind the scientific objectives of the study (or studies) that will be conducted using a particular model. Although the principles remain the same, the tests performed with a model developed to analysing the development of the global carbon cycle over the last million years (see section 5.3.2) are clearly different from those for a model providing projections of future climate changes at the highest possible **resolution** (see Chapter 6).

A first step is to ensure that the numerical model solves the equations of the physical model adequately. This procedure, often referred to as **verification** (Fig. 3.15), only deals with the numerical resolution of the equations in the model, not with the agreement between the model and reality. It checks that no coding errors have been introduced into the program. The numerical methods used to solve the model equations must also be sufficiently accurate. Different methods are available to achieve this goal. A standard one is to compare the numerical solution with the analytical one for highly idealised test cases for which an exact solution is available. It is also possible to formally state that some parts of the code are correct, for instance, the one that solves large systems of n linear algebraic equations with n unknowns (which are often produced as part of the numerical resolution of the **partial differential equations** on the model **grid**).

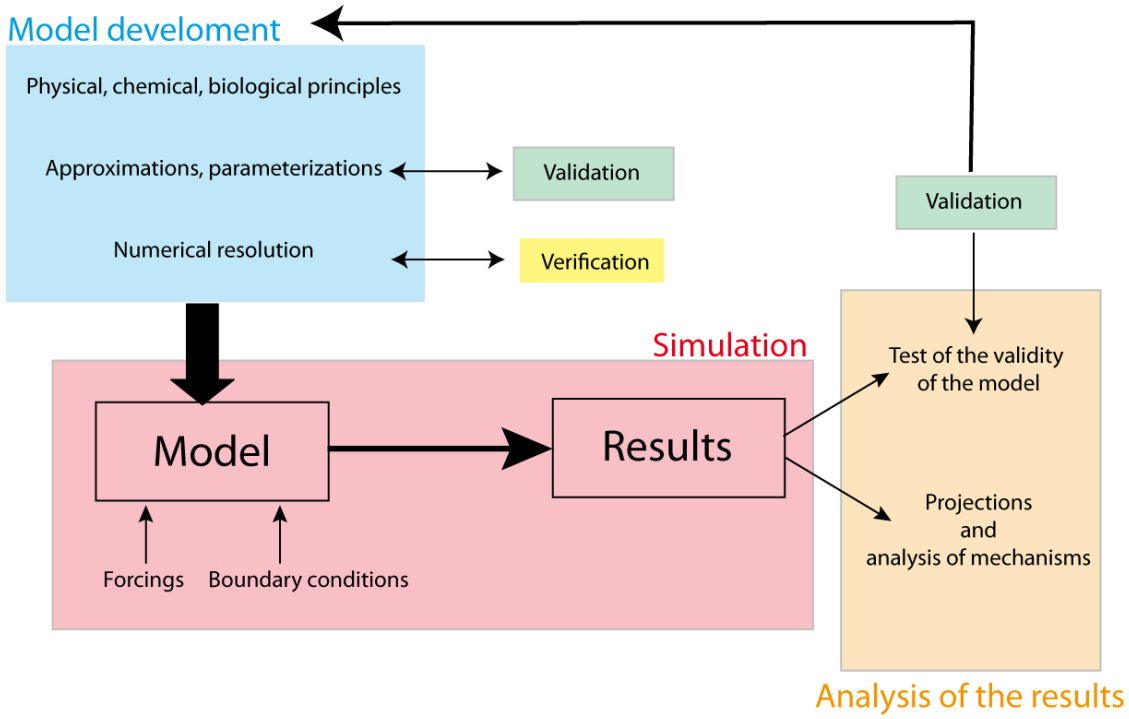

Figure 3.15: A modified version of Fig. 3.1 illustrating the verification and validation processes. An additional arrow from the analysis of the results towards model development has been added to show that **validation** is a continuous process.

The next step is the **validation** process, i.e. determining whether the model accurately represents reality. To do this, the model results have to be compared with observations obtained in the same conditions. In particular, this implies that the boundary conditions and forcings must be correctly specified to represent the observed situation. **Validation** must first be performed on the representation of individual physical processes, such as the formulation of the changes in the snow **albedo** in response to surface melting and temperature change. This is generally achieved for particular locations, during field campaigns specifically designed to study this process. They provide a much larger amount of very specific data than global data bases, allowing a detailed evaluation of the performance of the model on this topic. On a larger scale, the different components of the model (atmosphere, ocean, sea ice, etc, see section 3.3) have to be tested independently, ensuring that the boundary conditions at the interface with the other components are well defined. Finally, the results of the whole coupled model have to be compared with observations. All those steps are necessary because bad surprises are always possible after the different elements are coupled together, due to non-linear interactions between the components. Some problems with the model can also be masked by the formulation of the boundary conditions when components are run individually. However, having a coupled model providing reasonable results is not enough. In order to test whether the results occur for the correct reason, it is necessary to check that all the elements of the model are doing a good job, and that the satisfactory overall behaviour of the model is not due to several errors in its various elements cancelling each other out.

When discussing **verification** and **validation**, we must always recognize that both of them can only be partial for a climate model, except maybe in some trivial cases. The accuracy of the numerical solution can only be estimated for small elements of the code or in very special (simplified) conditions. Indeed, if it were possible to obtain a very accurate solution to compare with the numerical model results in all possible cases, there would be no point in developing a numerical model! The comparison of model results with observations is also limited to some particular conditions and completely validating a climate model in all the potential situations would require an infinite number of tests. *A climate model could thus never be considered as formally verified or validated.* A model is sometimes said to be validated if it has passed a reasonable number of tests. In such a case, the credibility of model projections performed with such a model could be very high. However, there is no way to formally guarantee that the results of the model will be correct even if the conditions are only slightly different from those used in the validation process, in particular for a very complex system like the climate. Furthermore, there is no agreement in climatology as to what a reasonable number of tests is.

The term “a validated model” and phrases like “the model has been validated” must therefore be avoided. Rather, the **verification** and **validation** should be considered as processes that never lead to a final, definitive product. The model should be continuously re-tested as new data or experimental results become available. The building of a model could then be viewed in the same way as a scientific theory. Hypotheses are formulated and a first version of the model developed. The results of the model are then compared to observations. If the model results are in good agreement with the data, the model could be said as to be confirmed for those conditions, so increasing its credibility. Nevertheless, this does not mean that the model is validated for all possible cases. If the model results do not compare well with observations, the model should be improved. This could lead to new hypotheses, to additional terms in the governing equations, or to the inclusion of new processes by new equations or new parameterisations.

Alternatively, a disagreement between the model and observations can be related to an inadequate selection of the values of some parameters that are not precisely known (for instance the exchange coefficients in Eqs. 2.33 and 2.34). Adjusting those parameters is part of the **calibration** of the model, also referred to as tuning. Model developers and

users also may decide that, if the model cannot reproduce the observations in some special cases, this indicates that it is not valid for such conditions, although it can still be used in other situations where the tests indicate better behaviour. For instance, we can imagine a climate model that cannot simulate the climate of Mars correctly without some modifications; however, this does not invalidate it for modelling conditions on Earth. On the other hand, if it works well for both Mars and Earth, this is a good test of its robustness.

The **calibration** of physical parameters is generally required and is perfectly justified as there is no a priori reason to select one particular value in the observed range of the parameters. It is also valid to calibrate the numerical parameters in order to obtain the most accurate numerical solution of the equations. However, care has to be taken to ensure that the **calibration** is not a way of artificially masking some deficiencies in the model. If this does occur, there is a high probability that the selected parameters will not provide satisfactory results for other conditions (e.g. the climate at the end of the 21st century). Performing many tests for widely different situations and for various elements of the model should limit the risk, but the number of observations is often too small to ensure that the problem has been completely avoided. An additional problem with the constant improvement of the model and of its calibration as soon as new data becomes available is the absence of independent data to really test the performance of the model. Ideally, some of the available information should be used for the model development and calibration, and some should be kept to assess its accuracy. Another good model practise is to choose or design models components for which the selection of one particular value of the parameters has only a small impact on model results, so reducing importance of the **calibration**.

In all the tests performed with the model, it is necessary to estimate the agreement between model results and observations. This is a complex and sometimes under-valued task. Indeed, the comparisons between the results of various models have shown that a single model is never the best for all the regions and variables analysed. Introducing a new parameterisation or changing the value of a parameter usually improves the results in some areas and worsens them in others. The agreement should then be related to the intended use of the model. This could be done more or less intuitively by visually comparing maps or plots describing both the model results and the observations. However, a much better solution is to define an appropriate metric. For a single field, such as the annual mean surface temperature T_s, a simple root mean square (RMS) error may be appropriate:

$$RMS = \sqrt{\frac{1}{n}\sum_{k=1}^{n}(T_{s,\mathrm{mod}}^{k} - T_{s,obs}^{k})^2} \qquad (3.30)$$

where n is the number of grid points for which observations are available, $T_{s,\mathrm{mod}}^{k}$ is the model surface temperature at point k and $T_{s,obs}^{k}$ is the observed surface temperature at point k. This estimate could be improved by taking into account the area of each grid point or by giving greater weight to the regions of most interest. If many variables have to be included in the metric, the RMS errors of different variables can be combined in various ways. The model data-comparison should also take into account the errors or uncertainties in both the model results and the observations. Errors in the observations can be directly related to the precision of the instruments or of the indirect method used to retrieve the climate signal (see for instance section 5.3.3). The uncertainties could also be due to the internal variability of the system (see sections 1.1 and 5.2), because

observations and model results covering a relatively short period are not necessarily representative of the mean behaviour of the system.

3.5.2 Evaluating model performance

Section 3.5.1 has stressed the absolute necessity of testing the quality of the model results fully. Here we will present some of the standard simulations that could be performed. However, we will not discuss the tests specifically designed to analyse the accuracy of numerical methods or of a particular parameterisation.

The first requirement is that the model is able to simulate reasonably well the climate in recent decades for which we have good estimates (Fig. 3.16). This implies performing simulations including the evolution of both natural and anthropogenic forcings (section 5.5.2) over that period. Numerical experiments with a constant forcing set at the mean for recent decades or for pre-industrial conditions (i.e. before any significant anthropogenic forcing, generally 1750 or 1850) can also be conducted in order to characterise a quasi-equilibrium behaviour of the model. In this case, it is necessary to take into account the difference between the pre-industrial conditions simulated by the model and present-day observations.

In these simulations, the long-term average of various variables, in all the model components, is compared with observations, generally interpolated on a common **grid**. Furthermore, the ability of the model to reproduce the observed climate variability on all time scales must be checked. This ranges from the relatively high frequency variations characteristic of temperature extremes such as heat waves to the most important modes of large-scale variability such as the El Niño-Southern Oscillation and the North Atlantic Oscillation (see section 5.2). Finally when driven by an adequate forcing, the climate models must be able to reproduce the observed warming of the Earth's surface over the last 150 years as well as the other recent climate changes.

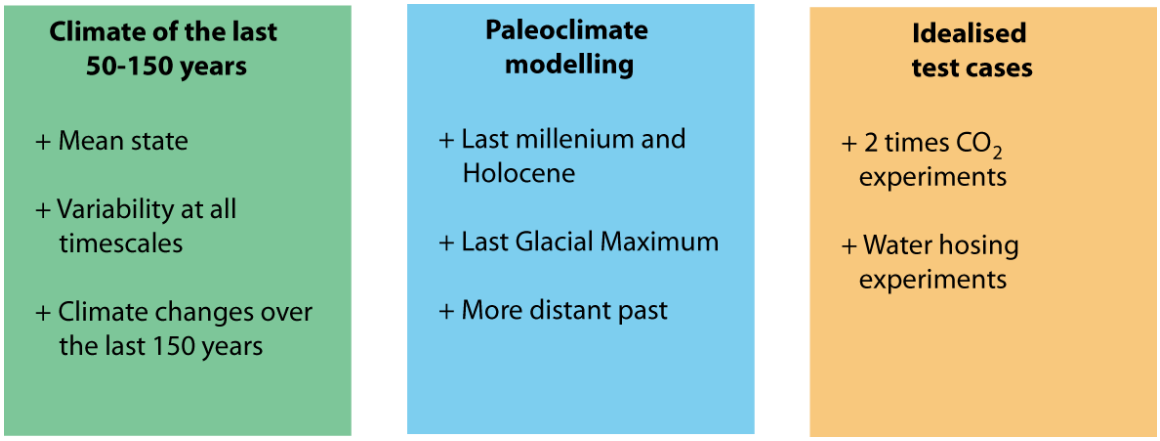

Figure 3.16: Classical tests performed on climate models.

Recent decades only cover a small fraction of the climate variations observed since the Earth's formation (see Chapter 5) and expected in the future (see Chapter 6). To test the ability of models to reproduce different climates, it is thus necessary to try to simulate some past conditions. The quality of the available observational data is (much) lower than that for recent decades and it may sometimes be hard to draw reliable conclusions from model/data comparisons for some past periods. Nevertheless, that is the only sample of possible states of the climate system that is available to us.

The second natural test period (Fig. 3.16) is the Holocene and the last millennium, for which we have a reasonably good knowledge of climate variations (see section 5.5). Although significant uncertainties are present, the forcing is much better known than for earlier periods. Furthermore, the boundary conditions (such as the topography or ocean bathymetry, see section 1.5) are similar to the present ones. The last glacial maximum is also a key period because it represents a relatively recent climate clearly different from that of recent decades (see section 5.4.2). In order to perform such simulations, unless the variables are computed interactively, it is necessary to specify variables such as the position and shape of the large ice sheets present on continents, the changes in the land/sea boundaries and ocean depth due to the lower sea levels, the modification in the vegetation cover and in the radiative properties of the atmosphere (in particular due to the higher dust content). All these elements can be sources of uncertainty for the climate simulation. Pre-quaternary climates (see section 5.3) offer an even wider range of climate variations but the uncertainties on the forcing, boundary conditions and the climate itself are larger. As a consequence, these periods are not currently used as standard tests for climate models, although this will probably change in the near future as new information becomes available.

Finally some idealised experiments are performed with climate models (Fig. 3.16). These could not be directly compared to observations as they do not correspond to any past or present situation. However, they are very useful to document the model response to a simple, well-defined perturbation. Two standard thought-experiments are generally conducted. The first is a doubling of the atmospheric CO_2 concentration in the model, a test required to estimate the climate sensitivity of the model (see section 4.1.3). In the second (water hosing), large amounts of freshwater are poured into the North Atlantic to analyse the climate changes induced by the associated modification of the oceanic circulation (see section 5.5.1). These tests also allow the behaviour of different models to be compared in exactly the same experimental conditions. This leads to model inter-comparison exercises whose goals are a better understanding of the causes of the different responses of the various models. The results of such inter-comparisons are archived in data bases to ensure wide access. The results of other simulations (for example, mid-Holocene or last glacial maximum climates, climate change during recent decades, future climate change) are also stored in public or semi-public databases so that they can be analysed independently by large numbers of scientists.

Cited references and further reading

Arakawa A. and V. Lamb (1977). Computational design of the basic dynamical processes in the UCLA general circulation model. In “General circulation models of the atmosphere”, methods in computational physics, 17, J. Chang, editor, Academic Press, 174-264.

Bonan G. (2008). Ecological climatology, concepts and applications. Cambridge University Press, 550pp.

Brovkin, V., A. Ganopolski, and Y. Svirezhev (1997). A continuous climate-vegetation classification for use in climate-biosphere studies. Ecological Modelling 101: 251-261.

Budyko M.I. (1969). The effect of solar radiation variations on the climate of the Earth. Tellus 21: 611-619.

Claussen M., L.A. Mysak, A. J. Weaver, M. Crucifix, T. Fichefet, M.F. Loutre, S.L. Weber, J. Alcamo, V.A. Alexeev, A. Berger, R. Calov, A. Ganopolski, H. Goosse, G. Lohman, F. Lunkeit, I. I. Mohkov, V. Petoukhov, P. Stone, and Z. Wang (2002). Earth

System Models of Intermediate Complexity : closing the gap in the spectrum of climate system models. Climate Dynamics 18: 579-586.

McGuffie K. and A. Henderson-Sellers (2005). A climate modeling primer (third edition). John Wiley & Sons, 280pp.

Oberkampf W.L., T.G. Trucano, and C. Hirsch (2002). Verification, Validation, and Predictive Capability in computational engineering and physics, Paper presented in the Foundation for verification and validation in the 21st century workshop, October 22-23, 2002, Johns Hopkins University/Applied Physics Laboratory Laurel, Maryland (Available at http://sokocalo.engr.ucdavis.edu/~jeremic/UsefulReadings/Oberkampf-Trucano-Hirsch.pdf)

Oreskes N., K. Shrader-Frechette, and K. Belitz (1994). Verification, validation, and confirmation of numerical modesl in the Earth sciences. Science 263: 641-646.

Sellers W.D. (1969). A global climatic model based on the energy balance of the Earth-atmosphere system. J. Appl. Met. 8: 392-400.

Trenberth K.E. (Editor), (1992). Climate System Modeling. Cambridge University Press. 787pp.

Washington W.M. and C.L. Parkinson (2005). An introduction to three-dimensional climate modeling (second edition). University Science Books, 353 pp.

Exercises

Exercises are available on the textbook website (http://www.climate.be/textbook) and on iCampus for registered students.

Chapter 4. The response of the climate system to a perturbation

4.1 Climate forcing and climate response

4.1.1 Notion of radiative forcing

The climate system is influenced by different types of perturbation: changes in the amount of incoming solar radiation, in the composition of the atmosphere, in the topography of the surface, etc. In order to compare the magnitude of those perturbations and to evaluate their effect on the climate, it is often convenient to analyse their impact on the radiative balance of the Earth. More precisely, **radiative forcing** is commonly defined as the net change in the Earth's radiative budget at the **tropopause** caused by the perturbation. According to this definition, when the modification of the upward and downward radiatives fluxes is evaluated, the stratospheric temperatures should be allowed to reach a new radiative equilibrium while the surface and tropospheric temperatures are fixed at their unperturbed values (Forster et al., 2007, Fig. 4.1). The reason for allowing stratospheric temperature changes is the rapid adjustment of the stratosphere to the perturbation (of the order of a month) compared to that of the troposphere (one or more decades). The forcing at the **tropopause** thus represents the influence of the perturbation on longer than a year.

The radiative forcing (ΔQ) associated with a perturbation is generally given in annual and global mean (e.g. Forster et al., 2007, see Chapter 6). The interest of this measure is dependent on the nature of the perturbation: it is generally more useful when the perturbation is relatively constant in space and over the seasons than for strongly seasonal or spatially variable changes.

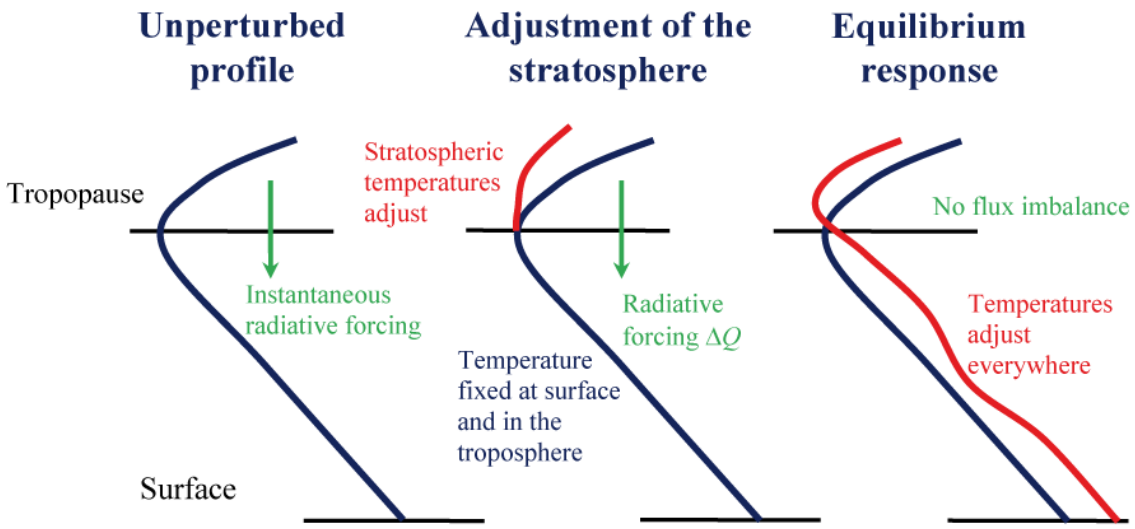

Figure 4.1: Schematic representation of the definition of radiative forcing. Modified from Foster et al. (2007)

4.1.2 Major radiative forcings

4.1.2.1 Greenhouse gases

The main radiative forcings that have affected the Earth's climate can be grouped into different categories. This has classically been done to estimate both the anthropogenic and natural forcings compared to preindustrial conditions corresponding typically to 1750 (Fig. 4.2, see also section 5.5.3). Over the last 250 years, the changes in greenhouse gas concentrations have played a dominant role (note that this also seems to be valid in a more remote past, see section 5.3). The largest contribution comes from the modification of the atmospheric CO_2 concentration, with a radiative forcing of about 1.7 W m^{-2} between 1750 and 2005. However concentrations of CH_4, N_2O and the **halocarbons** also have to be taken into account.

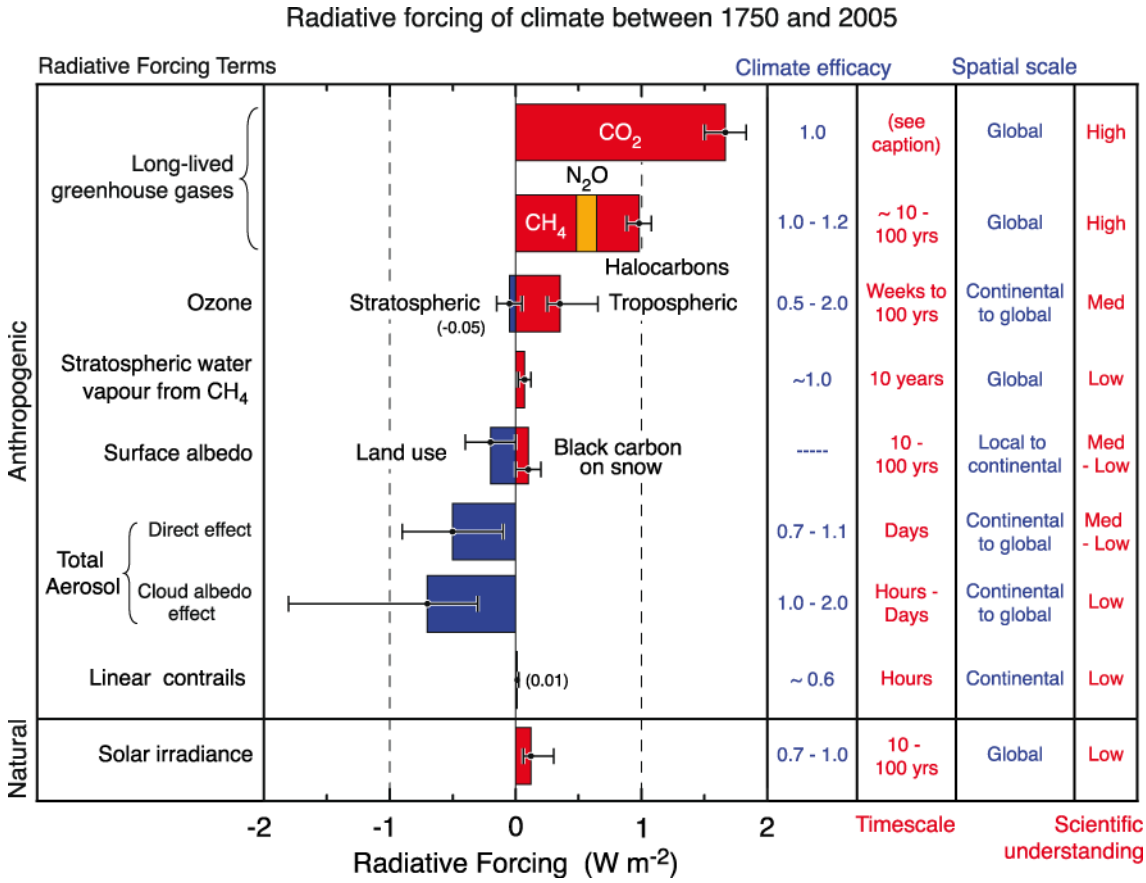

Figure 4.2: Global mean radiative forcings from various agents and mechanisms between 1750 and 2005. Time scales represent the length of time that a given radiative forcing term would persist in the atmosphere after the associated emissions and changes have ceased. No CO_2 time scale is given, as its removal from the atmosphere involves a range of processes that can span long time scales, and thus cannot be expressed accurately with a narrow range of lifetime values (see Chapter 6). Figure 2.20 from Forster et al. (2007) using a modified legend, published in: Climate Change 2007: The Physical Science Basis. Contribution of Working Group I to the Fourth Assessment Report of the Intergovernmental Panel on Climate Change, Cambridge University Press, copyright IPCC 2007. Reproduced with permission.

Estimating the radiative forcing ΔQ associated with the changes in the concentrations of these gases requires a comprehensive radiative transfer model. However, relatively good approximations can be obtained for CO_2 from a simple formula:

$$\Delta Q = 5.4 \ln\left(\frac{[CO_2]}{[CO_2]_r}\right) \tag{4.1}$$

where $[CO_2]$ and $[CO_2]_r$ are the CO_2 concentrations in ppm for the period being investigated and for a reference period, respectively.

Similar approximations can be made for CH_4 and N_2O:

$$\Delta Q = 0.036\left(\sqrt{[CH_4]} - \sqrt{[CH_4]_r}\right) \tag{4.2}$$

$$\Delta Q = 0.12\left(\sqrt{[N_2O]} - \sqrt{N_2O_r}\right) \tag{4.3}$$

where the same notation is used as in Eq. 4.1, the concentrations being in ppb.

For **halocarbons**, a linear expression appears valid. When evaluating the radiative forcing since 1750, reference values for this period are classically: CO_2 (278ppm), CH_4 (715 ppb), N_2O (270 ppb) (see in Forster et al 2007).

CO_2, CH_4, N_2O and halocarbons are long-lived gases that remain in the atmosphere for decades if not centuries. Their geographical distribution is thus quite homogenous, with only small differences between the two hemispheres. Other greenhouse gases such as O_3 (**ozone**) have a shorter life. As a consequence, their concentration, and thus the associated radiative forcing, tend to be higher close to areas where there are produced, and lower near areas where they are destroyed. **Tropospheric** ozone is mainly formed through photochemical reactions driven by the emission of various nitrous oxides, carbon monoxide and some volatile organic compounds. Globally, the impact of the increase in its concentration is estimated to induce a radiative forcing around 0.35 W m^{-2}. However, the forcing is higher close to industrial regions, where the gases leading to ozone production are released. By contrast, **stratospheric** ozone has decreased since pre-industrial time, leading to a globally average radiative forcing of –0.05 W m^{-2}. The stratospheric ozone changes are particularly large in polar regions, as the reactions responsible for the destruction of ozone in the presence of some chemical compounds (such as **chlorofluorocarbons**) are more efficient at low temperatures. The largest decrease is observed over the high latitudes of the Southern Hemisphere. There, the famous ozone hole, discovered in the mid 1980's, is a large region of the stratosphere where about half the ozone disappears in spring. Because of the Montreal Protocol which bans the use of chlorofluorocarbons, the concentration of these gases in the atmosphere is no longer increasing, and may even be decreasing slowly. However ozone recovery in the stratosphere is not yet clear.

4.1.2.2 Aerosols

Atmospheric **aerosols** are relatively small solid or liquid particles that are suspended in the atmosphere. They are largely natural: they may be generated by evaporation of sea spray, by wind blowing over dusty regions, by forest and grassland fires, by living vegetation (such as the production of sulphur aerosols by phytoplankton), by volcanoes (see section 4.1.2.4), etc. Human activities also produce aerosols by burning

fossil fuels or biomass, and by the modification of natural surface cover that influences the amount of dust carried by the wind. Among the anthropogenic aerosols, those that have received the most attention in climatology are sulphate aerosols and black carbon. Sulphate is mainly produced by the oxidation of sulphur dioxide (SO_2) in the aqueous phase, with fossil fuel burning, in particular coal burning, as their main source. Black carbon is the result of incomplete combustion during fossil fuel and biomass burning.

Since the majority of aerosols only remain in the atmosphere for a few days, anthropogenic aerosols are mainly concentrated downwind of industrial areas, close to regions where land-use changes have led to dustier surfaces (desertification) and where slash-and-burn agricultural practices are common. As a consequence, maximum concentrations are found in Eastern America, Europe, and Eastern Asia as well as in some regions of tropical Africa and South America (Fig. 4.3).

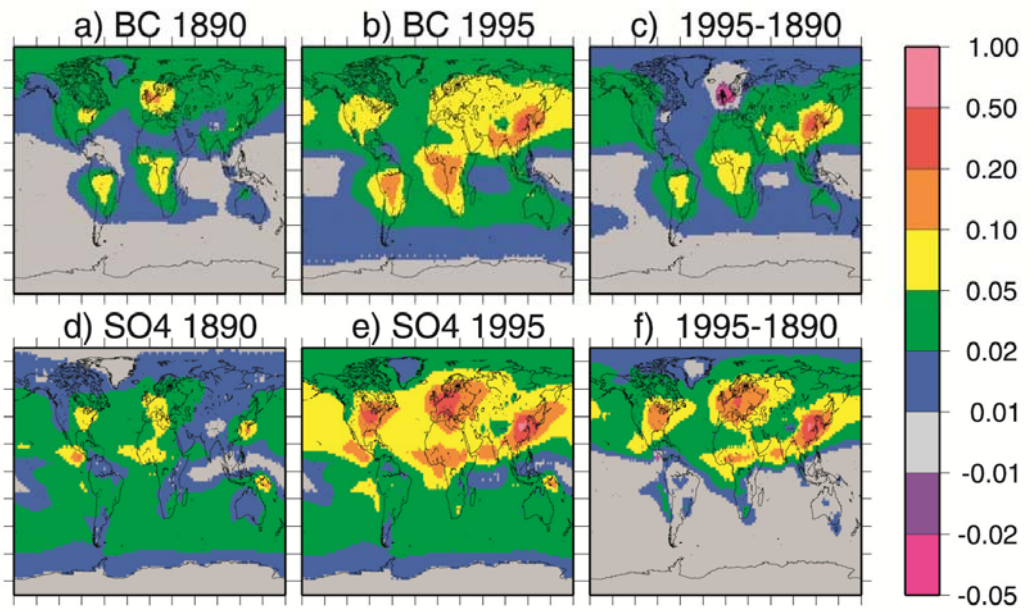

Figure 4.3: Aerosol **optical depths** (i.e. a measure of atmospheric transparency) for black carbon (BC, x10) (a) in 1890, (b) in 1995, and (c) the change between 1890 and 1995; (d)–(f) the same measures for sulphates (SO4). Reproduced from Koch et al. (2008). Copyright 2009 American Meteorological Society (AMS).

Aerosols affect directly our environment as they are responsible, for instance, for health problems and acid rain. They also have multiple direct, indirect and semi-direct effects on the radiative properties of the atmosphere (Fig. 4.4). The direct effects of aerosols are related to how they absorb and scatter **shortwave** and **longwave** radiation. For sulphate aerosols, the main effect is the net **scattering** of a significant fraction of the incoming solar radiation back to space (Fig. 4.4). This induces a negative radiative **forcing**, estimated to be around –0.4 W m^{-2} on average across the globe. This distribution is highly heterogeneous because of regional variations in the concentration of aerosols (see Fig. 4.3). By contrast, the main effect of black carbon is its strong absorption of solar radiation, which tends to warm the local air mass. The associated positive radiative forcing since 1750 is about +0.2 W m^{-2} on average. Furthermore, the deposit of black carbon on snow modifies snow's **albedo**, generating an additional small positive forcing (~+0.1 W m^{-2}). Taking all the aerosols (but not the effect of black carbon on albedo) into account, the global average of the total direct aerosol effect is about –0.50 W m^{-2} (Fig. 4.2).

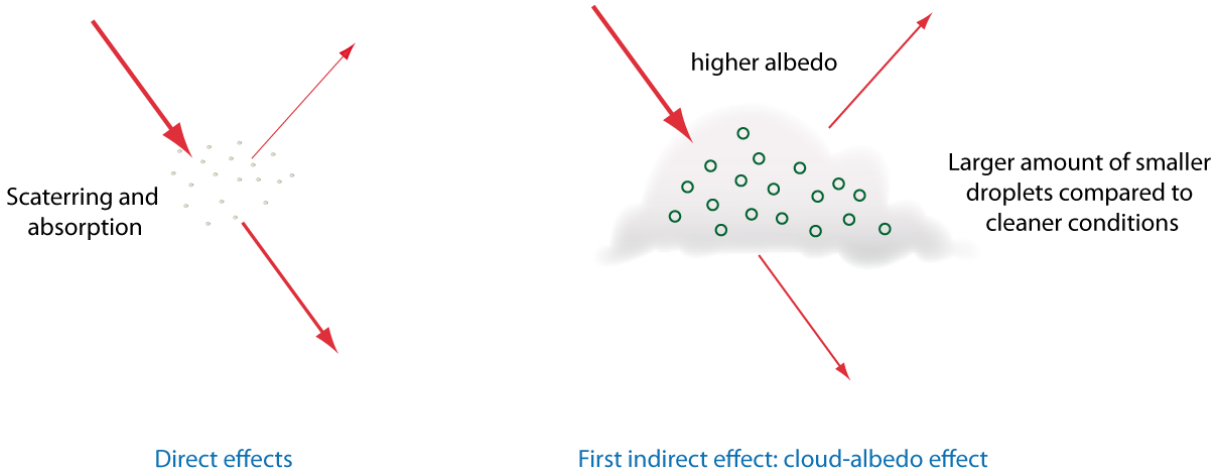

Figure 4.4: Schematic representation of the direct and first indirect effect of aerosols on the albedo of clouds. Other indirect effects such as the cloud lifetime effect and the semi-indirect effect are not represented.

The indirect effects of aerosols include their impact on **cloud microphysics** (which induces changes in clouds' radiative properties, their frequency and their lifetimes). In particular, aerosols act as nuclei on which water condenses. A high concentration of aerosols thus leads to clouds that contain many more, and hence smaller, water droplets than clouds with the same water content formed in cleaner areas. As such clouds are more highly reflecting (i.e. have a higher albedo), this induces a negative radiative forcing which is referred to as the first indirect, the cloud-albedo, or the Twomey effect. The effect of aerosols on clouds' height, lifetime and water content (related to the amount of water required before precipitation occurs) has classically been referred to as the second indirect effect although more explicit formulations such as the 'cloud lifetime effect' are now often preferred. Finally, the absorption of solar radiation by some aerosols modifies the air temperature, its humidity and the vertical stability of the air column. This affects the formation and lifetime of clouds, and is referred to as the semi-direct effect of aerosols.

The most recent estimates of the radiative forcing associated with the cloud-albedo effect are between –0.3 and –1.8 W m^{-2}, with a best estimate of around –0.7 W m^{-2}. The cloud lifetime effect also induces a negative radiative forcing but the uncertainties over its magnitude are even larger. For the semi-direct effect, even the sign of the radiative forcing is not well known at present, but its magnitude is probably smaller than those of the indirect effects. This illustrates that the aerosols represent one of the largest uncertainties in our estimates of past and future changes in radiative forcing. This is true for the twentieth century, but aerosols have also played a role, not yet known precisely, in past climate changes. For instance, during the last glacial period (see section 5.4), the drier conditions led to a higher number of aerosols in the atmosphere, producing a negative radiative forcing probably larger than 1W m^{-2} that contributed to amplifying the cold conditions at the time.

4.1.2.3 Land use changes

Humans have been modifying their environment for millennia, in particular through deforestation. Before 1950, this mainly occurred in Europe, North America, India and China, leading to a high fraction of cropland in these areas (Fig. 4.5). In the last 50 years, the extension of cropland has been stabilised in many places, some regions even showing an increase in the surface covered by forest. By contrast, deforestation has occurred rapidly over this period in many countries in the tropics.

Deforestation has a direct impact on emissions of CO_2 and CH_4 (see section 4.1.2.1) as well as on the production of dust aerosols and of aerosols due to biomass burning (see section 4.1.2.2). Furthermore, the anthropogenic changes in land use have altered the characteristics of the Earth's surface, leading to changes in the energy and moisture budgets. For instance, it has been estimated that past deforestation in tropical areas has led to a warming there of about 0.2°C, the changes in **evapotranspiration** being a significant contributor to this temperature rise. Several of these surface changes cannot be adequately represented by radiative forcing. However, it is possible to compute a radiative forcing for the modifications of **albedo** associated with land use changes, as this directly affects the radiative balance of the surface (although it is not always easy to separate this forcing from the feedbacks between vegetation and climate, see section 4.3.3). Forests have a lower albedo than crops or pasture, in particular when snow is present (see sections 1.5 and 4.3.3). The deforestation since 1750 has thus induced a radiative forcing which has been estimated to average around –0.2 W m^{-2} across the globe (Fig. 4.2). However, the forcing is much higher in regions where deforestation has been the most severe, reaching several W m^{-2} in some places.

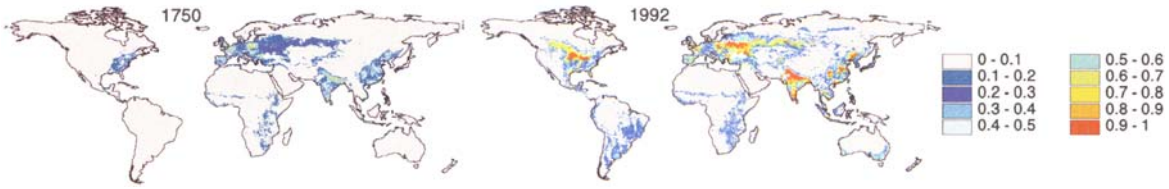

Figure 4.5: The fraction of land occupied by crops in 1750 and 1992. Figure from Ramankutty and Foley (1999). Copyright American Geophysical Union 1999.

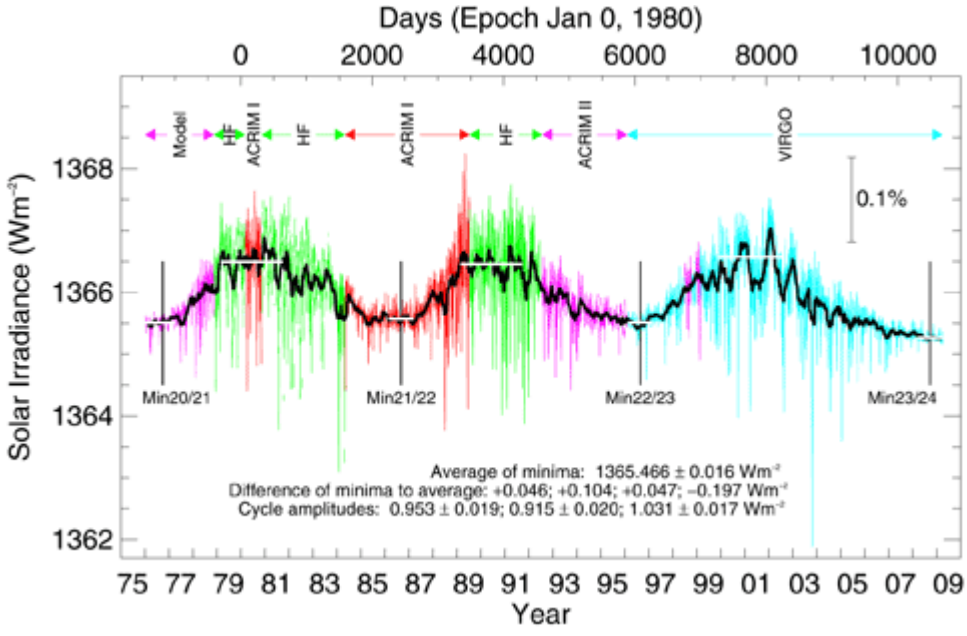

Figure 4.6: Changes in total solar irradiance estimated from a composite of measurements performed with different satellites (ACRIM, HF and VIRGO). The differences between the minimum values are also indicated, together with amplitudes of the three cycles. Figure from Claus Fröhlich, available at http://www.pmodwrc.ch/pmod.php?topic=tsi/composite/SolarConstant.

4.1.2.4 Solar and volcanic forcings.

The previous sections have been mainly devoted to anthropogenic forcings. However, natural forcings such as those associated with explosive volcanoes and changes in **total solar irradiance** (TSI), also affect the Earth's climate. Precise measurements of the TSI are available from satellites for the last 30 years. They clearly show an 11-year cycle, associated with the well-known periodicity of solar activity. However the long term trend since 1980 is very slow (Fig. 4.6). Over this period, the amplitude of the changes in TSI has been of the order of 0.1%, corresponding to a peak to peak change in TSI of about 1 W m^{-2}. Dividing by four to take into account the geometrical properties of the system (see Eq. 2.3), gives a value for the radiative forcing between high and low solar activity of about 0.25 W m^{-2}.

Various methods have been used to extend our estimates of the changes in TSI back in time. The number of sun spots (observed since around 1610) and the production of the **cosmogenic isotopes** ^{14}C and ^{10}Be are both known to be related to solar activity. However, additional work is still required before we can make a clear quantitative link between these indirect measurements and variations in TSI. As a consequence, the magnitude of the changes in TSI before the availability of satellite measurements is not well known (see section 5.5.2.1). However, the most recent estimates agrees on relatively small changes between present-day and pre-industrial times corresponding to an increase in TSI of the order of 0.1% since 1750 (e.g., Wang et al. 2005).

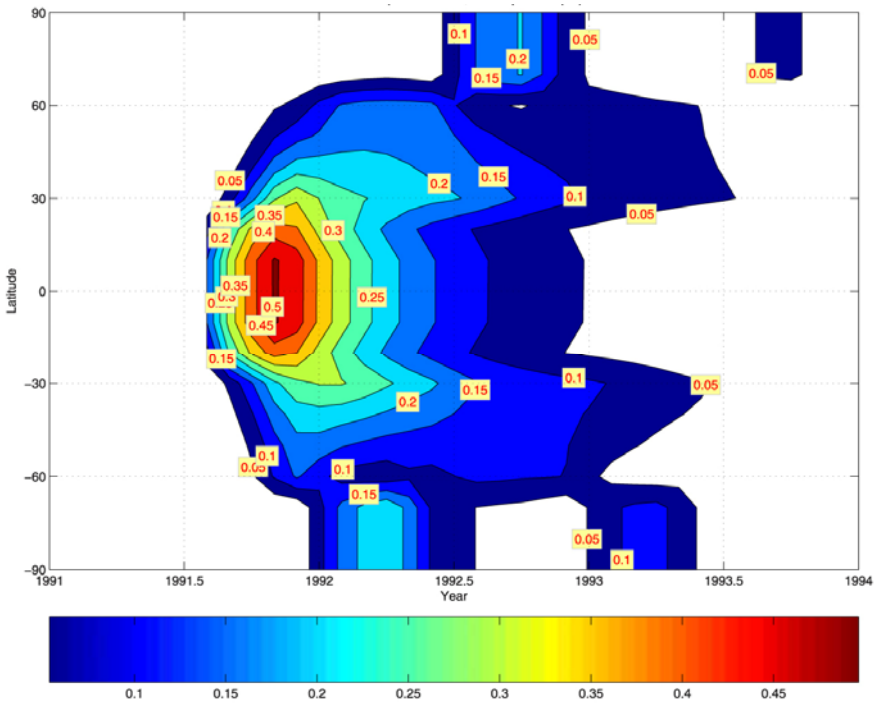

Figure 4.7: Aerosol **optical depth** after the 1991 Pinatubo eruptions as a function of latitude and time. Figure from Gao et al. (2008). Copyright American Geophysical Union 2008.

Major volcanic eruptions have a dramatic local impact causing fatalities and damage to properties, crops, forest etc. The ash produced can travel hundreds of kilometres, altering atmospheric properties for days or weeks and modifying the characteristics of the Earth's surface after its deposition. Explosive volcanic eruptions can even have an influence on a larger spatial scale, affecting the whole of the Earth's climate

significantly. Indeed, explosive eruptions can transport aerosols (mainly sulphates) directly to the stratosphere where they remain for a few years and affect nearly all regions (Fig. 4.7). As discussed for anthropogenic aerosols (section 4.1.2.2), the presence of sulphate aerosols in the stratosphere induces both a local warming in the stratosphere (mainly because of the enhanced absorption of solar radiation) and a cooling below (associated with the scattering of some radiation back to space). For major eruptions, the net radiative forcing reaches an average of several Wm^{-2} across the globe in the year following the eruption, and takes a few years to decrease to nearly zero.

4.1.3 Equilibrium response of the climate system – a definition of feedback

In response to the radiative forcing ΔQ, the various variables characterising the state of the climate system will change, modifying the radiative fluxes at the **tropopause**. These modifications involve very complex mechanisms. However, insights into the behaviour of the climate system can be gained by assuming that the changes in the radiative fluxes at the **tropopause** can be estimated as a function of the changes in global mean surface temperature, ΔT_s. If we denote ΔR the imbalance in the radiative budget, we can write:

$$\Delta R = \Delta Q + \lambda_f \Delta T_S \tag{4.4}$$

where λ_f is called the **feedback** parameter (expressed in W m^{-2} K^{-1}). In Eq. 4.4, downward fluxes are assumed to be positive.

If the perturbation lasts a sufficiently long time, the system will eventually reach a new equilibrium, corresponding to $\Delta R = 0$. This can be used to compute the global mean equilibrium temperature change in response to ΔQ as:

$$\Delta T_S = -\frac{1}{\lambda_f} \Delta Q \tag{4.5}$$

$(-1/\lambda_f)$ is a measure of the **equilibrium climate sensitivity**, i.e. the change in the global mean temperature at equilibrium in response to a radiative forcing. The **equilibrium climate sensitivity** is often determined using climate model simulations. For practical reasons, it is thus generally defined as the global mean surface temperature change after the climate system has reached a new equilibrium in response to a doubling of the CO_2 concentration in the atmosphere. It is measured in °C and according to the most recent estimates by the IPCC (Randall et al. 2007), its value is likely to be in the range 2-4.5°C.

The changes in surface temperature T_s are associated with modifications of many other variables that also affect the global heat budget. If we consider an ensemble of n variables x_i that affect R, neglecting the second order terms, we can express λ_f as a function of those variables as:

$$\lambda_f = \frac{\partial R}{\partial T_S} = \sum_{i=1,n} \frac{\partial R}{\partial x_i} \frac{\partial x_i}{\partial T_S} \tag{4.6}$$

λ_f can thus be represented by the sum of the feedback parameters associated with each variable x_i. The most common analyses generally focus on the variables that directly affect the balance at the **tropopause** through physical processes. For simplicity, we will

call these the direct physical feedbacks (section 4.2). The standard decomposition of λ_f then involves their separation into feedbacks related to the temperature (λ_T), the water vapour (λ_w), the clouds (λ_c) and the surface **albedo** (λ_α). The temperature feedback is itself further split as $\lambda_T = \lambda_0 + \lambda_L$. In evaluating λ_0, we assume that the temperature changes are uniform throughout the troposphere, while λ_L, is called the **lapse rate** feedback (see section 4.2.1), and is the feedback due to the non-uniformity of temperature changes over the vertical. Thus

$$\lambda_f = \sum_i \lambda_i = \lambda_0 + \lambda_L + \lambda_w + \lambda_c + \lambda_\alpha \tag{4.7}$$

Although indirect effects (such as changes in ocean or atmospheric dynamics and biogeochemical feedbacks) can also play an important role, they are excluded from this decomposition. Biogeochemical feedbacks will be discussed in section 4.3. Some indirect feedbacks, in which the dominant processes cannot be simply related to the heat balance at the **tropopause** will be mentioned briefly in Chapters 5 and 6, but a detailed analysis is left for more advanced courses.

The feedback parameter λ_0 can be evaluated relatively easily because it simply represents the dependence of the outgoing longwave radiation on temperature through the **Stefan-Boltzmann law**. Using the integrated balance at the top of the atmosphere (see section 2.1):

$$R = (1-\alpha)\frac{S_0}{4} - \sigma T_e^4 \tag{4.8}$$

and assuming the temperature changes to be homogenous in the troposphere

$$\Delta T_S = \Delta T_e = \Delta T \tag{4.9}$$

we obtain

$$\lambda_0 = \frac{\partial R}{\partial T}\frac{\partial T}{\partial T} = -4\sigma T_e^3 \tag{4.10}$$

This provides a value of λ_0~-3.8 W m^{-2} K^{-1}. More precise estimates using climate models gives a value of around –3.2 W m^{-2} K^{-1}.

We can then compute the equilibrium temperature change in response to a perturbation if this feedback was the only one active as:

$$\Delta T_{S,0} = -\frac{\Delta Q}{\lambda_0} \tag{4.11}$$

For a radiative forcing due to a doubling of the CO_2 concentration in the atmosphere corresponding to about 3.8 W m^{-2} (see Chapter 6), Eq. 4.11 leads to a climate sensitivity that would be slightly greater than 1°C.

If now, we include all the **feedbacks**, we can write:

$$\Delta T_S = -\frac{\Delta Q}{\sum_i \lambda_i} = -\frac{\Delta Q}{\lambda_0 + \lambda_L + \lambda_w + \lambda_c + \lambda_\alpha} \tag{4.12}$$

All these feedbacks are often compared to the blackbody response of the system, represented by λ_0, of:

$$\begin{aligned} \Delta T_S &= -\frac{1}{\left(1+\frac{\lambda_L}{\lambda_0}+\frac{\lambda_w}{\lambda_0}+\frac{\lambda_c}{\lambda_0}+\frac{\lambda_\alpha}{\lambda_0}\right)}\left(\frac{\Delta Q}{\lambda_0}\right) \\ &= \frac{1}{\left(1+\frac{\lambda_L}{\lambda_0}+\frac{\lambda_w}{\lambda_0}+\frac{\lambda_c}{\lambda_0}+\frac{\lambda_\alpha}{\lambda_0}\right)}\ \Delta T_{S,0} \\ &= f_f \Delta T_{S,0} \end{aligned} \tag{4.13}$$

Here f_f is called the feedback factor. If f_f is larger than one, it means that the equilibrium temperature response of the system is larger than the response of a blackbody. As λ_0 is negative, Eq. 4.13 also shows that, if a feedback parameter λ_i is positive, the corresponding feedback amplifies the temperature changes (positive feedback). However, if λ_i is negative, it damps down the changes (negative feedback).

The concepts of radiative forcing, climate feedback and climate sensitivity are very useful in providing a general overview of the behaviour of the system. However, when using them, we must bear in mind that the framework described above is a greatly simplified version of a complex three-dimensional system. First, it does not provide explicit information on many important climate variables such as the spatial distribution of the changes or the probability of extreme events such as storms or hurricanes. Second, the magnitude of the climate feedbacks and the climate sensitivity depends on the forcing applied. Climate sensitivity is usually defined through the response of the system to a increase in CO_2 concentration but some types of forcing are more 'efficient' than others for the same radiative forcing, meaning that they induce larger responses. Third, the feedbacks depend on the mean state of the climate system. For instance, it is pretty obvious that feedbacks related to the **cryosphere** (see section 4.3) play a larger role in relatively cold periods, where large amounts of ice are present at the surface, than in warmer periods. Fourth, non-linearities in the climate system lead to large modifications when a threshold is crossed as a response to the perturbation (see for instance section 4.3). In such cases, the climate change is mainly due to the internal dynamics of the system and is only weakly related to the magnitude of the forcing. Consequently, the assumptions leading to Eq. 4.4 are no longer valid.

4.1.4 Transient response of the climate system

Because of the thermal inertia of the Earth (see section 2.1.5), the equilibrium response described in section 4.1.2 is only achieved when all the components of the system have adjusted to the new forcing. It can take years or decades for the atmosphere, and centuries or millennia for the seas and the ice sheets, to reach this new equilibrium.

Following the same approach as in sections 4.1.1 and 4.1.2, we will assume that the thermal inertia can be represented at the first order by a slab with homogenous temperature T_s and heat capacity C_s. Using the same notation as for Eq. 4.4, the energy balance of the system can be written as:

$$C_s \frac{d\Delta T_S}{dt} = \Delta Q + \lambda_f \Delta T_S \tag{4.14}$$

If we assume that the radiative forcing ΔQ is equal to zero for $t<0$ and is constant for $t \geq 0$, this equation can easily be solved, leading to:

$$\Delta T_S = -\frac{\Delta Q}{\lambda_f}\left(1 - e^{-t/\tau}\right) \tag{4.15}$$

with

$$\tau = -\frac{C_s}{\lambda_f} \tag{4.16}$$

When t is very large, we obtain, as expected, the equilibrium solution described by Eq. 4.5. τ represents a timescale, and when $t= \tau$, the temperature change has reached 63% of its equilibrium value. τ is dependent on the heat capacity of the system C_s and on the strength of the feedbacks. This implies that with larger values of $(-1/\lambda_f)$ (i.e. greater climate sensitivity) the time taken to reach equilibrium will be longer. This is an important characteristic of the climate system, which also holds when much more sophisticated representations of the climate system than the one shown in Eq. 4.14 are used.

This behaviour can be clearly illustrated by an example (Fig. 4.8). Let us choose for the climate sensitivity values of 2 and 4°C (equivalent to values of λ_f equal to -1.9 and -0.95 W m^{-2} K^{-1}, respectively), a heat capacity corresponding to a depth of 200 meters of water distributed evenly over the whole globe (C_s=4180 10^3 x 200 = 8.36 10^8 J K^{-1} m^{-2}) and a radiative forcing corresponding to a doubling of the CO_2 concentration in the atmosphere (ΔQ = 3.8 W m^{-2}). As expected, the two different climate sensitivities produce a factor two between the equilibrium responses. However, the two curves are virtually identical during the first 15 years. It can easily be demonstrated that the slope of the curve at t=0 is independent of the climate sensitivity. As a consequence, knowing the temperature changes in the years immediately following the application of the perturbation does not necessarily provide clear information on the long term evolution of the system. This is one of the reasons why the magnitude of future climate change is still uncertain, even though several decades worth of observations of global warming are already available (see Chapter 6).

The long adjustment of the climate system to the forcing has led to the definition of a **transient climate response** (TCR), which is defined by the IPCC as the global average of the annual mean temperature change averaged over the years 60 to 80 in an experiment in which the CO_2 concentration is increased by 1% per year until year 70 (by which time it is double its initial value). The TCR values derived from models are generally between 1.4 and 2.5°C (Randall et al. 2007). The uncertainty on TCR is thus smaller than the ones of the equilibrium **climate sensitivity**, because TCR is more constrained by recent changes in temperature.

Before closing this section, it is important to mention that some changes can be classified as either forcing or response depending on the particular focus of the investigator. For instance, in a study of glacial-interglacial climate changes, the building of ice sheets is generally considered as a response of the system to orbital forcing, implying powerful **feedbacks** (see Chapter 5). On the other hand, if an investigator is mainly interested in atmospheric and oceanic circulation during glacial periods, the ice sheets could be treated as boundary conditions and their influence on the Earth's radiative balance (in particular through their **albedo**) as a radiative forcing. This distinction between forcing and response can, in some cases, be even more subtle. It is thus important in climatology, as in many other disciplines, to define precisely what we consider the system we are studying to be, and what are the boundary conditions and forcings.

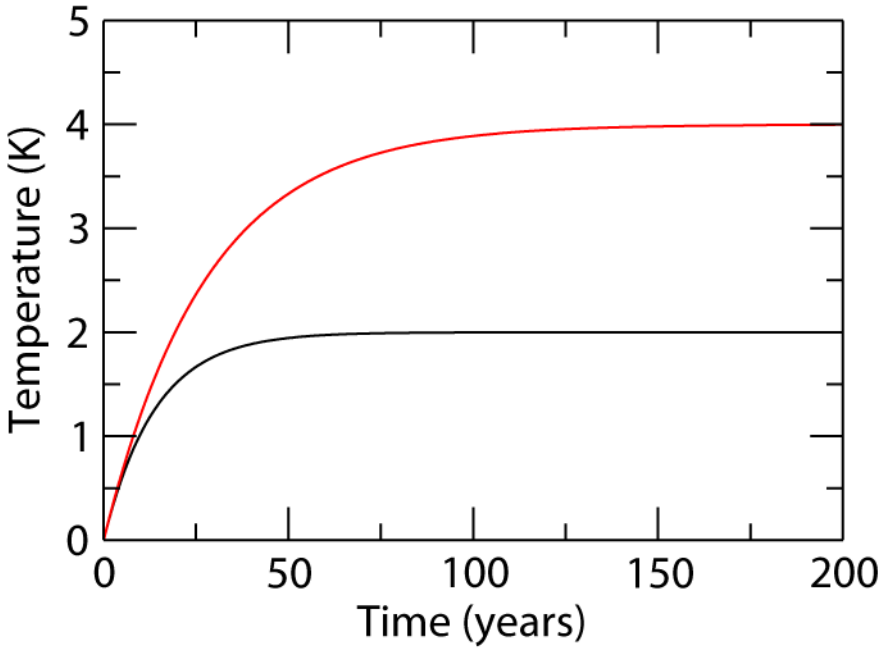

Figure 4.8: Temperature changes obtained as a solution of Eq. 4.14, using a forcing ΔQ of 3.8 W m^{-2},C_s equal to 8.36 10^8 J K^{-1} m^{-2} and values of λ_f of -1.9 (black) and -0.95 W m^{-2} K^{-1} (red).

4.2 Direct physical feedbacks

4.2.1 Water vapour feedback and lapse rate feedback

According to the **Clausius-Clapeyron equation**, the **saturation vapour pressure** and the **specific humidity** at saturation are quasi-exponential functions of temperature. Furthermore, observations and numerical experiments consistently show that the **relative humidity** tends to remain more or less constant in response to climate change. A warming thus produces a significant increase in the amount of water vapour in the atmosphere. As water vapour is an efficient greenhouse gas, this leads to a strong positive feedback (Fig. 4.9). The radiative effect of water vapour is roughly proportional to the logarithm of its concentration, and so the influence of an increase in water-vapour content is larger in places where its concentration is relatively low in unperturbed conditions, such as in the upper troposphere (see section 1.2.1).

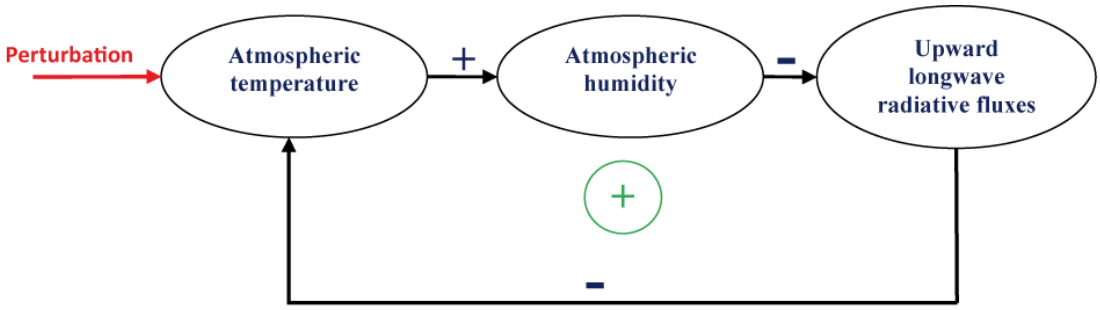

Figure 4.9: Simplified signal flow graph illustrating the water vapour feedback. A positive sign on an arrow means that the sign of the change remains the same when moving from the variable on the left of the arrow to the one on the right while a negative sign implies that an increase (decrease) in one variable induces a decrease (increase) in next one. The positive sign in a circle indicates that the overall feedback is positive.

The most recent estimates provide a value of λ_W of around 1.8 W m^{-2} K^{-1} (Soden and Held, 2006). This means that, in the absence of any other feedback, the surface temperature change due to a perturbation would be about 2.3 times as large as the blackbody response (see Eq. 4.11) because of this amplification associated with the water vapour. This makes the water-vapour feedback the largest of all the direct physical feedbacks.

The vertical variations of the temperature change also have a climatic effect through the **lapse-rate feedback** λ_L. For instance, the models predict enhanced warming in the upper troposphere of tropical regions in response to an increase in the concentration greenhouse gases. Because of this change in the lapse rate, the outgoing **longwave** radiation will be more than in an homogenous temperature change over the vertical. The system will then lose more energy, so inducing a negative feedback (Fig. 4.10). Moreover, at mid to high latitudes, more low-level warming is projected as a response to the positive radiative warming, providing a positive feedback (Fig. 4.10). The global mean value of λ_L thus depends on the relative magnitude of those two opposite effects. On average, the influence of the tropics dominates, leading to a value of λ_L of around -0.8 W m^{-2} K^{-1} (Soden and Held, 2006) in recent models driven by a doubling of the CO_2 concentration in the atmosphere.

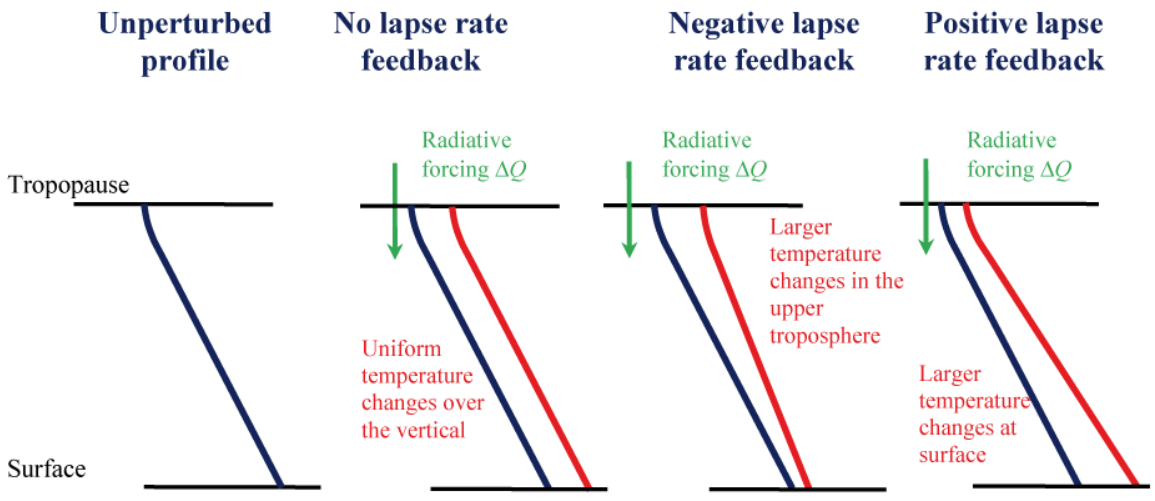

Figure 4.10: Schematic representation of positive and negative lapse-rate feedbacks.

The water-vapour feedback and the lapse-rate feedback can combine their effects. If the temperature increases more in the upper **troposphere** causing a negative **lapse-rate** feedback, the warming will also be associated with higher concentrations of water-vapour in a region where it has a large radiative impact, leading to an additional positive water vapour feedback. The exact changes in temperature and humidity at high altitude in response to a perturbation are not well-known. However, as the effects of the two feedbacks discussed in this sub-section tend to compensate each other, the uncertainty in the sum $\lambda_L + \lambda_W$ is smaller than in the two feedbacks individually. This uncertainty is estimated at about 0.1 W m^{-2} K^{-1}, the standard deviation of the values provided by the different models presented in the 4th IPCC assessment report (Randall et al., 2007).

4.2.2 Cloud feedback

Clouds affect the Earth's radiation budget in a variety of ways (Fig. 4.11). On the one hand, their presence tends to reduce the **longwave** emission from the Earth because their tops, thanks to their relatively high altitude, emit at a lower temperature than the surface. On the other hand, clouds reflect a significant amount of the incoming solar radiation, resulting in a net decrease in the amount of solar radiation absorbed by the Earth (see section 2.1.6). These two effects are often referred to as **longwave** and shortwave cloud radiative forcing (CRF). The **shortwave** CRF appears to be dominant on average in present-day conditions, and the clouds thus induce a reduction of the net downward radiation flux at the top of the atmosphere which is estimated to be around 20 W m^{-2}.

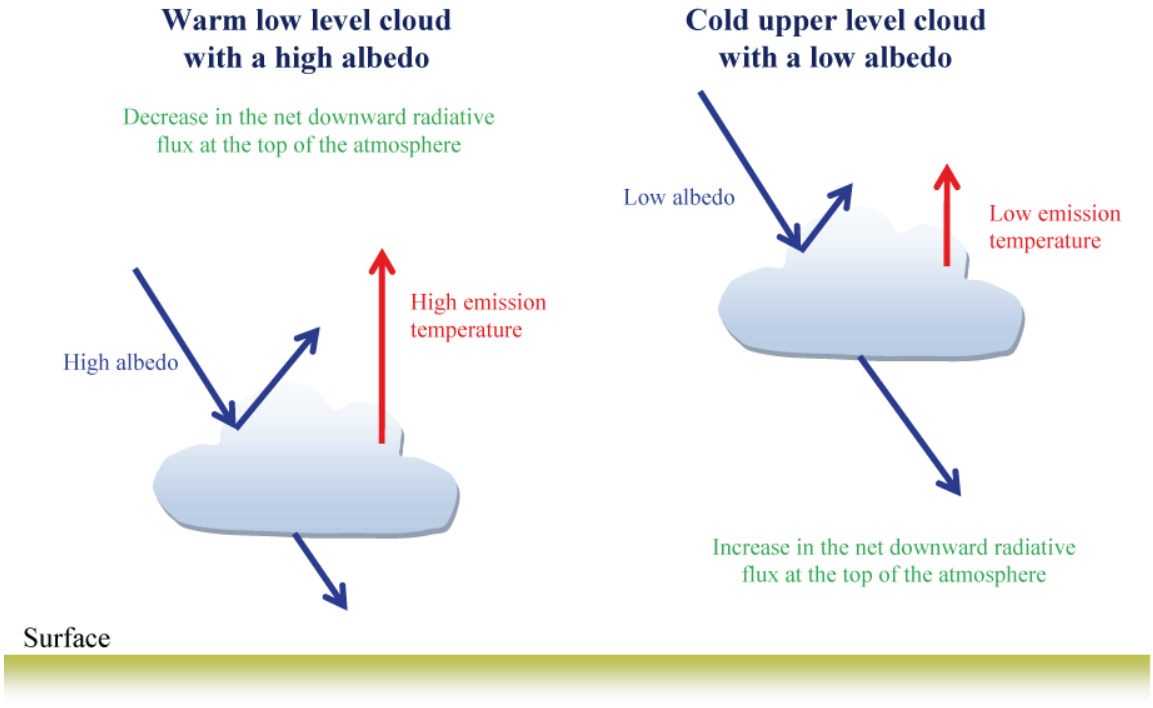

Figure 4.11: Schematic illustration of the influence of the different types of clouds on the Earth's heat budget.

However, the cloud radiative effect varies strongly with location and season. It is also very different for the various cloud types (Fig. 4.11). For instance, low level clouds tend to be relatively warm and thus have a small impact on the upward longwave flux

while they generally have a large **albedo**. They are thus associated with a reduction in the net radiative flux at the top of the atmosphere. By contrast, the majority of the high level clouds induce a higher radiative flux there, as they are cold and have a lower **albedo**.

As a consequence, an analysis of cloud feedback must take into account, for the different regions of the globe, the changes in the proportions of different cloud types, cloud temperatures (in particular related to cloud height) and cloud's radiative properties as a response to a perturbation. All these changes can be caused by direct thermodynamic effects, by the large-scale dynamics that influences changes in temperature and humidity as well as by small-scale processes occurring in the clouds themselves (called cloud microphysics).

Because of the complexity of the processes, cloud feedback is one of the less well-understood feedbacks, and this uncertainty is largely responsible for the spread of **climate sensitivity** in the present generation of climate models. The mean value provided by these models is λ_C =+0.68 W m^{-2} K^{-1} but the range is from nearly zero to more than 1 W m^{-2} K^{-1} (standard deviation of 0.4 W m^{-2} K^{-1}, i.e. nearly four times more than the standard deviation of the combined lapse-rate plus water-vapour feedback).

4.2.3 Cryospheric feedbacks

The most important feedback associated with the **cryosphere** is that due to the high **albedo** of snow and ice (see Table 1.3). If the temperature increases in response to a perturbation, snow and ice will tend to melt, leading to a reduction in the surface **albedo** (Fig. 4.12). As a consequence, the fraction of incoming solar radiation absorbed by the Earth will increase, leading to greater warming. The quantification of this feedback, which is referred to as the snow-and-ice-**albedo** feedback or the temperature-albedo feedback, depends on the exact change in the surface albedo in response to the temperature change. The albedo can be influenced by the changes in the surface covered by ice or snow (and thus also by **leads**) or by modifications of the snow and ice surface properties caused by surface melting (in particular the formation of **melt ponds** at the sea ice surface).

The snow-and-ice-albedo feedback has a significant impact on a global scale, with an estimated value based on the recent model simulations performed in the fourth assessment report of the IPCC of λ_α=0.26 W m^{-2} K^{-1}. The standard deviation of the results is 0.08 W m^{-2} K^{-1}, i.e. the same magnitude as the standard deviation of the combined water-vapour and lapse-rate feedbacks. However, its influence is larger at high latitudes where it can be responsible for about half of the response to a doubling of the CO_2 concentration in the atmosphere. For snow over land, the impact is particularly large in spring when warming can produce fast disappearance of the snow cover, leading to large albedo changes at a time when the incoming solar radiations are intense.

The snow-and-ice-**albedo** feedback is also important in producing the greater surface temperature changes at high latitude than at mid and low latitudes in response to a radiative perturbation (see Chapter 6). This polar amplification of climate change is a robust characteristic of climate model simulations. It is also strongly influenced by changes in the poleward energy transport (see section 2.1.5) and by water-vapour, lapse-rate and cloud feedbacks at high latitudes.

Another important **cryospheric** process is related to the insulation effect of sea ice. Sea ice has low thermal conductivity. It thus efficiently isolates the ocean from the atmosphere. If the temperature increases, the ice thickness will decrease. As a consequence, in winter, the heat flux from the relatively warm ocean to the cold atmosphere will increase, leading to winter warming of the atmosphere. This is not

strictly a radiative feedback, but it can explain why temperature changes at high latitudes are large in winter although the ice-albedo feedback mainly operates in spring and summer when the incoming solar radiation is at a maximum.

On longer timescales, the formation of ice sheets is a formidable amplifier of climate changes and plays a large role in glacial-interglacial cycles (see section 5.4.2). If the snow does not completely melt in summer, it accumulates from year to year, eventually forming large masses of ice (as currently observed on Greenland and Antarctica, see section 1.4). When such an ice sheet is formed, it induces an increase in the planetary **albedo** because of the ice-albedo feedback. Because of the high elevation of the ice sheet, the surface is cold and not prone to melting, further stabilising the ice sheet. Both these effects tend to maintain the cold conditions once they have been initiated by the forcing.

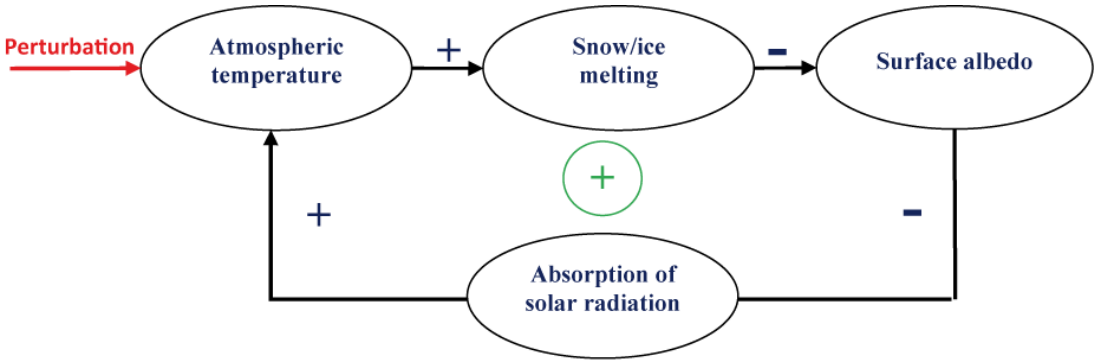

Figure 4.12: Flow graph illustrating the water snow-and-ice-albedo feedback. A positive (negative) sign on an arrow sign means that an increase in one variable produces an increase (decrease) in the one pointed by the arrow. The positive sign inside a circle indicates that the overall feedback is positive.

4.3 Geochemical, biogeochemical and biogeophysical feedbacks

4.3.1 The carbonate compensation

As discussed in section 2.3.4., the $CaCO_3$ burial in sediments is ultimately compensated for by the input from rivers. Because **weathering** and sedimentation rates appear relatively independent, there is no a priori reason why these two processes should be in perfect balance at any particular time. However, any imbalance between them can lead to large variations of the stock of calcium carbonate (and thus of the **alkalinity**, Eq. 2.45) in the ocean on millennial to multi-millennial **timescales**. This implies significant changes in the oceanic pCO_2 (section 2.3.2) and in the atmospheric CO_2 concentration. Such large shifts have not been observed, at least over the last tens of million years, because of a stabilising feedback between the oceanic carbon cycle and the underlying sediment referred to as **carbonate compensation**.

To understand this feedback, it is necessary to analyse the mechanisms controlling the dissolution of $CaCO_3$. First, let's define the **solubility** K^{CaCO_3} (similarly to the solubility of CO_2 in Eq. 2.43) from the equilibrium relationship for the dissolution of $CaCO_3$ (Eq. 2.47).

$$K^{CaCo_3} = \left[CO_3^{2-}\right]_{sat}\left[Ca^{2+}\right]_{sat} \tag{4.17}$$

where $\left[CO_3^{2-}\right]_{sat}$ and $\left[Ca^{2+}\right]_{sat}$ are the concentrations when the equilibrium between $CaCO_3$ and the dissolved ions is achieved, i.e at saturation. If at one location in the ocean the product $\left[CO_3^{2-}\right]\left[Ca^{2+}\right]$ is higher than K^{CaCO_3}, the water is said to be supersaturated with respect to $CaCO_3$. If the product is smaller than K^{CaCO_3}, the water is undersaturated. As the variations of the concentration in Ca^{2+} are much smaller than the variations in the concentration of CO_3^{2-}, saturation is mainly influenced by $\left[CO_3^{2-}\right]$.

Observations show that the concentration of CO_3^{2-} decreases with depth (inset of Fig. 4.13). The downward transport of inorganic carbon by the **soft tissue pump** and the **carbonate pump** might suggest the opposite. However, we must recall that the alkalinity is mainly influenced by the concentration of bicarbonate and carbonate ions (see the discussion of Eq. 2.45). Neglecting the small contribution of carbonic acid, *Alk* can be approximated by:

$$Alk \simeq \left[HCO_3^-\right] + 2\left[CO_3^{2-}\right] \tag{4.18}$$

If we also neglect the influence of the carbonic acid on the *DIC*, we can write:

$$DIC \simeq \left[HCO_3^-\right] + \left[CO_3^{2-}\right] \tag{4.19}$$

This leads to

$$\left[CO_3^{2-}\right] \simeq Alk - DIC \tag{4.20}$$

The dissolution of calcium carbonate releases CO_3^{2-} directly. This is consistent with Eq. 4.20 as the dissolution of 1 mole of $CaCO_3$ increases *Alk* by 2 and *DIC* by 1. By contrast, the remineralisation of organic matter mainly affects the DIC, producing a decrease in $\left[CO_3^{2-}\right]$, according to Eq. 4.20. In the present oceanic conditions, the influence of the **soft tissue pump** appears to dominate, leading to the observed decrease of CO_3^{2-} at depth. As the solubility of $CaCO_3$ increases in the deep ocean, mainly because of its pressure dependence, the upper ocean tends to be supersaturated while the deep ocean is undersaturated. The depth at which those two regions are separated is called the **saturation horizon** (inset of Fig. 4.13).

Some of the $CaCO_3$ that leaves the surface layer is dissolved in the ocean water column, but a significant part is transferred to the sediment. There, a fraction of the $CaCO_3$ is dissolved and reinjected into the ocean, the rest being buried in the sediment on a long timescale. In order to describe those processes, the **lysocline** is defined as the depth up to which $CaCO_3$ in sediments is subject to very little dissolution while below the **Calcite Compensation Depth** (CCD) nearly all the calcite is lost from the sediment by dissolution. The CCD is then the depth at which the input from sedimentation exactly balances the loss from dissolving calcite at the top of the sediment. The region between the **lysocline** and the CCD is called the transition zone (Fig. 4.13).

The position of the transition zone depends on several factors, in particular the presence of organic material in the sediment. It is significantly influenced by the

saturation of the waters above the sediment: if they are undersaturated, dissolution in the sediment tends to be relatively high, but if the waters are supersaturated dissolution is very low (as in the upper ocean). If the **saturation horizon** changes, the position of the transition zone is modified and the regions of the ocean where $CaCO_3$ is preserved in sediment change.

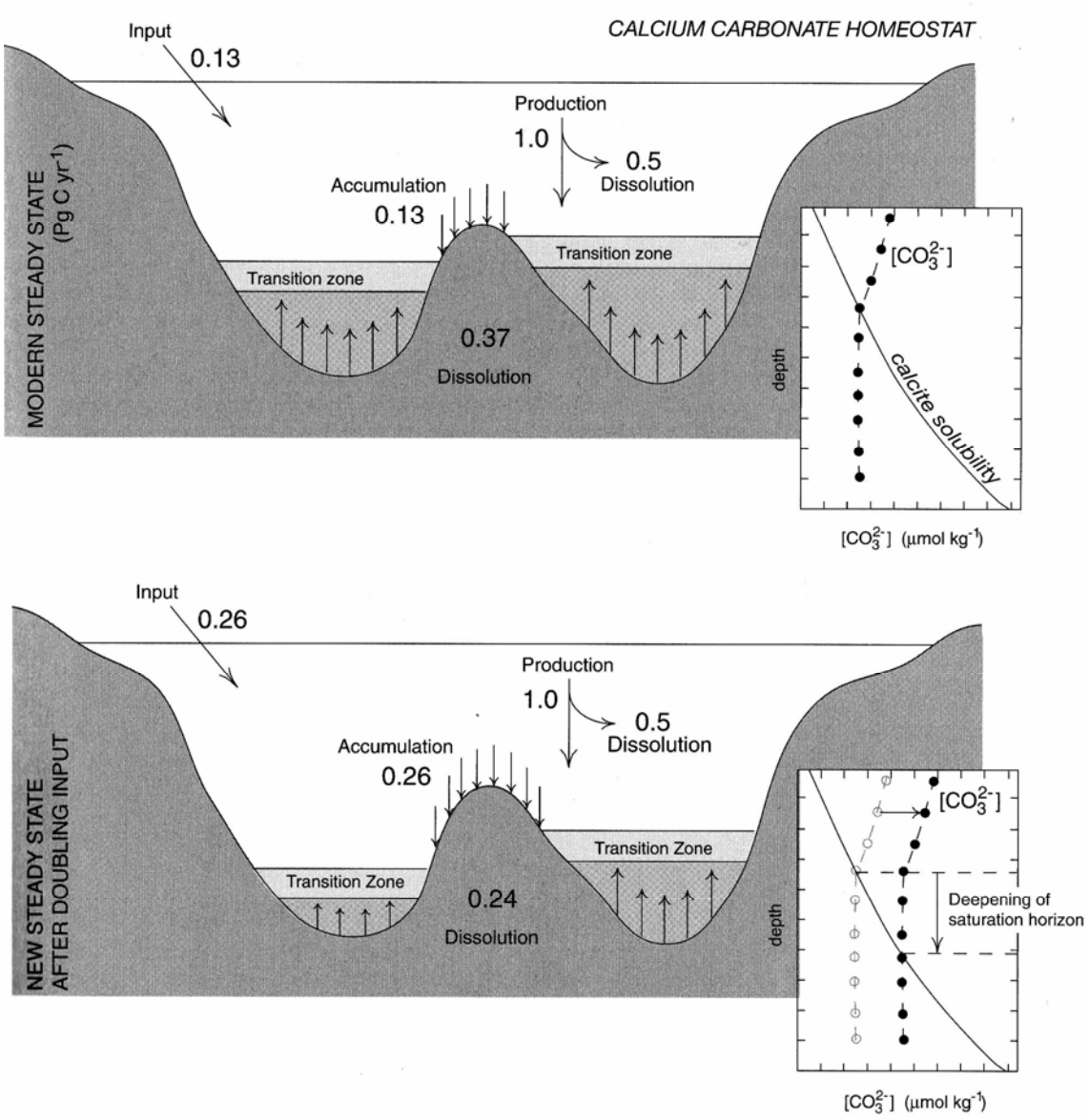

Figure 4.13: a) The current $CaCO_3$ budget in PgC yr^{-1}. 0.13 PgC yr^{-1} comes from the rivers and about 1.0 PgC yr^{-1} of $CaCO_3$ is produced in the ocean, of which 0.5 PgC yr^{-1} is dissolved in the water column and 0.5 PgC yr^{-1} is transferred to the sediment. Of the $CaCO_3$ transferred to the sediment, 0.37 PgC yr^{-1} is dissolved and goes back to the deep ocean, and 0.13 PgC yr^{-1} accumulates in the sediment, so balancing the input from rivers. b) If the river input doubles, the saturation horizon deepens, so that less $CaCO_3$ dissolves and more accumulates in the sediment a new balance is reached. Insets show the vertical profiles of $\left[CO_3^{2-}\right]$, solubility and the saturation horizon. Figure from Sarmiento and Gruber (2006). Reprinted by permission of Princeton University Press.

Those shifts in the **saturation horizon** are responsible for the stabilisation of the ocean alkalinity. Imagine for instance that the input of $CaCO_3$ from the rivers doubles because of more intense weathering on continents (Fig. 4.13). The alkalinity of the ocean will increase. As a consequence the $\left[CO_3^{2-}\right]$ will increase (Eq. 4.20) and the **saturation horizon** will fall. The fraction of the ocean floor which is in contact with undersaturated waters will increase. This would lead to a higher accumulation of $CaCO_3$ in sediment and thus a larger net flux of $CaCO_3$ from the ocean to the sediment. This fall in the saturation horizon will continue until a new balance is achieved between the increased input of $CaCO_3$ from the rivers and the greater accumulation in the sediment.

This feedback limits the amplitude of the variations in alkalinity in the ocean and thus of the atmospheric CO_2 concentration. For instance, it has been estimated that, in the example presented above, a doubling of the river input of $CaCO_3$ would only lead to a change of the order of 30 ppm in the concentration of atmospheric CO_2.

4.3.2 Interaction between plate tectonics, climate and the carbon cycle

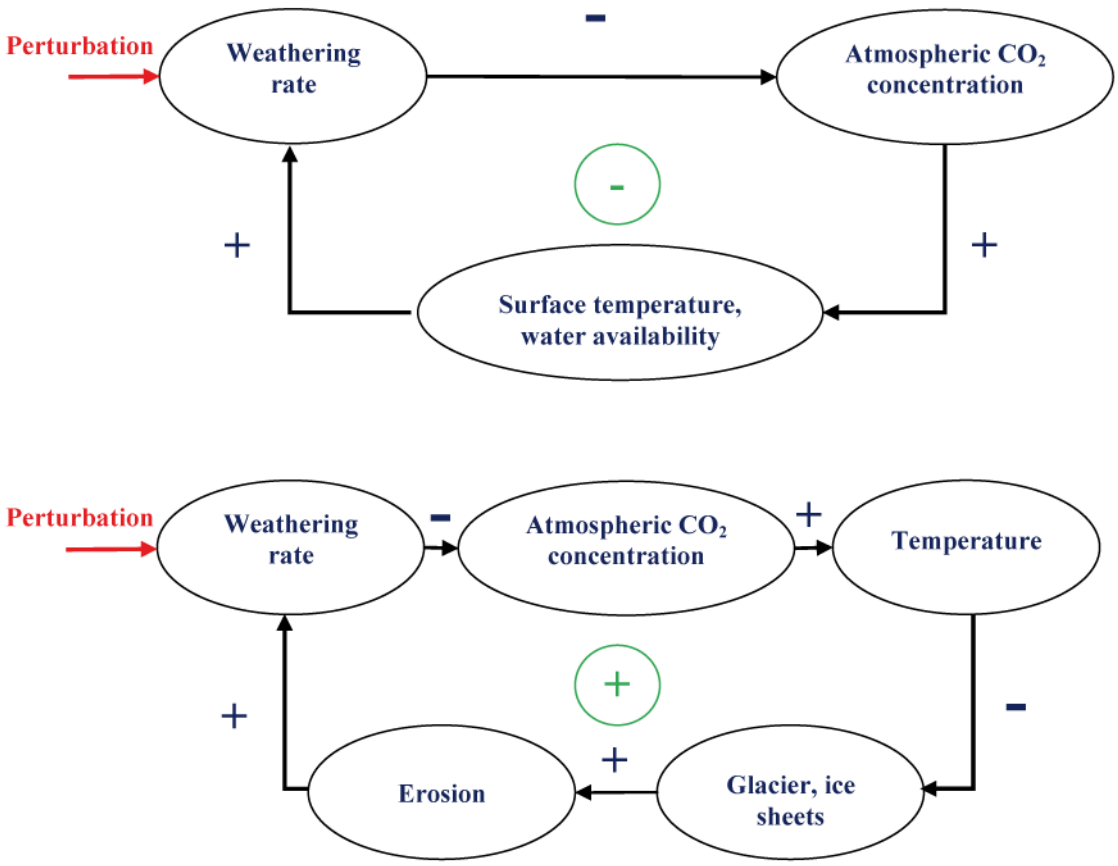

Figure 4.14: Flow graph illustrating two hypothetical feedback mechanisms affecting weathering, CO_2 concentration and climate change. A positive (negative) sign on an arrow sign means that an increase in one variable induces an increase (decrease) in the one pointed by the arrow. The positive sign in a circle indicates that the overall feedback is positive, a negative sign the opposite. Note that the perturbation can also occur at other locations in the cycle.

The chemical **weathering** of rocks (e.g., Eq. 2.49) is influenced by a large number of processes. In particular, high temperatures and the availability of water at the surface tend to induce higher weathering rates, at least for some rocks such as the basalts. As the weathering consumes atmospheric CO_2 (see section 2.3.4), this can potentially lead to a negative feedback that can regulate the long term variations in the atmospheric CO_2 concentration (Fig. 4.14). For example, more intense tectonic activity might cause the uplift of a large amount of calcium-silicate rocks to the surface, leading to an increase in the weathering rate. The atmospheric CO_2 concentration would then decrease, producing a general cooling of the climate system. This would lead to lower evaporation and so less precipitation and lower water availability. These climate changes would then reduce the weathering rates, so moderating the initial perturbation.

In a second hypothesis, we can postulate that the rate of weathering is mainly influenced by mechanical erosion, which increases the exposition of fresh, new rocks to the atmosphere and these can then be more efficiently altered. If the temperature decreases because of a higher rate of weathering, glaciers and ice sheets can cover a larger surface. As they are very active erosion agents, this would increase the mechanical weathering and so the chemical weathering, amplifying the initial perturbation (Fig. 4.14).

Although they both appear reasonable, these two feedback mechanisms are still being debated. Their exact role, if any, in the variations of CO_2 concentration on time scales of hundreds of thousands to millions of years is still uncertain.

4.3.3 Interactions between climate and the terrestrial biosphere

The terrestrial **biosphere** plays an important role in the global carbon cycle (section 2.3.3). Changes in the geographical distribution of the different **biomes**, induced by climate modifications, can modify carbon storage on land and so have an impact on the atmospheric concentration of CO_2. This can potentially lead to feedbacks that are commonly referred to as **biogeochemical feedbacks** as they involve the interactions between climate, biological activity and the biogeochemical cycle of an important chemical element on Earth (the carbon).

Figure 4.15: The difference in **albedo** between snow-covered forest and grass. The forest appears darker as it absorbs more of the incoming solar radiation. Photo courtesy of Ali Gillet.

In addition, changes in vegetation have a clear impact on the physical characteristics of the surface, in particular the albedo and water exchanges between the ground and the atmosphere (section 1.5). Feedbacks involving physical variables influenced by the terrestrial biosphere are referred to as **biogeophysical feedbacks**. One

important biogeophysical feedback is the **tundra-taiga** feedback that can be observed at high latitudes. The **albedo** of a snow-covered forest is much lower than that of snow over grass (Table 1.3, Fig. 4.15). As a consequence, if, because of warming, trees start to grow in the **tundra** (transforming the region in a **taiga**) the surface **albedo** will tend to decrease, in particular in spring (see section 4.2.3). This will lead more warming and thus a positive feedback.

However, one of the most spectacular examples of **biogeophysical** feedbacks occurs at low latitudes, linked to the relatively fast desertification of the Saharan region, which it has been estimated has been going on for between about 6 and 4 kyr BP (see Chapter 5). The standard explanation of this decrease is that a positive atmosphere-vegetation feedback was triggered by comparatively slow changes in orbital forcing (see Chapter 5). Because the intensity of the African monsoon decreased (due to the decrease in summer insolation), precipitation decreases in the Sahara during the Holocene. This produces a decrease in the vegetation cover and thus an increase in the surface **albedo** (Table 1.3). As a consequence, there was an additional cooling and reduction of precipitation that amplified the initial decrease in vegetation cover.

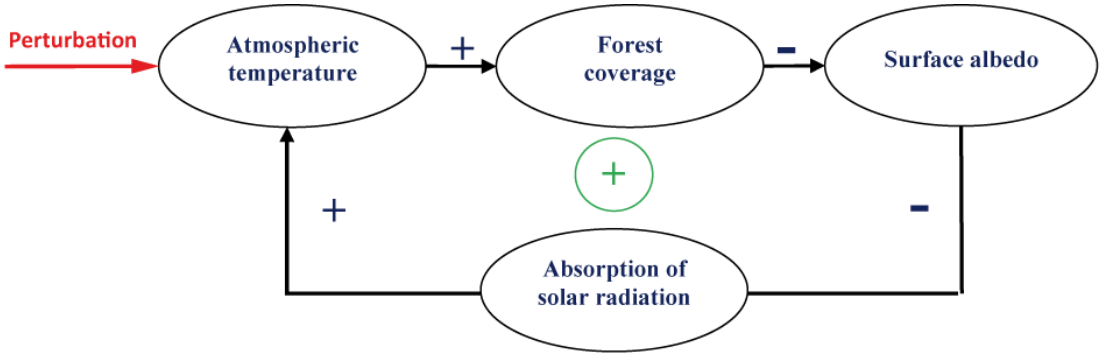

Figure 4.16: Flow graph illustrating the positive **tundra-taiga feedback** . A positive (negative) sign on an arrow sign means that an increase in one variable induces an increase (decrease) in the one pointed by the arrow. The positive sign inside a circle indicates that the overall feedback is positive.

Cited references and further reading

Adams J. (2007). Vegetation-climate interaction. How vegetation makes the global environment. Springer in association with Praxis Publishing, Chichester, UK, 232pp.

Bony S., R. Colman, V.M. Kattsov, R.P. Allan, C.S. Bretherton, J.L. Dufresne, A. Hall, S. Hallegatte, M.M. Holland, W. Ingram, D.A. Randall, B.J. Soden, G. Tselioudis, M.J. Webb (2006). How well do we understand and evaluate climate change feedback processes? J. Climate 19: 3445-3482.

Forster, P., V. Ramaswamy, P. Artaxo, T. Berntsen, R. Betts, D.W. Fahey, J. Haywood, J. Lean, D.C. Lowe, G. Myhre, J. Nganga, R. Prinn, G. Raga, M. Schulz and R. Van Dorland, 2007: Changes in Atmospheric Constituents and in Radiative Forcing. In: *Climate Change 2007: The Physical Science Basis. Contribution of Working Group I to the Fourth Assessment Report of the Intergovernmental Panel on Climate Change.* Solomon, S., D. Qin, M. Manning, Z. Chen, M. Marquis, K.B. Averyt, M.Tignor and

H.L. Miller (Eds.). Cambridge University Press, Cambridge, United Kingdom and New York, NY, USA.

Gao C., A. Robock and C. Ammann. (2008). Volcanic forcing of climate over the past 1500 years: an improved ice core-based index for climate models. Journal of Geophysical Research 113, D23111.

Hansen J., M. Sato and R.Ruedy (1997). Radiative forcing and climate response. J. Geophys. Res. 102 (D6): 6831-6884.

Hartmann D.L. (1994). Global physical climatology. International Geophysics series, volume 56. Academic Press, 412 pp.

IPCC (2007). Climate Change 2007: The Physical Basis. Contribution of Working Group I to the Fourth Assessment Report of the Intergovernmental Panel on Climate Change. Solomon, S., Qin, D., Manning, M., Chen, Z., Marquis, M., Averyt, K.B., Tignor, M., and Miller H.L. (Eds.), Cambridge Univ. Press, Cambridge, U.K. and New York, U.S.A., 996 pp.

Koch D., S. Menon, A.Del Genio, R. Ruedy, I.A. Alienov and G.A. Schmidt (2008). Distinguishing aerosol impacts on climate over the past century. Journal of Climate 22, 2659-2677.

Ramankutty N. and J.A., Foley 1999. Estimating historical changes in global land cover: croplands from 1700 to 1992, Global. Biogeochemical Cycles 13, 4:997-1027.

Randall, D.A., R.A. Wood, S. Bony, R. Colman, T. Fichefet, J. Fyfe, V. Kattsov, A. Pitman, J. Shukla, A. Noda, J. Srinivasan, R.J. Stouffer, A. Sumi and K.E. Taylor (2007). Climate models and their evaluation. In: Climate Change 2007: The Physical Science Basis. Contribution of Working Group I to the Fourth Assessment Report of the Intergovernmental Panel on Climate Change. Solomon, S., D. Qin, M. Manning, Z. Chen, M. Marquis, K.B. Averyt, M. Tignor and H.L. Miller (eds.). Cambridge University Press, Cambridge, United Kingdom and New York, NY, USA.

Rotaru M., J. Gaillardet, M. Steinberg and J. Trichet (2006). Les climats passés de la terre. Société Géologique de France, Vuibert, 195pp.

Sarmiento G.L and N. Gruber (2006). Ocean biogeochemical dynamics. Princeton University Press, 503pp.

Soden B.F. and I.M. Held (2006). An assessment of climate feedbacks in coupled ocean-atmosphere models. J. Climate, 19, 14, 3354-3360.

Wallace J.M. and P.V. Hobbs (2006). Atmospheric science: an introductory survey (2nd edition). International Geophysics Series 92, Associated press, 484pp.

Wang Y.M., J.L. Lean and N.R. Sheeley (2005). Modeling the sun's magnetic field and irradiance since 1713. Astrophysical Journal 625, 1, 522-538

Exercises

Exercises are available on the textbook website (http://www.climate.be/textbook) and on iCampus for registered students.

Chapter 5. Brief history of climate: causes and mechanisms

5.1 Introduction

Since the beginning of Earth's history, climate has varied on all timescales. Over millions of years, it has swung between very warm conditions, with annual mean temperatures above 10°C in polar regions and glacial climates in which the ice sheets covered the majority of the mid-latitude continents. It has even been postulated that, in some past cold periods, the whole surface of the Earth was covered by ice (this is the snowball Earth hypothesis). At the other end of the spectrum, lower amplitude fluctuations are observed at interannual and decadal timescales, no year being exactly the same as to a previous one.

The **timescale** of these variations is partly set up by the forcing (Fig. 5.1). Because of its own stellar evolution, the radiation emitted by the Sun has increased by roughly 30% over the 4.5 billion years of the Earth's history. Variations in the **total solar irradiance** on shorter timescales have a smaller amplitude, although this amplitude is not precisely known (see section 5.5). The low frequency changes of the characteristics of the Earth orbit (see section 5.4.1) modify the amount of solar energy received in a particular season on every point on the Earth's surface, with the most important fluctuations located in the 10-100 ka range. Individual volcanic eruptions produce a general cooling during the years following the eruption (see section 5.5.1). Furthermore, volcanic activity can be responsible for a low frequency forcing if large eruptions are grouped in a particular decade or century. On longer **timescales**, increased volcanic activity related to plate tectonics can lead to a strong cooling lasting thousands to millions of years.

On the other hand, internal dynamics also play a very important role in determining the variability of the Earth's climate. They can be a direct cause of variability, in the absence of any significant change in the forcing, through interactions between various elements of the system. Important examples are the El Niño Southern Oscillation (ENSO), the North Atlantic Oscillation (NAO) and the Southern Annular Mode (SAM). Secondly, because of the large inertia of the ocean and the ice sheets, the dominant effect of a perturbation can be related to the integration of the forcing over long time scales while higher frequency changes are damped. Inertia can also induce a delayed response to a perturbation (see section 4.1.4). Furthermore, the response of the system can involve complex mechanisms that lead to large differences between the characteristics of forcing and those of the climate changes induced by the forcing. For instance, if a forcing excites one mode of internal variability of the system at a particular frequency, leading to a kind of resonance, the magnitude of the response at that frequency will be large even though the forcing is not particularly intense at that frequency. Small changes in the forcing can also lead to large variations in the climate system if a threshold is crossed and, as a result the system evolves (nearly-) spontaneously from one state to another, possibly quite different, one. Such a transition, involving the deep oceanic circulation, has been proposed to explain some of the abrupt climate changes recorded in Greenland ice cores during the last glacial period.

This brief overview has described a few of the processes that have to be combined to explain past climate changes. Below, we will illustrate some of the most important concepts, starting with the variability that is due to internal processes only. For this, we will focus on processes characterised by relatively high frequency variations, because they are the ones for which we have the most information. The components of the climate

system that are mainly involved in those modes of variability are the atmosphere and the surface layer of the ocean. The internal variability of the deep ocean circulation and the ice sheets will not be discussed here. We will then review past climate changes, starting with very long timescales and finishing with the last millennium.

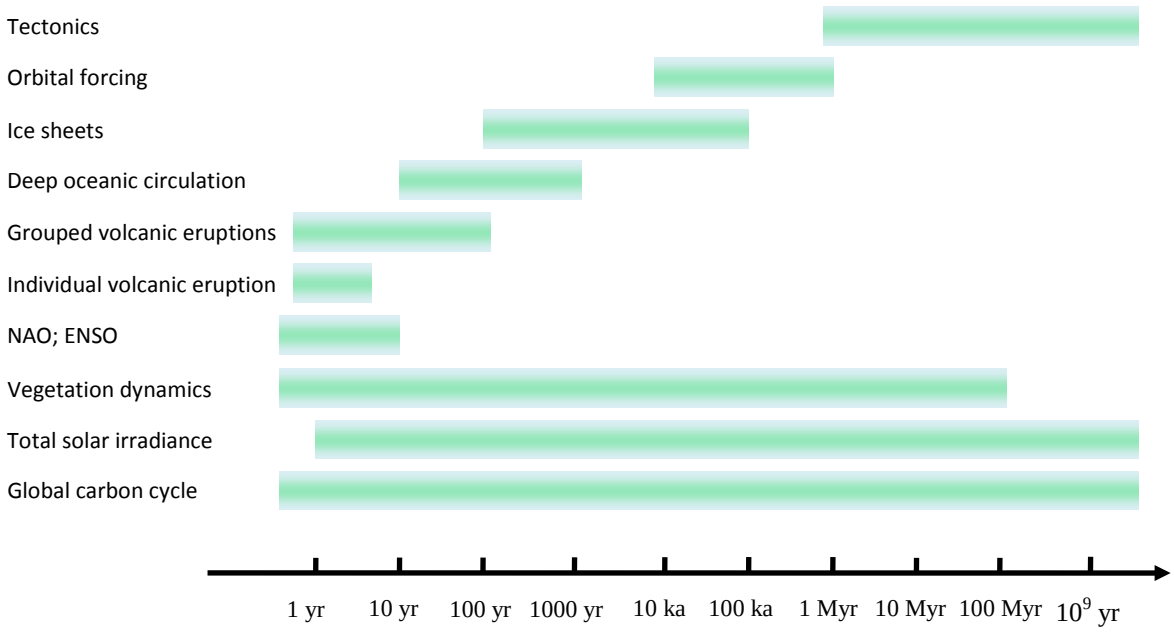

Figure 5.1: Schematic representation of the dominant timescales of some selected external forcing and processes related to internal dynamics that affect climate. For each of them, we have plotted here an indicative range. However, because of mutual interactions, they can exhibit variability on nearly all the timescales. For instance, orbital forcing could influence the distribution of temperature and precipitation at the Earth surface and then induce variations of the oceanic circulation and ENSO on multi-millennial timescales.

5.2 Internal climate variability

5.2.1 El Niño-Southern Oscillation

In equatorial regions, the **trade winds** induce a **zonal** transport from the East to the West Pacific that is responsible for warm sea surface temperatures and a relatively deep **thermocline** there. The **thermocline** is higher in the East Pacific. As a consequence, the equatorial **upwelling** (also caused by the **trade winds**) transports cold deep water to the surface more efficiently in the East Pacific, leading to a large cooling in this region (see section 1.3 and Fig. 5.2).

Because of those differences in sea surface temperatures (SSTs), atmospheric convection and **ascendant** air motion are observed over the West Pacific while **subsidence** occurs over the East Pacific. The circulation is closed by an movement transport in the upper troposphere and westward atmospheric flow in the lower layers (Fig. 5.2). The resulting **zonal** overturning circulation, referred to as the **Walker circulation**, thus reinforces the easterlies that are the **zonal** mean in this latitude band (see section 1.2). Consequently, the Walker circulation is associated with a positive **feedback**, called the Bjerknes **feedback** (Fig. 5.3), in which the easterly surface wind stress enhances the zonal SST **gradient** which in turns amplifies the wind stress.

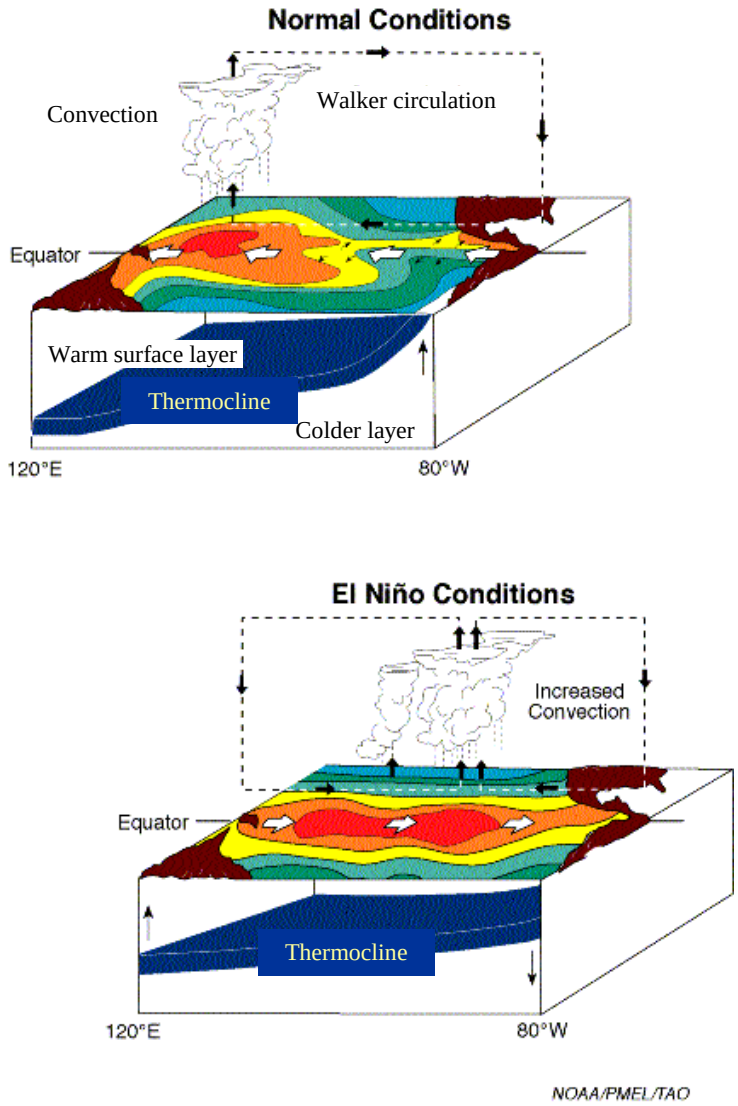

Figure 5.2: The Walker circulation in the atmosphere and the position of the thermocline in the ocean in normal conditions and in El Niño years. Red represents warm SST while green ones represents cold water. *Source*: http://www.pmel.noaa.gov/tao/elnino/el-nino-story.html. Following the policy of U.S. government agencies, this figure is not subject to copyright protection.

The Walker circulation exhibits irregular oscillations (Fig.5.4). They are characterised by a see-saw in sea level pressure (SLP) between the East and West Pacific that drives the surface easterlies (Fig. 5.5). Classically, the magnitude of this mode is measured by the Southern Oscillation Index (SOI):

$$SOI = 10 \frac{SLP'_{Tahiti} - SLP'_{Darwin}}{\sigma_{\Delta SLP}} \qquad (5.1)$$

where the SLP'_{Tahiti} and SLP'_{Darwin} are SLP **anomalies** (i.e. the difference between the current value and the long term mean) at Tahiti and Darwin (Australia), respectively and $\sigma_{\Delta SLP}$ is the standard deviation of the difference between these two SLP anomalies.

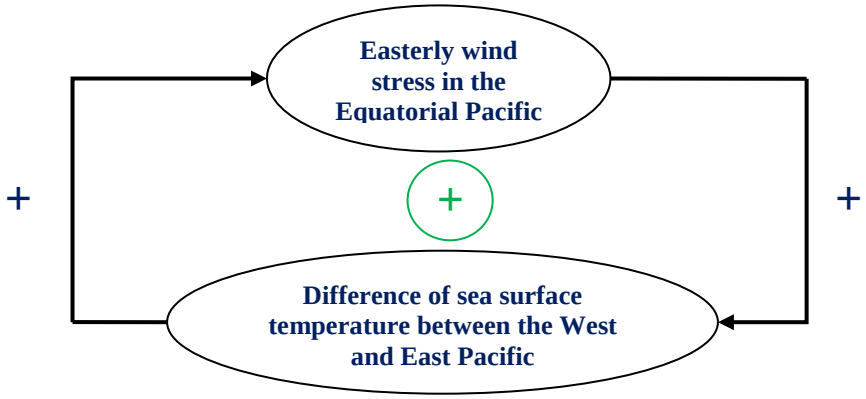

Figure 5.3: Flow graph illustrating the Bjerknes **feedback**. A positive sign on an arrow show that an increase in one variable produces an increase in the other. The positive sign inside a circle indicates that the overall feedback is positive.

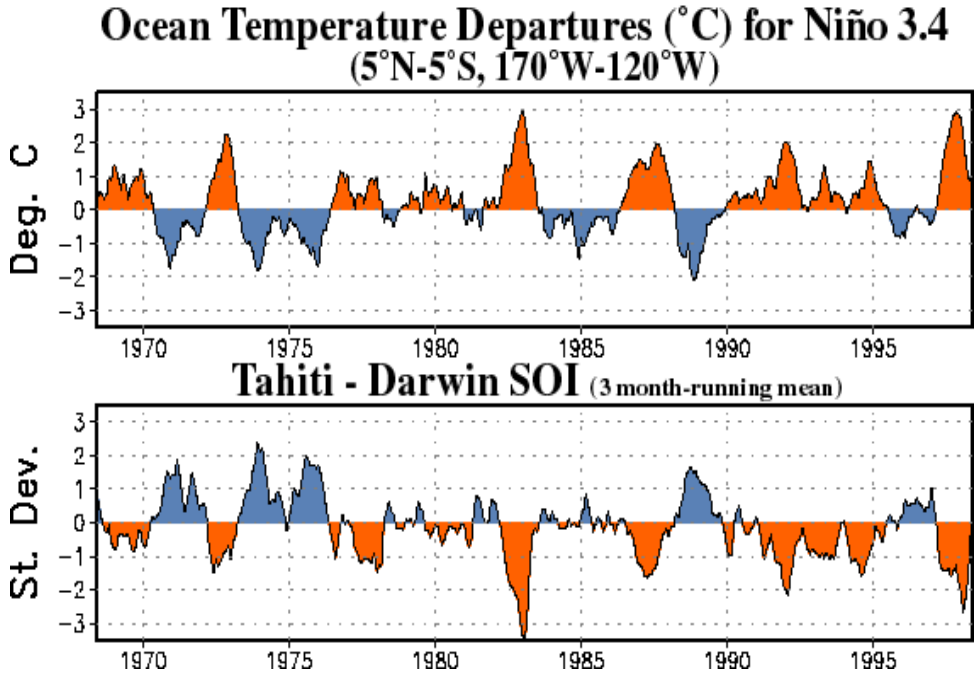

Figure 5.4: Time series of the temperature in the eastern equatorial Pacific (averaged over the area 5°N-5°S-170°W-120°W, the so-called Niño3.4 index) and the SOI index. A filter has been applied to remove fluctuations with periods less than a few months. Negative values of the SOI and positive temperature **anomalies** correspond to El Niño episodes (e.g., the years 1982/83 and 1997/98) while a positive SOI index and a negative temperature **anomaly** in the Eastern Equatorial Pacific are typical of La Niña periods (e.g., the years 1988/89, 1995/96). *Source*: http://www.cpc.ncep.noaa.gov/products/analysis_monitoring/ensocycle/soi.shtml. Following the policy of U.S. government agencies, this figure is not subject to copyright protection.

When the SOI is low, the long term mean gradient between the East and West Pacific decreases, leading to weaker easterlies. Prolonged negative values of the SOI are thus associated with reduced **upwelling** and weaker westward oceanic currents. This

induces a smaller east-west tilt of the **thermocline** and abnormally warm surface temperatures in the East Equatorial Pacific (Figs. 5.2 and 5.4). The temperature **anomaly** can reach 5°C locally. The associated warming close to the coast of Peru was originally referred to as El Niño, but the term is now used to describe all the oceanic changes that occur when temperature is high in the East Pacific Ocean. The opposite condition, corresponding to colder temperatures in the East Pacific, an increased tilt in the ocean **thermocline**, and warm surface water restricted to the West Pacific are called, by analogy, La Niña conditions.

Because of the strong interactions between oceanic and atmospheric changes, the Southern Oscillation and the El Niño phenomenon are strongly coupled (see Fig. 5.4). This has led to the choice of the acronym ENSO (El Niño Southern Oscillation) to refer to the whole process. Indeed, because of the Bjerknes **feedback**, a decrease in **zonal** SST gradient, caused for instance by a relaxation of the tilt of the **thermocline**, implies a reduction of the **zonal** wind stress that will amplify the initial perturbation. The anomalies then grow until negative feedbacks, mainly related to oceanic processes (in particular the adjustment of the **thermocline** depth) overwhelm the positive feedbacks. Those negative feedbacks are characterised by a delayed response compared to the SST and wind stress initial perturbation, allowing the development of the irregular oscillation described in Fig. 5.4.

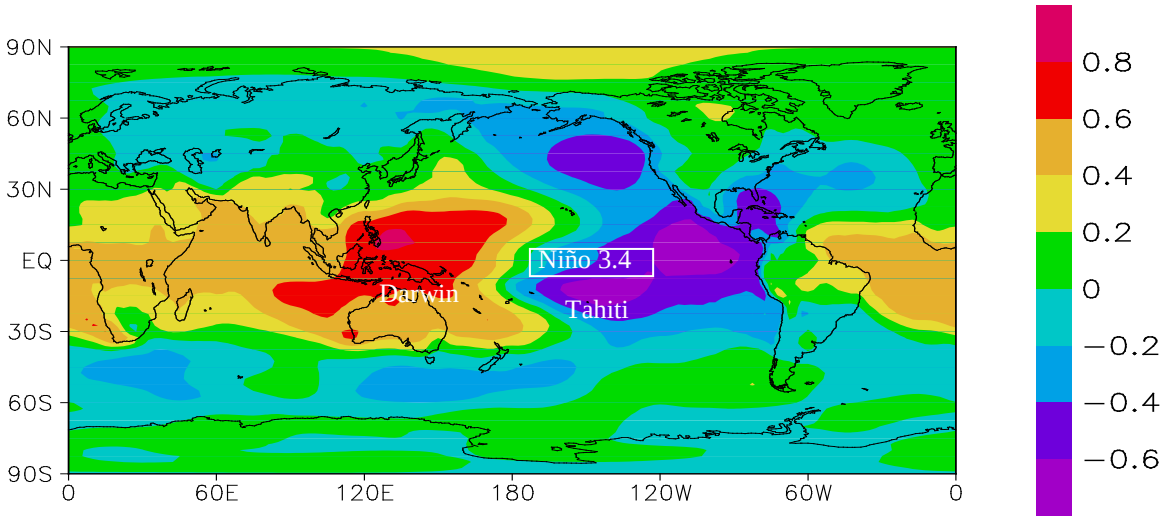

Figure 5.5: Correlation between the sea surface temperature in the eastern tropical Pacific (Niño3.4 index) and sea-level pressure in January. Figure performed on the site http://climexp.knmi.nl/ (Oldenburg et al., 2004) using NCEP-NCAR **reanalysis**. The approximate locations of the Tahiti and Darwin stations, used to define the SOI, and of the Niño 3.4 box are indicated.

In addition to their effect on the wind stress, the SST **anomalies** related to the ENSO in the Pacific induce an eastward migration of the atmospheric convection (Fig. 5.2) causing higher precipitation in the central Pacific and dry conditions over Indonesia and Northern Australia. ENSO is also associated with perturbations outside the tropical Pacific as it produces anomalies of the atmospheric circulation across nearly the whole world (Fig. 5.5). For instance, El Niño years tend to be much drier and warmer in Mozambique while the western USA tends to be wetter. Because of these global **teleconnections**, ENSO is probably the internal mode of variability which has the greatest impact on human activities. As a consequence, forecasting its development a few months in advance is an intense area of research.

5.2.2 The North Atlantic Oscillation

The large-scale atmospheric circulation in the North Atlantic at mid-latitudes is characterised by westerlies driven by the sea-level pressure difference between the Azores high and the Icelandic low (Fig. 1.5). As described in section 5.2.1 for the **Walker circulation**, there are irregular changes in the intensity and location of the maxima of these westerlies. This is associated with a North-South oscillation of the pressure, and thus of the atmospheric mass (Fig. 5.6), known as the North Atlantic Oscillation (NAO). The intensity of this mode of variability is measured by the normalised SLP difference between meteorological stations in the Azores and in Iceland:

$$NAO_{index} = \frac{SLP'_{Azores}}{\sigma_{Azores}} - \frac{SLP'_{Iceland}}{\sigma_{Iceland}} \qquad (5.2)$$

where SLP'_{Azores} and $SLP'_{Iceland}$ are the SLP **anomalies** in the Azores and Iceland and σ_{Azores} and $\sigma_{Iceland}$ the standard deviations of these **anomalies**. Because of the longer time series available, the station in the Azores is sometimes replaced by one in Portugal. When the NAO index is high, the westerlies are stronger than average while they are weaker than the mean when the NAO index is negative.

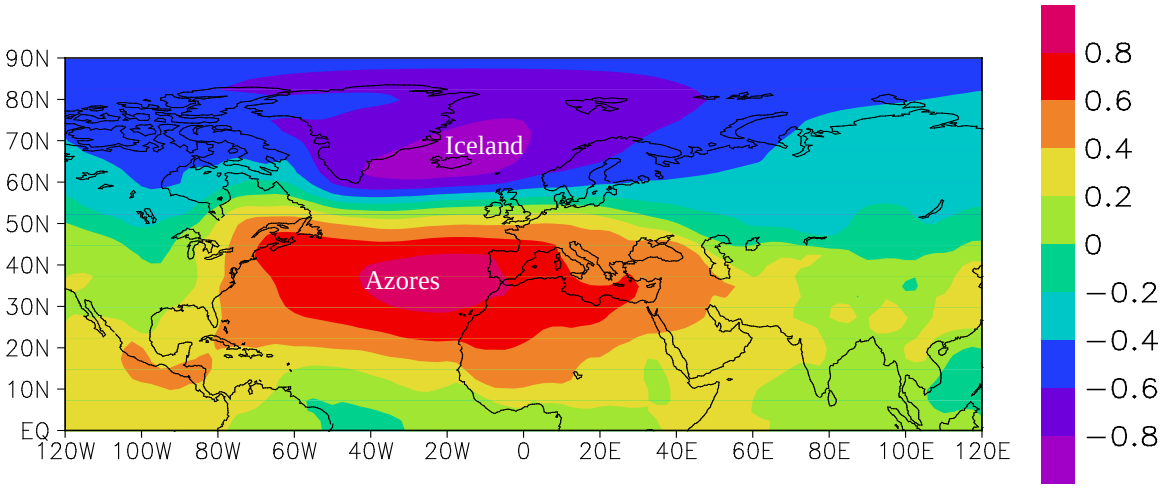

Figure 5.6: Correlation between the winter NAO index and the winter SLP (averaged over December, January, and February). Figure performed on the site http://climexp.knmi.nl/ (Oldenburg et al., 2004) using NCEP-NCAR **reanalysis**. The location of the Azores and Iceland stations, used to define the NAO index, is indicated.

The NAO can be observed in all seasons, but its amplitude is greater in winter when the atmosphere is more dynamically active. When the NAO index is positive in winter, the strong westerly winds transport warm and moist oceanic air towards Europe. This leads to warming and increased precipitation at mid and high latitudes in Europe as well as in large parts of northern Asia, the Greenland Sea and the Barents Sea (Fig. 5.7). In the Barents Sea, the warming is associated with a decrease in the sea ice extent.

By contrast, the anomalous circulation when the NAO index is high brings cold air to the Labrador Sea inducing cooling (Fig. 5.7) and an increase in the sea ice extent there. Further southward, the stronger flow around the subtropical high leads to a drop in temperature over Turkey and North Africa and a rise in the eastern US.

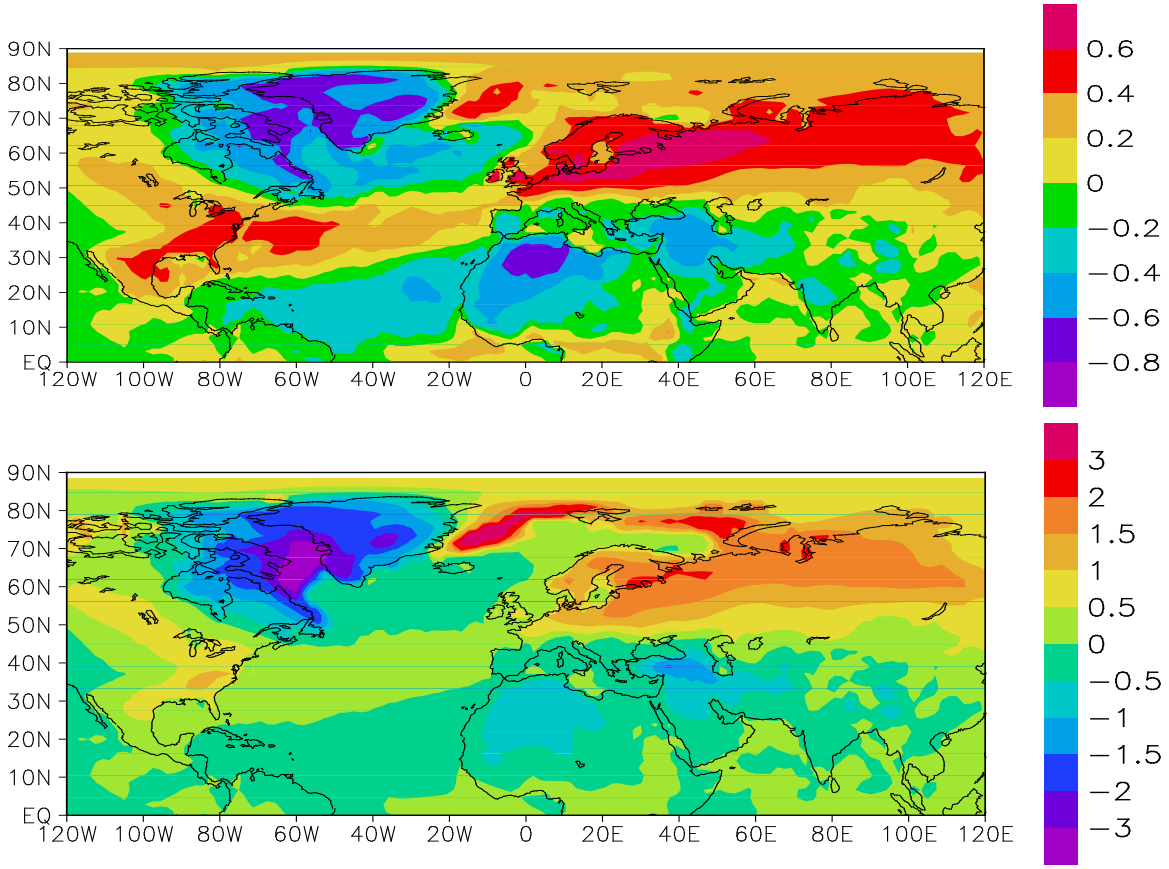

Figure 5.7: Correlation (top) and regression in °C (bottom) between the winter NAO index and the winter surface air temperature (averaged over December, January, and February). Figure performed on the site http://climexp.knmi.nl/ (Oldenburg et al., 2004) using NCEP-NCAR **reanalysis**.

A tripole is associated with positive NAO index over the Atlantic Ocean: the temperature anomaly is positive around 30°-40°N while it is negative north and south of this latitude band (Fig. 5.7). The dominant cause of this pattern appears to be the air-sea interactions. Indeed, the SSTs tend to be lower in areas where the wind speed is higher, leading to higher evaporation rates and heat losses from the ocean to the atmosphere.

In contrast to the ENSO, which is a coupled ocean-atmosphere mode, the NAO appears to be mainly an intrinsic mode of variability of the atmosphere. It has been found in many types of atmospheric models, whether or not they are coupled to an oceanic layer. The mechanisms governing its existence are related to interactions between the mean and the transient circulation (in particular transient cyclones and anticyclones). However, its amplitude can also be influenced, for instance, by changes in sea surface temperature and by the external forcing (see section 5.5).

Although interesting in its own right, the NAO is sometimes considered as a regional manifestation of a larger scale oscillation of the pressure between subtropical areas and high latitudes. As this nearly-hemispherical mode shows a high degree of **zonal** symmetry, it is referred to as the Northern Annular Mode (NAM, but is also called sometimes the Arctic Oscillation). Like the NAO (with which it is highly correlated), the NAM is associated with changes in the intensity of the westerlies at mid-latitudes.

5.2.3 The Southern Annular Mode

The equivalent of the NAM in the Southern Hemisphere is the Southern Annular mode (SAM). Various definitions of SAM have been proposed: a convenient one is the normalised difference in the **zonal** mean sea-level pressure between 40°S and 65°S. As expected, the sea level pressure pattern associated with SAM is a nearly annular pattern with a large low pressure anomaly centred on the South Pole and a ring of high pressure anomalies at mid-latitudes (Fig. 5.8). By **geostrophy**, this leads to an important zonal wind anomaly in a broad band around 55°S with stronger westerlies when SAM index is high.

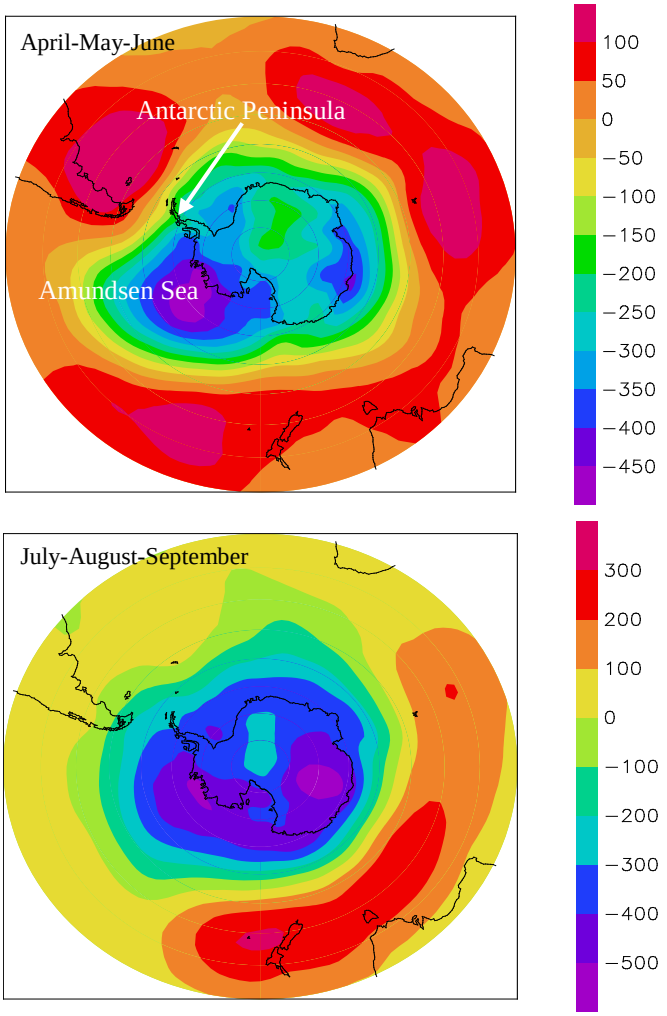

Figure 5.8: Regression between the atmospheric surface pressure and the SAM index for the period 1980-1999 in Pa for (top) the averages in April, May, and June and (bottom) July, August, and September. Data from NCEP-NCAR **reanalyses** (Kalnay et al. 1996).

Due to the southward shift of the **storm track**, a high SAM index is associated with anomalously dry conditions over southern South America, New Zealand and Tasmania and wet conditions over much of Australia and South Africa. The stronger westerlies above the Southern Ocean also increase the insulation of Antarctica. As a result, there is less heat exchange between the tropics and the poles, leading to a cooling of the Antarctica and the surrounding seas. However, the Antarctic Peninsula warms due to a western wind anomaly bringing maritime air onto the Peninsula (Fig. 5.9). Indeed, the ocean surrounding the Antarctic Peninsula is in general warmer than the Peninsula itself and stronger westerly winds mean more heat transport onto the Peninsula. Over the

ocean, the stronger westerly winds tend to generate stronger eastward currents. Furthermore, the divergence of the currents at the ocean surface around 60°S is enhanced because of a larger wind-induced **Ekman transport**. This results in a stronger oceanic **upwelling** there.

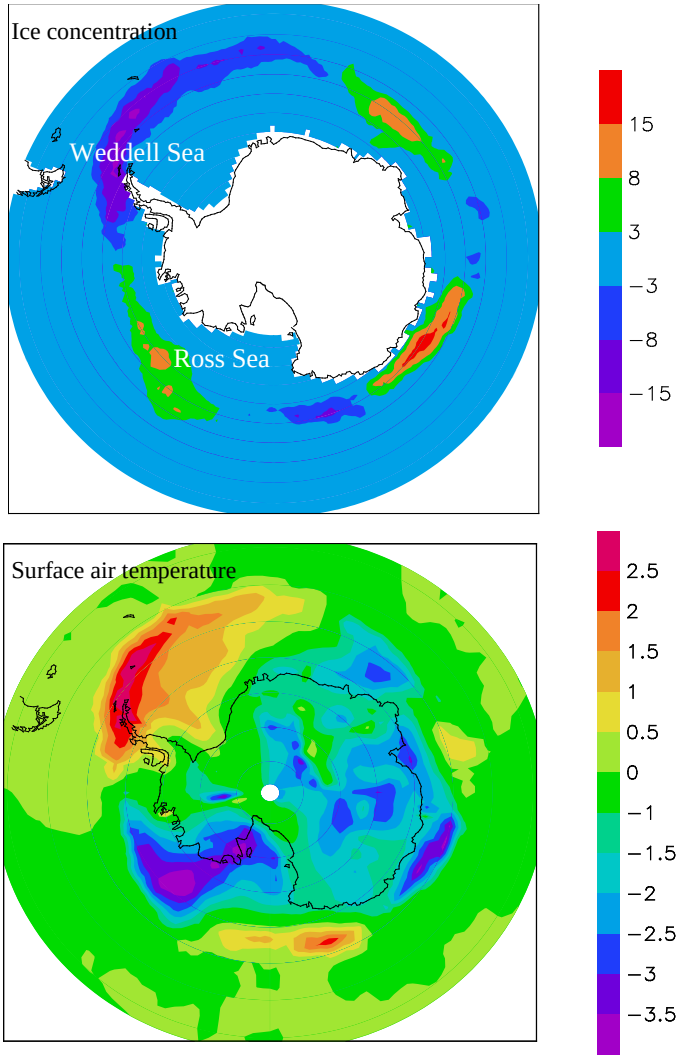

Figure 5.9: Regression between (top) the sea ice concentration in % (data from Rayner et al. 2003) and (bottom) the surface air temperature in °C (Kalnay et al. 1996) and the SAM index averaged over July, August, and September for the period 1980-1999.

The majority of the effects of SAM could be explained by its annular form and the related changes in **zonal** winds. However, the departures from this annular pattern have large consequences for sea ice as they are associated with meriodional exchanges and thus large heat transport. In particular, a low pressure **anomaly** is generally found in the Amundsen Sea during high SAM-index years (Fig. 5.8). This induces southerly wind **anomalies** in the Ross Sea (Pacific sector of the Southern Ocean) and thus lower temperatures and a larger sea ice extent there (Fig. 5.9). On the other hand, because of the stronger northerly winds, the area around the Antarctic Peninsula is warmer when the ice index is high,and the ice concentration is lower there.

5.3 The Climate since the Earth's formation

5.3.1 Precambrian climate

To study the Earth's climate during the first billion years of its history, we have to rely on indirect estimates. For instance, the presence of glacial sediments during a particular period indicates glaciation, at least on a regional scale. Specific conditions are required for the formation of various rock types, providing additional indications of past climate changes. However, the uncertainties are very large and the climate reconstructions, which are at best qualitative, are regularly modified as new information becomes available.

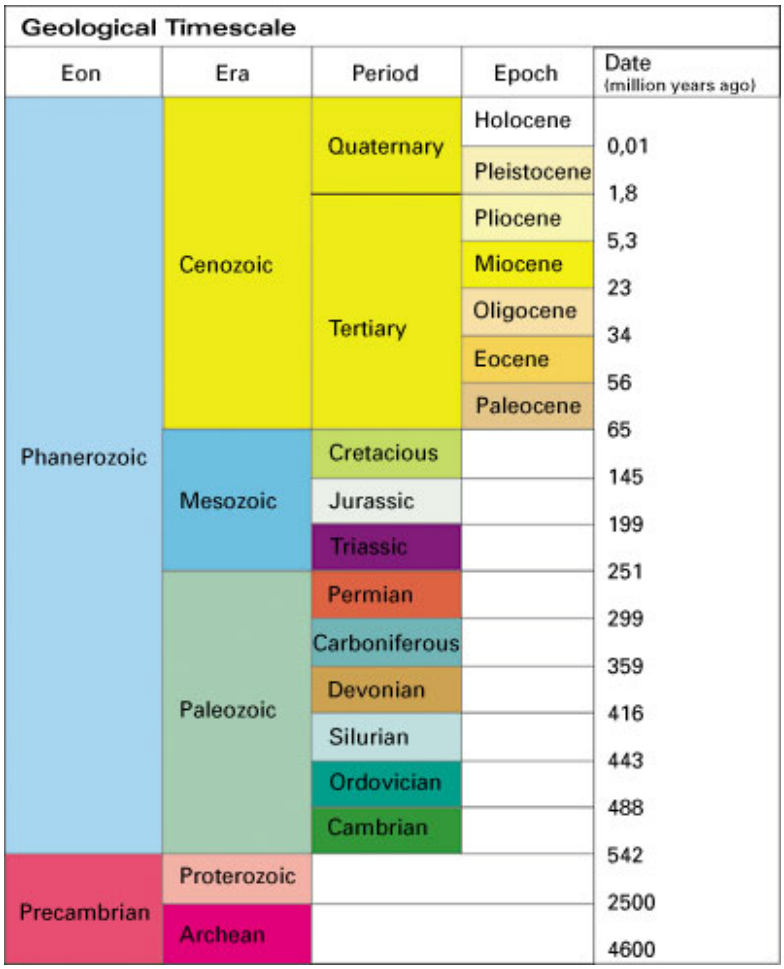

Figure 5.10: A simplified geological time scale. Be careful to the highly non-linear time scale. *Source*: http://www.naturalsciences.be/active/expeditions/archive2004/china/timescale. For a more detailed chart, see the site of the International Commission on Stratigraphy: http://www.stratigraphy.org/

The evidence for the climate of the early Earth is particularly scarce. When Earth was formed about 4.6 billion years ago, the solar irradiance was about 30% lower than at present. If the conditions (**albedo**, composition of the atmosphere, distance between the Earth and the Sun, etc) then had been the same as they are now, a simple calculation using the models described in section 2.1.2 leads to an averaged surface temperature 30°C below than today's. During the first 700-800 million years, of Earth's existence, the

continual bombardment by small planetesimals and meteorites would certainly have warmed the climate. Nevertheless, in such conditions, the Earth would have been frozen during a large part of its history. This contrasts with geological evidence for a liquid ocean at least 4 billion years ago. The apparent discrepancy is called the “faint early Sun paradox”.

The main cause of this paradox is thought to be that there was a much stronger greenhouse effect during the early lifetime of the Earth. The atmosphere was very different from today, with a much higher CO_2 concentration (probably reaching more than 10%, i.e. more than 100 times the present-day value) and nearly no oxygen. In the absence of oxygen, the methane was not quickly oxidised, as in the present atmosphere (see Eq. 2.37), and its concentration was much higher than today. It has been hypothesised that it was the dominant greenhouse gas at this time.

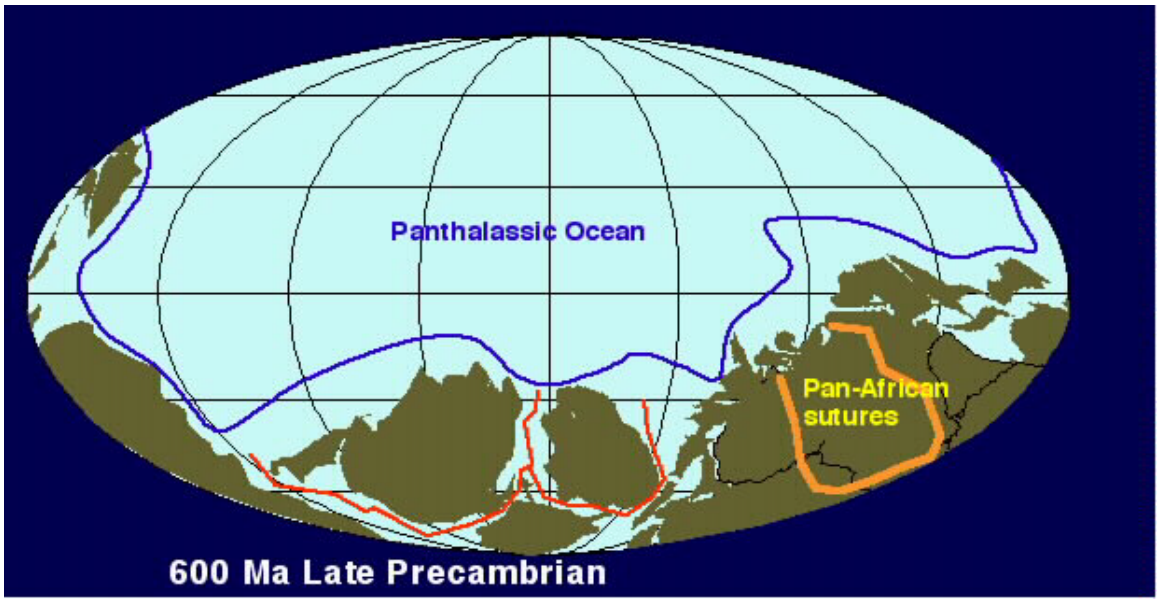

Figure 5.11: Land configuration about 600 million years ago. *Source*: http://jan.ucc.nau.edu/~rcb7/global_history.html. Reproduced with permission.

With time, the atmospheric composition has been modified, in particular because of the oxygen liberated by photosynthesis. This oxygen was first used to oxidise the minerals exposed to the atmosphere. Subsequently, it accumulated in the atmosphere, leading to a large increase in the atmospheric oxygen concentration 2.2. to 2.4 billion years ago as well as to the formation of an **ozone** layer in the stratosphere. Because of these higher oxygen concentrations, the oxidation of methane became more efficient and its concentration decreased markedly. As the rise in the amount of oxygen was concurrent with a glaciation, it has been suggested that the reduced methane concentration was responsible for the cooling. However, the evidence to confirm this hypothesis is still lacking.

Several large climate fluctuations occurred during the Precambrian eon (Fig. 5.10). One of the best documented is a glaciation that takes place around 600 to 750 million years ago. It was apparently so severe that the whole Earth might have been totally covered by ice during some of this glacial period. At that time, all the continents were grouped close to the South Pole (Fig. 5.11). This maybe have initiated a cooling of the continents, probably during a time when the orbital configuration favoured the growth of ice sheets (see section 5.4). After this initial cooling, the ice-albedo feedback (see section

4.2.3) was strong enough to generate an additional temperature decrease leading to a progression of ice towards the Equator and eventually covering the whole Earth.

This "snowball" hypothesis is still debated because it has been argued that such a configuration would be a stable equilibrium state of the climate system, and thus the Earth would have remained permanently frozen. However, it has also been postulated that during the snowball phase, volcanoes would have continued to outgas CO_2 into the atmosphere. As the Earth was covered by ice, no **weathering** of rocks would have compensated the CO_2 input and the atmospheric CO_2 concentration would have increased greatly. Furthermore, ash and dust might have modified the **albedo** of the ice in this very dry environment with very little precipitation. This may have eventually led to a melting of the ice in the tropics and a deglaciation of the Earth thanks to the ice-albedo feedback. Finally, as the CO_2 concentration was still high after this deglaciation, the adjustment of the carbon cycle to such perturbations being very slow, the snowball Earth may have been followed by very warm conditions.

5.3.2 Phanerozoic climate

On timescales of millions of years, the carbon cycle is mainly controlled by the exchanges between rocks and surface reservoirs (ocean, atmosphere, biosphere, see section 2.3.4). As this long-term carbon cycle determines the concentration of atmospheric carbon dioxide ($[CO_2]$), its change over time can be represented in a very simplified way by:

$$\frac{\partial [CO_2]}{\partial t} = Volc(t) - \left(Weath(t) + Org(t)\right) \tag{5.3}$$

The first term of the right-hand side of this equation (*Volc*) describes the outgassing of CO_2 associated with **metamorphism** during **subduction** and volcanic eruptions. The second term (*weath*) measures the combined influence of silicate **weathering** and calcium carbonate sedimentation in the ocean, which removes carbon from the atmosphere and the ocean. The last term (*Org*) is associated with long-term burial of organic matter. The imbalance between these three terms has been responsible for changes in the atmospheric CO_2 concentration and the climate for billions of years. Unfortunately, information about the various processes is not precise enough to estimate their magnitude in the Precambrian eon, but the situation is better for the Phanerozoic eon (the last 542 million years).

First, when tectonic activity is intense, high production rates of oceanic crust at the mid-ocean ridges results in more buoyant oceanic plates that push sea water upward. This results in flooding of the low-lying parts of the continents. As such high tectonic activity is related to large **subduction** rates and more frequent/stronger volcanic eruptions, it has been suggested that reconstructions of sea levels can be used to derive the time evolution of the outgassing of CO_2.

Second, the burial of organic matter can be estimated from the **isotopic** composition of the carbon in sea water. During photosynthesis, ^{12}C is taken preferentially to ^{13}C. This implies that organic matter has a lower content of ^{13}C than the atmosphere or the ocean. The isotopic composition is commonly measured by delta value $\delta^{13}C$ which is the ratio of ^{13}C and ^{12}C isotopes in the sample, compared to a reference standard:

$$\delta^{13}C = \left[\frac{\left({}^{13}C / {}^{12}C \right)_{sample}}{\left({}^{13}C / {}^{12}C \right)_{standard}} - 1 \right].1000 \qquad (5.4)$$

The past values of $\delta^{13}C$ in the ocean, which are related to those in the atmosphere at the same period, are recorded in carbonate sediments and can thus be measured. This provides estimates of the rate of burial of organic matter: a larger organic transfer to sediments is associated with a decrease in the relative amount of ^{12}C and thus to an increase in $\delta^{13}C$. Based on such measurements, it has been possible to determine that burial was particularly high during the transition the Carboniferous to the Permian period, around 300 million years ago, a period characterised by a relatively large production of fossil fuel-source rocks and relatively low atmospheric CO_2 concentration.

From the information presented above and the estimates of weathering rates based on the exposure of different types of rocks, it is then possible to build models of the long term carbon cycle. Those models can be very complex as they have to estimate the influence of various processes. They can also include, in addition to the carbon cycle, the cycles of other elements such as oxygen or sulphur. However, they still have large uncertainties and some of the hypotheses they use are contentious. For instance, Figure 5.12 illustrates the influence of **climate sensitivity** on the simulated CO_2 concentration in one of these models. **Climate sensitivity** affects the stabilizing feedback between the temperature increase due to higher CO_2 concentration and the intensity of weathering that tends to lower the CO_2 concentration (see section 4.3.2). With low climate sensitivity, this feedback is weak, as CO_2 has only a moderate influence on the climate. As a consequence, the variations of CO_2 concentration are large. By contrast, with high climate sensitivities, the feedback is strong enough to restrain the amplitude of the changes in CO_2. For the model presented in Figure 5.12, the best agreement with reconstructions of the atmospheric CO_2 concentration based on various **proxy** records is obtained for values of climate sensitivity around 3°C. This is in the middle of the range provided by global climate models for present-day conditions (see section 4.1.3), suggesting a relative stability of this number over long time scales.

The relatively good agreement between simulated and reconstructed CO_2 concentration gives us some confidence in the proposed interpretation of the dominant factor influencing the long-term carbon cycle. The production rate of oceanic crust by tectonic activity appears to play a particularly important role, since the relatively large divergences that followed the break-up of the super continents around 200 million years ago (super-continent Pangaea) and 550 million years ago (super-continent Pannotia, see Figure 5.11) are associated with significant increases in CO_2 concentration. Furthermore, the periods of low CO_2 concentration generally correspond well with recorded glaciation, for example during the Carboniferous period 300 million years ago. This gives us some confidence in the validity of the simulated and reconstructed CO_2 history, as well as the long term relationship between CO_2 and climate. However, the link between CO_2 and global temperature can not, on its own, explain all the past climate variations, in particular at regional scale. Other factors, such as the location of the continents must also be taken into account, as briefly discussed in section 5.3.1 above. For instance, when all the continents are grouped together, the interior of the continents tends to be very dry, leading to an extension of desert there.

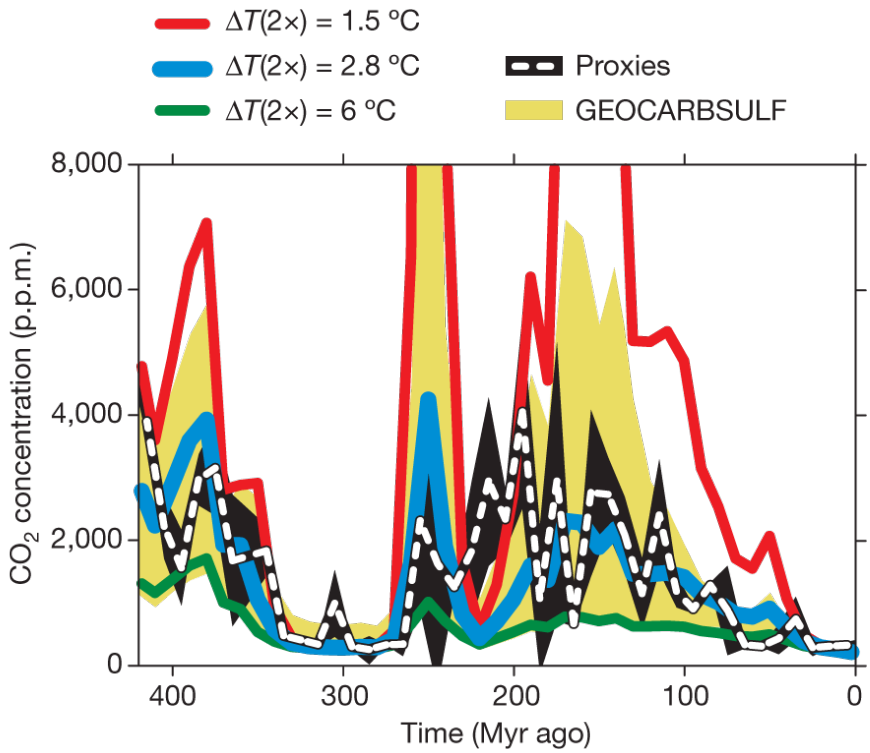

Figure 5.12: Comparison of the CO_2 concentration calculated by GEOCARBSULF model for varying climate sensitivities (noted *ΔT(2x)* on the figure) to an independent CO_2 record based on different **proxies**. All curves are displayed in 10 million years time-steps. The proxy error envelope (black) represents 1 standard deviation of each time-step. The GEOCARBSULF error envelope (yellow) is based on a combined sensitivity analysis of four different factors used in the model. *Figure from* Royer et al. (2007). Reprinted by permission from Macmillan Publishers Ltd: Nature, copyright 2007.

5.3.3 Cenozoic climate

Over the last 65 million years, the CO_2 concentration has gradually decreased from more than 1000 ppmv (part per million in volume) during the Paleocene and the beginning of the Eocene epochs to less than 300 ppmv during the Pleistocene. This long-term decrease is partly due to volcanic emissions, which were particularly large during the Paleocene and Eocene epochs, but which have diminished since then, and to changes in the rate of weathering of silicate rocks. The decline in the CO_2 concentration is associated with a cooling from the warm conditions of the early Eocene climatic optimum between 52 and 50 million years ago (Fig. 5.13). This shift is often referred to as a transition from a greenhouse climate to an icehouse, in which ice sheets are present over Antarctica (starting around 35 million years) and over Greenland (starting around 3 million years ago).

Climate reconstructions for this epoch are often based on the oxygen isotopic composition of the shell of small marine organisms called foraminifera (Fig. 5.13). Temperature influences the $^{18}O/^{16}O$ isotopic fractionation between seawater and the carbonate ions that form the shell. For some species the temperature-fractionation relationship is well known and appears to remain stable with time. So measuring the isotopic composition of the shell remains in sediments provides estimates of past temperatures. This relationship is strictly valid only for ice free conditions since ice sheets are built from water precipitating at high latitudes which is characterised by a very

low ^{18}O relative abundance. The growth of ice sheets is thus associated with a global decrease in the amount of ^{16}O available in the other reservoirs, in particular in the ocean. As a consequence, the signal recorded in the shell of foraminifera becomes related to a mixture of temperature and ice-volume influences. In a similar way as for ^{13}C (Eq. 5.4), the isotopic signal is described using the delta value $\delta^{18}O$ defined as:

$$\delta^{18}O = \left[\frac{\left({}^{18}O / {}^{16}O \right)_{sample}}{\left({}^{18}O / {}^{16}O \right)_{standard}} - 1 \right] .1000 \qquad (5.5)$$

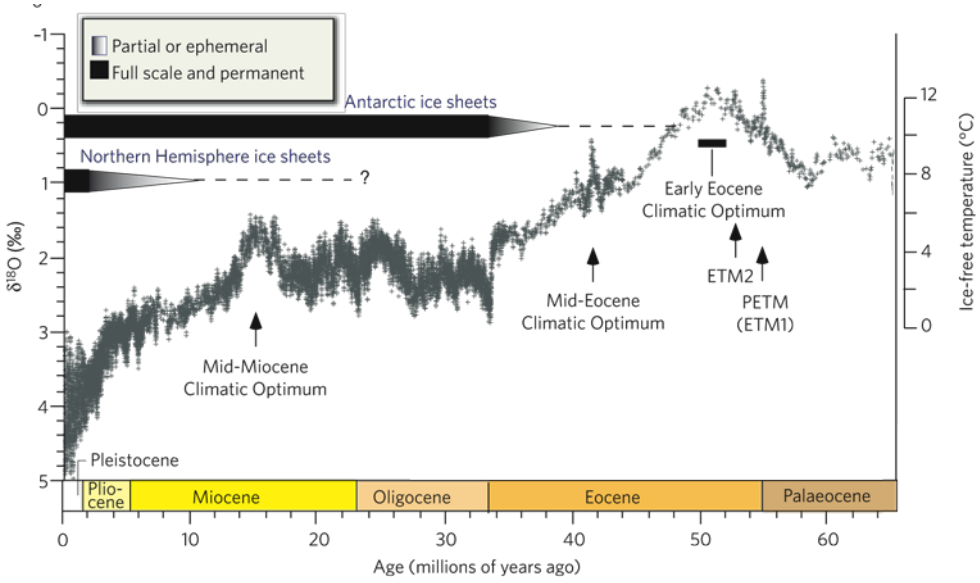

Figure 5.13: The development of the global climate over the past 65 million years based on deep-sea oxygen-isotope measurements in the shell of benthic foraminifera (i.e. foraminifera living at the bottom of the ocean). The $\delta^{18}O$ temperature scale, on the right axis, is only valid for an ice-free ocean. It therefore applies only to the time preceding the onset of large-scale glaciation in Antarctica (about 35 million years ago, see inset in the upper left corner). *Figure from* Zachos et al. (2008). Reprinted by permission from Macmillan Publishers Ltd: Nature, copyright 2008.

60 million years ago, the location of the continents was quite close to that of the present-day one (Fig. 5.14). However, a relatively large seaway was present between North and South America while Antarctica was still connected to South America. The uplift of Panama and the closure of the Central America seaway likely modified the circulation in the Atlantic Ocean, possibly influencing the glaciation over Greenland. More importantly, the opening, deepening and widening of the Drake Passage (between South America and Antarctica) and the Tasmanian Passage (between Australia and Antarctica) allowed the formation of an intense Antarctic Circumpolar Current that isolates Antarctica from the influence of milder mid-latitudes and increased the cooling there. Finally, the uplift of the Himalayas and the Tibetan Plateau strongly modified the monsoon circulation in these regions. Those few examples illustrate the strength of the driving force associated with the changes in boundary conditions due to plate tectonics. This role should not be underestimated.

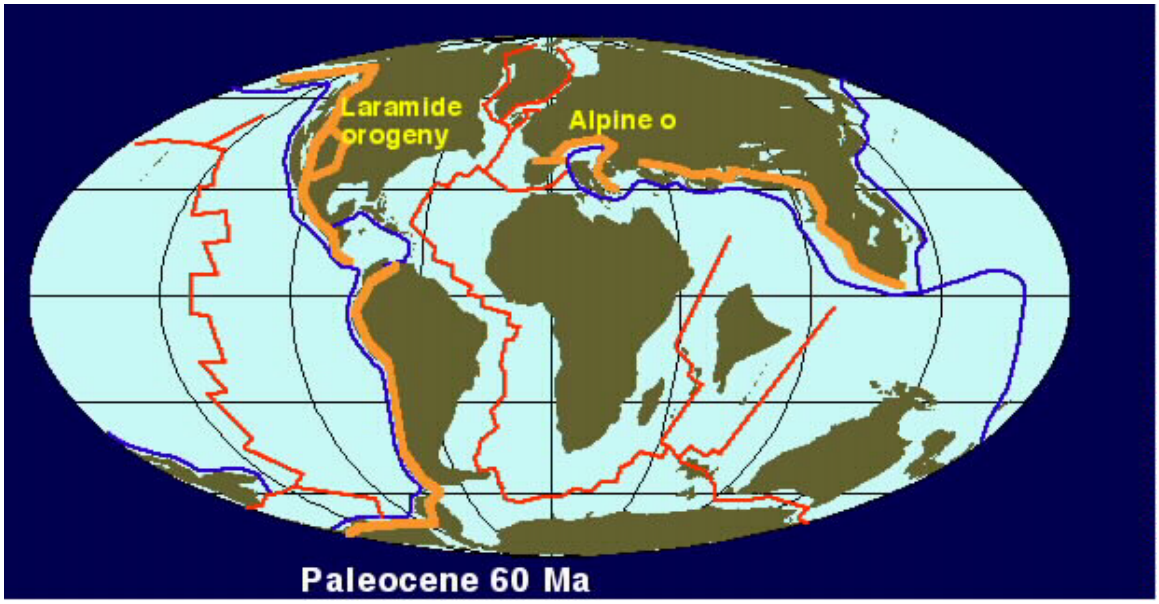

Figure 5.14: Land configuration about 60 million years ago. *Source* http://jan.ucc.nau.edu/~rcb7/global_history.html. Reproduced with permission.

In addition to the low frequency changes described above, relatively brief events are also recorded in the geological archives. One of the most spectacular is the large meteorite impact that occurred 65 million years ago at the boundary between the Cretaceous and Tertiary periods (or K-T boundary). This cataclysm has been hypothesised to have caused the extinction of many plant and animal species, including the dinosaurs, but its climatic impact is not well known and its long-term influence is not clear. The warming during the Paleocene Eocene Thermal Maximum (PETM, 55 million years ago, see Fig. 5.13), which also had a major impact on life on Earth, is better documented. During this event which lasted less than 170 000 years, the global temperature increased by more than 5°C in less than 10 000 years. This period is also characterised by a massive injection of carbon into the atmosphere-ocean system as recorded by variations in the $\delta^{13}C$ measured in sediments. The source of these massive inputs of carbon remains uncertain. It may be related to volcanism, or to the release of the methane stored in the sediments of the continental margins. Alternatively, the methane in these regions may have been destabilised by the initial warming, resulting in a strong positive feedback.

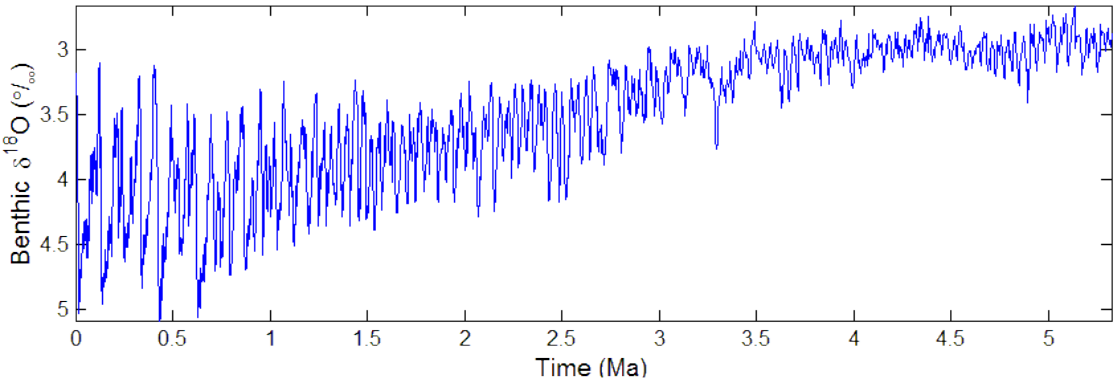

Figure 5.15: Benthic $\delta^{18}O$, which measures global ice volume and deep ocean temperature, over the last 5.3 million years as given by the average of globally distributed records. *Data* from Lisiecki and Raymo (2005). *Source* http://www.lorraine-lisiecki.com/stack.html. Reproduced with permission.

Closer to the present, large climate fluctuations have occurred over the last 5 million years. This is not clear on the scale of Figure 5.13, but a higher resolution plot shows fluctuations with a dominant period of 100 000 years over last million years and 41 000 years before that (Fig. 5.15). Those periodicities are very likely related to variations in the insolation, as discussed below.

5.4 The last million years: glacial interglacial cycles

5.4.1 Variations in orbital parameters and insolation

If we ignore the role of the atmosphere, the **insolation** at a particular time and location at the Earth's surface is a function of the Sun-Earth distance and the cosine of the solar zenith distance (Eq. 2.20). These two variables can be computed from the time of day, the latitude, and the characteristics of the Earth's orbit. In climatology, the Earth's orbit is determined by three **orbital parameters** (Fig. 5.16 and 5.17): the **obliquity** (ε_{obl}) measuring the tilt of the ecliptic compared to the celestial equator (Fig. 2.7), the **eccentricity** (*ecc*) of the Earth's orbit around the sun and the **climatic precession** ($ecc \sin\tilde{\omega}$) which is related to the Earth-Sun distance at the summer solstice. In this definition of the climatic precession, $\tilde{\omega}$ is the true longitude of the **perihelion** measured from the moving vernal equinox ($\tilde{\omega} = \pi + PERH$ on Fig. 2.8).

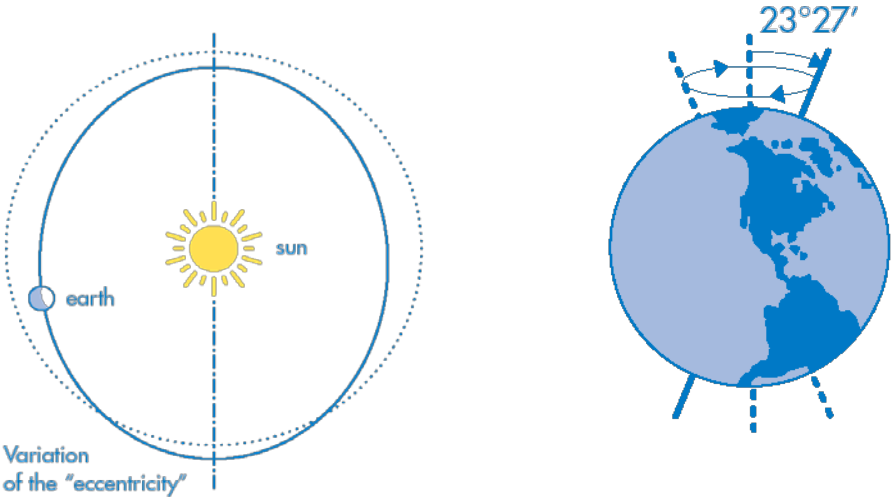

Figure 5.16: Schematic representation of the changes in the eccentricity *ecc* and the obliquity ε_{obl} of the Earth's orbit. *Source*: Latsis foundation (2001).

Because of the influence of the Sun, the other planets in the solar system and the Moon, the orbital parameters vary with time. In particular, the torque applied to the Earth by the Sun and the Moon because our planet is not a perfect sphere (the distance from the surface to the Earth's centre is larger at the Equator than at the poles) is largely responsible for the variations of the obliquity and plays an important role in the changes in $\tilde{\omega}$. The eccentricity is particularly influenced by the largest planets of the solar system (Jupiter and Saturn), which also have an impact on $\tilde{\omega}$.

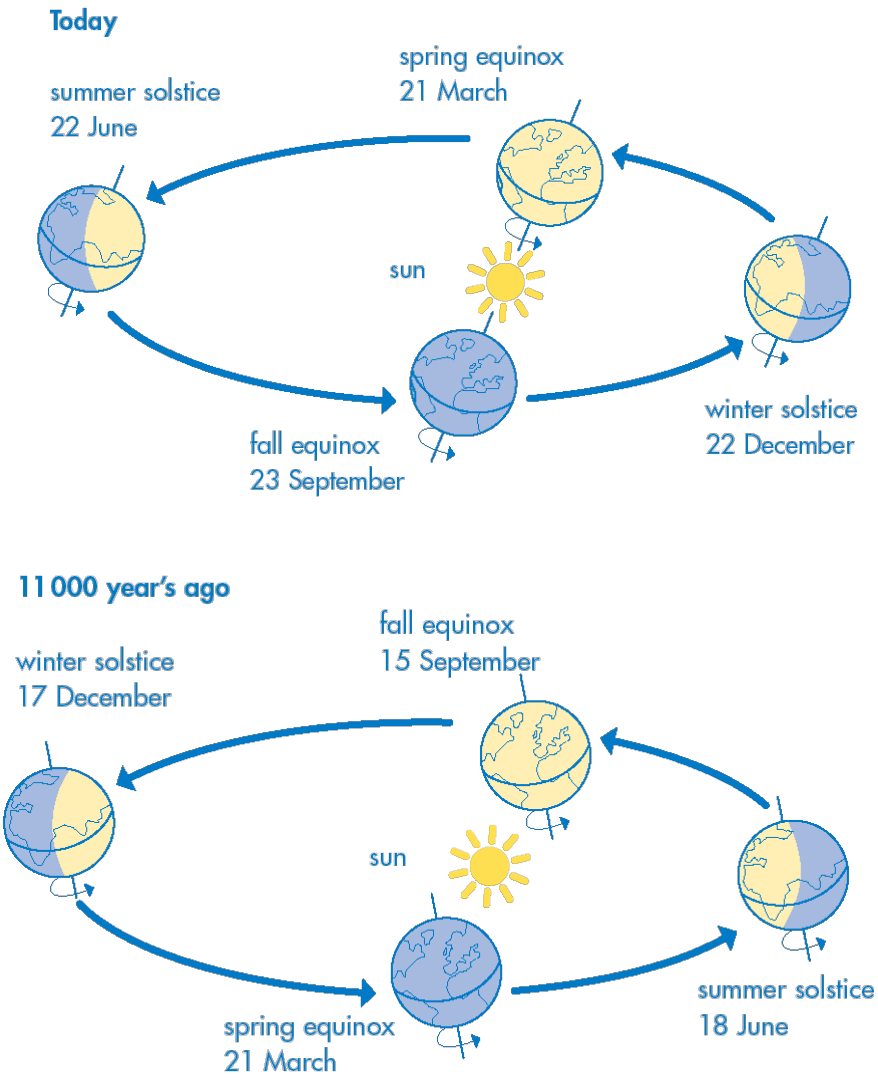

Figure 5.17: Because of the **climatic precession**, the Earth was closest to the Sun during the boreal summer 11 ka ago while it is closest to the Sun during the present boreal winter. *Source*: Latsis foundation (2001)

The way those parameters have developed over time has been calculated from the equations representing the perturbations of the Earth-Sun system due to the presence of other celestial bodies and to the fact that the Earth is not a perfect sphere. The solution can then be expressed as the sum of various terms:

$$\begin{aligned} ecc &= ecc_0 + \sum_i E_i \cos\left(\lambda_i t + \phi_i\right) \\ \varepsilon_{obl} &= \varepsilon_{obl,0} + \sum_i A_i \cos\left(\gamma_i t + \xi_i\right) \\ ecc \sin\tilde{\omega} &= \sum_i P_i \cos\left(\alpha_i t + \eta_i\right) \end{aligned} \tag{5.6}$$

The values of the independent parameters ecc_0, $e_{obl,0}$, of the amplitudes E_i, A_i, P_i, of the frequencies λ_i, γ_i, α_i, and of the phases ϕ_i, ξ_i, η_i are provided in Berger (1978), updated in Berger and Loutre (1991). Equations 5.6 clearly show that the orbital parameters vary

with characteristic periods (Fig. 5.18). The dominant ones for the eccentricity are 413, 95, 123 and 100 ka. For the climatic precession, the dominant periods are 24, 22, and 19 ka and for the obliquity 41 and 54 ka. To completely determine the Earth's orbit, it is also necessary to specify the length of the major axis of the ellipse. However, taking it as a constant is a very good approximation, at least for the last 250 million years.

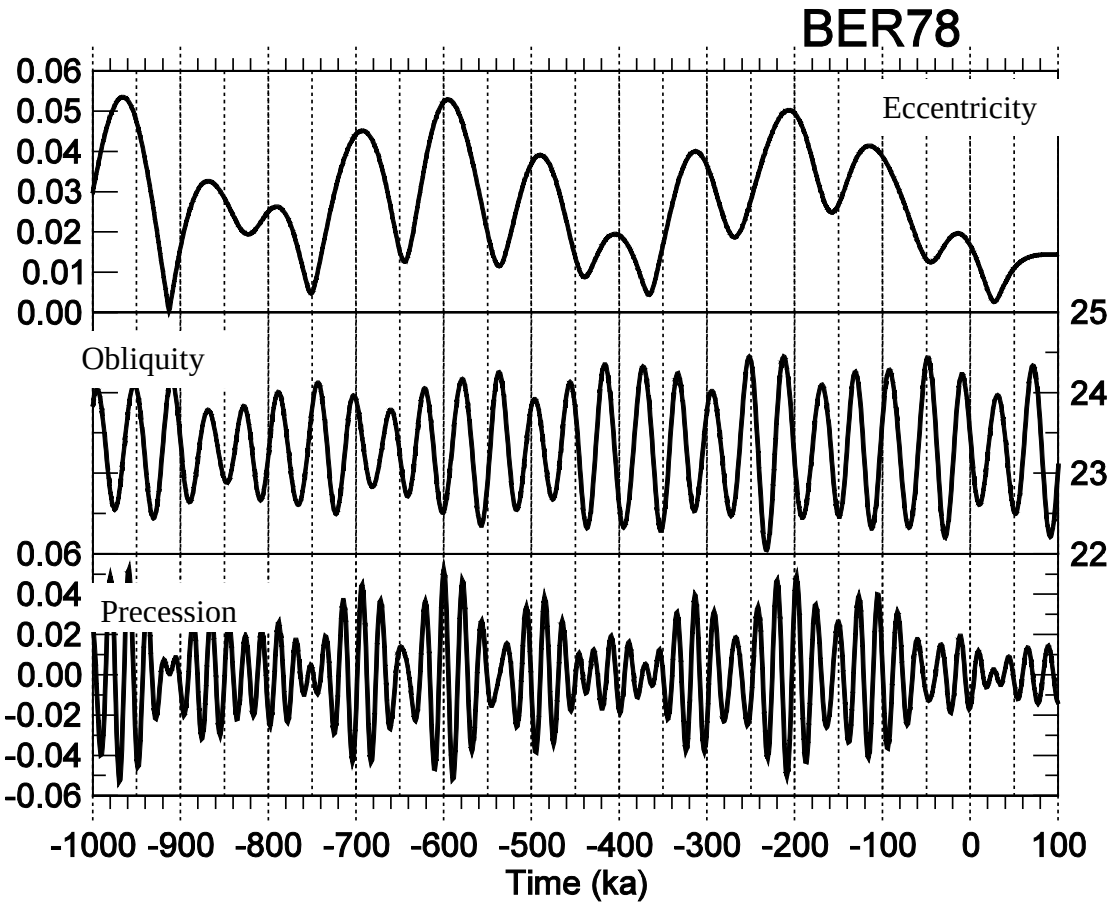

Figure 5.18: Long-term variations in eccentricity, climatic precession and obliquity (in degrees) for the last million years and the next 100 thousand years (zero corresponds to 1950 AD). The minimum value of the climatic precession corresponds to boreal winter (December) solstice at perihelion. computed from Berger (1978).

The eccentricity of the Earth's orbit (Fig.5.16) has varied over the last million years between nearly zero, corresponding nearly to a circular orbit, to 0.054 (Fig. 5.18). Using Eq. 2.24, it can be shown that the annual mean energy received by the Earth is inversely proportional to $\sqrt{\left(1-ecc^2\right)}$. As expected, this value is independent of the obliquity because of the integration over all latitudes, and is independent of $\tilde{\omega}$ because of the integration over a whole year. The annual mean energy received by the Earth is thus at its smallest when the Earth's orbit is circular and increases with the eccentricity. However, as the variations in eccentricity are relatively small (Fig. 5.18), there are only minor differences in the annual mean radiations received by the Earth. The maximum relative variation is 0.15% ($1.5\,10^{-3} = 1-1\Big/\sqrt{\left(1-0.054^2\right)}$), corresponding to about 0.5 W m^{-2} (0.5 = 1.5 10^{-3} x 342 W m^{-2}).

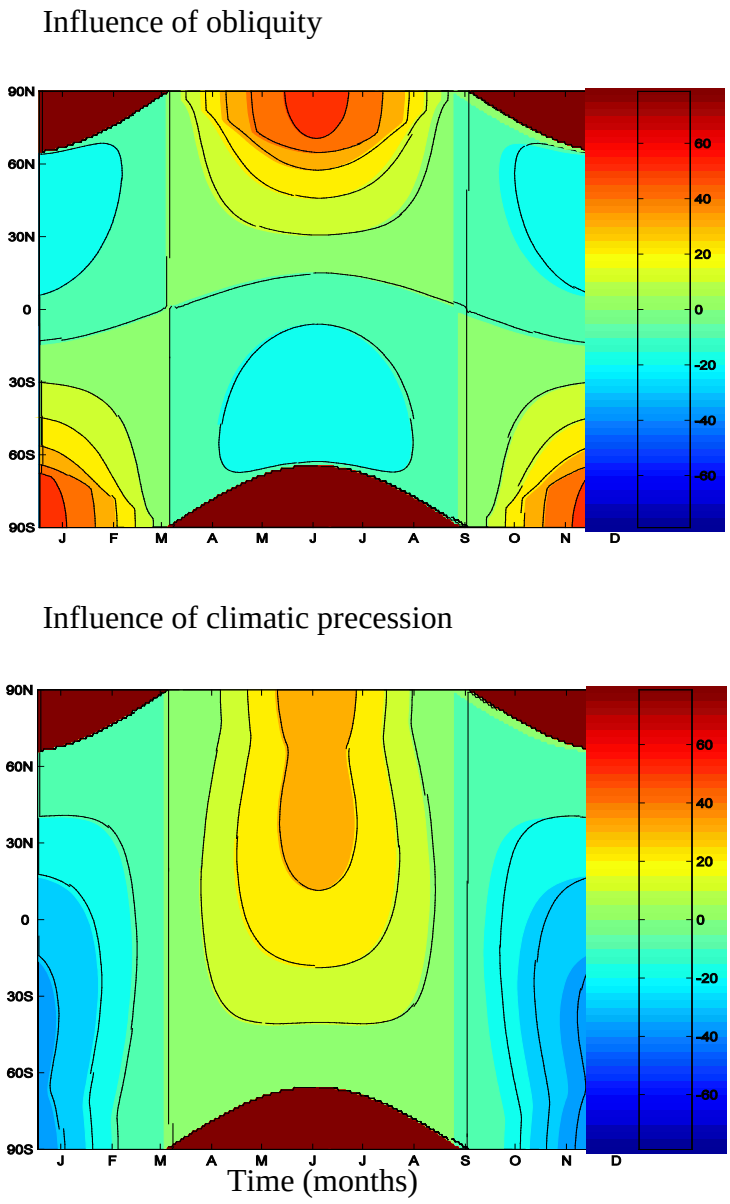

Figure 5.19: Changes in the seasonal contrast of insolation in W m^{-2} caused by (top) following an increase in the obliquity from 22.0° to 24.5° with *ecc*=0.016724, PERH=102.04, i.e. the present-day values, and (bottom) following an increase of the climatic precession from its minimum value (boreal winter at perihelion) to its maximum value (boreal summer at perihelion) with *ecc*=0.016724, ε_{obl}=23,446°, i.e. the present-day values. Contour interval is 10 W m^{-2}. The brown areas correspond to zone with a zero insolation. Time of the year is measured in term of true longitude λ_t. It is assumed that λ_t=-80° corresponds to the 1st of January and one month corresponds to 30° in true longitude.

The obliquity is responsible for the existence of seasons on Earth. If ε_{obl} were equal to zero night and day would be 12 hours long everywhere (Eq. 2.20 and 2.22) and if *ecc* were also equal to zero, each point on Earth would have the same daily mean **insolation** throughout the year (Eq. 2.20 and 2.24). With a large obliquity, the **insolation** is much higher in polar regions in summer, while it is zero in winter during the polar night. Over the last million years, the obliquity has varied from 22° to 24.5° (Fig. 5.18). This

corresponds to maximum changes in daily mean **insolation** at the poles of up to 50 W m^{-2}(Fig. 5.19). Obliquity also has an influence on the annual mean insolation, increasing it by a few W m^{-2} at high latitudes and decreasing it (but to a lesser extent) at the Equator.

Finally, the position of the seasons relative to the perihelion (i.e., the precession) also has an influence on insolation. If Earth is closer to the Sun during the boreal summer and further away during the boreal winter, the summer in the northern hemisphere will be particularly warm and the winter particularly cold. On the other hand, if the Earth is closer to the Sun during boreal winter, the seasonal contrast will be smaller in the northern hemisphere. This effect is particularly marked if the eccentricity is large. If the eccentricity is nearly zero, the distance between the Earth and the Sun is nearly constant, implying no impact of the changes in the position of the seasons relative to the perihelion. The climatic precession varies roughly between -0.05 and 0.05. This produces changes in **insolation** that can be greater than 20 W m^{-2} at all the latitudes (Fig. 5.19). As a consequence, the climatic precession dominates the variations of insolation at low and mid latitudes.

5.4.2 The orbital theory of paleoclimates

The information recorded in ice cores (Fig. 5.20) documents the alternation between long glacial periods (or Ice Ages) and relatively brief **interglacials** over the last 800 ka. We are currently living in the latest of these **interglacials**, the **Holocene.** The glacial period that is the best known is the latest one, which peaked around 21 ka BP, and is referred to as the Last Glacial Maximum (LGM). At that time, the ice sheets covered the majority of the continents at high northern latitudes, with ice sheets as far south as 40°N. Because of the accumulation of water in the form of ice over the continents, the sea level was lower by around 120 m, exposing new land to the surface. For instance, there was a land bridge occurred between America and Asia across the present-day Bering Strait and another between continental Europe and Britain. The **permafrost** and the **tundra** stretched much further south than at present while rain forest was less extensive. Tropical regions were about 2-4°C cooler than now over land and probably over the oceans as well (Fig. 5.21). The cooling was greater at high latitudes and the sea-ice extended much further in these regions. Overall, the global mean temperature is estimated to have been between 4 and 7°C lower than at present.

The orbital theory of paleoclimates assumes that the alternations of glacial and interglacial periods are mainly driven by the changes of the orbital parameters with time. In this context, the summer insolation at high northern latitudes, where the majority of the land masses are presently located, appears to be of critical importance. If it is too low, the summer will be cool and only a fraction of the snow that has fallen over land at high latitudes during winter will melt. As a consequence, snow will accumulate from year to year, after thousands of years large ice sheets (see section 4.2), characteristic of the glacial periods, will form. Conversely, if summer insolation is high, all the snow on land will melt during the relatively warm summer and no ice sheet can form. Furthermore, because of the summer warming, snow melting over existing ice sheet can exceed winter accumulation leading to an ice sheet shrinking and a deglaciation. Through this feedback (and other ones, see Chapter 4), the effect of relatively small changes in **insolation** can be amplified, leading to the large variations observed in the glacial-interglacial cycles.

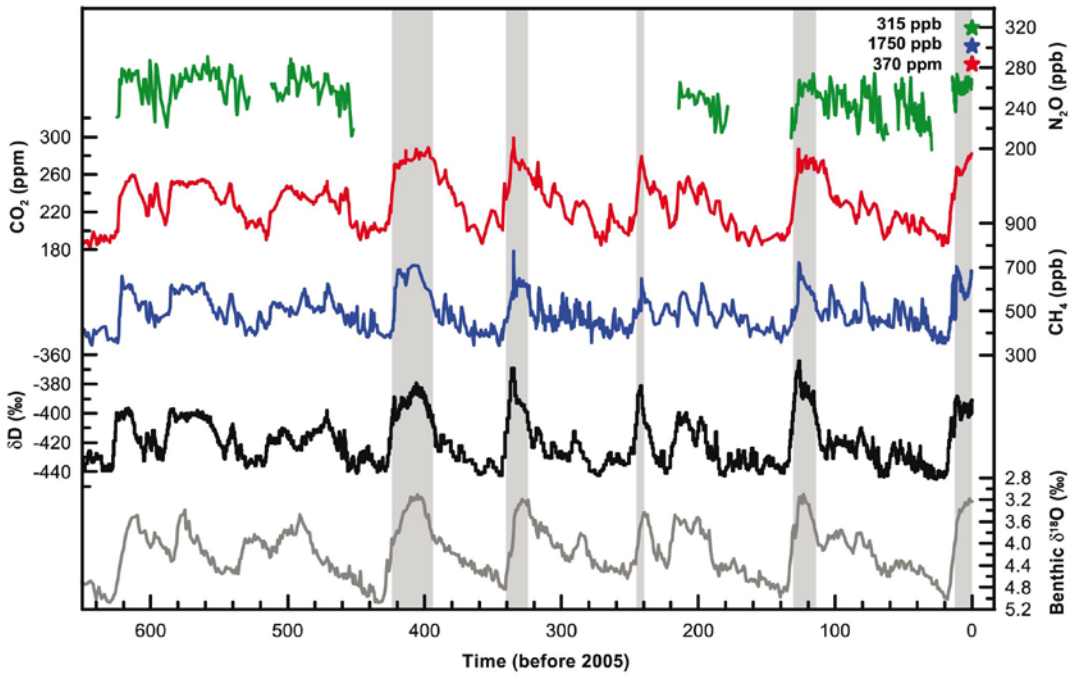

Figure 5.20: Variations in deuterium (δD; black), and in the atmospheric concentrations of the greenhouse gases CO_2 (red), CH_4 (blue), and nitrous oxide (N_2O; green) derived from air trapped within ice cores from Antarctica and from recent atmospheric measurements. The grey curve is a compilation of benthic $\delta^{18}O$ marine records from various sources. Deuterium is a **proxy** for local temperature, (here for the temperature in Antarctica) and benthic $\delta^{18}O$ is a proxy for the global ice volume fluctuations, a high value of benthic $\delta^{18}O$ corresponding to a low ice volume (see section 5.3.3). The stars and labels indicate the atmospheric concentrations in the year 2000. The shading indicates the last interglacial warm periods. *Source*: Figure 6.3 form Jansen et al. (2007). using a modified legend, published in: Climate Change 2007: The Physical Science Basis. Contribution of Working Group I to the Fourth Assessment Report of the Intergovernmental Panel on Climate Change, Cambridge University Press, copyright IPCC 2007. Reproduced with permission.

One of the most convincing arguments for the orbital theory of paleoclimate comes from the fact that the dominant frequencies of the orbital parameters are also found in many proxy records of past climate change (e.g. Fig. 5.20). This suggests a strong causal link. Another important argument comes from paleoclimate modelling. A climate model driven by changes in orbital parameters and by the observed evolution of greenhouse gases over the last 600 ka reproduced quite well the estimated past ice volume variations. If the changes in orbital parameters were not taken into account, it was not possible to simulate adequately the pace of glacial-interglacial cycles (Fig. 5.22).

However, the link between climate change and **insolation** is far from being simple and linear. In particular, the correspondence between summer insolation at high latitudes and ice volume is not clear at first sight (e.g. Fig. 5.22). It appears that ice sheets can grow when summer **insolation** is below a particular threshold (see, for instance, the low value around 120 ka BP when the last glaciation started). On the other hand, because of the powerful feedbacks, in particular related to the presence of ice sheets (see Chapter 4), the insolation has to be much stronger to induce a deglaciation. The insolation also changes in different ways at every location and every season, making the picture more complex than that presented by a simple analysis of the summer **insolation** at high latitudes.

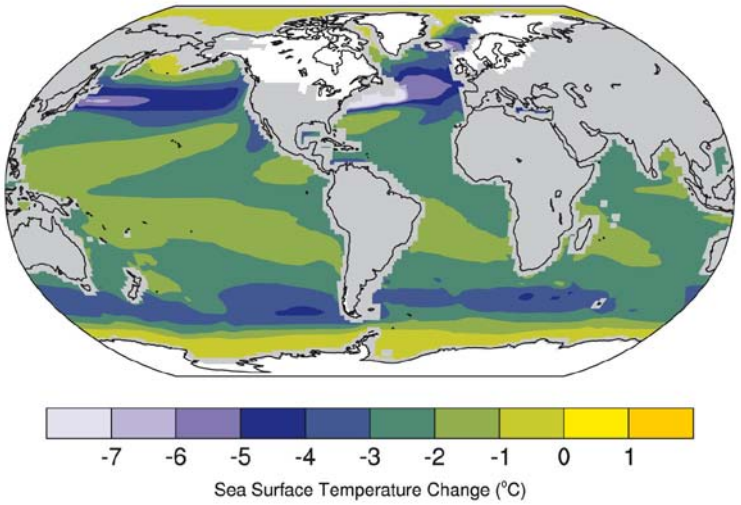

Figure 5.21: Multi-model average change in SST between the Last Glacial Maximum climate (approximately 21 ka ago) and the pre-industrial (1750 AD) climate. Ice extent over continents is shown in white. The selected model results were compiled in the framework of the PMIP2 project (http://pmip2.lsce.ipsl.fr/). Figure 6.5 from Jansen et al. (2007). using a modified legend, published in: Climate Change 2007: The Physical Science Basis. Contribution of Working Group I to the Fourth Assessment Report of the Intergovernmental Panel on Climate Change, Cambridge University Press, copyright IPCC 2007. Reproduced with permission.

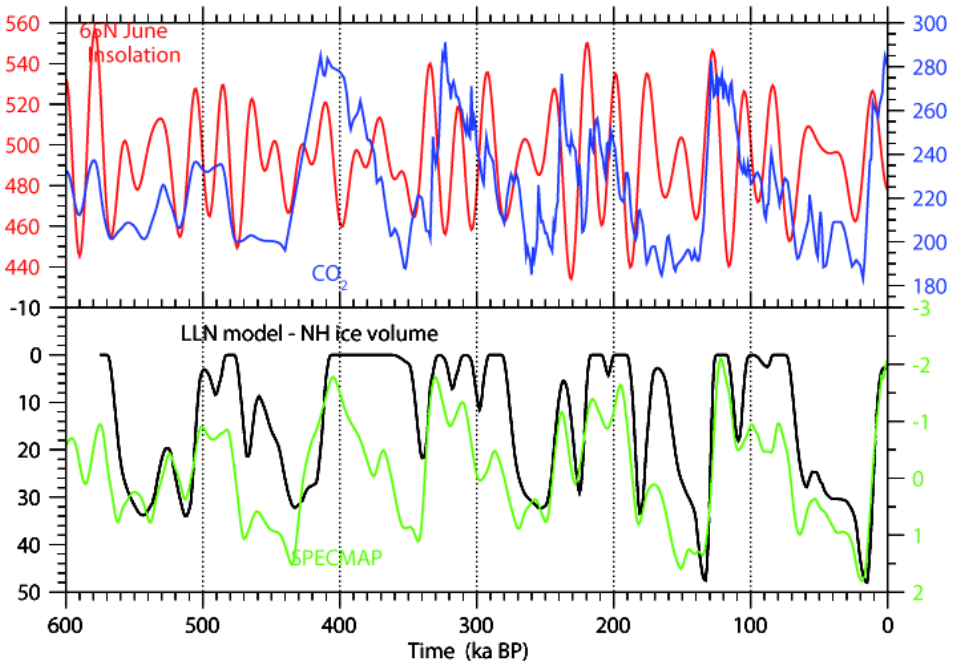

Figure 5.22: (Top panel) The atmospheric CO2 concentration (in ppm, blue) (as measured in the Vostok ice core over the last 414 ka (Petit et al., 1999) plus a statistical scenario for earlier dates) and the mid-month insolation value at 65°N at the June solstice (in Wm^{-2}, red) according to (Berger, 1978). (Bottom panel) The Northern Hemisphere ice volume (in 10^6 km^3) simulated by the LLN 2-D climate model (Berger and Loutre, 2003) forced by insolation (Berger, 1978) and atmospheric CO_2 concentration (as in top panel) and SPECMAP curve (stacked, smoothed oxygen-isotope record in deep sea cores, Imbrie et al., 1984)

One of the most intriguing points is the predominance of strong glacial-interglacial cycles with a period of around 100 ka while this period is nearly absent from the insolation curves. The eccentricity does exhibit some dominant periods around 100 ka but it is associated with very small changes in **insolation**. Furthermore, until 1 million years ago, the ice volume mainly varied with a period of 40 ka, corresponding to the dominant period of the **obliquity** (Fig. 5.15). The importance of the 100 ka cycle over the last million years is probably related to some non-linear processes in the system. However, explaining the mechanisms involved in detail and in a convincing way is still a challenge.

5.4.3 Glacial-interglacial variations in the atmospheric CO_2 concentration

The greenhouse gas concentrations have varied nearly synchronously with temperature and ice volume over the last 600 ka at least (Fig. 5.20) with the difference between interglacial and glacial periods reaching about 80 ppm for carbon dioxide and 300 ppb for methane. This corresponds to a radiative forcing of nearly 3 W m^{-2} and thus to a strong amplifying mechanism for the cooling during glacial periods. However, as mentioned in the latest IPCC report, “the qualitative and mechanistic explanation of these CO_2 variations remains one of the major unsolved question in climate research” (Jansen et al. 2007).

The land biosphere cannot be responsible for this decrease in the CO_2 concentration during glacial periods. Because of the advance of ice sheets, the land area available for vegetation growth declines significantly. Furthermore, the lower temperatures induce less evaporation over the oceans and less precipitation over land. The fraction of dry areas and desert, which only store a small amount of carbon compared to, for instance, forest is thus larger. All these factors lead to a decrease in the carbon storage over land which was not compensated for by the growth of terrestrial vegetation on the new land area associated with the lower sea level. As a consequence, changes in the land biosphere during glacial periods tend to increase the atmospheric CO_2 concentration by an amount which is estimated to be around 20 ppm.

The cause of the decline must thus lie in the ocean, the geological processes being too slow to account for the observed changes. Because of the accumulation of freshwater with nearly zero **dissolved organic carbon** and **alkalinity** in the ice sheets, the salinity, *DIC* and *Alk* of the ocean increases. This leads to an increase of pCO_2 in the ocean. However, it can be shown that this is outweighed by the greater solubility of CO_2 in the ocean due to cooling. The net effect is a small decrease in the atmospheric concentration of CO_2, but it is insufficient to explain all the 80 ppm decrease between interglacial and glacial periods.

This decrease must therefore be related to changes in the ocean circulation and/or the **soft tissue** and **carbonate pumps**. All these factors have a large influence on the distribution of *DIC* and *Alk* in the ocean and thus on the ocean-atmosphere CO_2 exchanges. Most hypotheses emphasises the role of the Southern Ocean. A strong argument in favour of this is the very similar evolution of atmospheric CO_2 concentration and Antarctic temperatures (Fig. 5.20). At present, there is a strong **upwelling** of deep water, rich in nutrients and *DIC*, in that area. Biological activity is insufficient to fix the excess carbon and some of the carbon coming from the deep ocean is transferred to the atmosphere. If in glacial periods, this upwelling (and more generally the connection between surface and deep water) or the biological production changed, this would have a considerable influence on the concentration of atmospheric CO_2.

The upwelling might have been reduced at the LGM by of a northward shift of the westerlies in the Southern Ocean, and thus by the divergence associated with the wind-

induced **Ekman transport**, but this still needs to be confirmed. The weaker hydrological cycle during cold periods, and the associated increase in the Earth's surface covered by dry areas had probably lead to a greater dust transport towards the Southern Ocean. This had brought a large amount of iron to the Southern Ocean. As a consequence, biological production might have been higher during glacial times as this micro-nutriment strongly limits the primary production for the present-day condition in the area. Both of these effects could thus have played a role in the observed atmospheric CO_2 concentration decrease.

It has also been suggested that the supply of iron to the Southern Ocean by dust have induced a large-scale shift in the ecosystem from phytoplankton producing calcium carbonate towards species which do not form $CaCO_3$. This would have decreased the intensity of the **carbonate pump**, so inducing a decrease in the CO_2 concentration.

Many other explanations have been suggested, but it seems that, on its own, none of them can explain the 80 ppm change. It is very likely that some of them play an important role, while others have a negligible influence. However the relative importance of the various explanatory factors is presently unknown.

5.5 The Holocene and the last 1000 years

5.5.1 The current interglacial

In addition to the low frequency variability of glacial-interglacial cycles, more rapid changes have been observed during the past million years. Those that are best documented, in particular in Greenland ice cores (Fig.5.23), are associated with the millennium-scale variability that took place during the last glacial period. These variations are generally attributed to changes in the oceanic circulation and the oceanic heat transport, implying a large-scale shift in the climate. The deglaciation was also characterised by a strong millennium-scale cooling called the Younger Dryas that followed a period of warming that peaked around 14 000 years ago. By contrast, the climate of the latest interglacial appears to be relatively stable. Although some fluctuations are observed, their amplitude over Greenland is much smaller than those seen in glacial periods.

Mainly because of the influence of **precession**, the **insolation** at the top of the atmosphere was very different 10 000 years ago than it is at present (Fig. 5.24). In particular, the summer insolation at the North Pole was up to 50 W m^{-2} higher than now. As a consequence, the summer temperature in the northern hemisphere was relatively high during the Early Holocene and this period is often referred to as the Holocene Thermal Optimum or Holocene Climatic Optimum. However, the timing of the temperature maximum depends strongly on location, as during the Early Holocene ice sheets were still present over parts of Canada, inducing strong local cooling, and changes in oceanic and atmospheric circulation have a strong influence at the regional scale. Nevertheless, if we ignore the last 150 years for which different forcing were in action (see section 5.5.3), the highest summer temperatures of the Holocene are generally found between 9 and 6 kyr BP.

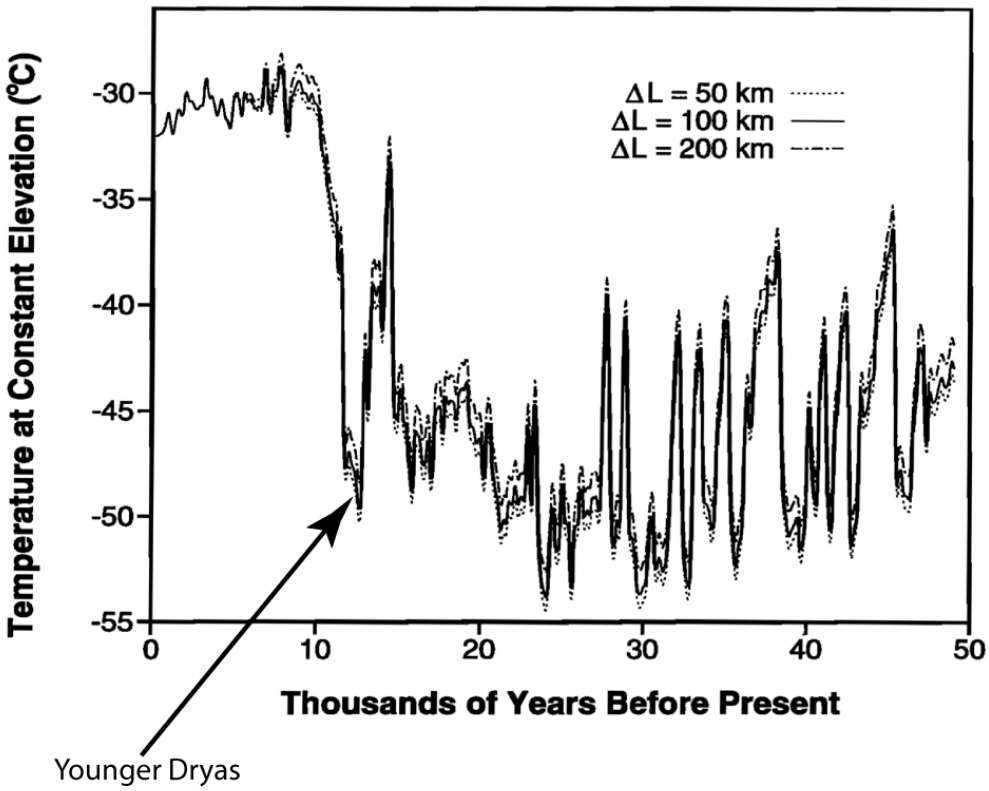

Figure 5.23: Temperature history derived from $\delta^{18}O$ measurements in Greenland (Greenland Ice Sheet Project 2 ice core), using three different corrections for elevation changes. Be careful that time is going from right to left. Figure from Cuffey and Clow (1997).

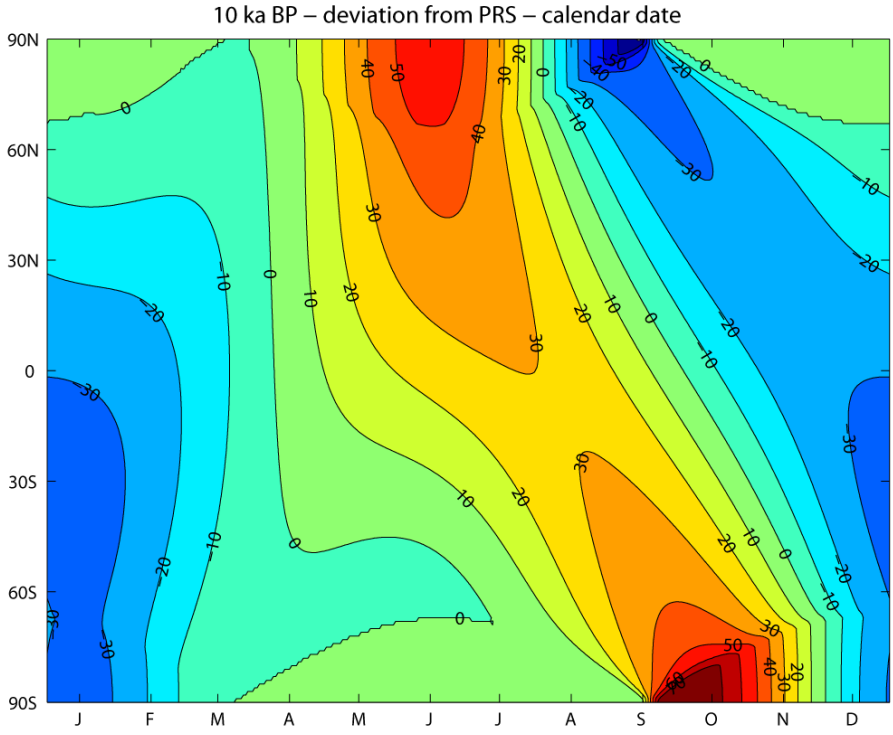

Figure 5.24: Deviations from present-day values of the calendar 24h mean solar irradiance (daily **insolation**) around 10 000 years ago (i.e. at 10ka BP) (in Wm^{-2})

The decrease in Northern Hemisphere **insolation** during the Holocene is associated with a long term summer cooling, which is stronger over land than over the ocean because of the larger seasonal cycle of the temperature over land. As the **monsoons** are strongly influenced by temperature contrasts between land and ocean, this leads to a weakening of the summer **monsoons**. Over North Africa, the weaker monsoon circulation is associated with a marked reduction in precipitation that produced a shift from a Sahara largely covered by savannah and lakes during the Early Holocene to the dry desert state that we know now (Fig. 5.25). The changes in insolation were relatively smooth. However, some studies, mainly those focusing on the Western Sahara, have suggested that the desertification was relatively abrupt, taking place in less than 1000 years about 4000 years ago. This could be due to some **biogeophysical feedbacks** (see Chapter 4) amplifying the initial perturbation caused by radiative forcing. Another hypothesis is that a steep decrease in the vegetation cover can occur if the precipitation crosses a threshold related to the biological characteristics of the plant, leading to a highly non-linear response to changes in precipitation. By contrast, recent observation shows a gradual transition from a "green" to a desert state in the eastern Sahara. Additional work is still needed to understand this important transition in detail.

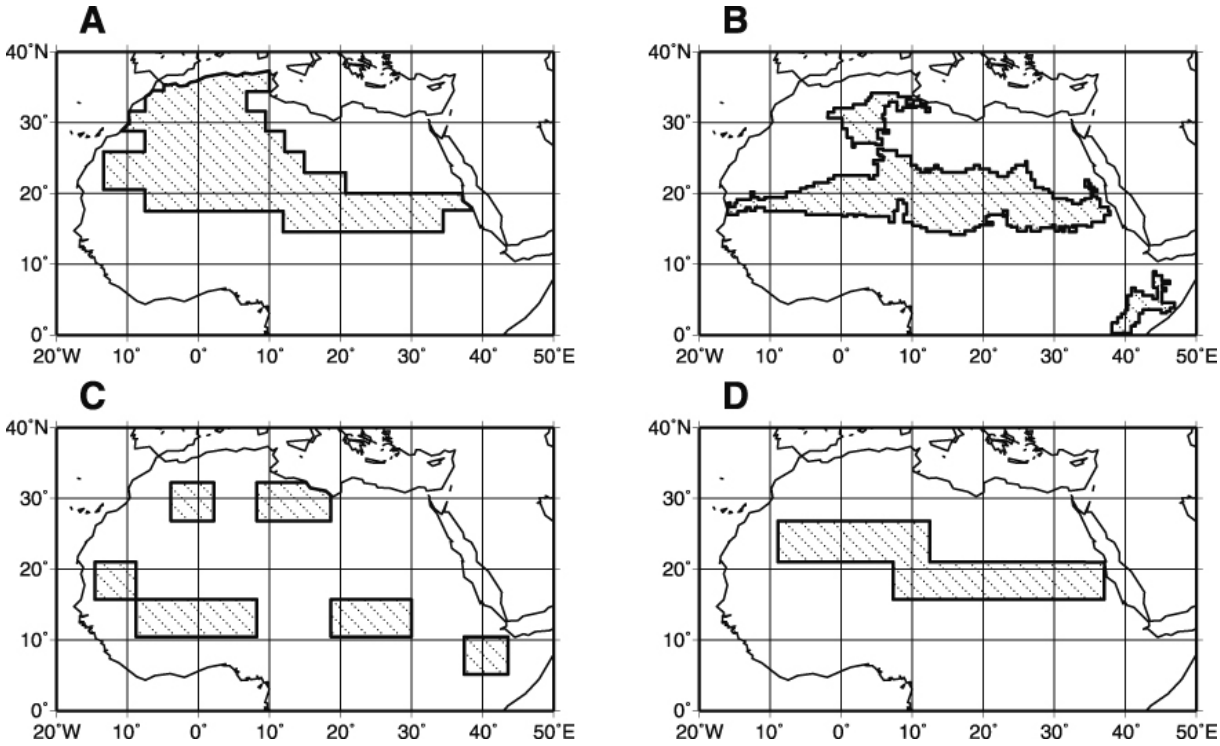

Figure 5.25: Differences in vegetation cover in the Sahara between present-day and mid-Holocene, as simulated by various coupled vegetation-climate models (compiled by Claussen, 2009). The hatched area indicates the region that is presently a desert and that was covered by some vegetation in the mid-Holocene. Copyright Claussen (2009).

5.5.2 The last 1000 years

5.5.2.1 Hemispheric-scale changes

The last millennium is certainly the period in the past for which we have the greatest number of proxy records. Tree rings, lake and marine sediments, ice cores, etc, all provide very useful information on past climate changes. Nevertheless, the uncertainty

over temperature changes is still significant (Fig. 5.26). All the available reconstructions show relatively mild conditions around 1000 AD (the so-called Medieval Warm Period), followed by a cooling that culminated around the 17-19th centuries (the so-called Little Ice Age). However, the amplitude and the exact time of the changes vary strongly between the different reconstructions. However, all the reconstructions have their absolute maximum during the 20th century.

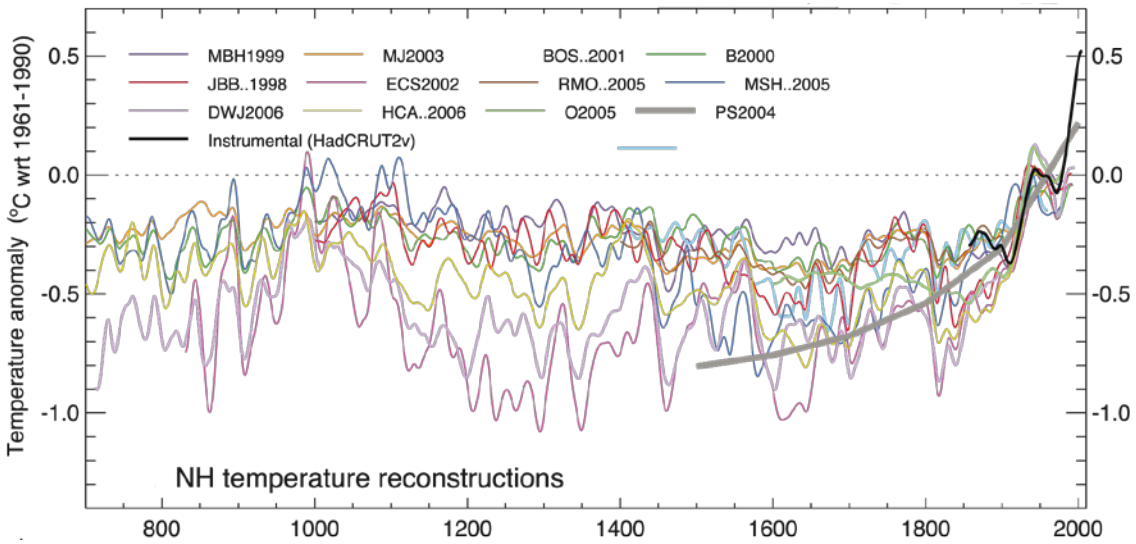

Figure 5.26: Reconstructions of Northern Hemisphere temperature variations over the last 1300 years using multiple climate proxy records and the instrumental record for the last 150 years. All series have been smoothed to remove fluctuations on time scales less than 30 years. All temperatures represent anomalies (°C) from the 1961 to 1990 mean. Figure 6.10 from Jansen et al. (2007), using a modified legend, published in: Climate Change 2007: The Physical Science Basis. Contribution of Working Group I to the Fourth Assessment Report of the Intergovernmental Panel on Climate Change, Cambridge University Press, copyright IPCC 2007. Reproduced with permission. See Jansen et al. (2007) for a full reference to all the reconstructions.

When analysing climate changes over periods of the order of several millennia, orbital forcing is generally dominant. However, for shorter periods, such as the last 1000 years, variations in insolation at the top of the atmosphere due to changes in orbital parameters are relatively weak and other forcings have to be taken into account. On these time scales, the two dominant natural forcings are changes in **total solar irradiance** (TSI) and large volcanic eruptions (see section 4.1.2.4). The majority of volcanic eruptions have a dramatic local impact but only a weak large-scale influence on climate. By contrast, some major eruptions can transport large amounts of aerosols into the stratosphere where they can stay for a few years. These aerosols modify the radiative properties of the atmosphere, decreasing the solar irradiance at the surface and thus lowering the temperature, in particular in summer. In addition, volcanic aerosols have an impact on the atmospheric circulation and tend to favour a positive phase of the North Atlantic Oscillation. As a consequence, a major volcanic eruption is often followed by a warm winter over Europe, a characteristic of a positive NAO index.

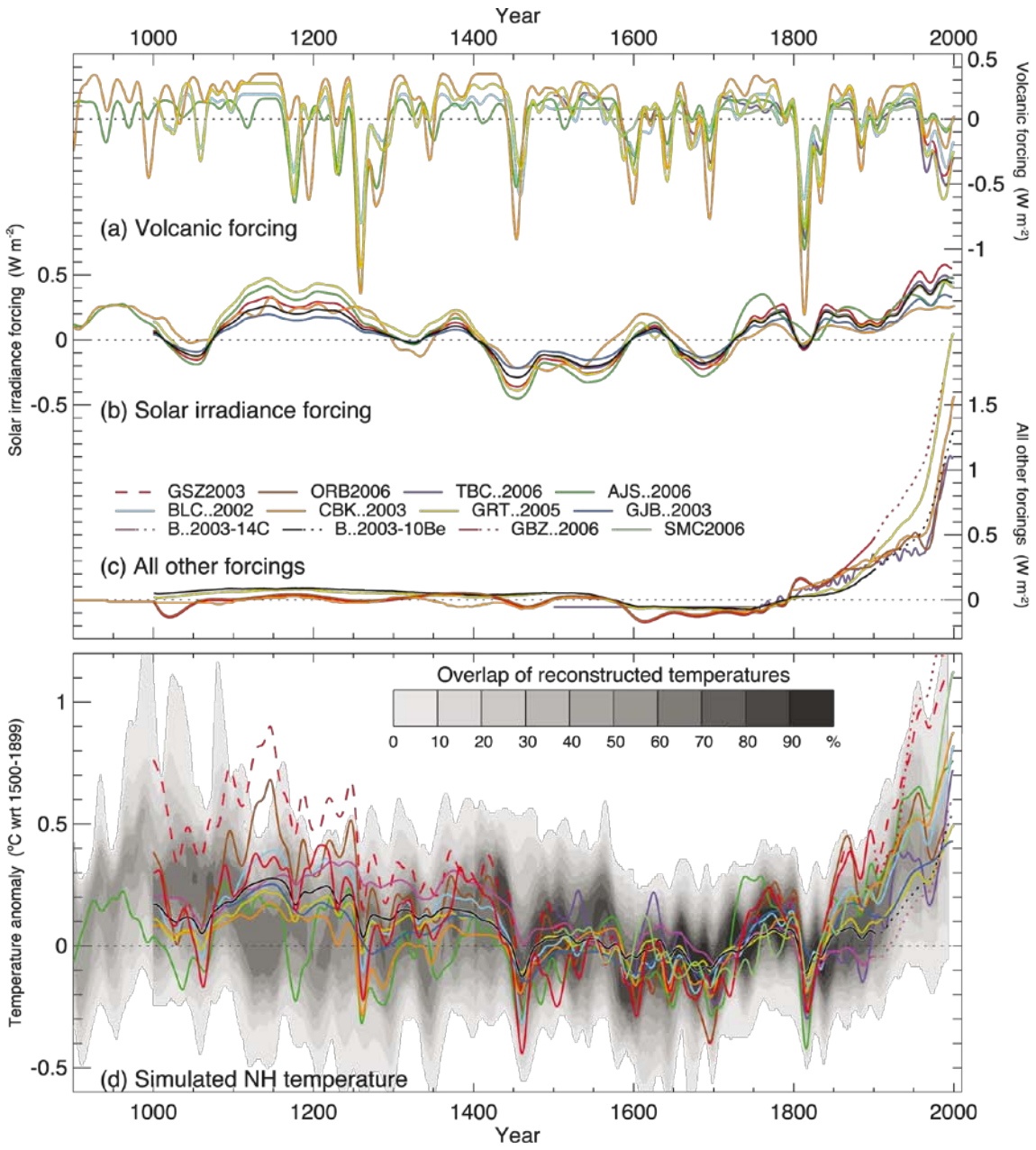

Figure 5.27: Radiative forcings and simulated temperatures during the last 1100 years. The global mean radiative forcing (W m^{-2}) used to drive climate model simulations due to (a) volcanic activity, (b) solar irradiance variations and (c) all other forcings (which vary between models, but always include greenhouse gases, and, except for those with dotted lines after 1900, tropospheric sulphate aerosols). (d) Annual mean Northern Hemisphere temperature (°C) simulated under the range of forcings shown in (a) to (c), compared to the concentration of overlapping Northern Hemisphere temperature reconstructions. All forcings and temperatures are expressed as **anomalies** from their 1500 to 1899 means and then smoothed with a Gaussian-weighted filter to remove fluctuations on time scales less than 30 years. Figure 6.13 from Jansen et al. (2007) using a modified legend, copyright IPCC 2007, reproduced with permission. See Jansen et al. (2007) for a full reference to all the time series.

In contrast to the orbital forcing whose time development is very well known, we are still uncertain about both solar (TSI) and volcanic forcings. On the one hand, the

volume and characteristics of the aerosols released by the volcanic eruptions have to be derived indirectly from the measurements of sulphate loads in ice cores (Fig. 5.27). On the other hand, we have precise measurement of TSI from satellites over the last 30 years. For earlier times, measurement of the concentration of cosmogenic isotopes, such as ^{10}Be and ^{14}C, in ice cores can be used as a **proxy** for TSI. When solar activity is low, the shielding of the Earth from energetic cosmic ray is weaker, and there is an increase in the production of those isotopes. However, the link between the concentration of cosmogenic isotopes in ice cores, solar activity and solar forcing is far from simple. It has even been suggested that some of the widely used reconstruction (e.g. Fig. 5.27) overestimate the long term changes in TSI by up to a factor five.

The last millennium is an ideal test case for climate models to compare natural and human induced changes. Whether driven by solar and volcanic forcings as well as by anthropogenic forcings (increase in greenhouse gas concentration, sulphate aerosol load, land use changes, see section 5.5.3), the simulated temperatures are within the range provided by the reconstructions. This gives us some confidence in the validity of models. Furthermore, simulations can be used to analyse the causes of the observed changes. In particular, the cold periods during the Little Ice Age correspond well to times with a relatively low TSI and frequent volcanic eruptions.

5.5.2.2 Regional-scale changes

Although the forcings in the last millennium have relatively small amplitudes, they have played a dominant role in the changes in the temperature on a hemispheric scale (Fig. 5.27). By contrast, on a regional scale, changes in the oceanic or atmospheric circulation can completely mask the influence of the forcing in some periods. As a consequence, the Medieval Warm Period and the Little Ice Age can by no means be considered as globally or even nearly globally synchronous phenomena. This is the reason some climatologists avoid using these terms. The temperature in the first part of the second millennium was generally higher than in the period 1500-1900 but warm and cold periods occurred at different times in different locations (e.g., Fig. 5.28).

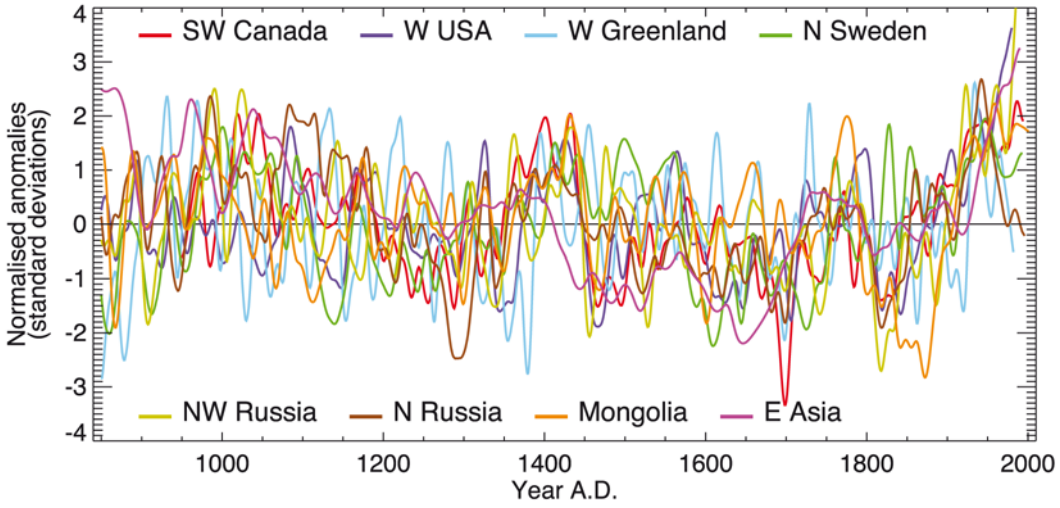

Figure 5.28: The heterogeneous nature of climate during the Medieval Warm Period is illustrated by the wide spread of values in the individual records that have been used to reconstruct the mean temperature in the Northern Hemisphere (see fig. 5.26). These records have been smoothed with a 20-year filter and scaled to have zero mean and unit standard deviation over the period 1001 to 1980. Figure 1, Box 6.4 from Jansen et al. (2007), reproduced with permission from IPCC. See Jansen et al. (2007) for a full reference to all the time series.

Analysing the sources of climate variations on a regional scale is extremely complex because some changes in the circulation can be part of the response of the climate system to the forcing. This was briefly described in section 5.5.2.1 where the tendency towards a positive NAO index in the winter following a major volcanic eruption was mentioned. It is thus very hard to disentangle the response of the circulation to the forcing from the internal variability that would be present in the absence of any forcing change. Nevertheless, a significant part of the climate variability on a regional scale in the last millennium is probably related to this internal variability, which is associated with the chaotic nature of the climate system and is thus similar to the daily changes in the weather. This can be illustrated by performing an ensemble of experiments using a climate model. For figure 5.29, five simulations have been run with exactly the same forcing but slightly different initial conditions. Because of those small differences, and of the sensitivity of the climate system to initial conditions, each simulation reproduces a different realisation of the internal variability of the modelled system (note that the observed climate also corresponds to one realisation of the internal variability of the real system among all the possibilities). While the response to the forcing is nearly identical resulting in some common characteristics for all the simulations, the large differences between the five experiments indicate that the internal variability can be the dominant source of climate changes before the 20th century.

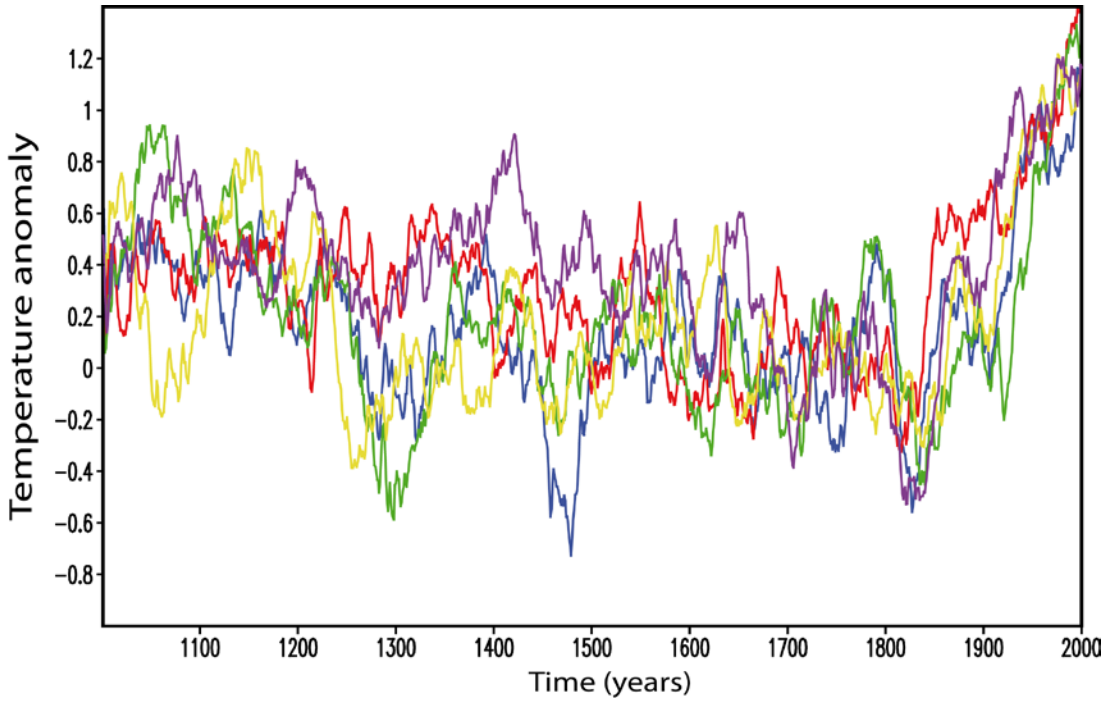

Figure 5.29: Five different simulations of the surface temperature anomaly (°C) in the Arctic (defined here as the area northward of 65°N) over the last millennium using the climate model LOVECLIM (http://www.astr.ucl.ac.be/index.php?page=LOVECLIM%40Description) driven by both natural and anthropogenic forcings. In the 5 experiments displayed with various colours, only the initial conditions are different resulting in a different sample of the model internal variability in each simulation. The reference period is 1601-1850 AD. Data from E. Crespin.

5.5.3 The last century

In the period 1906-2005, the global mean surface temperature rose by 0.75 ± 0.18°C (Fig. 5.30). Moreover, the rate of warming increased sharply, with the increase in the last 50 years being almost double that in the last 100 years. This warming, which has lead to the highest mean temperatures in at least several centuries (Fig. 5.26), is clear at global and hemispheric scale as well as over all the continents except Antarctica (Fig. 5.32).

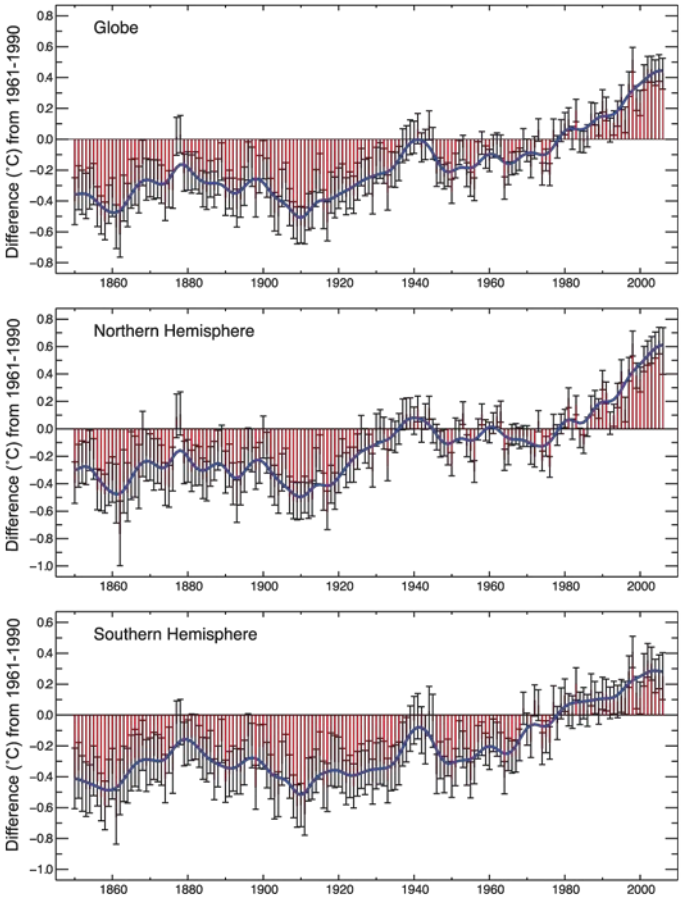

Figure 5.30: Global and hemispheric annual combined land-surface air temperature and SST anomalies (°C) (red) from 1850 to 2006 relative to the 1961 to 1990 mean, along with the 5 to 95% error bars (from HadCRUT3, adapted from Brohan et al., 2006). The smooth blue curves show decadal variations. Figure 3.6 from Trenberth et al. (2007), reproduced with permission from IPCC.

The surface temperature of the oceans has also increased, although generally more slowly than that of the continents. Some oceanic areas, e.g. close to the Southern tip of Greenland, even display a slight cooling during the 20th century (Fig. 5.31). The warming is associated with clear modifications of the **cryosphere**, such as a retreat of the large majority of glaciers, the permafrost and seasonally frozen ground, as well as a decline in the snow cover over land, especially in spring. In the Arctic, the sea ice extent has declined by about 3% per decade since 1978. The decrease in the extent of the sea ice is even larger in summer, at a rate of about 8% per decade. By contrast, the sea ice in the Southern Ocean appears to have been relatively stable over the last 30 years.

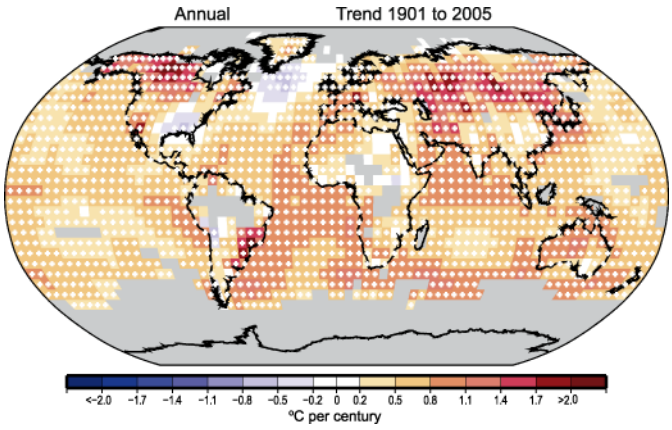

Figure 5.31: Linear trend of annual temperatures between 1901 and 2005 (°C per century). Areas in grey have insufficient data to produce reliable trends. The minimum number of years needed to calculate a trend value is 66 years between 1901 and 2005. An annual value is available if there are 10 valid monthly temperature anomaly values. Figure 3.9 from Trenberth et al. (2007), reproduced with permission from IPCC.

When driven by natural forcings only, climate models cannot reproduce the observed warming. By contrast, if anthropogenic forcings are included, the results are compatible with the observed changes. The dominant anthropogenic forcing is the increase in greenhouse gas concentrations in the atmosphere. This is associated with a strong radiative forcing of about 2 W m^{-2} in 2000 compared to preindustrial conditions (see section 4.1.2). Although the effect of sulphate-aerosol emission by human activities is less precisely known, one of its more robust effects is a net negative radiative forcing that partly compensates for the warming due to the greenhouse gases. Humanity has also strongly affected the land use, in particular through deforestation. This has an impact on the chemical composition of the atmosphere, for instance when wood is burned and releases CO_2. It also modifies the physical characteristics of the surface such as the **albedo**, roughness and water availability. While most of the human-induced changes in greenhouse gas concentrations and in sulphate aerosols have occurred in the last 150 years, land-use modifications started thousands of years ago in some regions, and certainly had an impact on climate at regional scale and perhaps at the global one.

The large changes in climate observed recently thus appear to be outside the range of natural variability on decadal to centennial timescales, but these changes are compatible with those predicted by models including anthropogenic forcings. This has led the IPCC to conclude, in its 4th assessment report, that: “It is very likely that anthropogenic greenhouse gas increase caused most of the observed increase in global average temperature since the mid-20th century. Without the cooling effect of atmospheric aerosols, it is likely that greenhouse gases alone would have caused a greater global mean temperature rise than observed during the last 50 years” (Solomon et al. 2007). ‘Very likely’ in this sentence means a likelihood higher than 90 %, while ‘likely’ corresponds to the 66% level. In the future, additional changes are expected, as discussed in the next chapter.

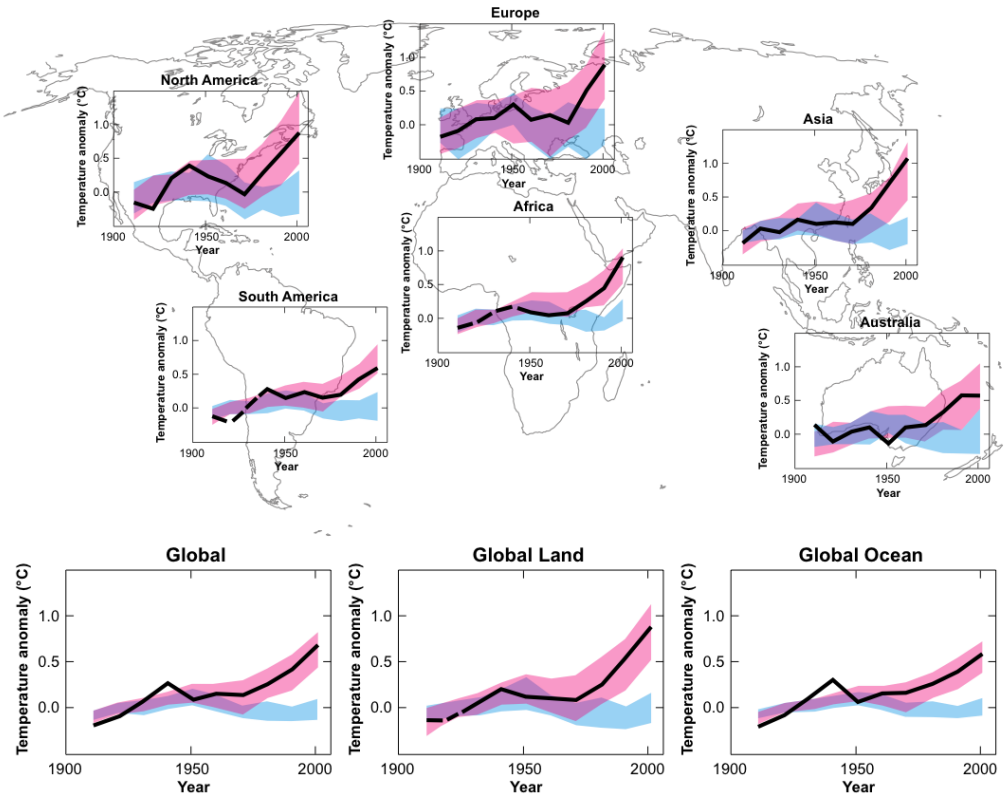

Figure 5.32: Comparison of observed continental- and global-scale changes in surface temperature with results simulated by climate models using natural and anthropogenic forcings. The decadal averages of the observations are shown for the period 1906 to 2005 (black line) plotted against the centre of the decade and relative to the corresponding average for 1901 to 1950. Lines are dashed where spatial coverage is less than 50%. Blue shaded bands show the 5% to 95% range for 19 simulations from 5 climate models using only the natural forcings due to solar activity and volcanoes. Red shaded bands show the 5% to 95% range for 58 simulations from 14 climate models using both natural and anthropogenic forcings. Figure TS22 from Solomon et al. (2007), reproduced with permission from IPCC.

Cited references and further reading

Berger A.L. (1978). Long-term variations of daily insolation and Quaternary climatic changes. J. Atmos. Sci. 35: 2363-2367.

Berger A. and M.F. Loutre (1991). Insolation values for the last 1000000 years. Quaternary Science Reviews, 10, 4, 297-317.

Berger A. and M.F. Loutre (2003). Climate 400,000 years ago, a key to the future?. In : Earth's Climate and Orbital Eccentricity. The marine isotope stage 11 question. A.W.Droxler, R.Z.Poore, L.H.Burckle (Eds). Geophysical Monograph 137. AGU, Washington, DC, 17-26.

Brohan P, J.J. Kennedy, I. Harris, S.F.B. Tett, and P.D.Jones (2006). Uncertainty estimates in regional and global observed temperature changes: A new data set from 1850. J. Geophys. Res. 111 (D12): Art. No. D12106.

Claussen M. (2009) Late Quaternary vegetation – climate feedbacks. Climate of the Past 5, 203-216, 2009 Available at http://www.clim-past.net/5/203/2009/cp-5-203-2009.pdf .

Committee on Abrupt Climate Change, National Research Council (2002). Abrupt Climate Change: Inevitable Surprises. Freely available at http://books.nap.edu/openbook.php?isbn=0309074347.

Cuffey K.M. and G.D. Clow (1997). Temperature, accumulation, and ice sheet elevation in central Greenland through the last deglacial transition. J. Geophys. Res. 102, 26,383-26,396.

Gong, D. and S. Wang (1999). Definition of Antarctic oscillation index. Geophys. Res. Let. 26(4):459-462

Hurrell, J.W., Y. Kushnir, M. Visbeck, and G. Ottersen (2003). An Overview of the North Atlantic Oscillation. *The North Atlantic Oscillation: Climate Significance and Environmental Impact*, J.W. Hurrell, Y. Kushnir, G. Ottersen, and M. Visbeck, Eds. Geophysical Monograph Series, **134**, pp. 1-35. Available at http://www.cgd.ucar.edu/cas/jhurrell/publications.html.

Imbrie J., J. Hays, D.G. Martinson, A. McIntyre, A.C. Mix, J.J. Morley, N.G. Pisias, W.L. Prell, and N.J. Shackleton (1984). The orbital theory of Pleistocene climate: support from a revised chronology of the marine ^{18}O record. In: "Milankovitch and Climate", A. Berger, J. Imbrie, J. Hays, G. Kukla, B. Saltzman (eds), 269-305, D. Reidel Publ. Comp., Dordrecht, Holland.

IPCC (2007). *Climate Change 2007: The Physical Science Basis. Contribution of Working Group I to the Fourth Assessment Report of the Intergovernmental Panel on Climate Change* [Solomon, S., D. Qin, M. Manning, Z. Chen, M. Marquis, K.B. Averyt, M.Tignor and H.L. Miller (eds.)]. Cambridge University Press, Cambridge, United Kingdom and New York, NY, USA.

Jansen, E., J. Overpeck, K.R. Briffa, J.-C. Duplessy, F. Joos, V. Masson-Delmotte, D. Olago, B. Otto-Bliesner, W.R. Peltier, S. Rahmstorf, R. Ramesh, D. Raynaud, D. Rind, O. Solomina, R. Villalba and D. Zhang (2007). Palaeoclimate. In: *Climate Change 2007: The Physical Science Basis. Contribution of Working Group I to the Fourth Assessment Report of the Intergovernmental Panel on Climate Change* [Solomon, S., D. Qin, M. Manning, Z. Chen, M. Marquis, K.B. Averyt, M. Tignor and H.L. Miller (eds.)]. Cambridge University Press, Cambridge, United Kingdom and New York, NY, USA.

Jones P.D. and M.E. Mann (2004). Climate over past millennia. Rev. Geophys. 42(2) : RG2002, DOI 10.1029/2003RG000143

Kalnay, E. and twenty-one others (1996). The NCEP/NCAR 40-year reanalysis project. Bull. Amer. Meteor. Soc. 77: 437-471

Lisiecki, L. E. and M. E. Raymo (2005). A Pliocene-Pleistocene stack of 57 globally distributed benthic $\delta^{18}O$ records. Paleoceanography 20: PA1003, doi:10.1029/2004PA001071.

Oldenborgh, G.J. van, M.A. Balmaseda, L. Ferranti, T.N. Stockdale and D.L.T. Anderson(2004). Evaluation of atmospheric fields from the ECMWF seasonal forecasts over a 15 year period. J. Climate 18: 2970-2989.

Petit J.R., J. Jouzel, D. Raynaud, N.I. Barkov, J.M. Barnola, I. Basile, M. Bender, J. Chapellaz, M. Davis, G. Delaaygue, M. Delmotte, V.M. Kotlyakov, M. Legrand, V.Y. Lipenkov, C. Lorius, L. Pépin, C. Ritz, E. Saltzman., and M. Stievenard (1999). Climate

and atmospheric history of the past 420,000 years from Vostok ice core, Antarctica. Nature, 399 (6735): 429-436.

Rayner N.A., D.E. Parker, E.B. Horton, C.K. Folland, L.V. Alexander, D.P. Rowell, E.C. Kent and A. Kaplan (2003). Global analyses of sea surface temperature, sea ice, and nigh marine aire temperature since the late nineteenth century. J. Geophys. Res. 108 (D14): 4407, doi:10.1029/2002JD002670

Ropelewski C.F., and M.S. Halpert (1987). Global and regional precipitation associated with El Niño/Southern Oscillation. Mon. Wea. Review 115: 1606–1626.

Royer, D.L., R. A. Berner and J. Park (2007). Climate sensitivity constrained by CO2 concentrations over the past 420 million years. Nature 446: 530-532.

Solomon, S., D. Qin, M. Manning, R.B. Alley, T. Berntsen, N.L. Bindoff, Z. Chen, A. Chidthaisong, J.M. Gregory, G.C. Hegerl, M. Heimann, B. Hewitson, B.J. Hoskins, F. Joos, J. Jouzel, V. Kattsov, U. Lohmann, T. Matsuno, M. Molina, N. Nicholls, J. Overpeck, G. Raga, V. Ramaswamy, J. Ren, M. Rusticucci, R. Somerville, T.F. Stocker, P. Whetton, R.A. Wood and D. Wratt (2007). Technical Summary. In: Climate Change 2007: The Physical Science Basis. Contribution of Working Group I to the Fourth Assessment Report of the Intergovernmental Panel on Climate Change [Solomon, S., D. Qin, M. Manning, Z. Chen, M. Marquis, K.B. Averyt, M. Tignor and H.L. Miller (eds.)]. Cambridge University Press, Cambridge, United Kingdom and New York, NY, USA.

Sterl A., G.J. van Oldenborgh, W. Hazeleger and G. Burgers (2007). On the robustness of ENSO teleconnections. Climate Dynamics 2: 469-485.

Trenberth, K.E., P.D. Jones, P. Ambenje, R. Bojariu, D. Easterling, A. Klein Tank, D. Parker, F. Rahimzadeh, J.A. Renwick, M. Rusticucci, B. Soden and P. Zhai, 2007: Observations: Surface and Atmospheric Climate Change. In: Climate Change 2007: The Physical Science Basis. Contribution of Working Group I to the Fourth Assessment Report of the Intergovernmental Panel on Climate Change [Solomon, S., D. Qin, M. Manning, Z. Chen, M. Marquis, K.B. Averyt, M. Tignor and H.L. Miller (eds.)]. Cambridge University Press, Cambridge, United Kingdom and New York, NY, USA.

Wallace, J.M. and D. S. Gutzler (1981). Teleconnections in the Geopotential Height Field during the Northern Hemisphere Winter. Mon. Wea. Review.109. 784-812.

Wanner H., S. Brönnimann, C. Casty, D. Gyalistras, J. Lutebacher, C. Schmutz, D.B. Stephenson and E. Xoplaki (2001). North Atlantic Oscillation – Concept and studies. Surveys in Geophysics 22:321-382.

Xie, P., and P. A. Arkin, 1997: Global Precipitation: A 17-Year Monthly Analysis Based on Gauge Observations, Satellite Estimates, and Numerical Model Outputs. Bull. Amer. Meteor. Soc. 78, 2539--2558.

Zachos J.C., G.R. Dickens and R.E. Zeebe (2008). An early Cenozoic perspective on greenhouse warming and carbon-cycle dynamics. Nature 451: 279-283.

Exercises

Exercises are available on the textbook website (http://www.climate.be/textbook) and on iCampus for registered students.

Chapter 6. Future climate changes

6.1 Emission scenarios

6.1.1 The purpose of the scenarios and scenario development

As discussed in Chapter 5, the changes in external **forcing** have to a large extent driven past climate variations. In order to "predict" the climate of the 21st century and beyond, it is thus necessary to estimate future changes in the forcing. This is achieved by the development of **scenarios** for the emission of **greenhouse** gases, **aerosols**, various pollutants in the atmosphere, land use, etc. These **scenarios** depend on many uncertain factors (as discussed below) and some of the uncertainties in the estimates of future climate changes are related to these factors (see Fig. 6.8). This is the reason why, in the scientific literature, the term climate **projection** is generally preferred to the term climate prediction, as it emphasises the fact that the results depend on the **scenarios** chosen and the hypothesis made in those scenarios. The scenarios are also used for analysing impact, adaptation and vulnerability, thus providing a consistent approach for socio-economic and climatic issues.

Various types of scenarios have been proposed in recent years and decades. In the forth assessment report of the IPCC, the climate **projections** were based on the SRES scenarios (Special Report on Emission Scenarios, see Section 6.1.2) which cover the whole of the 21st century. Those scenarios were derived in a sequential form (Fig.6.1). First, the main driving forces influencing the emissions from demographic, social and economic development have to be identified. This implies estimating population growth, future levels of economic activity, the way exchanges between different countries will be organised, the technology choices/opportunities of the countries, etc. On the basis of these estimates, some models produce scenarios for future emissions of greenhouse gases and aerosols, and for land-use changes. Different combinations of demographic and socio-economic change can lead to similar emission paths. For instance, large population growth combined with efficient technologies and renewable energy can lead to similar emissions to a smaller increase in the Earth's population with less efficient and more energy-demanding technologies. In addition to the emission scenarios, the concentrations of greenhouse gases and aerosols in the atmosphere are also provided for models that do not include a representation of the carbon and/or aerosols cycle.

For the next IPCC assessment report (IPCC AR5), a slightly different approach was followed. Four representative concentration pathways (RCPs) were selected, covering a wide range of future changes in **radiative forcing** (see Section 6.1.3). The emissions (and concentrations) of greenhouse gases corresponding to these four RCPs were then provided to the climate-modelling community, so that they could perform climate **projections**. In parallel, possible socio-economic scenarios compatible with those RCPs were developed, providing different socio-economic alternatives for the same RCP. If needed, the information provided by the climate-model projections can be used in the socio-economic scenarios to assess the impact of climate change on society. Such a parallel approach strengthens the collaboration between the different communities, while ensuring that the climate-modelling groups only have to run a small set of well contrasted emission scenarios with their models (which are very demanding of computer time). Another advantage of the new scenarios is that they include both more detailed short term estimates (to about 2035) and stylised estimates to about 2300, in addition to the classical, long-term estimates up to 2100 provided by the SRES scenarios.

Neither the SRES nor the RCPs made any attempt to provide a best guess or to assess the likelihood of the various scenarios. Many elements of the scenarios are too

unpredictable for this to be feasible. As a consequence, all the scenarios should be considered as reasonable possible and equally probable.

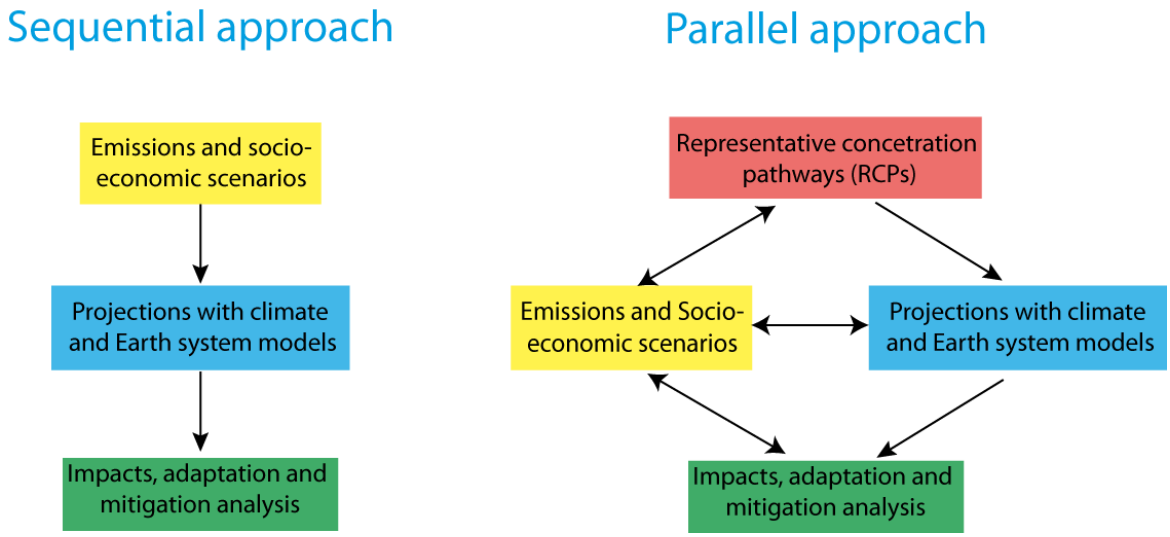

Figure 6.1: Sequential and parallel approaches to the development of scenarios. In contrast to the sequential approach, in the parallel approach the projections with climate models (driven by RCPs) and the choice of emission and socio-economic scenarios (corresponding to those RCPs) are performed concurrently. Modified from Moss et al. (2007).

6.1.2 Special Report on Emission Scenarios (SRES)

Among the infinite number of possible alternative futures, four families have been proposed, comprising 40 SRES scenarios covering a wide range of possibilities. Each family includes a so-called storyline, providing a coherent descriptive narrative of the choices made. The four families can be described very briefly as follows (for more details see Nakicenovic and Swart, 2000):

+ A1 corresponds to very rapid economic growth, low population increase, and the rapid introduction of efficient technologies. The A1 family assumes strong interactions between different countries and a reduction in regional differences in per capita income. In addition, the A1 family is separated into four groups related to technology choices, one group for instance being devoted to fossil-intensive energy production.

+ A2 corresponds to a slow convergence between regions and a high population growth. Technological changes are more slowly implemented than in the other storylines, with more disparity between the regions.

+ B1 corresponds to a low population growth and strong convergence between regions, but with faster introduction of clean and resource-efficient technologies than A1.

+ B2 corresponds to intermediate population and economic growth with less rapid introduction of new technologies than in the B1 and A1 storylines. It assumes an emphasis on local and regional solutions.

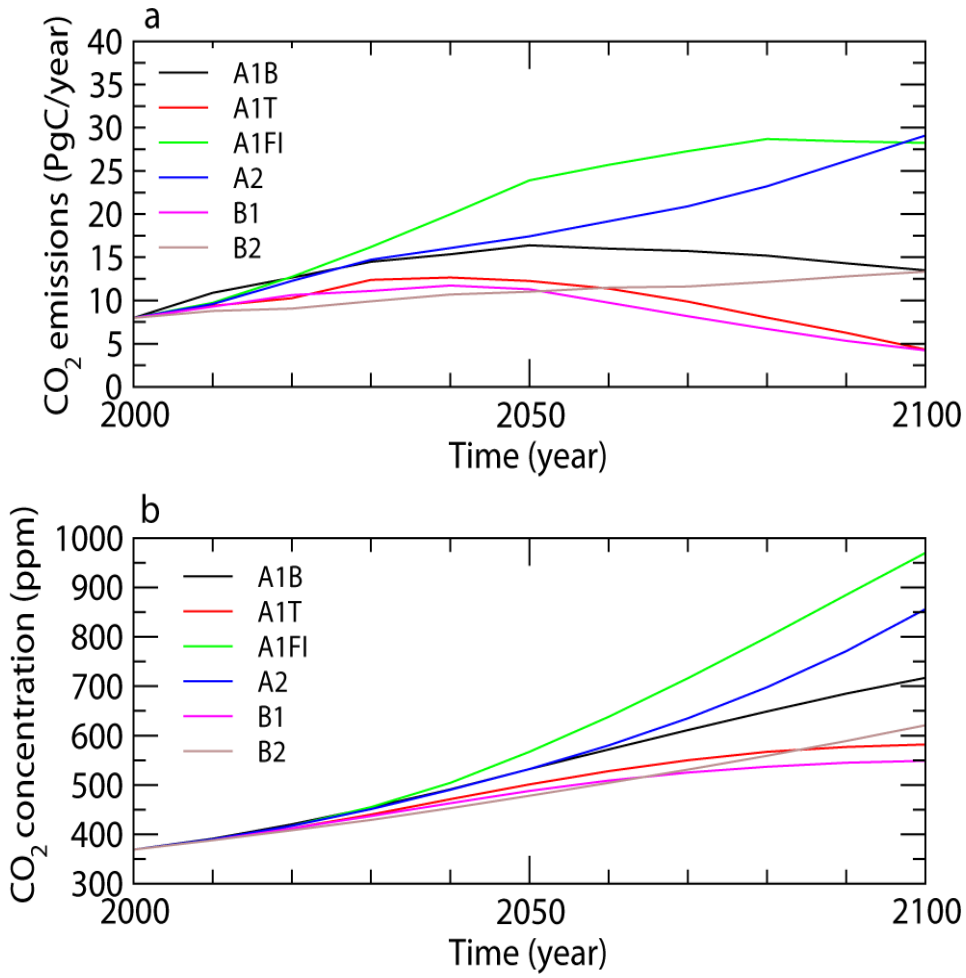

Figure 6.2: (a) Global emission (in $PgCO_2$ per year) and (b) atmospheric concentration of CO_2 (in ppm) in the 6 illustrative SRES scenarios (A1B, A1T, A1FI, A2, B1, B2).

From those storylines, different research groups have proposed different scenarios. From these, four marker scenarios were selected, one to illustrate each storyline. Two additional scenarios were selected in the A1 family to illustrate alternative developments in energy systems. This resulted in six scenarios, which have been used to perform climate projections (see Section 6.2).

It is important to remember that none of those storylines involves clear climate initiatives or climate-related regulations, although the policy choices described in the various scenarios would have a substantial impact on the emissions of greenhouse gases and aerosols.

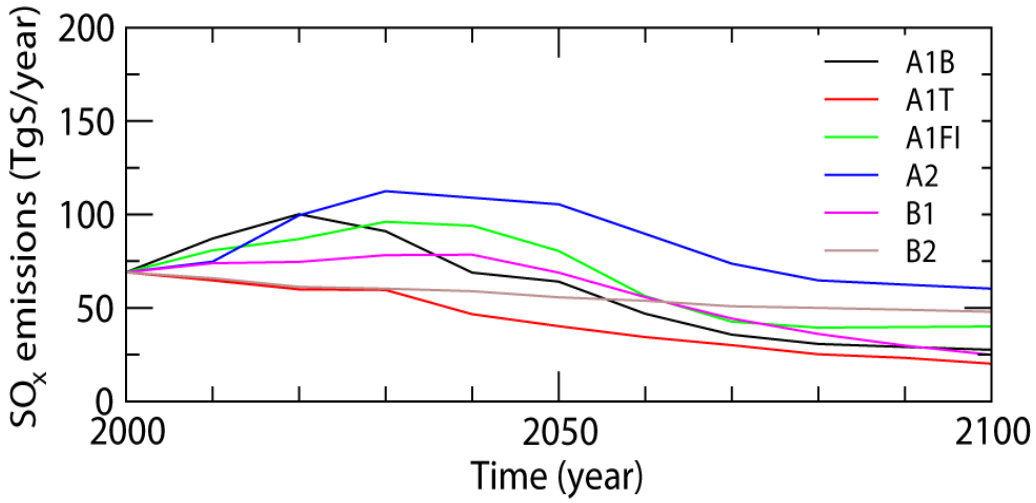

Figure 6.3: Global emissions of sulphur oxides in six illustrative SRES scenarios (in TgS per year).

In all six illustrative scenarios, the emissions of CO_2 increase during the first decades of the 21st century (Fig. 6.2). This trend continues up to 2100 in three scenarios, while the emissions peak between 2030 and 2050 and then decrease in scenarios A1T, B1 and A1B. Based on computations made by the teams that developed the scenarios, this induces an increase in atmospheric CO_2 concentration in 2100 up to nearly 1000 ppm in scenario A1F and a bit less than 600 ppm in scenario B1. This last value roughly corresponds to a doubling of the CO_2 concentration compared to the pre-industrial level (around 280 ppm, see Section 2.3.1). Note that those concentrations were derived using a particular model and some specific hypotheses. A climate model including a carbon-cycle model and thus its own representation of climate/carbon feedbacks, driven by the same SRES emission scenario, will lead to atmospheric CO_2 concentrations different to those plotted in Figure 6.2 (as discussed in Section 6.2.3, below).

SRES scenarios also provide estimates for future emissions and concentrations of other greenhouse gases (such as N_2O and CH_4), as well as emissions of sulphur dioxide (SO_2) which leads to the production of sulphate **aerosols** in the atmosphere. In contrast to CO_2, SO_2 emissions reach their maximum in all the scenarios during the first half of the 21st century and then decrease (Fig. 6.3) thanks to policies devoted to reducing air pollution. Because of the relatively short life of aerosols in the atmosphere (see Section 4.1.2.2), sulphate concentration changes in roughly the same way over time as the emissions. As a consequence, the negative **radiative forcing** due to aerosols (see Fig. 4.2) will decrease during a large part of the 21st century, while the positive forcing due to greenhouse gases will increase continuously in the majority of the scenarios.

6.1.3 Representative concentration pathways (RCPs)

A set of four RCPs were selected. The most extreme one, RCP8.5 displays a continuous rise in **radiative forcing** during the 21st century, leading to a value of about 8.5 W m^{-2} in 2100. RCP6.0 and RCP4.5 are characterised by a steady rise during the 21st century, up to a **radiative forcing** of about 6 and 4.5 Wm^{-2} respectively, and a stabilisation after 2100. Finally, in RCP3-PD (peak and decline), the **radiative forcing** peaks before 2100 at about 3 Wm^{-2} and then declines. Emissions and atmospheric concentrations of CO_2 corresponding to those RCPs are shown in Figure 6.4. As expected, CO_2 being the largest contributor to **radiative forcing** (see Fig. 4.2), the time series of atmospheric CO_2 concentration have the same shape as the time series for **radiative forcing**. By construction, the emissions cover a wide range of possibilities,

with, for instance, nearly no emission of CO_2 after 2080 in RCP3-PD while in RCP8.5 the emissions are more than 25 PgC per year (i.e. more than 3 times greater than in 2000).

The RCP also includes estimates of emissions of a large number of greenhouse gases and atmospheric pollutants (CH_4, N_2O, **chlorofluorocarbons**, SO_2, black carbon, etc.) as well as estimates of future changes in land use. For instance, in all the RCPs, the decrease in SO_2 emissions (Fig. 6.5) is even larger than in the SRES (Fig. 6.3).

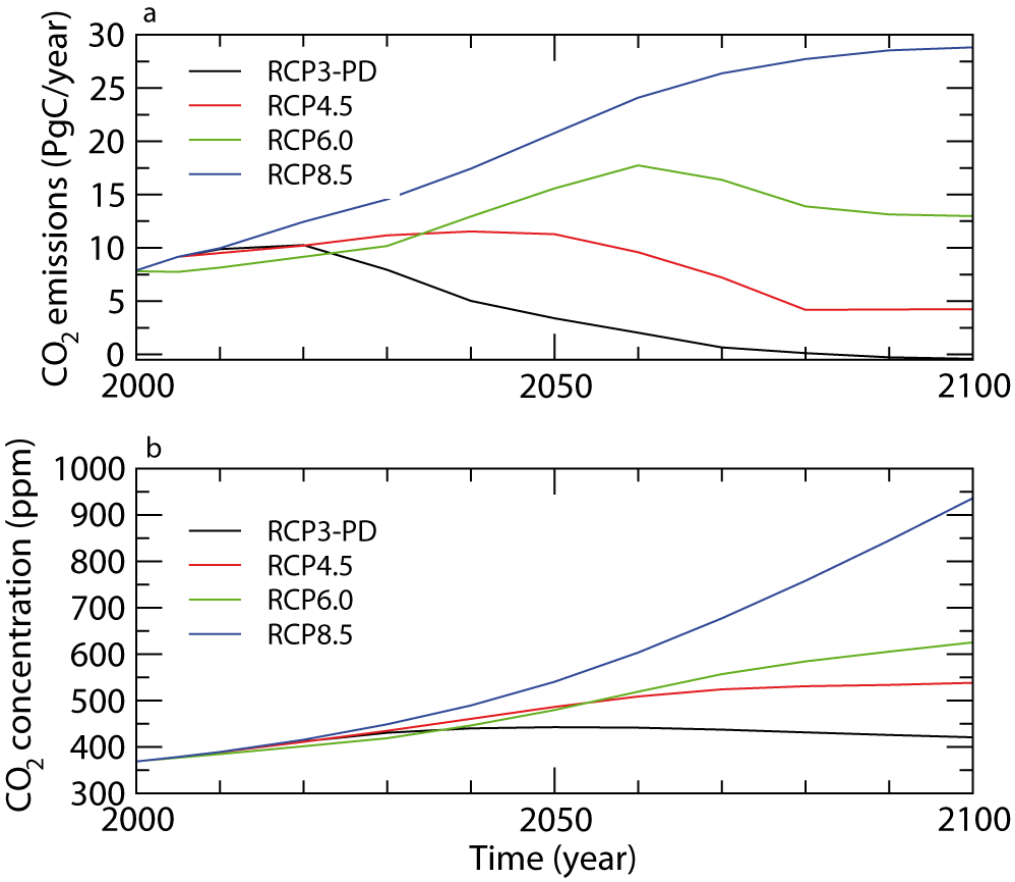

Figure 6.4: (a) Global emission (in PgC per year) and (b) atmospheric concentration of CO_2 (in ppm) in four RCP scenarios.

Furthermore, the RCPs have been extended to 2300 and even 2500 for studies of long-term climate change (Fig. 6.6). Because of the very large uncertainties in the driving forces influencing the emissions, the long-term scenarios are kept as simple as possible and thus highly idealised. Nevertheless, they provide a reasonable range for the possible changes, give time developments compatible with the RCPs over the 21st century, and display a common framework in which the results of different models can be displayed. Among the various possible extrapolations, a forcing stabilisation path emerges for RCP4.5 and RCP6.0. For RCP3-PD, the forcing is assumed to continue to decrease after 2100. For RCP8.5, the extension suggests an increase in forcing until at least 2200, although the emissions growth slows in the second part of the 21st century, leading to a nearly flat profile after 2100.

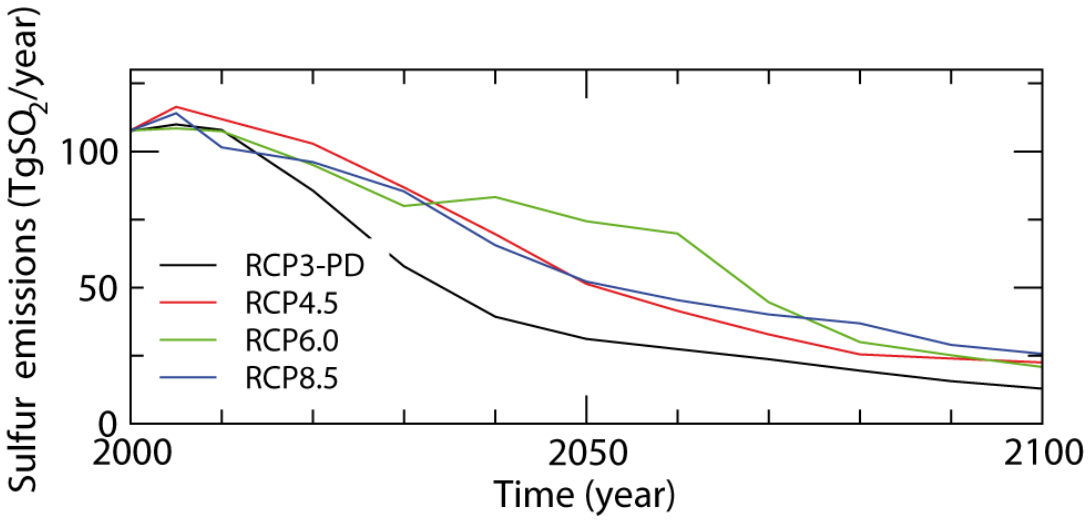

Figure 6.5: Global emissions of sulphur oxide in four RCP scenarios (in $TgSO_2$ per year).

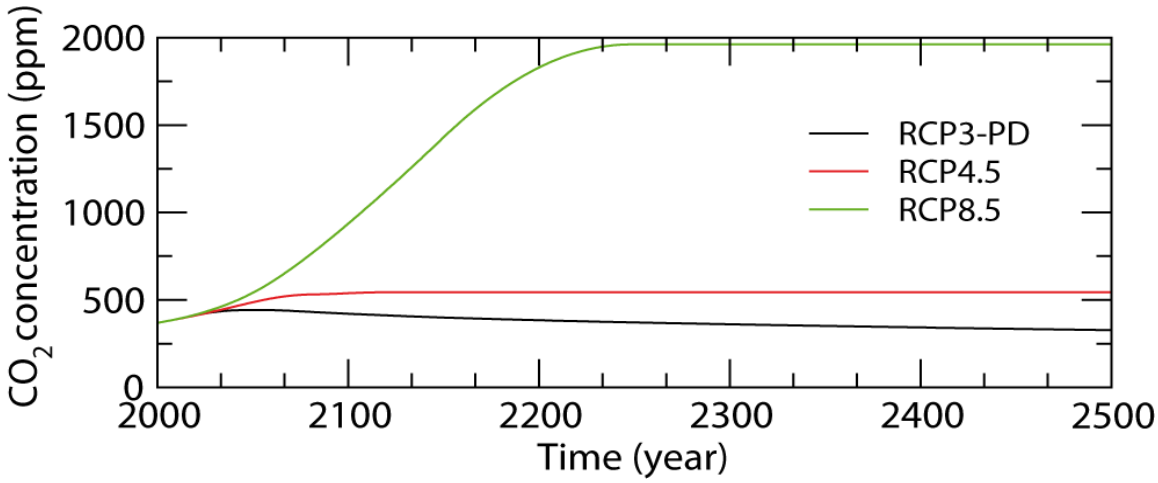

Figure 6.6: Global atmospheric concentration of CO_2 (in ppm) in three RCP scenarios.

6.2 Climate projections for the 21st century

6.2.1 Changes in global mean surface temperature

Nearly all the simulations covering the 21st century available up to now have been obtained using the SRES scenarios (see Section 6.1.2 above). The average of the results of the General Circulation Models (GCMs) is a warming of nearly 2°C by 2100 for scenario B1, a bit less than 3°C for scenario A1B and about 3.5°C for scenario A2 (Fig. 6.7). Fewer models have been driven by the other scenarios, but A1T and B2 generally lead to a forecast warming intermediate between those obtained with scenarios B1 and A2, while scenario A1F1 predicts more warming than A2. An additional scenario that has been widely tested is the so-called constant commitment scenario in which the concentration of greenhouse gases is held constant at year 2000 values for the whole of the 21st century. Even in this extreme case, the GCM simulations predict an average warming of more than 0.5°C by 2100 on average (Fig. 6.7). This is because the climate was far from equilibrium with the forcing in 2000.

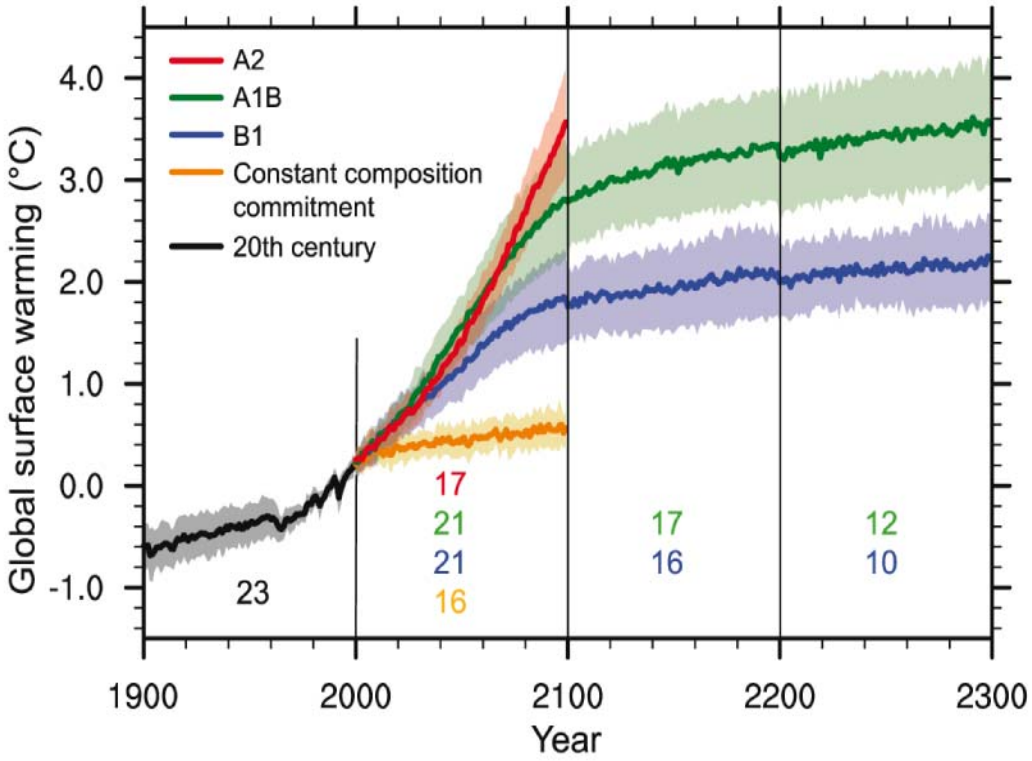

Figure 6.7: Multi-model means of surface warming (relative to 1980-1999) for the SRES scenarios A2, A1B and B1, shown as continuations of the 20th-century simulation. Values beyond 2100 are for the stabilisation scenarios in which the forcing in 2100 is kept constant for the 22nd and 23rd centuries. For the constant composition commitment, the composition in 2000 in maintained during the whole 21st century. Linear trends from the corresponding control runs have been removed from these time series. Lines show the multi-model means, shading denotes the 1 standard deviation range of individual-model annual means. Discontinuities between different periods have no physical meaning and are caused by the fact that the number of models that have run a given scenario is different for each period and scenario, as indicated by the coloured numbers given for each period and scenario at the bottom of the panel. Figure 10.4 of Meehl et al. (2007) with a modified legend, reproduced with permission from IPCC.

Figure 6.7 illustrates two sources of uncertainty in climate projections. The first is related to the scenario, as discussed above. A second is due to model uncertainty, different models displaying a different response to the same forcing. This is indicated on Figure 6.7 by the range of the results of all the models. Additional uncertainty is related to the internal variability of the system, i.e. the natural fluctuations that would occur even in the absence of any change in **radiative** forcing.

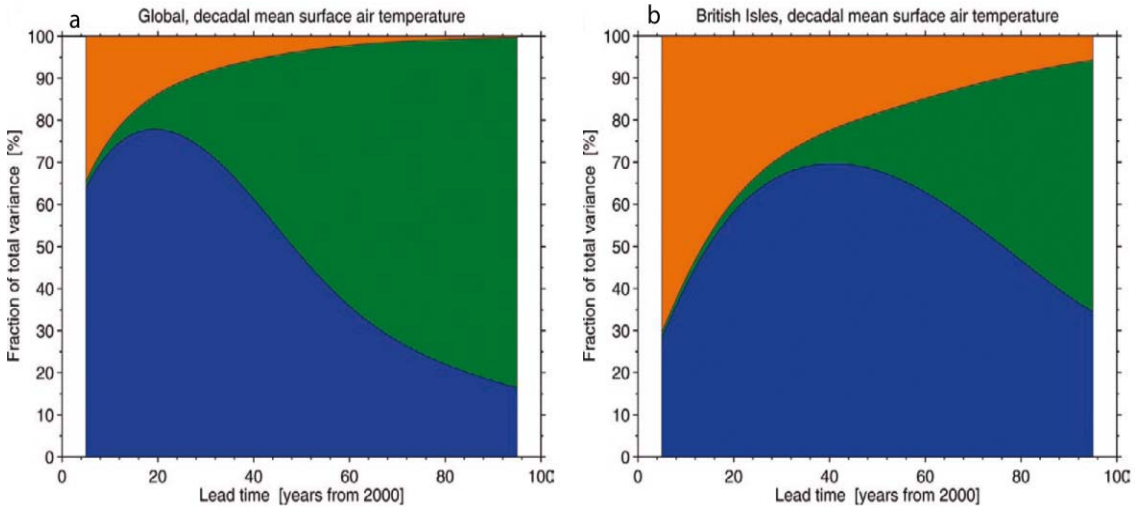

Figure 6.8: The fraction of total variance in decadal mean surface air temperature predictions explained by the three components of total uncertainty is shown for (a) a global mean and (b) a British Isles mean. Green regions represent scenario uncertainty, blue regions represent model uncertainty, and orange regions represent the internal variability component. As the scope of the model is reduced (e.g. from the world to the British Isles), the relative importance of internal variability increases. Figure form Hawkins and Sutton (2009), copyright American Meteorological Society 2009.

The relative importance of the three sources of uncertainty can be estimated for projections over different time periods (also known as lead times). For estimates of the global mean temperature over the next decade, the influence of the uncertainty about future emissions of greenhouse gases is small. This is consistent with Figure 6.7, where the curves for all the SRES scenarios lie close to each other until 2030–2040. On a global scale (Figure 6.8a), the relative importance of the scenario uncertainty increases with time, and is dominant in **projections** for the end of the 21st century. The internal variability only plays a role for a few decades, the natural fluctuations in global mean temperatures over decades and centuries being much smaller than the changes expected by 2100. The model uncertainty is dominant for projections up to 40 years ahead, but its relative contribution then decreases, although it is still significant in 2100.

When analysing temperature changes over a smaller region such as the British Isles (Figure 6.8b), each source of uncertainty has more or less the same behaviour as discussed for the Earth as a whole. The only clear change is that internal variability makes a larger contribution to the total uncertainty. Natural fluctuations also have a much larger amplitude on a regional scale than on the global one (see Section 5.5.2.2).

6.2.2 The spatial distribution of surface temperature and precipitation changes

The increase in global mean temperature by 2010 is associated with a warming in all regions according to the multi-model average (Fig. 6.9). The regional pattern is similar in all the scenarios, with a larger change over the land than over the ocean. This is due to the larger thermal inertia of the ocean and to the increase in latent heat loss that mitigates the temperature changes there. The amplitude of changes is particularly low over the high latitude oceans because of the deeper mixed layer and the contact with colder deep water which has not recently been exposed to surface warming. Additionally, in some models, changes in ocean currents may be responsible for the very small warming, or even a small cooling predicted for the North Atlantic (see Section 6.2.3 below). The changes simulated for the Arctic are also much larger than at mid-latitudes, partly because of the temperature/**albedo** feedback and other feedbacks related to the **cryosphere** (see Section

4.2.3). Changes in heat transport, clouds and the water-vapour feedback also play a role in this behaviour.

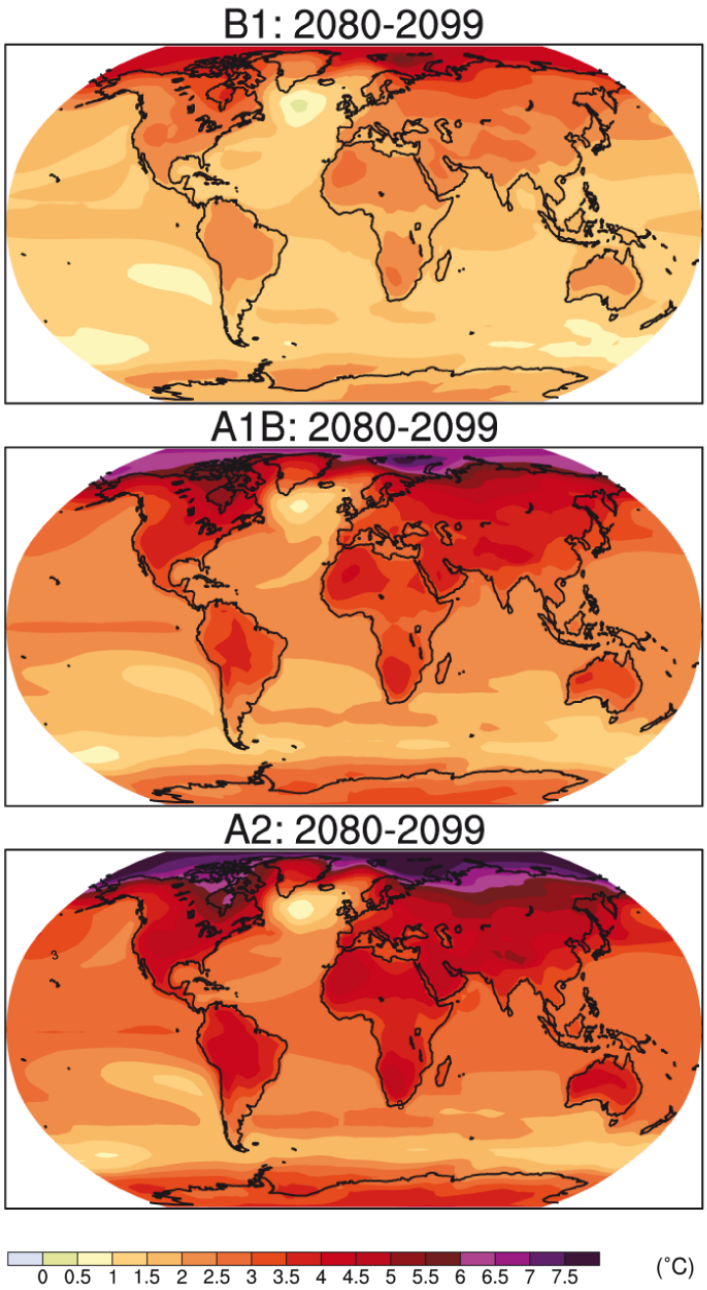

Figure 6.9: Figure 6.9: Multi-model mean of annual mean surface warming (surface air temperature change, °C) for the scenarios B1 (top), A1B (middle) and A2 (bottom), for the time period 2080 to 2099. Anomalies are relative to the average of the period 1980 to 1999. Modified from Figure 10.8 of Meehl et al. (2007), reproduced with permission from IPCC.

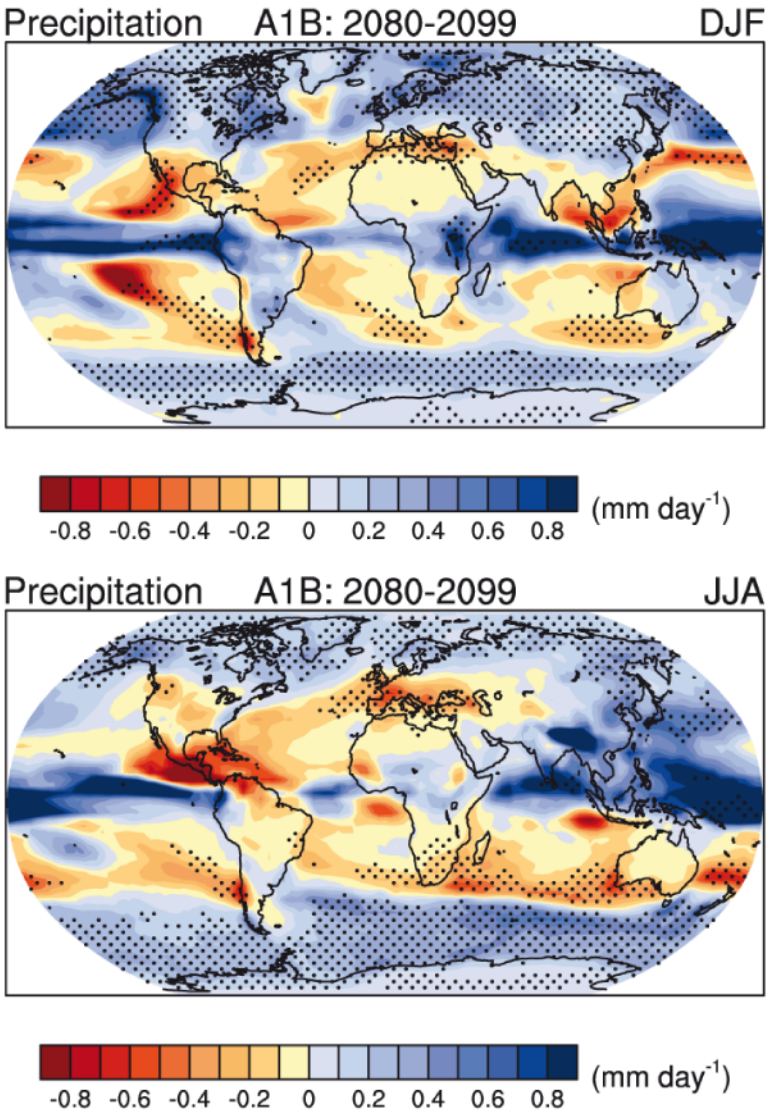

Figure 6.10: Multi-model mean changes in precipitation (mm day^{-1}) for boreal winter (DJF, top) and summer (JJA, bottom). Changes are given for the SRES A1B scenario, for the period 2080 to 2099 relative to 1980 to 1999. Stippling denotes areas where the magnitude of the multi-model ensemble mean exceeds the inter-model standard deviation. Modified from Figure 10.9 of Meehl et al. (2007), reproduced with permission from IPCC.

Global warming is associated with a global increase in precipitation (see Fig. 6.10). This is because of the greater evaporation over the ocean and the larger water-holding capacity of the atmosphere in a warmer world, as described by the **Clausius-Clapeyron equation**. Depending on the model and the scenario, the predicted increase by 2100 is between 1 and 8% compared to the late 20th century. More importantly, this increase in precipitation is far from being spatially uniform and varies strongly over the seasons. At high latitudes, both the multi-model mean and the large majority of individual models predict an increase in precipitation in both winter and summer. An increase in precipitation is also predicted over the tropical oceans, and in the regions influenced by the summer monsoon in South Asia. By contrast, precipitation is predicted to decrease over many subtropical areas and in particular regions such as tropical Central America and the Caribbean, and the Mediterranean.

These changes in the annual and seasonal mean temperature and precipitation are important elements of the projected climate for the 21st century. However, many other characteristics of the atmospheric state, such as wind intensity or cloud amount, are also expected to change. For instance, nearly all the models simulate an increase in the intensity of the westerly winds over the Southern Ocean in the near future, which can also be related to an increase in the Southern Annular Mode (SAM) index (see Section 5.2.3). A particularly sensitive point is the change in the probability of extreme events (such as major storms and heat waves) in a warmer climate. Such extreme events are difficult to model and the available time series are usually too short for reliable predictions to be made for rare events. However, some simple arguments suggest that even a small change in the mean temperature greatly increases, for example, the probability of experiencing a temperature above a particular threshold, and thus of an increase in the number of very hot days (Fig. 6.11). A rise in average temperature also decreases the probability of the temperature falling below a particular level, and so decreases the probability of cold days. This simple reasoning is in agreement with model results which suggest an increase in heat waves in summer and a decline in the incidence of frosts in many regions.

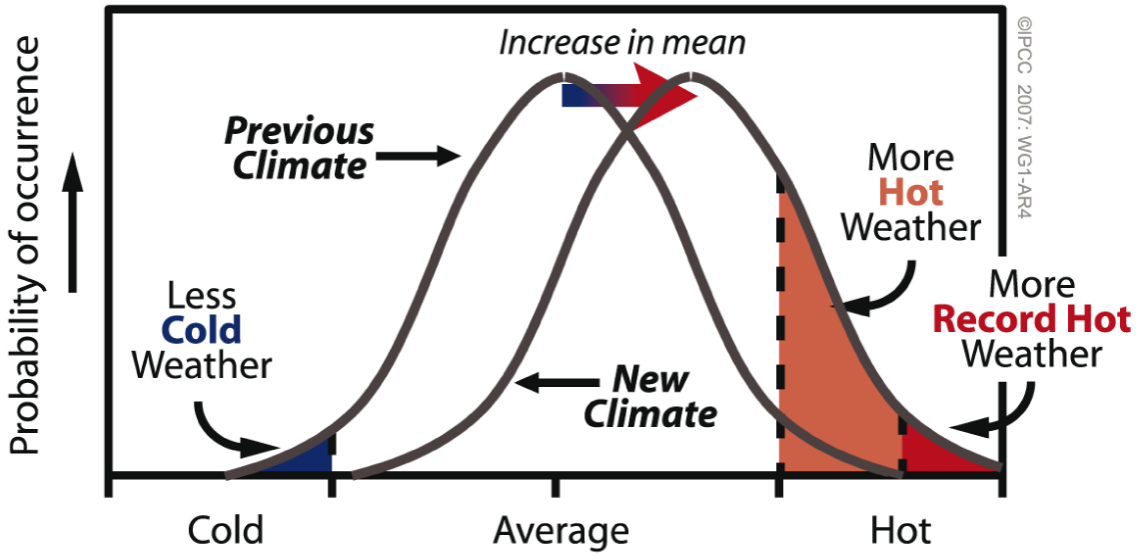

Figure 6.11 Schematic diagram showing the effect of mean temperature increases on extreme temperatures, for a normal temperature distribution. Figure1, Box TS5 of Solomon et al. (2007). Reproduced with permission of IPCC.

Fig. 6.11 is based on a simple shift in the distribution but the shape of the distribution can also change. Indeed, some studies suggest that the future climate will also be more variable in some regions (corresponding to a wider distribution on Fig. 6.11 and thus even more frequent extremes), although those results are not always robust between the different models.

6.2.3 Changes in the ocean and sea ice

The warming simulated at high latitudes is associated with year-long decreases in the extent and in the thickness of sea ice in both hemispheres. The projected decrease is larger in summer than in winter, and particularly pronounced in the Arctic. As a consequence, both hemispheres are predicted to move towards seasonal ice cover during the 21st century. The differences between the projections provided by the various models are quite large and so are the uncertainties, but many simulations forecast a totally ice-

free Arctic in summer before the end of the 21st century, although some ice would still be present in winter (Fig. 6.12).

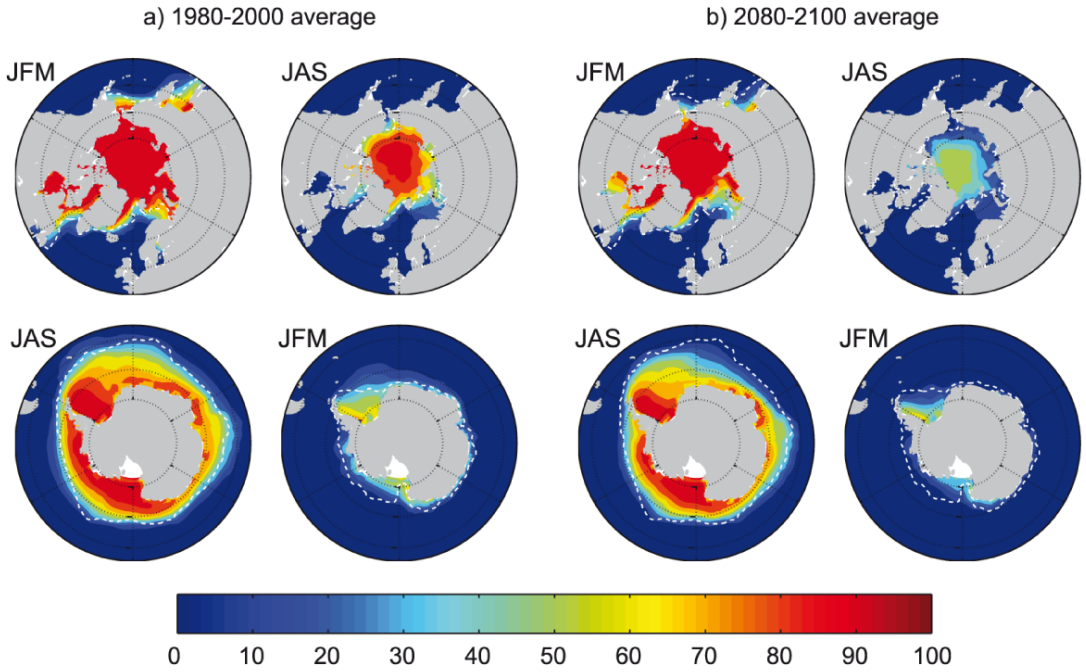

Figure 6.12: Multi-model mean sea ice concentration (%) for January to March (JFM) and June to September (JAS), in the Arctic (top) and Antarctic (bottom) for the periods (a) 1980 to 2000 and b) 2080 to 2100 for the SRES A1B scenario. The dashed white line indicates the present-day 15% average sea ice concentration limit. Figure 10.14 of Meehl et al. (2007), reproduced with permission from IPCC.

Ocean circulation is also projected to change during the 21st century. Because of the warming and the increase in precipitation at high latitudes (see Section 6.2.2), the density of the water at the surface will tend to decrease, increasing the stratification in many regions. In the North Atlantic, this would imply less sinking of dense water and a weaker southward transport of dense water. As a consequence, the northward transport of warm surface water will also decrease with potential implications for the heat budget of the North Atlantic and the surrounding regions.

The intensity of this **thermohaline circulation** is generally measured by the maximum of the **meridional overturning circulation** (MOC) in the North Atlantic, although the two concepts are slightly different (the overturning circulation also including the contribution from the winds). The scatter of the results for the thermohaline circulation from the different GCMs is very large, both for present-day conditions and for the whole 21st century (Fig. 6.13). Three simulations show a clear slow down during the 20th century. This is not related to the forcing during this period, but rather to a slow drift of the model to a state that is inconsistent with observational estimates. All the other models have more realistic predictions for the 20th century, with the meridional overturning circulation ranging from a more or less stable situation over the 21st century to decreases of more than 50% compared to the late 20th century. None of them simulates a complete collapse of the circulation, a state which is sometimes referred to as the off-state of the meridional overturning circulation.

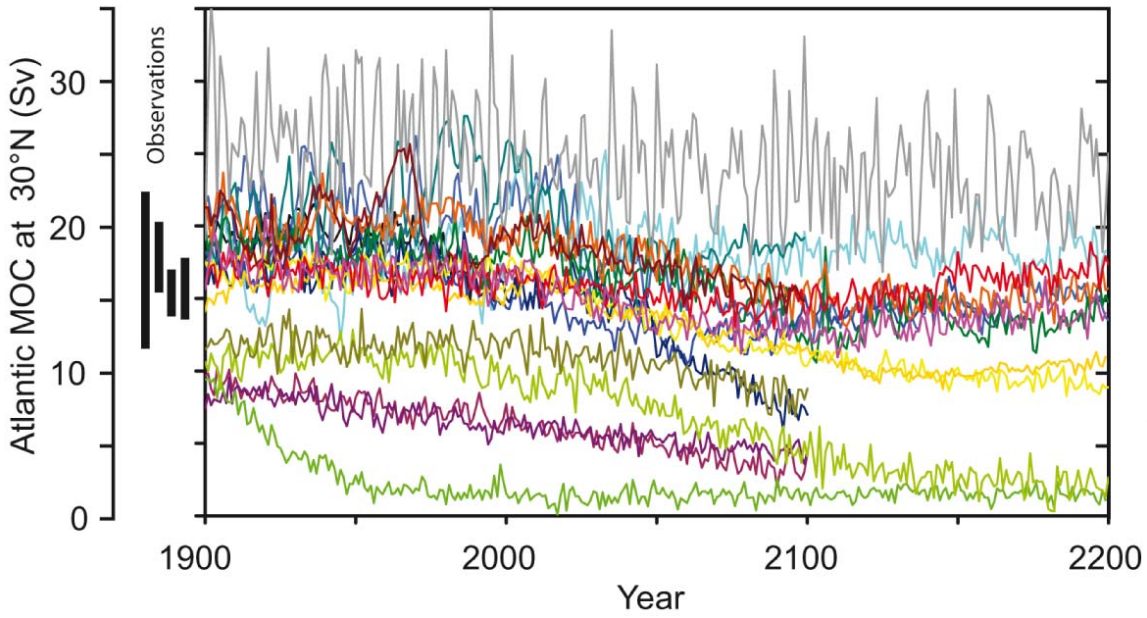

Figure 6.13 The changes in the Atlantic **meridional overturning circulation** (MOC) at 30°N in simulations with several coupled climate models from 1850 to 2100 using the SRES A1B emissions scenario for 1999 to 2100 (in Sv=10^6 m^3 s^{-1}). Some of the models continue the integration to year 2200 with the forcing held constant at the values of year 2100. Observationally based estimates of late-20th century MOC are shown as vertical bars on the left. Modified from Figure 10.15 of Meehl et al. (2007), reproduced with permission from IPCC

6.2.4 Changes in the carbon cycle and climate-carbon feedbacks

In the previous two sections, we have briefly described the influence of anthropogenic forcing on climate. In turns, climate changes have impacts on the biogeochemical cycles, leading to modifications of the **radiative forcing** with potential feedback effects on climate. Among all the complex mechanisms involved, we will focus here on CO_2 as it is the dominant anthropogenic gas (see Section 4.1.2.1).

As mentioned in Section 2.3.1, about half of the anthropogenic CO_2 emitted by fossil-fuel burning and changes in land use has stayed in the atmosphere. The remaining half is stored approximately equally in the ocean and terrestrial biosphere. However, this division of anthropogenic emissions between atmospheric, oceanic and land reservoirs will change in the future.

First, the changes in atmospheric CO_2 concentration itself modify the atmosphere-ocean and atmosphere/land CO_2 fluxes. The balance between H_2CO_3, HCO_3^- and carbonate ions CO_3^{2-} explains why the ocean is able to store large amounts of CO_2. (see section 2.3.2.1). In particular, the CO_2 which is transferred from the atmosphere reacts with the water to form H_2CO_3 and with carbonate ions (CO_3^{2-}) to obtain bicarbonate ions (HCO_3^-), the dominant form of inorganic carbon in the ocean:

$$H_2CO_3 + CO_3^{2-} \rightleftharpoons 2HCO_3^- \qquad (6.1)$$

The CO_2 flux from the atmosphere to the ocean during the 20th and 21st centuries will tend to decrease the availability of carbonates ions (at least on time scales from decades to centuries, see Section 6.3.1). This will reduce the efficiency of reaction (6.1)

to form bicarbonates from CO_2. A larger fraction of the **dissolved inorganic carbon** (*DIC)* will remain as H_2CO_3, increasing the partial pressure of carbon dioxide in the ocean and thus reduce the oceanic uptake (see Eq. 2.38). As a consequence, the ocean will continue to store some anthropogenic CO_2, but its relative contribution will decrease.

Over land, the increase of CO_2 concentration in the atmosphere generally implies more assimilation and sequestration of carbon by the terrestrial biosphere through photosynthesis (see Equation 2.46). This CO_2 fertilisation effect is not related to any limitation of plant productivity by CO_2 availability in present-day conditions, but rather to the predicted better regulation of the plant/atmosphere gas exchanges through **stomata** in future. With high levels of CO_2, smaller exchanges are required for the same CO_2 uptake, implying less transpiration and thus an increase in plants' efficiency of water use. However, many factors limit plant growth, including the availability of nutrients. The long term and large-scale effect of the CO_2 fertilisation effect have not yet been precisely assessed.

These biogeochemical effects (also referred to as concentration effects) will occur even in the absence of any climate change induced by changes in the atmospheric composition. Global warming will also reduce the oceanic solubility of CO_2 (see Section 2.3.2.1). This is one example of a positive climate-carbon cycle feedback. In addition, increased stratification and slower oceanic circulation (see Section 6.2.3) are expected to reduce the exchanges between the surface layers rich in anthropogenic carbon and the deeper layer. The deeper water does not yet contain a significant amount of anthropogenic carbon because of the relatively slow oceanic overturning and diffusion rates (see Section 1.3.2), so the slower renewal of surface waters will tend to induce higher levels of *DIC* at the surface and thus reduce the oceanic uptake of carbon, providing another positive climate/carbon feedback. Changes in marine **biota** could also lead to some feedback loops, but they are not currently well understood. Present-day models suggest that their role is relatively unimportant, but the modelling of marine ecosystems is still very simple, and more precise estimates of those effects are required.

Temperature and precipitation changes also affect the carbon cycle on land. Warming tends to accelerate decomposition in soils, which releases CO_2 to the atmosphere. The primary production is enhanced by warming in cold areas and by an increase in precipitation in dry areas. In addition, in warm, dry areas where water availability is a limiting factor, a decrease in precipitation produces a reduction in productivity and thus in the uptake of CO_2 by vegetation. In addition, climate changes influence the distribution of biomes (see, for instance, Section 4.3.3) as well as the frequency and extent of wildfires (savannah and forest fires) which emit substantial quantities of CO_2. This illustrates that both positive and negative carbon/climate feedbacks are expected over land in different regions.

In order to estimate the influence of the feedback between climate changes and the carbon cycle, simulations have been performed with climate models including a representation of the carbon cycle (Friedlingstein et al., 2006). In the first group of numerical experiments, both the carbon cycle and the climate were allowed to change in response to anthropogenic CO_2 emissions (SRES A2 scenario). In the second group, the models were again driven by CO_2 emissions, but the climate was kept constant. In other words, the increase in CO_2 was not associated with any change in the **radiative forcing**. Because of this constant climate, the climate/carbon feedback loops were inactive, and it was thus possible in this idealised set-up to measure the contribution of biological processes (the concentration effects) to the changes in the carbon cycle. By studying the difference between the two groups of models, it was then possible to make a first-order estimate of the influence of the carbon/climate feedback loops.

In the fully coupled experiments, where climate and the carbon cycle interact, the concentration of atmospheric CO_2 is predicted to be between 20 and 220 ppm higher than in the constant-climate system by 2010 (Fig. 6.14). The net climate/carbon feedback effect is positive for all the models. This clearly indicates that the modifications in climate mean that a larger fraction of anthropogenic CO_2 will remain in the atmosphere in the future. The models suggest that this is mainly due to the terrestrial biosphere, which will display changes in primary productivity and increased soil respiration in future.

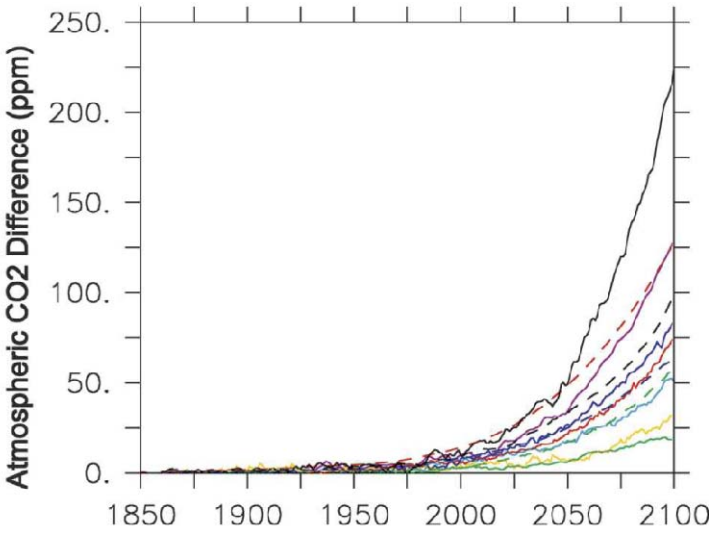

Figure 6.14: Difference between the atmospheric CO_2 predicted by different models of the coupled and uncoupled carbon cycles (ppm) (Friedlingstein et al. 2006). Copyright AMS 2006.

The projections made by models including a carbon cycle driven by emissions of CO_2 can be compared to those directly driven by CO_2 concentrations (Fig. 6.15). It must be recalled here that the concentrations in the SRES scenarios (Section 6.1.2) were obtained using a carbon-cycle model that includes its own representation of climate/carbon feedbacks. Consequently, Figure 6.15 does not display the results of simulations with and without climate/carbon feedbacks, but rather illustrates the impact of different representations of those feedbacks. A first important feature is the large increase in the range of projections in the simulations including carbon-cycle models. Changes in the carbon cycle are thus a key source of uncertainty in climate projections. Second, in the majority of the cases, the projected temperature changes in 2100 are larger in the coupled climate/carbon cycle models, leading to a range of temperature increases of 2.3–5.6°C for Scenario A2.

Another consequence of the flux of anthropogenic carbon from the atmosphere to the ocean is oceanic acidification (see Eqs. 2.39 to 2.41). Over the period 1750-1994, the surface **pH** of the global ocean decreased by about 0.1. The expected decrease by 2100 is about 0.3–0.4 for a standard scenario, the precise value depending on the level of CO_2 emissions. By the year 3000, the decrease may be as high as 0.7. This would lead to **pH** values lower than those estimated for the last few hundred million years.

This ocean acidification increases the solubility of $CaCO_3$, (see Section 4.3.1); this could also be related to the reduced CO_3^{2-} concentration due to oceanic uptake of CO_2. This will have a clear impact on $CaCO_3$ production by corals as well as by calcifying phytoplankton and zooplankton, and thus on their life cycles (see Section 2.3.2.2). The **aragonite** produced by, for instance, corals, will be particularly influenced by this change as it is less stable than **calcite**.

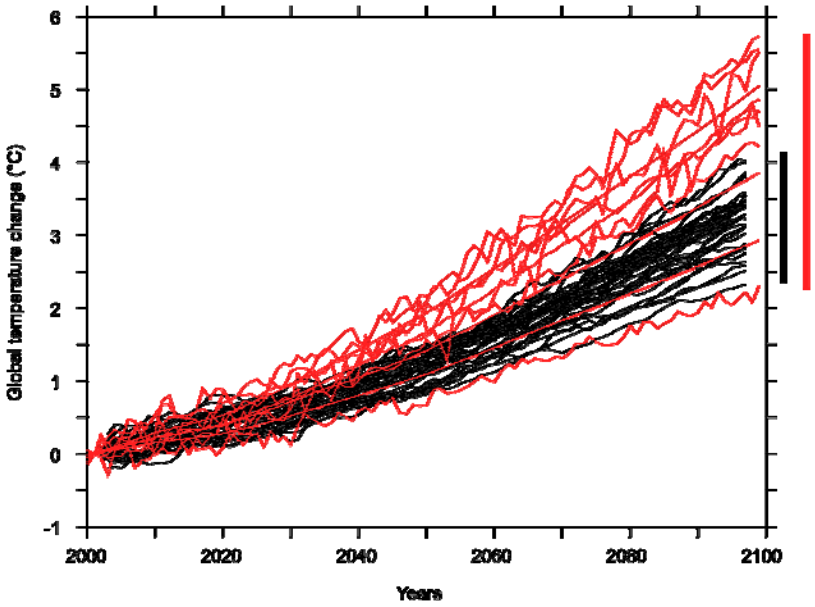

Figure 6.15: Globally averaged surface temperature change (relative to 2000) derived from the coupled climate-carbon cycle models (red) compared to simulations performed with climate models driven by CO_2, other greenhouse gas and anthropogenic aerosols concentrations (black, as in Section 6.2.1). (Cadule et al. 2009). Copyright AGU 2009.

6.3 Long-term climate changes

6.3.1 The carbon cycle

The interactions between the atmosphere, the land biosphere and the ocean surface layer take place relatively rapidly, and are predicted to play a dominant role in the changes in atmospheric CO_2 concentration over the 21st century (see Section 6.2.4). By contrast, the exchanges of CO_2 with the deep ocean are much slower, taking place on timescales from centuries to millennia. Consider, for instance, a strongly idealised scenario in which CO_2 emissions follow a pathway that would lead to a long-term stabilisation at a level of 750 ppm but, before reaching this level, the emissions were abruptly reduced to zero in 2100. The goal here is not to provide a realistic projection but to analyse the long-term changes in the system after all emissions cease. Figure 6.7 includes an estimate of the warming during the 21st century if the CO_2 concentrations were stabilised at the 2000 level; here, Figure 6.16 shows the changes in CO_2 and surface temperature which will still take place even if there are no additional emissions after 2100.

In all the models driven by this scenario, atmospheric CO_2 concentration decreases after 2100. The deep ocean is not in equilibrium with the surface in 2100, and so carbon uptake by the deep ocean continues during the whole of the third millennium. Depending on the model, the concentrations reached by the year 3000 are between 400 and 500 ppm, i.e. much higher than the pre-industrial level.

Despite this decrease in the CO_2 concentration, the global mean surface temperature is more or less stable during the third millennium, with the majority of models predicting only a slight cooling. The **radiative** forcing due to CO_2 decreases after 2100 but the heat uptake by the ocean also decreases (see Section 4.1.4) as the ocean warms. The two effects nearly balance each other, leading to the simulated stabilisation of temperature.

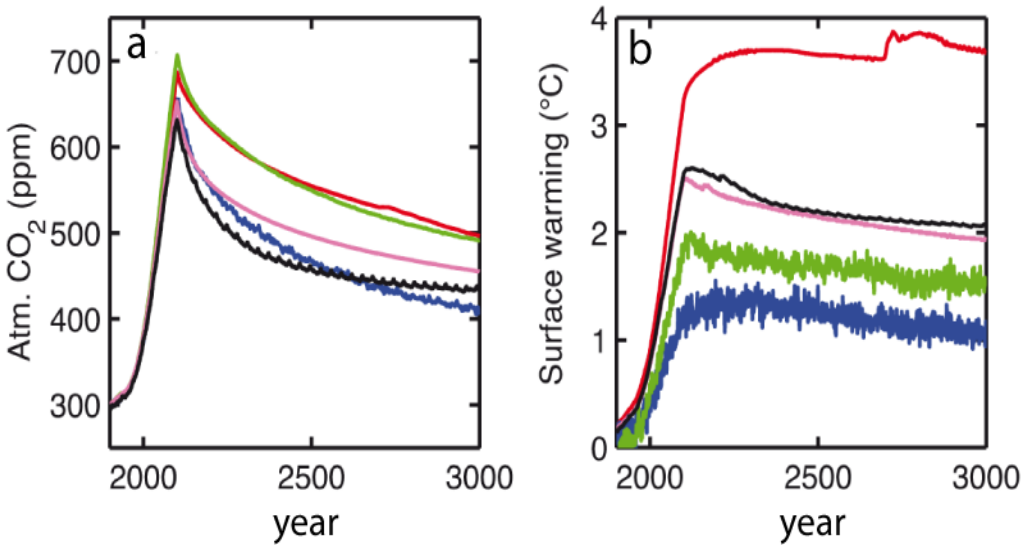

Figure 6.16: Changes in (a) atmospheric CO_2 and (b) global mean surface temperature relative to the pre-industrial period simulated by five intermediate-complexity models for a scenario where the emissions follow a pathway leading to stabilisation of the atmospheric CO_2 at 750 ppm, but, before reaching this target, the emissions are reduced to zero in the year 2100. Modified from Figure 10.35 of Meehl et al. (2007), reproduced with permission from IPCC.

The results displayed in Figure 6.16 mainly deal with the long-term adjustment between the ocean and the atmosphere. However, on long timescales, the changes in acidity caused by the oceanic uptake of CO_2 induce dissolution of some of the $CaCO_3$ in the sediments (carbonate compensation, see Section 4.3.1), modifying the ocean **alkalinity** and allowing an additional uptake of atmospheric CO_2. Those processes are neglected in the models used in Figure 6.16. If they are included, the interaction with $CaCO_3$ in the sediments increases the ability of the ocean to store CO_2, producing a further reduction of the atmospheric concentration. However, this process is very slow and after 10,000 years, the atmospheric CO_2 concentration is still predicted to be significantly higher than in pre-industrial times (Fig. 6.17). Even after several tens of thousands of years, the atmospheric CO_2 will not return to pre-industrial levels through this mechanism. On even longer timescales, this will be achieved by the reactions of CO_2 with some rocks, and in particular by the negative feedback caused by weathering (see Section 4.3.2). Because of this long term perturbation of the carbon cycle, the temperature remains significantly higher than in pre-industrial times during the whole period investigated in Figure 6.17, the amplitude of the temperature rise over several millennia being related to the release of carbon at the end of the second and the beginning of the third millennia.

This section illustrates that, because of the wide variety of processes involved, we cannot reliably estimate the timescale for the response of atmospheric CO_2 concentration to fossil fuel burning, as we could for other anthropogenic **forcings** (Figure 4.2). To give an accurate representation of the time changes of atmospheric CO_2 concentration, several different timescales, corresponding to the dominant mechanisms, are required

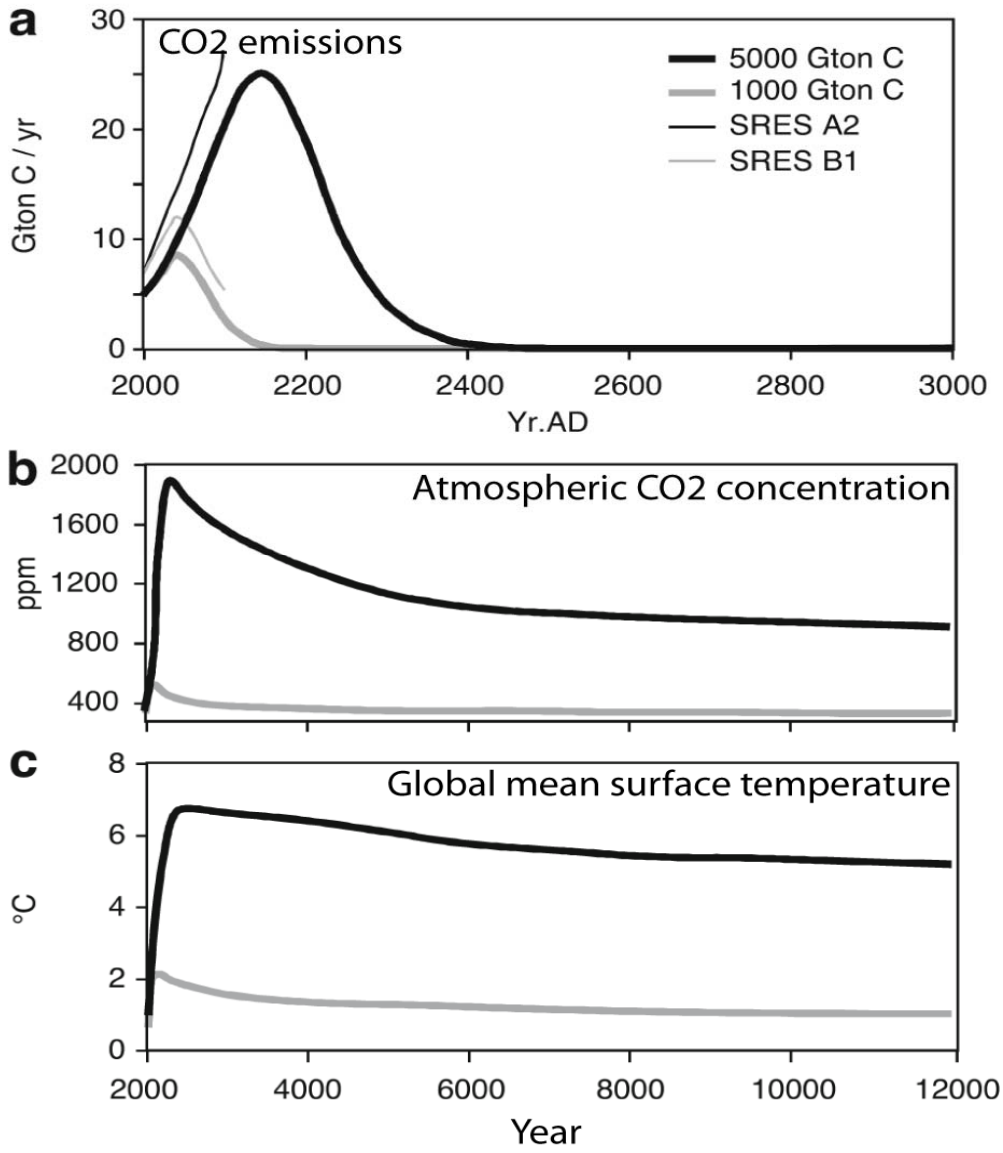

Figure 6.17: The response of the climate model of intermediate complexity CLIMBER-2 to moderate (1,000 Gton C) and large (5,000 Gton C) total fossil fuel emissions. The equilibrium climate sensitivity of the model is 2.6°C. The land carbon cycle was neglected in these simulations while deep sea sediments were explicitly simulated using a sediment model. (a) Emissions scenarios and reference IPCC SRES scenarios (B1 and A2, see Fig. 6.2). (b) Simulated atmospheric CO_2 (ppm). (c) Simulated changes in global annual mean air surface temperature (°C). Figure from Archer and Brovkin (2008). Copyright Archer and Brovkin (2008).

6.3.2 Sea level and ice sheets

Sea levels have changed for two main reasons in recent decades (Fig. 6.18). First water has been added to the ocean from other reservoirs. The main contributors are the glaciers and ice caps that have experienced considerable mass losses during the 20th century because of the large-scale surface warming observed over this period (see Section 5.5.3). The melt water flow from Greenland and Antarctica is relatively small on this time scale, and it is not even clear whether the net flow from the Antarctic is positive or negative.

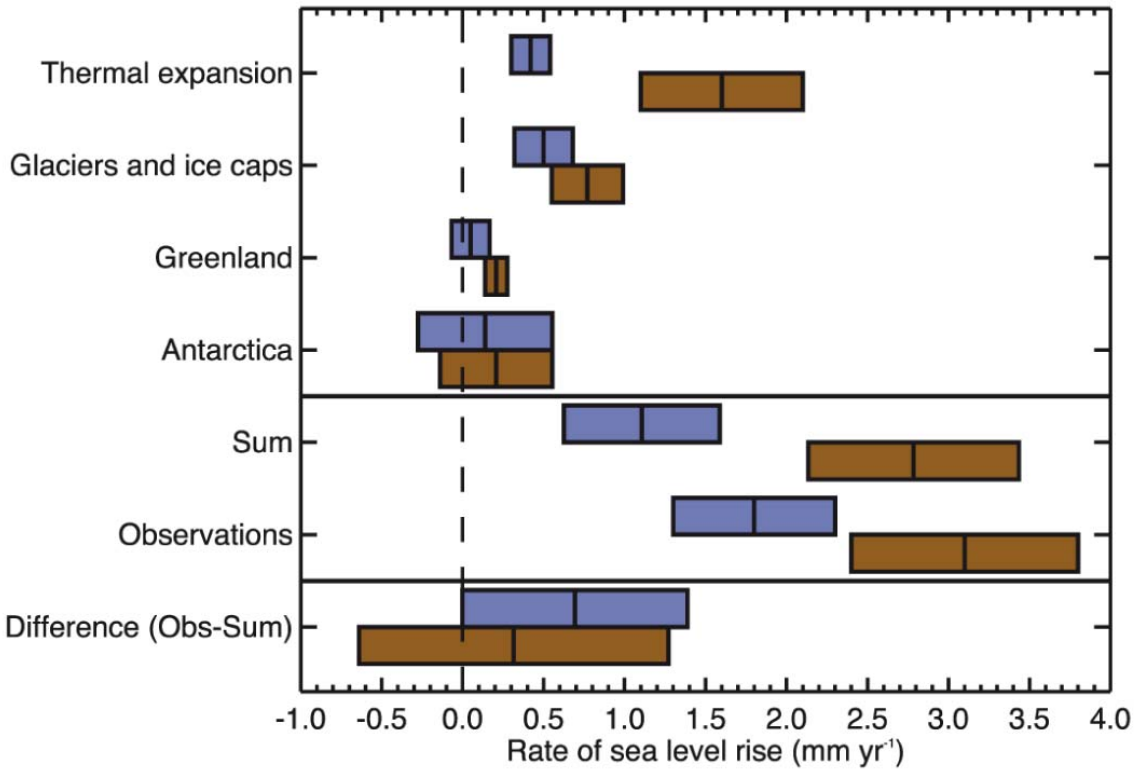

Figure 6.18: Estimates of the various contributions to the budget of the global mean sea level change (upper four entries), the sum of these contributions and the observed rate of rise (middle two), and the observed rate minus the sum of contributions (lower), all for 1961 to 2003 (blue) and 1993 to 2003 (brown). The bars represent the 90% error range. For the sum, the error has been calculated as the square root of the sum of squared errors of the contributions. Likewise the errors of the sum and the observed rate have been combined to obtain the error for the difference. Figure 5.21 of Binoff et al. (2007) with a modified legend, reproduced with permission from IPCC.

The second cause of sea level change is related to the ocean density. For a constant oceanic mass, any modification of the density affects the ocean volume and thus the sea level. As the density variations are mainly ruled by the water temperature, this term is often referred to as **thermal expansion**, although salinity changes can play a non negligible role in some regions. The contribution of this process is similar to that of glaciers and ice caps over the period 1961-2003 but it is clearly the largest contributor if the analysis is restricted to the period 1993-2003. However, this is maybe related to decadal climate variability (Fig. 6.18). Overall, the sea level rise has been estimated at about 1.8 mm yr^{-1} over the period 1961-2003. This is not very different from estimates for the first half of the 20^{th} century but much less than those for the years 1993-2003. Integrated over the whole 20^{th} century, the total sea level rise is then a bit less than 20 cm.

Over the 21^{st} century, the melting of glaciers and ice caps and thermal expansion are expected to remain the two main causes of rising sea levels. Greenland will likely make a small positive contribution. However some frozen water may accumulate over Antarctica, the additional precipitation over a large area of the continent, related to warming (see Section 6.2.3), being approximately equal to the additional melting close to the shore. Indeed, temperatures in the centre of Antarctica are so low that the warming estimated for the 21^{st} century is far too small to produce melting there.

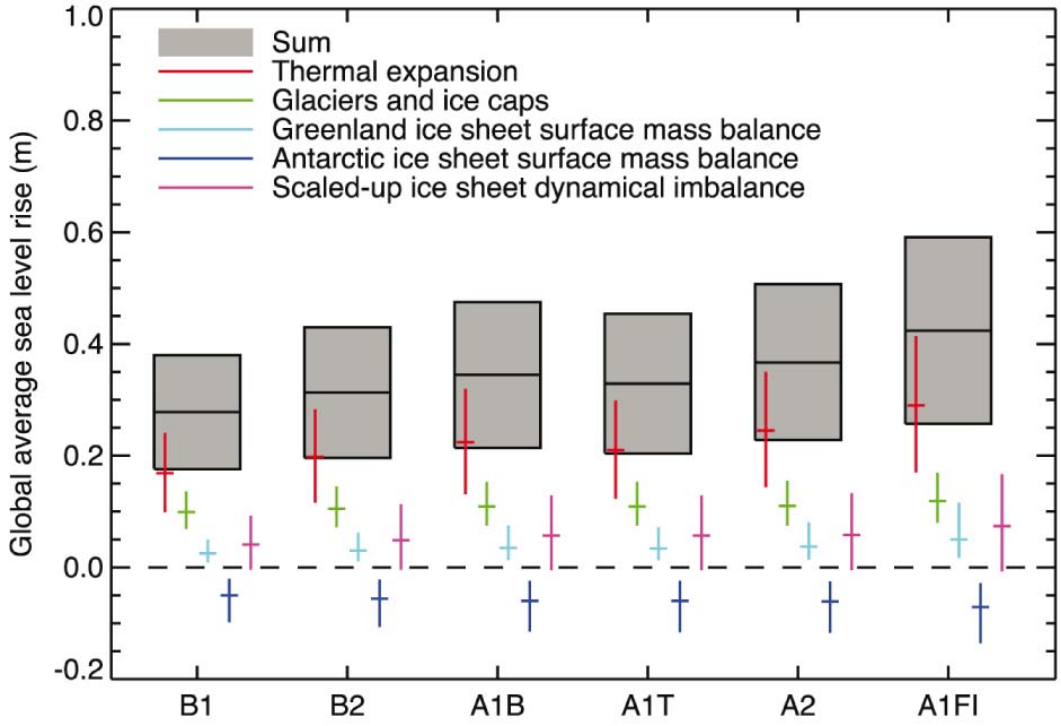

Figure 6.19: Projections and uncertainties (5 to 95% ranges) of global average sea level rise and its components in 2090 to 2099 (relative to 1980 to 1999) for the six SRES marker scenarios. The projected sea level rise assumes that the part of the present-day ice sheet mass imbalance that is due to recent ice flow acceleration will persist unchanged. Figure 10.33 of Meehl et al. (2007) with a modified legend, reproduced with permission from IPCC.

Depending on the scenario, the estimates of sea levels at the end of the 21st century range from 20 to 60 cm higher than in the late 20th century in the latest IPCC report (Figure 6.19). However, many uncertainties remain. The ice-sheet models used to obtain these estimates (see Section 3.3.6) do not include an adequate representation of the rapid ice flow changes that occur on relatively small scales (a kilometre or even less, to a few hundreds of metres), which may transport ice to the ocean or to warmer areas where it would melt relatively quickly. These fast ice-flow changes may be high frequency fluctuations that average out when looking at changes over a century or more. However, it has also been hypothesised that they could induce large-scale destabilisation of parts of the ice sheets, with potentially large consequences for the mass balance of the ice sheet and thus for sea-level rises. As a consequence, alternative methods have been proposed, based on simple statistical relationships between the rises in surface temperatures and sea levels. These studies predict that sea-level rises ranging from 75 to 190 cm by the end of the 21st century are not unlikely (e.g., Vermeer and Rahmstorf, 2009).

Even if the concentration of atmospheric CO_2 stabilises or decreases after 2100, sea levels are predicted to continue to rise fast (see Figure 6.16). First, the deep ocean will have to come into equilibrium with the new surface conditions, leading to warming at deeper levels, and thus thermal expansion over several centuries (Fig. 6.20).

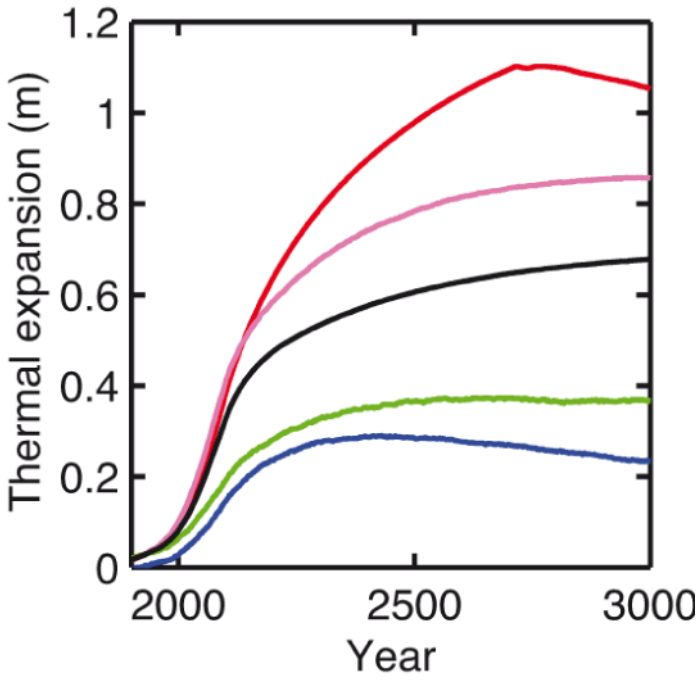

Figure 6.20: Changes in sea level (relative to the pre-industrial period) caused by thermal expansion, as simulated by the same five intermediate-complexity models as in Figure 6.16, for a scenario where emissions follow a pathway leading to stabilisation of atmospheric CO_2 at 750 ppm, but before reaching this target, emissions are reduced to zero instantly at year 2100. Modified from Figure 10.35 of Meehl et al. (2007), reproduced with permission from IPCC.

Second, the thermal inertia of the ice sheets is very large, taking several millennia to tens of millennia to completely melt, even when the warming is considerable. For Greenland, it has been estimated that a sustained local warming of the order of 3–6°C, which is not incompatible with the values provided by models of several scenarios, may be sufficient to induce a complete melting of the ice sheet. The ice sheet would start to melt on its periphery, and would gradually retreat to the centre of the island, to finally survive only in the eastern mountains (see Figure 6.21). As the Greenland ice sheet retreats, the bedrock will slowly rebound because of the smaller weight on the surface. This will initially cause a series of big inland lakes to appear below sea level. After 3000 years, almost all the initial depressed areas will have risen above sea level again. Such a complete melting of the Greenland ice sheet is predicted to produce a rise in sea level of about 7m.

The melting in Antarctica will be much smaller and slower even than that in Greenland, because of the size of the ice sheet and the very cold temperatures there at present. However, some regions of East Antarctica may experience a significant melting on similar timescales to those of Greenland.

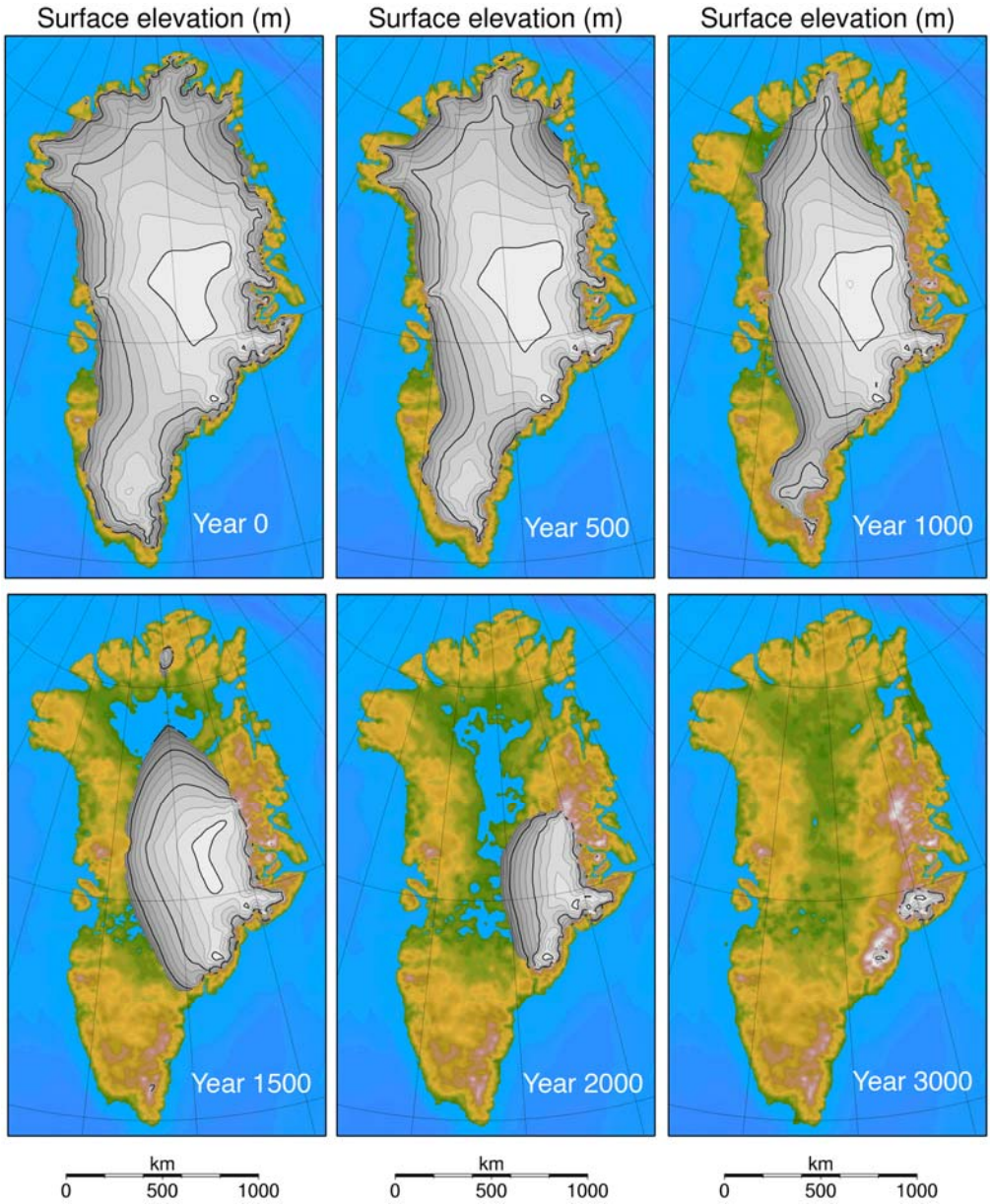

Figure 6.21: Snapshots of the changes in the Greenland ice sheet in a scenario in which the CO_2 concentration is maintained at four times the pre-industrial value (4-times CO_2 scenario) for 3000 years. The results come from the intermediate-complexity climate model LOVECLIM, and show the conditions at the present land surface. The sea and land below sea level is shown in blue, ice-free tundra in brown and green, and the ice sheet in grey. The contour intervals over the ice are 250 m, with thick lines at 1000 intervals (Fichefet et al., 2007).

Cited references and further reading

Archer D. and V. Brovkin (2008). The millennial atmospheric lifetime of anthropogenic CO_2 Climatic Change 90, 283-297.

Bindoff, N.L., J. Willebrand, V. Artale, A, Cazenave, J. Gregory, S. Gulev, K. Hanawa, C. Le Quéré, S. Levitus, Y. Nojiri, C.K. Shum, L.D. Talley and A. Unnikrishnan, (2007). Observations: Oceanic Climate Change and Sea Level. In: Climate Change 2007: The Physical Science Basis. Contribution of Working Group I to the Fourth Assessment Report of the Intergovernmental Panel on Climate Change [Solomon, S., D. Qin, M. Manning, Z. Chen, M. Marquis, K.B. Averyt, M. Tignor and H.L. Miller (eds.)]. Cambridge University Press, Cambridge, United Kingdom and New York, NY, USA. (www.ipcc.ch).

Cadule P;, L. Bopp, and P. Friedlingstein (2009). A revised estimate of the processes contributing to global warming due to climate-carbon feedback. Geophys. Res. Lett. 36, L14705, doi:10.1029/2009GL038681

Fichefet, T., E. Driesschaert, H. Goosse, P. Huybrechts, I. Janssens, A. Mouchet, and G. Munhoven, 2007: Modelling the evolution of climate and sea level during the next millennium (MILMO). Scientific Support Plan for a Sustainable Development Policy, SPSD II, Part 2: Global Change, Ecosystems and Biodiversity, Atmosphere and Climate, Belgian Science Policy, Brussels, 131 pp.

Friedlingstein P., P. Cox, R. Betts, L. Bopp, W. Von Bloh, V. Brovkin, P. Cadule,S. Doney, M. Eby, I. Fung, G. Bala, J. John, C. Jones, F. Joos, T. Kato, M. Kawamiya,W. Knorr, K. Lindsay, H. D. Matthews, T. Raddatz, P. Rayner, C. Reick, E. Roeckner,K.-G. Schnitzler, R. Schnur, K. Strassmann,A. J. Weaver, C. Yoshikawa, and N. Zeng (2006). Climate–carbon cycle feedback analysis: results from the C4MIP model intercomparison. Journal of Climate, 19, 3337, 3353.

Hawkins E. and R. Sutton (2009). The potential to narrow uncertainty in regional climate predictions', Bulletin of the American Meteorological Society, 90, 1095-1107 (http://journals.ametsoc.org/doi/abs/10.1175/2009BAMS2607.1).

Meehl, G.A., T.F. Stocker, W.D. Collins, P. Friedlingstein, A.T. Gaye, J.M. Gregory, A. Kitoh, R. Knutti, J.M. Murphy, A. Noda, S.C.B. Raper, I.G. Watterson, A.J. Weaver and Z.-C. Zhao, 2007: Global Climate Projections. In: Climate Change 2007: The Physical Science Basis. Contribution of Working Group I to the Fourth Assessment Report of the Intergovernmental Panel on Climate Change [Solomon, S., D. Qin, M. Manning, Z. Chen, M. Marquis, K.B. Averyt, M. Tignor and H.L. Miller (eds.)]. Cambridge University Press, Cambridge, United Kingdom and New York, NY, USA. (www.ipcc.ch).

Moss R., M. Babiker, S. Brinkman, E. Calvo, T. Carter, J. Edmonds, I. Elgizouli, S. Emori, L. Erda, K. Hibbard, R. Jones, M. Kainuma, J. Kelleher, J.-F. Lamarque, M. Manning, B.Matthews, J. Meehl, L. Meyer, J. Mitchell, N. Nakicenovic, B. O'Neill, R. Pichs, K. Riahi, S. Rose, P. Runci, R. Stouffer, D. van Vuuren, J. Weyant, T. Wilbanks, J. P. van Ypersele, M. Zurek (2007). Towards new scenarios for analysis of emissions, climate change, impacts, and response strategies, IPCC expert meeting report, 19–21 September, 2007, Noordwijkerhout, The Netherlands, 166 pp. (http://www.aimes.ucar.edu/docs/IPCC.meetingreport.final.pdf).

Moss R.H., J. A. Edmonds, K. A. Hibbard, M. R. Manning, S. K. Rose, D. van Vuuren, T. R. Carter, S. Emori, M. Kainuma, T. Kram, G. A. Meehl, J. F. B. Mitchell, N.

Nakicenovic, K. Riahi, S. J. Smith, R. J. Stouffer and A. M. Thomson (2010). The next generation of scenarios for climate change research and assessment. Nature 463, 747-756.

Nakicenovic N. and R. Swart (eds.) (2000). IPCC Special report on emission scenarios Cambridge University Press, UK. pp 570 (http://www.ipcc.ch/ipccreports/sres/emission/index.php?idp=0).

Solomon, S., D. Qin, M. Manning, R.B. Alley, T. Berntsen, N.L. Bindoff, Z. Chen, A. Chidthaisong, J.M. Gregory, G.C. Hegerl, M. Heimann, B. Hewitson, B.J. Hoskins, F. Joos, J. Jouzel, V. Kattsov, U. Lohmann, T. Matsuno, M. Molina, N. Nicholls, J. Overpeck, G. Raga, V. Ramaswamy, J. Ren, M. Rusticucci, R. Somerville, T.F. Stocker, P. Whetton, R.A. Wood and D. Wratt, 2007: Technical Summary. In: Climate Change 2007: The Physical Science Basis. Contribution of Working Group I to the Fourth Assessment Report of the Intergovernmental Panel on Climate Change [Solomon, S., D. Qin, M. Manning, Z. Chen, M. Marquis, K.B. Averyt, M. Tignor and H.L. Miller (eds.)]. Cambridge University Press, Cambridge, United Kingdom and New York, NY, USA.

Vermeer M. and S. Rahmstorf, 2009. Global sea level linked to global temperature. Proceedings of the National Academy of Sciences, 106 21527-21532 (http://www.pnas.org/content/106/51/21527)

Exercises

Exercises are available on the textbook website (http://www.climate.be/textbook) and on iCampus for registered students.

Web links

RCP Database http://www.iiasa.ac.at/web-apps/tnt/RcpDb/dsd?Action=htmlpage&page=welcome#intro

Glossary

This glossary is not intended to provide a general definition of the terms selected but rather to give an explanation of the meaning of those terms as employed in climatology. The glossary of the IPCC 2007 (http://www.ipcc.ch/pdf/assessment-report/ar4/wg1/ar4-wg1-annexes.pdf) and Wikipedia, the free encyclopaedia (http://en.wikipedia.org/wiki/Main_Page) were very helpful in preparing it. We encourage the reader to refer to these sources for more information.

Aerosols
Atmospheric aerosols are relatively small solid or liquid particles that are suspended (float) in the atmosphere. They can be produced naturally or by human activities. Their size typically ranges from a few hundredths of a micrometer to several micrometers. Aerosols have an influence on the radiative balance of the Earth.

Albedo
The albedo (α) is the ratio between reflected and incoming **radiation**. It varies between 0 for a perfect **black body** that absorbs all the incoming radiation to 1 for a surface that reflects it all. It depends on the wavelength, but the general term usually refers to some appropriate average across the spectrum of visible light or across the whole spectrum of solar radiation.

Alkalinity
The total alkalinity *(Alk)* is defined as the excess of bases over acid in sea water.

Anomaly
The anomaly of a variable (e.g., temperature) is the difference between the value under consideration and the long-term mean for the corresponding period or location.

Aphelion
The aphelion is the point in the Earth's orbit that is furthest from the Sun.

Aragonite
Aragonite is a form of calcium carbonate ($CaCO_3$). It has a different crystal lattice and crystal shape than **calcite**.

Ascendance
An ascendance is an upward movement of air in the atmosphere.

Atmospheric boundary layer
The atmospheric boundary layer is the lowest part of the atmosphere which is in direct contact with the Earth's surface. The properties of this layer are directly influenced by the presence of the surface, and in turn they influence the exchanges between the surface and the atmosphere. Vertical mixing is usually strong in this layer because of the relatively intense turbulent motions.

Austral
Austral is a synonym for 'southern'.

Bathymetry
Bathymetry is the topography of the floor of the ocean. It also refers to the measurement of the depth of the oceans.

Biogeochemical feedbacks
Biogeochemical feedbacks are **feedbacks** that involve interactions between **climate**, biological activity and the biogeochemical cycles on Earth.

Biogeophysical feedbacks
Biogeophysical feedbacks are **feedbacks** that involve the interactions between **climate** and some physical characteristics of the surface that are influenced by biological activity.

Biomes
Biomes are regions with distinctive large-scale vegetation types.

Biosphere
The biosphere is the part of the Earth System comprising all the living organisms in the atmosphere, on land (terrestrial biosphere) and in the ocean (marine biosphere), including derived dead organic matter, such as litter, soil organic matter and oceanic detritus (from IPCC, 2007).

Biota
Biota is the total collection of organisms of a geographic region or a time period.

Black body
A black body is an object or system that absorbs all **electromagnetic radiation** incident upon it.

Blooms
Phytoplankton blooms are rapid increases in the mass of **phytoplankton**.

Boreal
Boreal is a synonym for 'northern'.

Calcite
Calcite is a form of calcium carbonate ($CaCO_3$). It is one of the most widely distributed minerals on Earth and is a constituent of sedimentary rocks, in particular **limestone**.

Calcite compensation depth
The calcite compensation depth (CCD) is the depth at which the input of calcite from **sedimentation** exactly balances the **dissolution** at the top of the sediments. At the CCD there is thus very little calcite left in the old sediment, because it has all dissolved.

Calibration
Calibration is the adjustment of the numerical or physical parameters in a model to improve the agreement between the results of the model and observations.

Canopy
The canopy is the above-ground portion of a plant community formed by plant crowns.

Carbonate compensation
Carbonate compensation is a negative **feedback** between the oceanic carbon cycle and the underlying sediments that tends to reduce the variations in the **alkalinity** in the ocean and thus to stabilise the atmospheric CO_2 over long timescales.

Carbonate pump
The carbonate pump is a net downward flux of carbon associated with the transport of calcium carbonate from the surface layer, where it is produced because of biological activity, to the deeper layers where it can be dissolved.

Celestial equator
The celestial equator is the projection of the Earth's equator onto the **celestial sphere**.

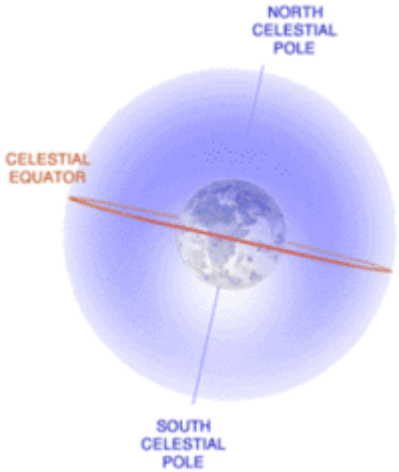

The celestial equator. Source: NASA. Following the policy of U.S. government agencies, this figure is not subject to copyright protection.

Celestial sphere
The celestial sphere is an imaginary sphere with a very large radius whose centre is the centre of the Earth.

Chlorofluorocarbons
Chlorofluorocarbons (or CFCs) are gases derived from alkanes (e.g., methane or ethane) in which all the hydrogen atoms have been replaced by chlorine or fluorine. They are a subset of the **halocarbons**. Chlorofluorocarbons have been widely used in refrigerators, insulation and aerosol spray cans. However, because they have been shown to contribute to **stratospheric ozone** depletion, their use is now banned.

Clausius-Clapeyron equation
The Clausius-Clapeyron equation gives the relationship between the **latent heat** associated with a transition from Phase 1 to Phase 2 ($L_{1\to 2}(T)$) at the equilibrium temperature T, the volume $V_1(T,P)$ of the matter in Phase 1, the volume $V_2(T,P)$ of the matter in Phase 2 and the slope of the line separating the two phases in a T-P diagram (i.e. dP/dT)

$$L_{1\to 2}(T) = T\left(V_2(T,P) - V_1(T,P)\right)\frac{dP}{dT}$$

For the transition between the liquid and vapour phase in the atmosphere, the Clausius-Clapeyron equation can be written as:

$$L_v(T) = T\left(V_{vapour} - V_{liquid}\right)\frac{de_s}{dT}$$

where V_{vapour} and V_{liquid} are the volumes of the water in the vapour and liquid phases, and e_s is the saturation vapour pressure. This relationship can be used to compute the variation of e_s as a function of temperature:

$$\frac{de_s}{dT} = \frac{T}{L_v(T)}\left(V_{vapour} - V_{liquid}\right)$$

If we consider water vapour as a perfect gas, the volume of the vapour is much larger than that of the liquid, and if we also assume that L_v is a constant (which is a strong approximation), we can express e_s as a function of the temperature T by integrating this equation between 273.15K (for which e_s = 611 Pa) and the temperature T:

$$e_s = 611\exp\left[\frac{L_v}{R_V}\left(\frac{1}{273.15} - \frac{1}{T}\right)\right]$$

where R_v is the gas constant for water vapour (461.39 J kg^{-1} K^{-1}).
This relationship can be used to compute the **specific humidity** at saturation q_{sat}, using the relationship between the **saturation vapour pressure** and **humidity** and knowing the air pressure p ($q_{sat} \simeq 0.622\, e_{sat}/p$).

Climate
Climate is traditionally defined as the description, in terms of the mean and variability over a 30-year reference period, of the relevant atmospheric variables (temperature, precipitation, winds). In a wider sense, it is the statistical description of the **climate system**.

Climate model
A climate model is a simplified representation of the **climate system**, generally in the form of a set of mathematical equations.

Climate sensitivity
See **equilibrium climate sensitivity**.

Climate system
The climate system consists of five major components: the atmosphere, the **hydrosphere**, the **cryosphere**, the land surface and the **biosphere**.

Climatic precession
Climatic precession ($ecc\ \sin\tilde{\omega}$) is related to the distance between the Earth and the Sun at the summer solstice.

Climatological
The climatological value of a variable is its mean over a reference period (generally 30 years).

Cloud microphysics
Cloud microphysics describes the physical processes that occur in clouds at scales smaller than a few centimetres.

Cloud radiative forcing
The cloud radiative forcing (CRF) is a measure of the effect of clouds on the Earth's radiation budget. It could be evaluated by computing the difference of the radiative fluxes at the top of the atmosphere with and without clouds. CRF is often separated in a **longwave** and a **shortwave** contribution. Clouds reduce the longwave losses from the Earth because their tops emit at a lower temperature than the Earth surface. On the shortwave part of the spectrum, clouds reflect a part of the incoming solar radiation because of their relatively high **albedo** and thus tend to cool the Earth. The sum of those two effects is negative and presently amounts to a net cloud **radiative forcing** of around -20 W m^{-2}.

Convection
In thermal convection, some of a fluid (liquid or gas) receives heat. It thus warms, becomes less dense and rises. It is continuously replaced by colder fluid which is subsequently heated and thus also rises, forming a convection loop or convection current. Convection stops when the temperature differences between different parts of the fluid are too small to create any movement.

Coriolis force
The Coriolis force causes an apparent deflection of moving objects towards the right in the Northern Hemisphere and towards the left in the Southern Hemisphere when viewed from a frame of reference attached to the Earth (or equivalently when viewed by an observer who is standing on the Earth). This occurs because of the Earth's rotation, and the Coriolis effect is actually present whenever a rotating frame of reference is used.

Correlation
A correlation is a measure of the strength of a linear relationship between two variables. It is often estimated by the Pearson correlation coefficient *r*.

Cosmogenic isotopes
Cosmogenic isotopes are created when elements in the atmosphere or on Earth are bombarded by **cosmic rays.**

Cosmic rays
Cosmic rays are high energy particles coming from outer space.

Cryosphere
The cryosphere is the portion of the Earth's surface where water is in solid form (**sea ice**, lake and river ice, snow cover, **glaciers**, **ice caps** and **ice sheets**).

Cyclones
A cyclone is a low pressure system in the atmosphere.

Deep water formation
Deep water formation is the process through which the water masses acquire their characteristics (in particular, their temperature and salinity) at the surface before sinking to great depths. In the deep ocean, the temperature and salinity change very slowly. As a consequence, the properties of the waters found at great depths in the ocean can be traced over very large distances to their origins (their 'formation') at the surface. See also **water mass formation** and **thermohaline circulation**.

Diapycnal
The diapycnal direction lies at right angles to the local **isopycnal** surface. Consequently, the angle between the diapycnal direction and the vertical is very small.

Dissolution
Dissolution is the process by which a solid or liquid forms a homogeneous mixture with a solvent (in climatology the solvent is generally water). During this process the crystal lattice of the solid is broken down into individual ions, atoms or molecules.

Dissolved inorganic carbon
Dissolved inorganic carbon (*DIC*) is the sum of the concentration of the three forms of inorganic carbon present in the ocean (i.e. carbonic acid, H_2CO_3, bicarbonate, HCO_3^- and carbonate ions, CO_3^{2-}).

Downwelling
A downwelling is a downward movement of water in the ocean.

Dry air
Dry air is air without its water vapour. Air (or moist air) is composed of dry air plus water vapour.

Earth system
The Earth system can be divided in five spheres: the atmosphere (gaseous envelope), the **hydrosphere** (liquid water), the **cryosphere** (solid water, i.e. ice), the **lithosphere** (solid Earth) and the **biosphere** (life). The Earth system is generally considered as broader than the **climate system** as it explicitly includes some processes (such as some geological processes) that do not influence **climate**. The description of the Earth system also generally takes human activities into account.

Earth system model
An Earth system model is a model that includes a representation of several components of Earth system (atmosphere, ocean, sea ice, land surface, land vegetation, carbon cycle, ice sheet, etc) while the term **climate model** is generally used for model that includes representation of the atmosphere, sea-ice, ocean and land surface only.

Easterlies
Easterlies are winds coming from the east that are typically found in the tropics.

Eccentricity
Eccentricity (*ecc*) describes the shape of an ellipse (such as that described by the Earth's orbit around the Sun) with a semi-major axis *a* and a semi-minor axis *b*. It is defined as:

$$ecc = \frac{\sqrt{(a^2 - b^2)}}{a}$$

Ecliptic plane
The ecliptic plane is the geometric plane containing the mean orbit of the Earth around the Sun. The ecliptic is the intersection of the **celestial sphere** with the ecliptic plane and it corresponds to the apparent path that the Sun traces out in the sky.

Eddies

Eddies are whirlpool like transient features in the ocean and atmosphere. Their spatial extent is smaller than that of the general circulation. Eddies in the atmosphere are called **cyclones** or anticyclones. Mesoscale eddies in the ocean have a typical size of a few kilometres to a few tens of kilometres.

Ekman transport

Because of the Earth's rotation, the surface ocean transport induced by the wind is directed (outside the equatorial regions) to the right of the prevailing wind in the Northern Hemisphere and to the left in the Southern Hemisphere. This is called the Ekman transport. The integral over the vertical of the ocean transport caused by the wind is perpendicular to the wind direction.

Electromagnetic spectrum

Electromagnetic radiation is classified by wavelength into radio, microwave, infrared, visible, ultraviolet, X-rays and gamma rays. We perceive the radiation in the visible region as light.

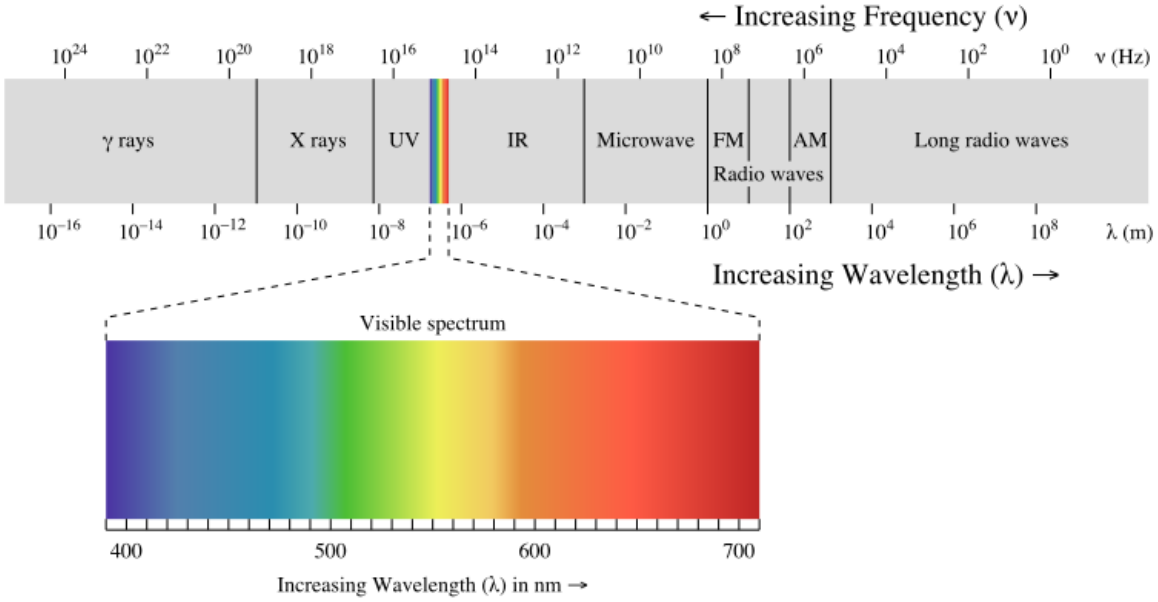

Spectrum of electromagnetic radiations. Based on the article from Wikipedia: electromagnetic radiation http://en.wikipedia.org/wiki/Electromagnetic_radiation.

Emissivity

The emissivity of an object (ε) is the ratio of energy radiated by the object to the energy radiated by a **black body** at the same temperature. It is a measure of a material's ability to absorb and radiate energy. A true black body would have an $\varepsilon = 1$, while any real object has $\varepsilon < 1$.

Equilibrium climate sensitivity

The equilibrium climate sensitivity is generally defined as the change in the global mean surface temperature after the climate system has reached a new equilibrium in response to a doubling of the CO_2 concentration in the atmosphere.

Equinox
The equinoxes are the moments when the Sun is positioned directly over the Earth's equator and, by extension, the apparent position of the Sun at that moment. The equinox during which the Sun passes from south to north is known as the vernal equinox.

Evapotranspiration
The evapotransipration is the transfer of water from Earth's surface to the atmosphere. It is the sum of evaporation form the soils, leaves, etc and the transpiration of plants.

Feedback
A feedback tends to amplify (positive feedback) or reduce (negative feedback) the response of a system to a perturbation through mechanisms internal to the system itself.

Finite difference method
Finite difference methods are numerical methods used to solve differential equations by approximating the derivatives by finite differences.

Forcing
A climate forcing is a perturbation, originating in elements which are not part of the **climate system** being investigated, that induces changes in the climate system. For instance, a change in total solar irradiance is a forcing, as it modifies the Earth's climate. Forcings can be natural or anthropogenic depending of their origin.

Fourier series
A Fourier series decomposes a function into a sum of sines and cosines.

Fourier's law
Fourier's law (also called the conduction law) states that the heat flux trough a material (F_{cond}) is proportional to the negative temperature gradient in the material. In one dimension (along the x axis), this can be expressed as:

$$F_{cond} = -k \frac{\partial T}{\partial x}$$

where k is the thermal conductivity.

Geostrophic equilibrium
In the atmosphere and the ocean, on a large scale and away from the boundaries (surface, coast) and the equator, the dominant terms in the horizontal equation of motion are the **Coriolis force** and the force due to the horizontal pressure gradient. The geostrophic balance, which assumes a balance between those two forces, is thus a reasonable approximation:

$$f v_g = \frac{1}{\rho} \frac{\partial p}{\partial x}$$

$$-f u_g = \frac{1}{\rho} \frac{\partial p}{\partial y}$$

In this equation p is the pressure, ρ the density, f the Coriolis parameter and u_g, v_g the components of (geostrophic) velocity in the two horizontal directions. f equals $2\Omega \sin \phi$, where Ω is the Earth's angular velocity and ϕ the latitude. f is positive in the Northern Hemisphere and negative in the Southern Hemisphere. When this balance is achieved, the

fluid is said to be in geostrophic equilibrium and, knowing the horizontal pressure distribution, the horizontal velocity can be computed. The geostrophic equilibrium explains why the flow is clockwise around a high pressure in the Northern Hemisphere, and anticlockwise around a low pressure.

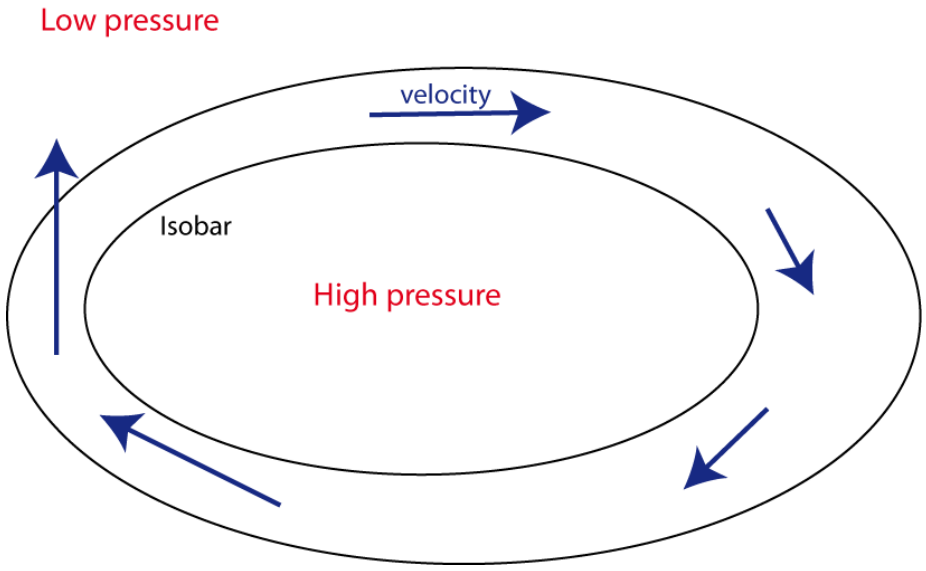

Geostrophic flow around closed isobars in the Northern Hemisphere.

Glacial inception
The glacial inception is the start of a glacial period characterised by an increase in the volume of the **ice sheets**.

Glacier
A glacier is a mass of ice that originates on land, and usually has an area larger than 0.1 km^2.

Gradient
The gradient of a scalar field is a vector that points in the direction of the greatest increase of the scalar field and whose magnitude is proportional to the rate of change. The gradient of f(x,y,z) denoted grad(f), $\vec{\nabla} f$ or ∇f is defined by:

$$\vec{\nabla} f = \left(\frac{\partial f}{\partial x}, \frac{\partial f}{\partial y}, \frac{\partial f}{\partial z} \right)$$

The projection of the gradient over one direction is often called the gradient in this direction. For instance $\partial f / \partial z$ is often called the vertical gradient of f.

Greenhouse gas
A greenhouse gas is a gas that has an impact on the radiative properties of the atmosphere by its ability to absorb radiation in specific infrared wavelengths, leading to the greenhouse effect.

Grid
The numerical resolution of the equations governing the development of the **climate system** generally requires the definition of a grid, whose nodes correspond to the locations where the model variables are computed. The values computed at these nodes provide enough

information to reconstruct, over the whole domain, an approximation of the corresponding field (such as the temperature). An important characteristic of a grid is its spatial resolution, which is related to the distance between two different values computed by the **model**.

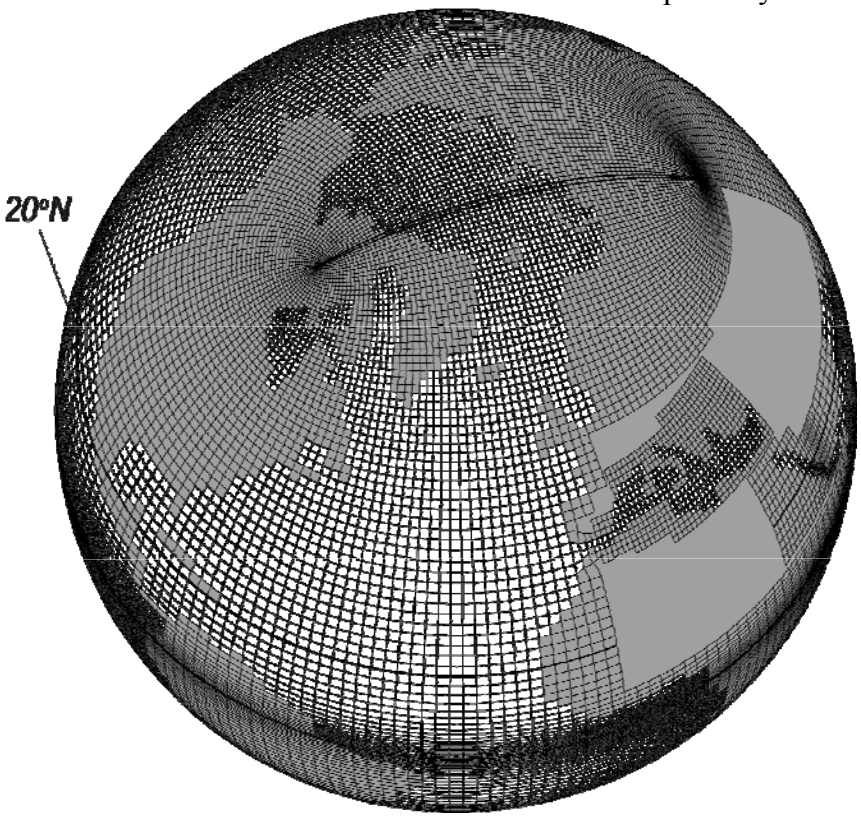

Example of a numerical grid for the ocean model NEMO (http://www.lodyc.jussieu.fr/NEMO/, ORCA2 configuration). Variables such as the temperature are obtained at the center of all the oceanic elements whose sides are defined by the grid coordinates (i.e. the lines on the figures). The resolution of the grid variable but is of the order of 2°, meaning that the distance between two points were variables are computed is of the order of 200 km. Copyright NEMO team, 2008.

Gulf Stream

The Gulf Stream is a strong current found along the southeast coast of the USA. The current is mainly wind driven and forms the western boundary of the subtropical **gyre** in the Atlantic. To the general public, the Gulf Stream also means the whole northern branch of the subtropical gyre, including the North Atlantic Drift. As the Gulf Stream transports warm water northward, its path is associated with relatively high temperatures compared to other oceanic regions at the same latitude. However, rather than stressing the climate role of the Gulf Stream, it is more appropriate to analyse the oceanic heat transport associated with the wind driven and **thermohaline circulations**, both of which contribute to the Gulf Stream mass transport. In particular, the thermohaline circulation in the Atlantic contributes to the relative mild conditions found in Europe. Nevertheless, the main reason for the different winter temperatures in Eastern Canada and Western Europe is the atmospheric circulation that brings relatively warm air of oceanic origin to Europe.

Gyres

Gyres are quasi-circular patterns of circulation in the ocean. For instance, the subtropical gyres are almost closed loops of ocean currents present at latitudes between roughly 15 and 45°.

Hadley cell
Hadley cells are thermally driven cells with rising air near the equator in the **intertropical convergence zone** (ITCZ), poleward flow in the upper **troposphere**, subsiding air in the subtropics at around 30°, and return flow from the subtropics to the equatorial regions as part of the **trade winds**.

Halocarbons
Halocarbons are organic compounds in which one or more carbon atoms are linked with one or more halogen atoms (fluorine, chlorine, bromine or iodine).

Holocene
The Holocene is the name given to the latest **interglacial** period that started around 10 000 years ago and is still continuing.

Hour angle
The hour angle *HA* indicates the time since the Sun was at its local meridian, measured from the observer's meridian westward. *HA* is thus zero at the local solar noon. It is generally measured in radians or in hours (2π rad = 24 hours).

Humidity
Atmospheric humidity is the amount of water vapour in the air. Different definitions are available, based on the mass ratio of water vapour compared to that of air, or the partial pressure of the vapour. See also **specific humidity**, **relative humidity** and **saturation vapour pressure.**

Hydrosphere
The hydrosphere is the water on and underneath the Earth's surface (ocean, seas, rivers, lakes, underground water).

Hydrostatic equilibrium
On a large scale in the atmosphere and the ocean, the dominant terms in the vertical equation of motion are gravity and the force due to the vertical pressure gradient. The hydrostatic balance, which assumes these two forces balance each other, thus holds to a very good approximation:

$$\frac{\partial p}{\partial z} = -\rho g$$

In this equation, p is the pressure, ρ the density and g the gravitational acceleration. When this balance is achieved, the fluid is said to be in hydrostatic equilibrium and, knowing the density, the pressure can be computed by integrating the equation along the vertical. The equation shows that sea level pressure depends on the mass of the whole air column above the surface.

Iceberg
An iceberg is a large piece of ice, which originates on land, floating in open water.

Ice cap
An ice cap is a dome-shaped mass of ice that covers less than 50 000 km² of land.

Ice sheet
An ice sheet is a dome-shaped mass of ice that covers more than 50 000 km² of land.

Ice shelf
An ice shelf is a thick platform of floating ice originating on land, which has flowed across the coastline onto the sea. The boundary between the grounded ice that rests on bedrock and the floating ice shelf is called the grounding line.

Insolation
The instantaneous insolation is the energy received per unit time on 1 m^2 of a horizontal plane at the top of the atmosphere (or equivalently on a horizontal plane at the Earth's surface if we neglect the influence of the atmosphere). It is measured in W/m^2. The daily insolation is the total insolation received during one day (J/m^2).

Internal energy
The internal energy of a system is the sum of the energy of all the particles in the system, measured by reference to the centre of mass of the system. For a perfect gas (a good approximation for the atmosphere), a solid, and an incompressible fluid (a good approximation for the ocean), it is function of the temperature alone.

Interglacial
An interglacial is a relatively warm period between two glacial periods (ice ages).

Intertropical convergence zone
The intertropical convergence zone (ITCZ) is a band close to the equator where the trade winds of the two hemispheres meet, resulting in a convergence, rising air and heavy precipitation.

Isopycnal
An isopycnal is a surface of equal potential density in the ocean. The adjective isopycnal refers to changes or processes that take place along surfaces of equal potential density. Isopycnals are always very close to the horizontal but small deviations from the horizontal may have a large impact on ocean dynamics and on the representation of some processes (such as diffusion) in ocean models.

Isotope
Isotopes are atoms whose nuclei contain the same number of protons (and are therefore the same element) but a different number of neutrons. Isotopes have very similar chemical properties but different masses and different physical properties (some of which have an influence on chemical reactions). Isotopes can be divided into stable and unstable (radioactive) varieties. Radioactive isotopes decay and their abundance decreases with time, unless new isotopes are produced.
The isotopic composition of various archives, such as the water in ice cores, sediments in the ocean, three rings, etc, provides very valuable information on past temperatures, sea level changes, and exchanges between the various carbon reservoirs.
The isotopic composition is often estimated through a delta value (δ) . For instance for ^{18}O, a stable isotope of the oxygen, it is given by:

$$\delta^{18}O = \left[\frac{\left({}^{18}O / {}^{16}O \right)_{sample}}{\left({}^{18}O / {}^{16}O \right)_{standard}} - 1 \right].1000$$

where $\left({}^{18}O / {}^{16}O \right)_{sample}$ is the ratio of ${}^{18}O$ to the dominant isotope ${}^{16}O$ in the sample being analysed, compared to the ratio in a standard reference sample.

Isotopic fractionation
Because of the different properties of the various **isotopes**, they can be partially separated during chemical reactions, phase changes or exchanges between different media, resulting in variations of the isotope ratio in different substances or phases. This isotopic fractionation can be due to isotope exchange reactions at equilibrium, or to kinetic processes which depend on differences in the reaction rates of the isotopes.

Laplacian
The Laplacian operator ∇^2 is a differential operator that can be written in Cartesian coordinates in three dimensions, x, y, z, as:

$$\nabla^2 = \frac{\partial^2}{\partial x^2} + \frac{\partial^2}{\partial y^2} + \frac{\partial^2}{\partial z^2}$$

Lapse rate
The temperature lapse rate (Γ) is the negative of the vertical **gradient** of temperature.

Latent heat
The latent heat (L) is the energy released or absorbed by a substance during a change of phase. More formally, it is the change in enthalpy associated with a phase transition at temperature T. The latent heat of fusion is the energy associated with changes between the solid and the liquid states, while the latent heat of vaporisation is associated with transitions between the liquid and the gaseous state. See **Clausius-Clapeyron equation**.

Lead
A lead is an elongated area of open water inside the sea-ice pack.

Legendre polynomials
Legendre polynomials $P_n(\mu)$ are polynomial of degree n defined as.

$$P_n(\mu) = \frac{1}{2^n n!} \frac{d^n (\mu^2 - 1)^n}{d\mu^n}$$

The first four Legendre polynomials are thus

$$P_0(\mu) = 1$$
$$P_1(\mu) = \mu$$
$$P_2(\mu) = \frac{1}{2}\left(3\mu^2 - 1\right)$$
$$P_3(\mu) = \frac{1}{2}\left(5\mu^3 - 3\mu\right)$$

Limestone
Limestone is a sedimentary rock mainly composed of **calcite**.

Lithosphere
The lithosphere is the outermost part of the solid Earth. It includes the Earth's crust and the upper part of the mantle.

Longwave radiation
The thermal radiation emitted by the Earth in the infrared part of the **electromagnetic spectrum** is often referred to as longwave radiation.

Lysocline
The lysocline is the depth above which the rate of dissolution of $CaCO_3$ is very low.

Melt ponds
Melt ponds are pools of water that form at the surface of sea ice in spring and summer mainly in the Arctic. They occur because of the ice and snow melting. They have a lower albedo than the ice and have a significant influence on the surface heat balance.

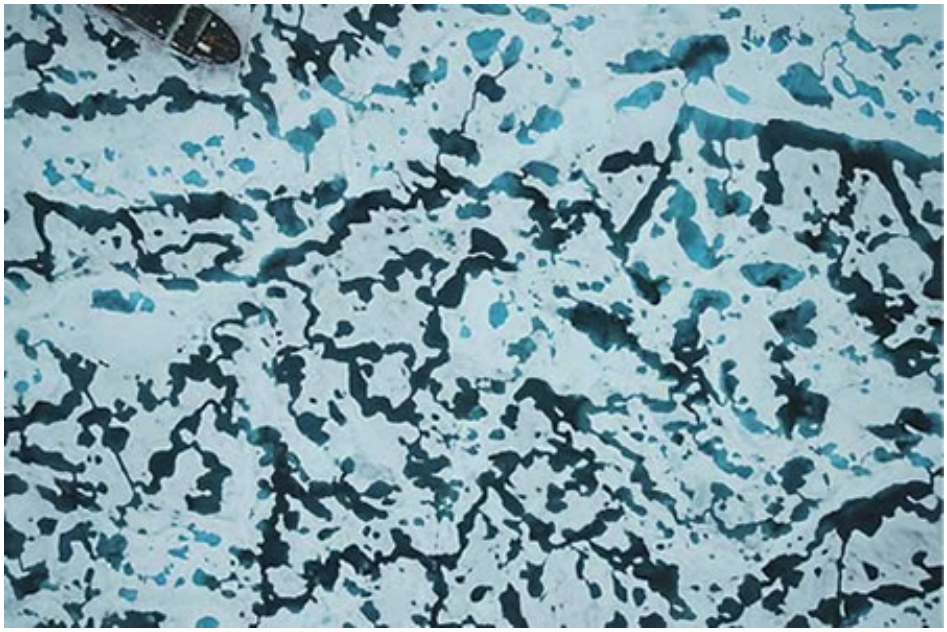

Melt ponds at the surface of Arctic sea ice. The boat in the upper left corner provides a rough scale to the figure. Source: http://psc.apl.washington.edu/arctic_basin/field2005/westward.html. Photo D. Perovich, reproduced with permission.

Meridional
The adjective meridional refers to the north-south direction. The meridional transport (of mass or heat for instance) is a net transport from one latitudinal band to another, either northward or southward.

Meridional overturning circulation
The **meridional** overturning circulation (MOC) of the ocean is a circulation defined in the latitude-depth plane. It is represented by a stream function obtained as the integral of the velocity between the east-west boundaries of the oceanic basin and from the surface to the

depth considered. The MOC in the Atlantic is often related to the **thermohaline circulation** but the difference should be kept in mind as the MOC also includes shallow wind driven cells, such as the one observed in the equatorial regions.

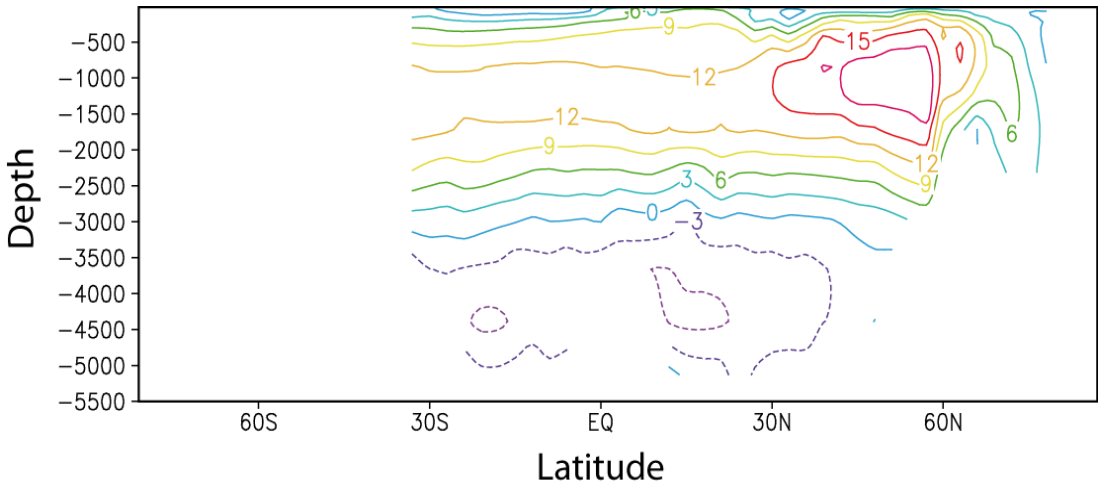

Meridional overturning stream function (in Sv = 10^6 m^3 s^{-1}) in the Atlantic for present-day conditions, as given by the climate model LOVECLIM. By convention, solid contours show clockwise flows and dashed contours (corresponding to negative values) show anti-clockwise flows. The values plotted at a particular depth represent the mass (actually the volume) transported between the surface and the point considered. For instance, there is a northward mass transport with a maximum value of about 13 Sv at 30°S over the top 1400 m of the Atlantic. Below this depth, the transport is southward while close to the bottom, the transport is northward again. This figure also shows a large sinking (downward mass transport) in the North Atlantic.

Metamorphism
Metamorphism is changes in solid rocks caused by changes in temperature and pressure.

Moisture availability function
The moisture availability function is an estimate of the fraction of water that can be evaporated from a surface, compared to a wet surface at the same temperature and in the same atmospheric conditions. It is defined by the ratio between the evaporation rate of the given surface (E) and the potential evaporation (E_p), i.e. the evaporation that would occur on a wet homogenous surface such as a lake:

$$\beta = E/E_p$$

Monsoon
A monsoon is a seasonal reversal of surface winds and their associated precipitation, caused by the differential heating of a land mass and its adjacent ocean.

Net primary production
The net primary production (NPP) is the rate of carbon uptake related to photosynthetic activities. It is the difference between the uptake by **photosynthesis** (gross primary production) and respiration of plants or **phytoplankton**.

Numerical grid
See **grid**.

Obliquity of the ecliptic
The obliquity (ε_{obl}) is the angle between the equator and the **ecliptic**. It corresponds to the angle between the axis of rotation of the Earth and the perpendicular to the **ecliptic plane**.

Oceanic mixed layer
The oceanic mixed layer is the upper part of the ocean which is in direct contact with the surface. The properties of this layer are influenced by the presence of the surface and in turn influence the exchanges between the ocean and the atmosphere. Vertical mixing is generally strong in the oceanic mixed layer because of the relatively intense turbulence there, and the oceanic properties (temperature, salinity, etc) are fairly uniform in the layer because of the mixing.

Optical depth
The optical depth measures the fraction of light that is **scattered** or absorbed during its path through a medium, so producing a reduction of the intensity of the beam. If I_0 is the density of the radiation at the source (for instance the top of the atmosphere) and I the intensity at a particular point (usually the Earth's surface), the optical depth τ is defined by

$$\tau = ln\ I/I_0,$$

corresponding to

$$I/I_0 = e^{-\tau}$$

In atmospheric sciences, τ is usually defined along a vertical path.

Orbital parameters
In climatology, the characteristics of the Earth's orbit are determined by three parameters, called the orbital parameters: the **obliquity** (ε_{obl}), the **eccentricity** (ecc) and the **climatic precession** ($ecc\ \sin\tilde{\omega}$).

Ozone
Ozone is a molecule consisting of three oxygen atoms (O_3). Its presence in the **stratosphere** protects the Earth's surface from dangerous ultraviolet radiation by absorbing it. In the lower **troposphere**, it is a dangerous, strongly irritating pollutant.

Parameterisation
Some processes are not explicitly included in models because of simplifications, lack of knowledge of the mechanisms, or because the spatial resolution of the model is not high enough to include them. To take the first order effects of these processes into account, they are represented by parameterisations in models.

Partial differential equations
Partial differential equations (PDEs) are equations involving an unknown function of several independent variables and its partial derivatives with respect to these variables.

Perihelion
The perihelion is the point in the Earth's orbit that is the closest to the Sun.

Permafrost
The permafrost is a layer of soil or rock beneath the surface that remains below 0° C throughout the year. It occurs when the summer warming is insufficient to reach the bottom of the layer of frozen ground. Permafrost can include ground ice, or simply soil or rock at subzero temperatures (dry permafrost).

pH
The pH is a measure of the acidity of a solution, for instance sea water, generally estimated by the logarithm of its concentration of hydrogen ions (H^+):

$$pH= -\log_{10}[H^+]$$

An acidic solution has a pH lower than 7 (at 25°C), a neutral solution a pH of 7 and an alkaline (basic) solution a pH higher than 7.

Photosynthesis
Photosynthesis is the process by which plant, algae and some bacteria produce complex organic compounds from carbon dioxide using energy from light.

Phytoplankton
Phytoplankton is a type of **plankton** that produces complex organic compounds from simple inorganic molecules. This can be achieved by using energy from light (by **photosynthesis**) or through inorganic chemical reactions.

Planetesimals
Planetesimals are small bodies (much smaller than a planet) in the solar system.

Plankton
Plankton consists of organisms (mostly microscopic plants and animals) that drift in the seas or in bodies of fresh water. See **phytoplankton** and **zooplankton**.

Plant functional type
Plant functional types (PFTs) are groups of plants that share common characteristics (e.g. tropical trees, deciduous temperate trees, needle leaf boreal trees, different types of grass).

Polynya
A polynya is a region of open water, larger than a lead, inside the ice pack.

Potential temperature
The potential temperature is the temperature that a sample of seawater or air initially at some depth z would take if it were lifted adiabatically (i.e. without heat or mass exchanges with surrounding parcels) to a reference level z_r.

Precession
See c**limatic precession**.

Projection
A climate projection is a potential future state of the climate system. The main difference between predictions and projections is the additional uncertainty in projections as they depend on the **scenario** selected for future changes in external **forcings**.

Proxy data
Proxy data is indirect information on climate variability collected from various climate sensitive recorders (tree rings, corals, ice and marine cores, lake sediments, historical data, etc).

Radiation
See **electromagnetic radiation**.

Radiative forcing
Radiative forcing is the change in the net, downward minus upward irradiances (expressed in W m^{-2}) at the **tropopause** due to a change in an external driver of climate change, such as, for example, a change in the concentration of carbon dioxide or in the output of the Sun. Radiative forcing is computed with all tropospheric properties held fixed at their unperturbed values, and after allowing for stratospheric temperatures to readjust to radiative-dynamical equilibrium. Radiative forcing is called instantaneous if no change in stratospheric temperature is accounted for. (*Definition from IPCC 2007*).

Reanalyses
Weather forecasting centres analyse the present atmospheric configuration every day, using models to interpolate observations in order to construct physically consistent estimates of the atmospheric state. Because of changes in the structures of the models and in the procedures used, those analyses are not necessary consistent over long periods. In order to reduce the long-term biases, reanalyses are performed, using the same model and the same procedure over the whole period. However, biases are still present as the amount of available data change over time. The most widely used reanalyses are those computed by the National Center for Environmental Prediction and the National Center for Atmospheric Research (NCEP/NCAR) (http://www.cdc.noaa.gov/cdc/reanalysis/reanalysis.shtml) and of the European Centre for Medium-Range Weather Forecasts (ECMWF) (ERA-40) (http://www.ecmwf.int/research/era/).

Regression
Linear regression is a statistical procedure that represents a variable (the dependent variable) as a linear function of one or more other variables (the independent variables). The model parameters that link the dependent and independent variables are called the regression coefficients.

Relative humidity
The relative **humidity** (*RH*) of an air parcel is defined as the ratio of the partial pressure of the water vapour in the parcel to the **saturation vapour pressure** at the temperature of the air parcel. At saturation (i.e. equilibrium between the liquid and vapour phases) the relative humidity is 1 (or 100%).

Resolution
See **grid**.

Saturation horizon
The saturation horizon of calcium carbonate is the transition depth between the supersaturated upper ocean and the undersaturated deep ocean.

Saturation vapour pressure
The saturation vapour pressure (e_s) is the partial pressure of a vapour when the vapour phase is in equilibrium with the liquid phase. When the water vapour pressure of the atmosphere is equal to the saturation vapour pressure, the **relative humidity** is one.

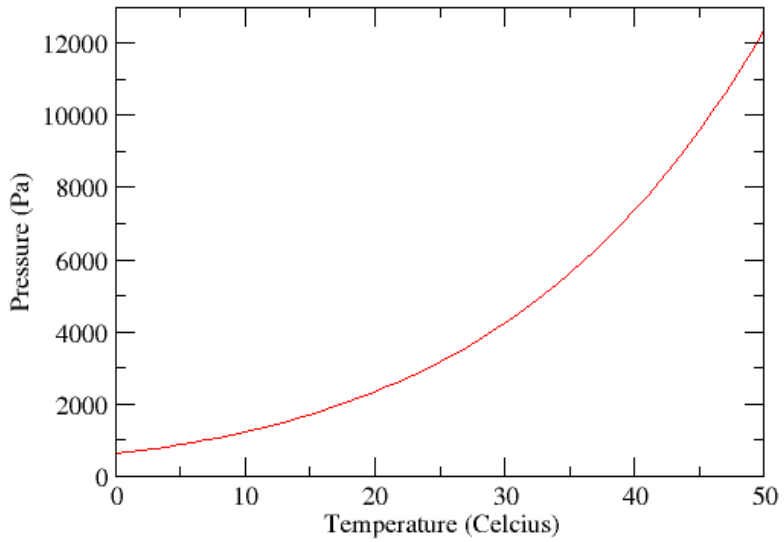

Saturation vapour pressure over water surface as a function of the temperature.

Scattering
Scattering describes a process in which radiation deviates from a straight trajectory, for instance because of the presence of some particles in the gas it passes through.

Scenario
A climate scenario is an estimate of future changes in external forcing, the emission and/or concentration of **greenhouse** gases, **aerosols**, various pollutants in the atmosphere, land use, etc. These factors are often related to estimates of future socioeconomic and technological developments.

Sea ice
Sea ice is the ice that forms when seawater freezes.

Sedimentation
Sedimentation in the ocean is the tendency of particles in suspension or molecules in solution to settle out towards the ocean floor.

Sensible heat
The sensible heat is the energy that can be transferred in the form of thermal energy or heat.

Shortwave radiation
Shortwave radiation is another name for the radiation emitted by the Sun and received by the Earth.

Soft tissue pump
The soft tissue pump is the net downward flux of carbon associated with the transport of organic matter from the surface layer where it is produced, to the deeper layers where it can be remineralised.

Solar constant
The solar constant (S_0) is the amount of incoming solar **electromagnetic radiation** per unit area at the mean Earth−Sun distance, measured on the outer surface of the Earth's atmosphere, in a plane perpendicular to the rays (in W m^{-2}). As this value is not constant in time, the term **total solar irradiance** is often preferred in recent years.

Solar declination
The solar declination (δ) is the angle between a line from the centre of the Earth towards the Sun and the **celestial equator**.

Solubility
At equilibrium, the partial pressure of a gas A above a liquid is proportional to the concentration of A in the liquid (Henry's law). We can thus define the solubility S_A as the ratio between the equilibrium concentration $[A]$ and the partial pressure p^A:

$$S_A = \frac{[A]}{p^A}$$

For exchanges between the ocean and the atmosphere, the solubility is mainly a function of the temperature and, to a lesser extent, the salinity.

Specific heat capacity at constant pressure
The specific heat capacity at constant pressure of a body (c_p) is the energy required to increase the temperature of 1 kg of the body by 1°C at a constant pressure

Specific heat capacity at constant volume
The specific heat capacity at constant volume of a body (c_v) is the energy required to increase the temperature of 1 kg of the body by 1°C at a constant volume.

Specific humidity
Specific **humidity** (q) is the ratio of the mass of water vapour to the mass of dry air plus water vapour in a particular volume of air. As the mass of the water vapour is much less than the mass of the air, the specific humidity is very close to the *mixing ratio*, defined as the ratio of the mass of water vapour to the mass of dry air.

Statistic
A statistic is the result of applying a statistical algorithm to some data. The commonest statistics are the average and standard deviation of a range of observations.

Stefan-Boltzmann' s law
Stefan-Boltzmann's law, also known as Stefan's law, states that the total energy radiated per unit surface area of a **black body** in unit time is directly proportional to the fourth power of the temperature T:

$$E = \sigma T^4$$

where σ is the Stefan-Boltzmann constant ($\sigma = 5.67\ 10^{-8}$ W m^{-2} K^{-4}).

Stomata
A stoma is a pore, found for instance in leaves, that is used by plants for gas exchanges with the atmosphere. Air containing carbon dioxide and oxygen necessary for **photosynthesis** and respiration enters the plant through these openings while the oxygen produced by photosynthesis is expelled through them. These exchanges include a release of water vapour to the atmosphere (transpiration).

Storm track
The storm track is the path that **cyclones** tend to follow in mid-latitudes.

Stratification
The stratification is a measure of the vertical density gradient.

Stratosphere
The stratosphere is the layer of the atmosphere located above the **tropopause**, at an altitude between roughly 10 and 50 km.

Subduction
Subduction occurs in regions where two tectonic plates meet, resulting in one plate sliding underneath the other and moving down into the mantle. In subduction, lighter continental plates generally ride above denser oceanic plates.

Subsidence
The subsidence is a downward (air) motion.

Surface boundary layer
See **atmospheric boundary layer**.

Taiga
Taiga is a **boreal** forest covered by conifers.

Taylor series
A Taylor series is the representation of a function as an infinite sum of terms. These terms are calculated from the values of the derivatives of the function at a single point. If the series is truncated to a finite number of terms, the resulting Taylor polynomial provides a polynomial approximation of the function around that point.

Teleconnection
A teleconnection is usually indicated by the correlation between the values observed at two separate locations. This link is related to a pattern of variability, associated with wave propagation, the presence of mountains, etc.

Thermal expansion
Thermal expansion is the change in the volume of a constant mass (e.g. of oceanic water) as a result of a change in its temperature. In the sea, a temperature increase produces an increase in the volume of water (also called dilation or dilatation) and thus a rise in sea levels if the oceanic mass remains unchanged.

Thermocline
A thermocline is a region in the ocean with a strong temperature gradient. Oceanographers usually make a distinction between the seasonal thermocline (which is formed at the base of the summer **mixed layer**) and the permanent thermocline (which separates the surface layer from the relatively homogenous deep ocean).

Thermohaline circulation
The thermohaline circulation is a large-scale circulation in the ocean, which involves circulation at both the surface and at great depths. It is, at least partly, driven by the density contrasts in the ocean.

Timescale
A timescale is related to the dominant periodicity of the phenomena of interest to an investigator. For instance, if someone is interested in variations on a seasonal timescale, the analysis will be mainly devoted on the differences between the various seasons. Timescales can also be daily, monthly, annual, decadal, centennial, millennial, etc.
The timescale of variation of a process represents the time over which significant variations of the processes can be expected to be observed. It takes millions of years for plate tectonics to induce movements of the continents that have a clear impact on the climate. This process is thus said to be important for climate on the timescale of millions of years. The timescale can represent an order of magnitude or be defined very precisely, for example, on the basis of spectral analysis or on an exponential decay.

Total solar irradiance
The total solar irradiance is the radiant energy (i.e., the energy of **electromagnetic** waves) emitted by the Sun over all wavelengths, that falls each second on 1 square meter perpendicular to the Sun's rays at the mean Earth−Sun distance, measured at the top of the Earth's atmosphere. It measures the solar energy flux in W m^{-2}, and is sometimes called **solar constant**.

Tracer
A tracer is a constituent that is transported by a flow. A distinction is often made between active tracers that modify the flow through their influence on density (such as temperature and salinity in the ocean), and passive tracers that do not influence the motion (such as **chlorofluorocarbons** in the ocean). In oceanography, **phytoplankton** and **zooplankton** are generally treated as tracers because their movement is mainly determined by the ocean circulation.

Trade winds
Trade winds are easterly winds (from the northeast in the Northern Hemisphere and the southeast in the Southern Hemisphere) characteristic of tropical regions.

Transient climate response
The transient climate response (TCR) is defined as the global average of the annual mean temperature change averaged over years 60 to 80 in an experiment in which the CO_2 concentration is increased by 1% per year until year 70 (i.e. until it reaches double its initial value).

Trophic level
Trophic levels are the various stages within food chains. Standard examples of trophic levels are the primary producers, the primary consumers (herbivores), and higher-level consumers

(predators), as well as the decomposers that transform dead organisms and waste materials into nutrients available for the producers.

Tropopause
The tropopause is the boundary between the **troposphere** and the **stratosphere** located at an altitude of about 10 km.

Troposphere
The troposphere is the lowest part of the Earth's atmosphere. Its average depth is about 10 km.

True longitude
The true longitude (λ_t) is the angle on the **ecliptic plane** between the position of the Earth relative to the Sun at any given time and at the vernal **equinox**.

Truncation error
In a numerical scheme using finite differences, the truncation error is the difference between the partial differential equation and the finite difference equation.

Tundra
The tundra is a **biome**, characteristic of regions where trees cannot grow because the temperature is too low.

Upwelling
An upwelling is an upward movement of water in the ocean.

Validation
Validation is the process of determining the degree to which a model is an accurate representation of the real world from the perspective of the intended uses of the model. Definition from the American Institute of Aeronautics and Astronautics (AIAA, http://www.aiaa.org/index.cfm) "Guide for the Verification and Validation of Computational Fluid Dynamics Simulations", Reston, VA 1998

Verification
Verification is the process of determining that a model implementation accurately represents the developer's conceptual description of the model and the solution to the model. Definition from the American Institute of Aeronautics and Astronautics (AIAA, http://www.aiaa.org/index.cfm) "Guide for the Verification and Validation of Computational Fluid Dynamics Simulations", Reston, VA 1998.

Vernal equinox
See **equinox**.

Walker circulation
The Walker circulation is a zonal convection loop in the equatorial regions. In the Pacific, it is associated with **ascendance** over the warm Western Pacific, **subsidence** over the cold East Pacific, eastward transport in the upper troposphere and westward atmospheric flow in the lower layers.

Water mass formation
Oceanographers talk about water mass formation when a volume of water acquires specific properties, such as temperature and salinity, in interactions with the atmosphere and keeps them while being transported by ocean currents. See **deep water formation** and **thermohaline circulation**.

Weathering
Weathering is the decomposition of rocks and soils at or near the Earth's surface.

Westerlies
Westerlies are winds coming from the west that are typically found at mid latitudes.

Wien' s law
Wien's law states that the wave length at which the radiant energy of a **black body** is greatest is only a function of temperature. For the Sun, this maximum is located in the visible part of the **spectrum**, while for the Earth it is located in the infrared.

Zenith distance
The solar zenith distance is defined as the angle between the solar rays and the normal to the Earth's surface at a particular point.

Zonal
The adjective zonal refers to the east-west direction. For instance, the zonal mean, for any latitude, is the average over all longitudes.

Zooplankton
Zooplankton is the type of **plankton** that consumes (or grazes) **phytoplankton**.